Piano acoustics : string's double polarisation and piano source identification

Jin Jack Tan

NNT : 2017SACLY014

THÈSE DE DOCTORAT
DE L'UNIVERSITÉ PARIS-SACLAY
PRÉPARÉE ENSTA PARISTECH

Ecole doctorale n°579
L'école Doctorale Sciences Méchaniques et Énergétiques,
Matériaux et Géosciences (SMEMaG)
Spécialité de doctorat: Acoustique

par

M. JIN JACK TAN

Piano acoustics: string's double polarisation and piano source identification

Thèse presentée et soutenue à Palaiseau le 30 Novembre 2017.

Composition du Jury :

M.	FRANÇOIS GAUTIER	Université du Maine	(Rapporteur)
M.	XAVIER BOUTILLON	CNRS	(Rapporteur)
M.	BERTRAND DAVID	Télécom ParisTech	(Président)
Mme.	JULIETTE CHABASSIER	INRIA	(Examinatrice)
M.	KEREM EGE	INSA de Lyon	(Examinateur)
M.	CYRIL TOUZÉ	ENSTA ParisTech	(Directeur de thèse)
M.	BENJAMIN COTTÉ	ENSTA ParisTech	(Co-directeur de thèse)

To my late uncle, Tan Cheng Kee,
and
my late aunt, Ch'ng Chin Nigh,
both of whom have passed away during the final few months of my thesis preparation.

université PARIS-SACLAY
ÉCOLE DOCTORALE
Sciences mécaniques et énergétiques, matériaux et géosciences (SMEMAG)

Titre : Acoustique du piano : double polarisation de la corde et identification de sources

Mots clefs : modele physique de piano, simulation numerique, corde, chevalet, identification de sources

Résumé : L'objectif de cette thèse est d'améliorer la compréhension de l'acoustique du piano dans le contexte de la synthèse sonore par modèles physiques. Le manuscrit est décomposé en trois parties principales, dont les deux premières ont pour but la compréhension de l'origine de la double polarisation de la corde de piano, tandis que la dernière se focalise sur l'identification de sources d'un piano complet.

Dans la première partie, la non linéarité géométrique, intervenant lorsque les amplitudes de vibration sont grandes, est étudiée afin de comprendre si le couplage non linéaire peut transmettre de l'énergie à une polarisation non initialement excitée et mener ainsi au phénomène de double polarisation. Un développement en échelles multiples est mené sur un modèle de corde de Kirchhoff-Carrier avec les deux extrémités fixes, restreint au mode fondamental de chacune des polarisations. Les deux oscillateurs ont alors des fréquences très proches, on parle de résonance 1:1. La condition d'existence et le critère de stabilité pour l'apparition de double polarisation sont obtenus et validés numériquement sur la base des équations de Kirchhoff-Carrier, ainsi qu'avec un modèle de corde enrichi. Des expériences sont menées sur un dispositif monocorde où les angles de polarisation naturelle de la corde, le désaccord entre les deux polarisations et le comportement non linéaire son observés et identifiés.

La seconde partie se concentre sur le couplage entre la corde et le chevalet. Les degrés de liberté de la corde sont couplés au chevalet dont les mouvements (translation/rotation) sont représentés par un ensemble d'oscillateurs. Les fréquences propres des différents systèmes couplés sont analysés. Des schémas numériques sont proposés et mis en œuvre pour une résolution directe. Ces schémas résolvent les équations de corde par une méthode d'éléments finis d'ordre élevé et les équations du chevalet analytiquement. Les conditions de couplage entre corde et chevalet sont assurées par des multiplicateurs de Lagrange. Expérimentalement, la corde est tendue sur le chevalet dans une configuration de type zig-zag et excitée verticalement ou horizontalement. Dans les deux cas, les phénomènes de double polarisation et de double décroissance sont observés et des résultats qualitativement similaires sont obtenus avec les modèles numériques.

La dernière partie s'attache à décrire quantitativement les différentes sources vibro-acoustiques d'un piano complet. Une étude est menée en utilisant une analyse des chemins de transfert (transfer path analysis en anglais) sur un piano Bösendorfer 280VC-9. Les contributions de la table d'harmonie, des parties interne et externe de la ceinture, du cadre en fonte et du couvercle sont étudiées dans le domaine fréquentiel. L'analyse montre que la table d'harmonie est le principal contributeur mais que le cadre en fonte et le couvercle jouent également un rôle significatif, en particulier à hautes fréquences.

Title : Piano acoustics: string's double polarisation and piano source identification

Keywords : physical modelling of piano, numerical simulation, string, bridge, source identification

Abstract : The objective of this thesis is to improve the understanding of the acoustics of the piano in the context of physically-based sound synthesis. The manuscript is decomposed in three parts, the first two being devoted to the understanding of the origin of the double polarisation in piano string, while the third one is dedicated to the identification of sound sources of a complete piano.

In the first part, the geometric (large-amplitude) nonlinearity is studied in order to understand if the nonlinear coupling can transfer energy to an initially non excited polarisation, thus leading to the double polarisation phenomenon. A multiple-scale analysis is conducted on a Kirchhoff-Carrier string model with fixed boundary conditions at both ends. Each polarisation is restrained to its fundamental mode and thus presenting a 1:1 internal resonance. The existence condition and stability criteria for double polarisation to occur are obtained and validated numerically based on the Kirchhoff-Carrier equations, as well as a more enriched geometrically exact string model. Experiments are carried out on a monochord setup where the natural polarisation angles of the string, detuning between the two polarisations and its nonlinear behaviour are observed and identified.

The second part is devoted to the string/bridge coupling. The degrees of freedom of the string are coupled to the bridge whose translational and rotational motions are represented by a set of oscillators. The eigenfrequencies of various coupled systems are analysed. Numerical schemes are proposed and implemented where the string is solved via high-order finite-element method while the lumped bridge is solved analytically and coupled to the string by Lagrange multipliers. Experimentally, the string is strung over a bridge in a zig-zag configuration and excited vertically and horizontally. In both cases, double polarisation and double decay are observed and similar results are also obtained qualitatively in numerical models.

The last part is devoted to a quantitative description of the vibroacoustic sources of a Bösendorfer 280VC-9 piano via operational transfer path analysis. The contribution of the soundboard, inner and outer rim, iron frame and lid are investigated in the frequency domain. It is found out that the soundboard is the primary contributor but the iron frame and the lid also play a significant role, especially at high frequencies.

Université Paris-Saclay
Espace Technologique / Immeuble Discovery
Route de l'Orme aux Merisiers RD 128 / 91190 Saint-Aubin, France

Acknowledgment

This whole thesis would not have been possible without the generous supports from the BATWOMAN Initial Training Network (ITN) (European Commission grant 605867). The BATWOMAN ITN is a Marie Skłodowska-Curie Actions project under the Framework Programme 7 (FP7) fund. I express my utmost gratitude and appreciation for their supports.

– see batwoman.eu for more information.

I still remembered the night when I first received the email from Antoine Chaigne in March 2014 about my recruitment as a PhD candidate for the so-called "piano project". I was on my way to meet my girlfriend and she was the first person I broke the good news to. Upon reflection, perhaps she foresaw the difficulties of being apart for 3 years back then and broke down in tears. As of writing, I am one day away from fulfilling my contract with my thesis ready to submit and we are still together. These 3 years are simply monumental to me, for which I make a giant step for my career as well as in building my own family. All her dedications, commitment and sacrifices are deeply remembered and I am forever in her debt. Thank you, Sin Yong, for being the pillar despite being more than 10,000km away.

Over these three years, I have been very lucky to be under the wings of Cyril Touzé, Benjamin Cotté, Patrick Joly and Antoine Chaigne. They are all incredible supervisors and have guided this lost deer to the right track numerously. It has been a wild ride with the final result obtained just weeks before the deadline (thanks Benjamin for showing me the important figure). If anyone thinks of being a student under them or wanting to collaborate on research, I would wholeheartedly recommend them without any hesitation.

I have been glad to be part of an amazing Tan family who have been visiting me as often as they could and provide emotional supports whenever I need it despite the time difference and distance. I am sure they are also proud of my achievement. A special shout out to my sister in Manchester whom I visited and freeloaded every year during the Christmas break.

In ENSTA, I am blessed to meet some great friends and colleagues. Honorable mention to the real Batwoman Àngels Aragonès who understands life as a foreigner in France. I am also fortunate to have met Tommy, Aurélien, Simon and Luca during different time of my stay in ENSTA. They might not know about it but a lot of their little gestures or small talks during lunch time have been so helpful for me to get through every day in France.

Lahcene, Nicolas and Thierry have been tremendous in helping me to succeed in this PhD project. I would not have been able to achieve so much without their assistance in setting up experiment and getting myself out of trouble in dire situations. Qi Chen, the intern I worked a lot with, has been the man for helping out in the experiments towards to the end of my thesis. I am also thankful of Juliette

Chabassier and Marc Duruflé at INRIA Bordeaux. Both of them have helped me massively in learning the MONTJOIE code and making advances on the numerical aspects of the thesis.

Similarly for the colleagues in Vienna, Werner and Alex Mayer have been extremely helpful in the research during my secondment. Wilfried and the University of Music and Performing Arts Vienna (MDW) have been extremely accommodating. Thanks Sascha for hosting me in a wonderful room right next to the Hundertwasser Museum.

Coming back to France, I have been fortunate enough to meet Alden, Kit and Desmond, the three rare Malaysians who made me feel like home during our times together. I am also glad to have met so many friends on the basketball court. Xiaojun, Wang Jun, Hongye, Yahui, Shaobing, Pengji, Huixing, Jianglaoshi and Shuanglong, I thank all of you for your generosity in allowing a poor player like me to play with you. Apart from that, you all have been great friends to me as well. I could not forget about Minh Hang Nyugen, too. My arrival in France would have been much more difficult without her unselfish help.

Last but not least, I will definitely miss all of the BATWOMAN fellows. I have always been looking forward to see them during every BATWOMAN meeting. You all may not know it, but I have always thoroughly enjoyed my time with all of you. Each of those meetings have been a highlight during my 3 years in Europe, except for the trip to Detmold. Nobody wants to go to Detmold. Thank you (in no particular order) Tatiana, Saranya, Alejandro, Toros, Sebastià, Antonio, Drasko, Philipp, Winfried, Anna, Amaya, Emin and once again Àngels.

Sekian, terima kasih[1].

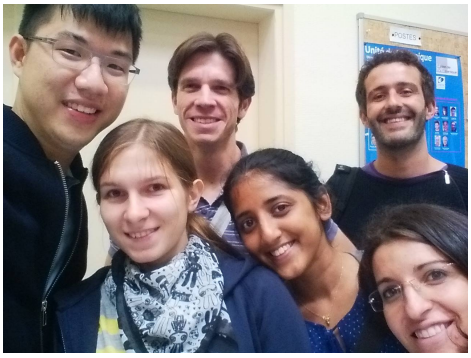

(a) From left to right: me, Tatiana, Alejandro, Saranya, Anna, Toros. Palaiseau 2014.

(b) From left to right: Emin, Sebastià, Philipp, me, Drasko, Toros, Alejandro, Àngels, Antonio. Edinburgh 2017.

The awesome BATWOMAN fellows. The elusive members are Amaya and Winfried.

[1]Thank you everyone (in Malay).

Contents

1

Introduction

Piano is a musical instrument and an engineering wonder. Composers like Maurice Ravel, Frédéric Chopin and Claude Debussy have completed acclaimed musical masterpieces on a piano and have moved emotions of the world. At the core of these amazing works[1] is the engineering marvel in the form of a piano. As shown in Figure 1.1, piano is made up of several key components. Each plays a role in the production of the desired piano sound. They have been through centuries of evolution yet there are new innovations to improve piano. The study of piano spans a long time and over several domains of research. To provide an informed overview, it is perhaps useful to first understand the mechanism of sound production in a piano.
It is easy to make sound from a piano: when a key on a piano is pushed, a sound could then be heard. However, series of events happen right after the key push before the sound is actually heard. First, the energy spent to push the key (K in Figure 1.2) is transferred to the "hammer" (H in Figure 1.2) via a mechanical device called the "action" as is shown in detail in Figure 1.2. The hammer, covered in felt, travels upwards and hits the "piano string" (C in Figure 1.2). As a result of the impact, the string vibrates. At one end of the string, it is connected to the "soundboard" via the "bridge" (see Figure 1.1). Thus, as the string vibrates, the soundboard also vibrates. The vibration of the soundboard compresses and pushes the air around it which forms sound waves that are transmitted to a listener's ear. The physical movement of the sound waves are captured by inner ear before it is being converted to neural signals that are sent to the human brain. The human brain registers these signals as sound, and thus it is heard.
It is no coincidence that a piano could sound pleasant. Piano is about 300 years old and has went through countless design iterations and refinements until today. In the 1700s, piano was invented by Bartolomeo Cristofori in need of an improvement to the existing clavichord and harpsichord that could be played more expressively with different loudness. Cristofori designed and built a piano that came with a hammer striking action with escapement device that allows the playing of pianis-

[1] Personal favourites: Ravel's Piano Concerto in G, Chopin's "Heroic" Polonaise and Debussy's "L'île joyeuse".

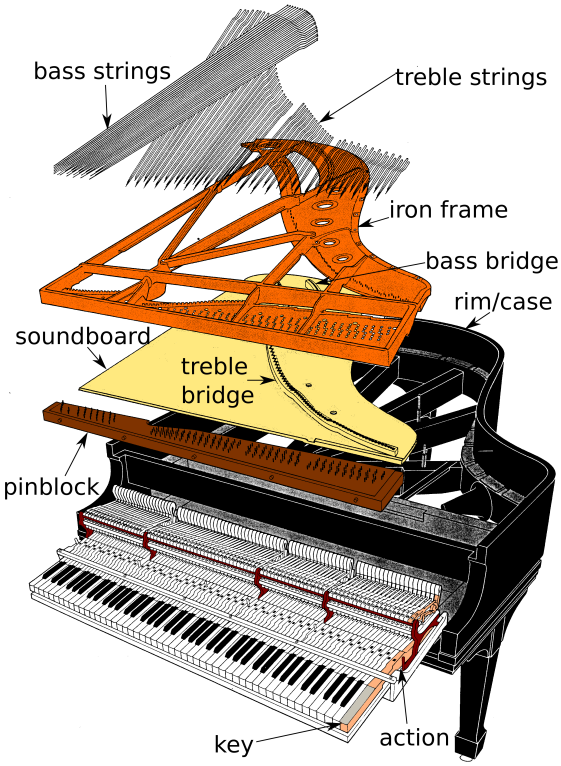

Figure 1.1: Exploded view of a piano, image extracted and edited from Blackham [1].

simo (soft sound) and fortissimo (loud sound) [2]. This gives the original name "pianoforte" that is later shortened to be simply "piano". By the 1820s, piano needed to be louder and richer in tone. To cope with the use of heavier strings, Alpheus Babcock invented the full cast iron frame. Steinway & Sons further developed the full iron frame and introduced the overstrung technique where the bass strings are strung above the treble strings [2]. Also in the 1820s, Erard developed the "double escapement" action which allows fast repetition of the notes to be played. The full iron frame, overstrung setup and Erard action are still in use despite being technologies from the 19th century. However, they have also evolved by incorporating new materials and manufacturing methods [3, 4] as well as with innovative engineering designs [5, 6]. These mixtures of new and old technologies are the perfect testament of how piano is a marvellous combination of scientific knowledge and traditional know-how.

Scientific studies of piano was pioneered by Hermann Helmholtz in the late 19th century [7] although active research only began in the 1920s as reported in [8]. That being said, the most relevant literature are probably published within the past 40 years or so. In the next section, a comprehensive review of the research and development on piano acoustics is presented. The review is by no means exhaustive

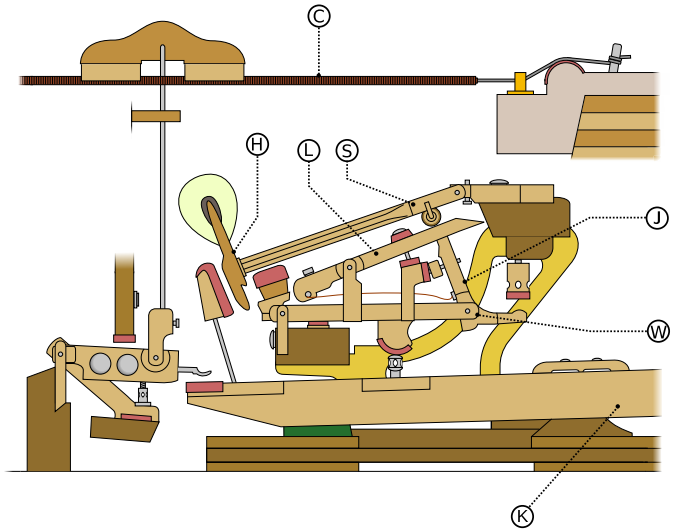

Figure 1.2: Grand piano action. The label C, H, L, S, J, W and K represent the string (**c**orde in French), **h**ammer, repetition **l**ever, **s**hank, **j**ack, **w**hippen and **k**ey respectively. The original image "Piano mechanism — english type" is created by Olek Remesz (wiki-pl: Orem, commons: Orem) and is licensed under GFDL ver. 1.2 and CC-BY-SA ver. 2.5, 2.0, 1.0.

as a lot of research and development activities of piano manufacturers are carried out in-house and the outcomes are not shared in the public domain. It is, however, relevant and would provide a context on why this PhD thesis is necessary and how it could contribute to the growing knowledge pool of musical acoustics.

1.1 State-of-the-art of piano acoustics

Piano is a multi-component device and each component itself presents a physics problem and warrants research efforts. They can be loosely categorised into the following areas:

- piano action,
- hammer and its interaction with string,
- string vibrations,
- soundboard vibrations and acoustic radiation.

The categorisation is based on the review paper by Suzuki and Nakamura [8] where pre-1990s research work conducted have been comprehensively summarised. To be more relevant, an additional category of "modelling and sound synthesis" is also studied to reflect the latest research effort.

Piano Action

Research on piano action is motivated by a need of understanding how the touch input applied to a key will affect the key travel time, hammer velocity and subsequently its impact on the string. The main challenge of studying the piano action mechanism is its intrinsic nonlinear behaviour and also difficulty in predicting friction constants. In earlier works summarised by Suzuki and Nakamura [8], most of them are restricted to experimental studies. For instance, Lieber's effort investigated the relationship between the energy input to the key and the key travel time [9]. It is observed that the key takes less time to travel with increasing energy. Similar finding is echoed by Askenfelt & Jannson [10], whose work investigated the contact timing and motions of various components in piano action. Ultimately, these shed lights on the dynamic behaviour of a piano action before computational studies became feasible.
Gillespie has developed a few grand piano action models, each with different number of components and complexity [11,12]. Hirschkorn et al. developed a model with 5 rigid body components (key, whippen, jack, repetition lever, and hammer, see Figure 1.2) with experimentally determined parameters [13]. A further extension of the model was done by Izadbakhsh et al. [14] where a flexible shank is also considered. In the same research group led by Birkett, Masoudi has recently developed and validated a vertical piano action model [15, 16]. Thorin et al. [17, 18] also presented a grand piano model based on non-smooth dynamics where the forces instead of the displacements of the components are simulated. Although the piano action does not directly affect the piano sound, it holds an important role as it is the main input for pianists to control the sound. Thus, it is important to have accurate models of the action, which could aid in the study of the interaction between hammer and string.

Hammer-string interaction

The interaction between hammer and string is an important subject as it is where vibrations start. Information on the hammer force like its amplitude and contact point over the contact duration could influence the excitation of the string, and subsequently the soundboard dynamics. The interaction is complicated as hammer is covered by felt which compresses upon impact. This results in a nonlinear relationship between the hammer force and displacement. In addition to that, accounting for the flexibility of the hammer shank also influences the interaction between the hammer and string [14, 19].
In Suzuki and Nakamura's review [8], some of the very early models can be attributed to Helmholtz [7] and Kaufmann [20] which could still be useful for simple analysis. Early experimental work are also reported in the review, such as those done by Boutillon [21]. He developed a nonlinear finite-difference hammer model by modelling the felt with a hysteretic spring. With advances in computation power in the 1990s, more sophisticated models are developed where modelling parameters are extracted from experiments [22–24]. In recent years, detailed experimen-

tal framework has been established to more accurately and consistently study the hammer-string interaction [25]. A numerical method has also been proposed to reconstruct the hammer forces from string velocity measurements [26]. Research on the hammer-string interaction is still very much active and ongoing in pursue of accurate representation of the phenomenon.

String

The piano strings are one of the most important components in a piano. It is the cornerstone of the pitch and tonal colour of the piano sound. The piano sound can be characterised by acoustic features like the double decay, inharmonicity, precursor signals and phantom partials.
The double decay gains its name as the piano sound can be loosely grouped into the initial "attack" phase followed by the "sustain" phase, each decaying at a different rate as is shown in Figure 1.3. Weinreich proposed two mechanisms that cause the double decay rate [27, 28], one applicable to a single string and one applicable for duplets or triplets of strings. Following the reference of a grand piano, when the hammer strikes the string vertically, the string not only vibrates vertically but also horizontally. The two vibrations have different decay rates. As the string is coupled to the bridge, its energy is dissipated quickly and this makes up the initial fast decay. As the vertical displacement reduces, horizontal displacement becomes more dominant and exhibits the second slower decay. The phenomenon where there are both vertical and horizontal vibrations are known as "double polarisation". When the hammer strikes duplets or triplets of strings, the initial vibrations of the strings are in phase with each other. The forces exerted to the bridge are also in phase and more energy is transmitted to the bridge. However, due to detuning among the strings, the vibrations slowly get out of phase. The out-of-phase forces cancel each other which reduces the net bridge forces, and consequently slow down the energy transfer. The different energy transfer rate thus results in the different decay rates of the strings. In addition to that, as the vibrations go in and out of phase, beatings can also be observed as is shown in Figure 1.3b. These mechanisms have been validated by various authors [29–31].
Inharmonicity is the phenomenon when the partials of the string are not exact integer multiples of the fundamental frequency. Inharmonicity occurs due to the stiffness of the string and is an essential feature for accurate description of piano string. The stiffness of the string can be described by various models such as the Euler-Bernoulli beam theory [21, 22], Timoshenko beam theory [32] or more recently by shear beam theory [33] which is a slightly reduced version of the Timoshenko model.
The precursor is a small initial signal that precedes the transverse displacement while the phantom partials are additional partials observed on the spectrum of a string that are sum of the longitudinal and transverse frequency [34]. Precursor signals and phantom partials can be attributed to the nonlinear vibrations of the string, where longitudinal displacement is generated even though the string

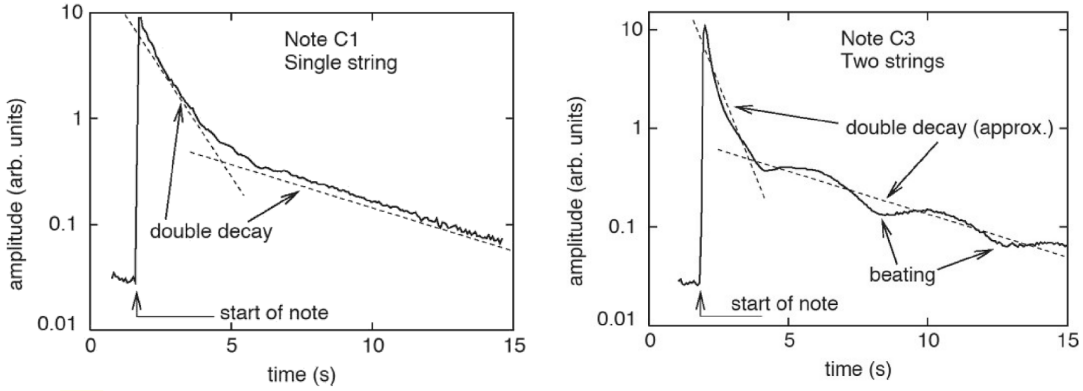

(a) Single string C1.

(b) Two strings C3.

Figure 1.3: Root-mean squared sound pressure of different piano notes, extracted from [28]. Approximate decay rates are shown as dotted lines.

is struck vertically (i.e. transverse displacement) [35]. These two phenomena contribute to the characteristic piano sound and have drawn research efforts from authors like Bank and Sujbert [36], Chabassier and Joly [37] and Kurmyshev [38].

Soundboard and radiation

In a piano, the soundboard is essentially a resonator which "receives" the string vibration at the bridge and amplifies it so that the vibration is audible to the human ear. Despite its simple mechanism, the soundboard is more than just a diaphragm. Ribs are glued to the soundboard to improve its stiffness and longevity while treble and bass bridges are glued to it in order to couple the strings and the soundboard. The soundboard is also tapered and curved slightly upwards forming a frown (⌒) shape. The frown shape is more commonly known as a "crown" [39]. The soundboard can be evaluated by its many characteristics, such as its vibrational patterns in different frequency ranges, mechanical mobility and its radiation pattern.
As summarised by Ege [40], the first few resonant frequencies are influenced by the presence of rim, bridge and downbearing forces from the string. It also appears that the average modal frequency spacing is between 20 to 30Hz regardless of the dimension of the piano up to 500Hz. Indeed, Askenfelt remarked that global soundboard properties might be more important than actually investigating the precise eigenfrequencies [41]. Among other studies conducted by Berthaut et al. [42], Suzuki [43] and Ege et al. [44], consistent modal loss factor between 2 to 3% is also identified. Modal shapes are also experimentally studied by Moore et al. [45], Ege et al. [44] and Chaigne et al. [46] where interestingly, at higher frequencies, vibration is localised between the ribs.
The mechanical mobility defines the loudness and sustain of a piano tone. Ideally, strings will have to transmit an initial bulk of energy quickly to the soundboard

to make up the loud "attack" tone of a piano and follow up with a slower energy transmission for the slow-decaying "sustain" tone. The admittance of the string forces at the bridge of a piano are studied by Wogram [47], Nakamura [48], Conklin [49] and Giordano [50]. A general trend of higher bridge fundamental frequency and reduced mobility is observed when strings are loaded onto the bridge as shown in Figure 1.4. Measurement of admittance of a bridge remains a challenge even for other musical instruments [51].

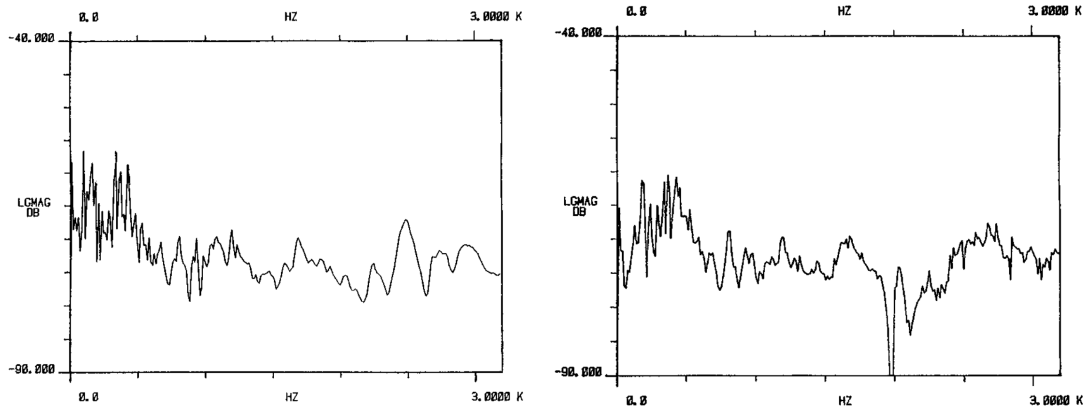

(a) (b)

Figure 1.4: Treble bridge mobility measurement in the direction normal to soundboard at terminating point of string C6 (a) before and (b) after the strings and plate are assembled, extracted from [49].

Early soundboard radiation study is completed by Suzuki [43]. In his experimental study, it is observed that acoustical short-circuit occurred below 80Hz, which results in very low radiation efficiency. The efficiency fluctuates up to 1kHz as it hits a plateau of 16%. More recently, radiation study has been conducted [46, 52, 53] with aids from numerical tools in which the effect of the ribs or string coupling points on the soundboard's radiation has been discussed.
A special mention for the work by Debut et al. [54] is also necessary. While the work is based on the 12-string Portuguese guitar, they showed numerically that a bridge could induce a horizontal vibration even if the string is excited vertically (see Figure 1.5). The coupling is achieved by the rotational motion of the bridge. As the string forces act on the top of the bridge (instead of through its centre of gravity), it introduces a moment to the bridge and thus a rotational motion.

Modelling and sound synthesis

A common trend can be observed in the direction of research on the acoustics of piano. As computational effort becomes cheaper, modelling becomes more viable. Complicated problems like nonlinear string vibration can be studied more easily

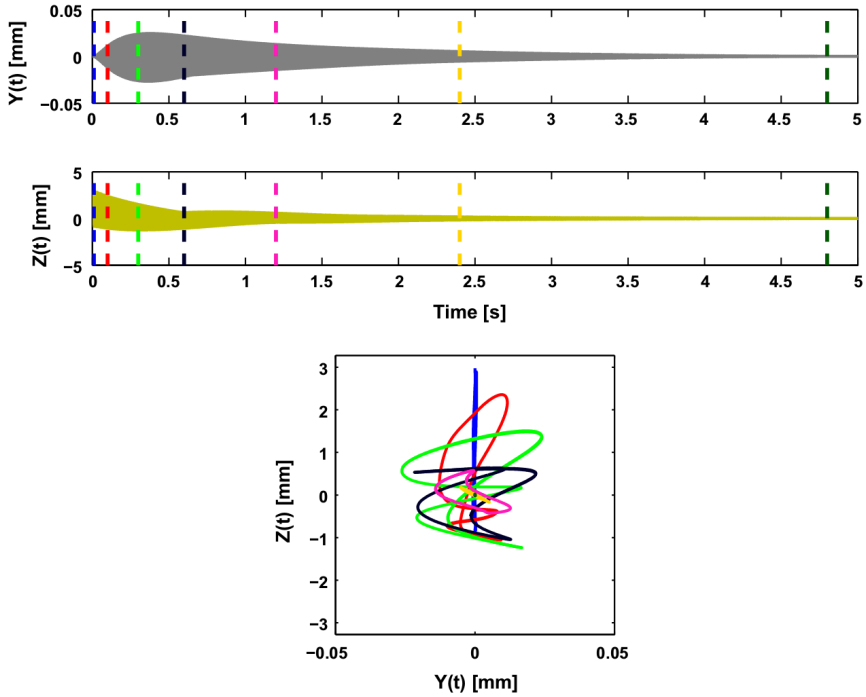

Figure 1.5: Time history of the string vibration on a linear one-string/body model in Z-direction (vertical) and Y-direction (horizontal) when it is first excited vertically. The top two plots show the displacement-time plots and the bottom plot presents the snapshots of displacement in Y-Z plane at various times. [54].

and accurately without the need of excessive simplification. This also unlocks the possibility of synthesising piano sound based on physical models.

Physics-based piano sound synthesis can be achieved by several methods. A popular technique used for sound synthesis is the digital waveguide method [55]. Digital waveguide synthesis models the motion of the string based on known traveling wave solutions where each traveling wave has its own "delay line" to describe its spatial and temporal coordinates. It has been used by numerous authors [36, 56–59] and is also featured in commercial synthesiser such as the Yamaha VL1 [60]. Another popular method is the finite difference method. Finite difference method transforms a partial differential equation to an ordinary differential equation that can be solved by approximating the derivatives in the differential equations [60]. Some of the early uses of this method are pioneered by Boutillon [21] and Chaigne & Askenfelt [61]. It is also used by Giordano & Jiang to simulate a complete piano [62] (more on that later).

To date, there are two complete physics-based time-domain piano models that are published, namely by Giordano & Jiang [62] and by Chabassier et al. [63]. For the purpose of clarification, a complete model is defined where the hammer, string, soundboard and the room/surrounding air are all simulated. The action can be

omitted as it does not directly affect the sound production of a piano tone. In Giordano and Jiang's work, the string is based on a linear stiff string equation that is struck by a hammer model proposed by Stulov [64]. The string is coupled to a simple soundboard model that includes the ribs and bridges such that the stiffness of the soundboard is position dependent [65]. The room model is the three-dimensional linearised Euler equations which is driven by the vibration of the soundboard. All of the components are coupled and solved by finite difference methods. The main challenge is that there are a large number of room elements to be solved and the soundboard model is highly dispersive and requires small time step for stability. To cope with it, multiple time steps are used: the soundboard and strings are iterated for 6 and 4 times respectively before an iteration is carried out for the room.

Almost a decade after Giordano & Jiang's work [62], Chabassier et al. published the second complete time-domain piano model [63]. The model is a significant improvement with more accurate descriptions of the physics. While the hammer model is still based on Stulov's work [64], the string model is significantly enriched. In addition to solving the transverse displacement, Chabassier et al.'s model is nonlinear and solves for the longitudinal displacement as well as the string cross-sectional area's rotation. The string rotation is a result of including the stiffness contribution by Timoshenko beam theory. By solving for the longitudinal displacement, the model can thus replicate the precursor signal and phantom partial phenomena. The soundboard is modeled as a Reissner-Mindlin plate, which is essentially a 2D version of the Timoshenko formulation. Thus, in addition to the transverse soundboard displacement, its cross-sectional area's rotation is solved as well. Similar to Giordano & Jiang's implementation, ribs and bridges are modeled by modifying the thicknesses and material parameters at different parts of the soundboard to account for its heterogeneous material properties. Lastly, for the room, it is modeled the same way as Giordano & Jiang's using the three-dimensional linearised Euler equations.

Chabassier et al. choose to solve their model by high-order finite element method. An implicit energy-preserving numerical scheme is proposed to solve the nonlinear string [37]. The soundboard is solved semi-analytically. The modes are first determined before it is coupled to the nonlinear string. To ensure stability for the coupling, the vertical string forces are solved at interleaved time steps before it is being input to the soundboard. Finally, the soundboard is coupled to the air which is solved by finite element method explicitly.

Remarks

In light of Chabassier et al.'s achievement [63], new research opportunities arise. With its ability to model piano of any dimension, systematic study on historical pianos becomes possible [26, 66]. The multi-component structure of the numerical models also make it possible to study and improve specific components. New improvement like consideration of the hammer shank vibration has since been in-

cluded [67]. Nonetheless, the work by Chabassier et al. [63] is not without room for improvement:

1. The string model employed is a nonlinear stiff string model that solves only one transverse (vertical), one longitudinal and one rotational displacement of the string. Weinreich proposed that the horizontal polarisation of the string also plays a role in the double decay phenomenon [27]. By omitting the second transverse (horizontal) displacement of the string, the model thus fails to include any interaction between the horizontal and vertical displacement of the string.

2. The bridge model is a rigid body that moves in a vertical direction only as is shown in Figure 1.6. As remarked by Chabassier et al. in another paper [68], the bridge model is "probably oversimplified compared to reality and would deserve to be improved in a future work".

3. The reproduction of the spectral contents at the low register was not satisfactory when compared against measured piano sound samples. Despite efforts in adjusting parameters (e.g. soundboard's damping), the origin of the problem remains unknown.

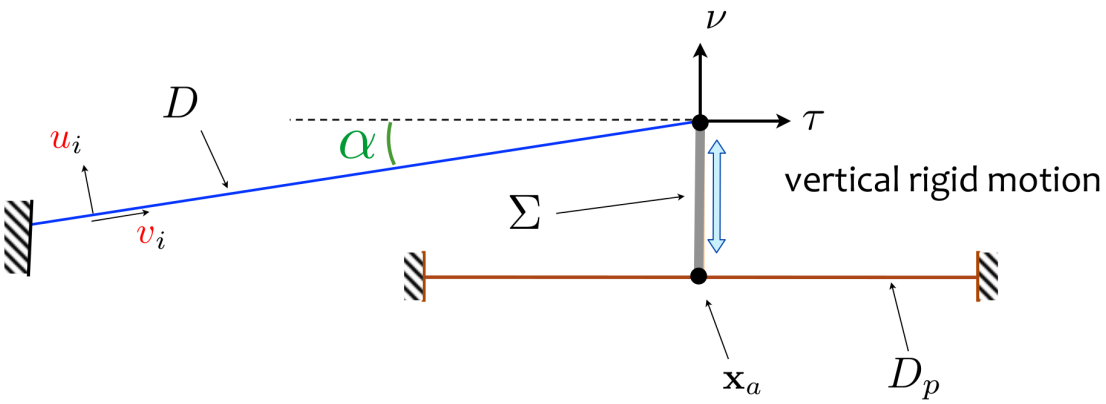

Figure 1.6: Rigid vertical bridge used in Chabassier et al. model [63], as extracted from [68].

1.2 Motivation and Objectives

The three concerns in Chabassier et al.'s model as outlined in the "Remarks" subsection of Section 1.1 are the inspiration of this PhD thesis. While the thesis shares the global vision of improving the realism in piano sound synthesis, efforts are concentrated to inspect thoroughly the local phenomena happening on the string and

the bridge, which tackle the first two flaws of the model. To overcome the third issue, an exploratory project is engaged. With these in mind, the thesis sets out to achieve the following objectives:

1. **to investigate the nonlinear interaction between the horizontal and vertical vibration of the string, or otherwise known as the double polarisation effect.**
   The origin of double polarisation in musical instruments is not exactly clear. Weinreich postulated that double polarisation can be due to irregularities of the hammer face or the position of the string which causes the horizontal vibration to be excited [69]. However, similar double polarisation effect can also be seen in nonlinear vibrating string that is excited by an external force [70, 71]. In piano, the strings are struck by the hammer and are allowed to vibrate freely which is different from forced excitation. However, this could still lead to a hypothesis that the double polarisation of a freely vibrating string is caused by the nonlinear relationship between the two transverse modes (horizontal and vertical). A dinstinction must be made from the nonlinear string in Chabassier et al.'s model which couples the longitudinal displacement to the vertical transverse displacement [63].

2. **to study the coupling between a freely vibrating string with double polarisation and a lumped bridge.**
   Debut et al. [54] has shown that the rotation of the bridge on a Portuguese guitar can provide coupling between the string's polarisation. On the other hand, Weinreich also remarked that the horizontal and vertical string vibration decay at different rates due to different admittances at the bridge [27]. Owing to these observations, rather than directly attempting to improve the bridge model in Chabassier et al.'s work [63], a first step is to understand properly the coupling between the string and the bridge. To achieve that, the bridge can be represented by a lumped bridge, which is essentially a set of oscillator(s) in different direction(s) that are all located on a single point.

3. **to determine the contribution of other constitutive components of the piano in the production of the sound.**
   To mitigate the third issue of Chabassier et al.'s model [63], one of the strategies could be to identify additional vibrational parts in a piano that remains unmodeled in the model. When a piano is played, vibration can be felt not only on the soundboard but also the rim, the frame, the lid etc. In a Bösendorfer piano, spruce, a wood commonly used for soundboard by other manufacturers, is used extensively in building the case of the piano. Bösendorfer claims that the use of spruce, especially on the rim of the piano, allows the whole instrument to vibrate and is the reason that gives the unique Bösendorfer sound [72]. Based on the fact that vibration is felt on other parts of the piano and how Bösendorfer uses spruce extensively, it is thus justified to investigate those vibrating components.

1.3 Structure of thesis

To be in line with the three objectives proposed, the thesis is divided into three main parts.
Part I (named "String") is divided into three chapters. In Chapter 2, several string equations that are used in this thesis are derived. The equations include the geometrical exact equations, third-order nonlinear string equations, the Kirchhoff-Carrier nonlinear string equations and the linear wave equation. To complement the derivations, energy conservation properties of these equations are also shown. In what follows, modal solution of the linear wave equation is presented and numerical schemes to solve the two nonlinear equations are introduced and compared. In Chapter 3, the nonlinear coupling between the string polarisations are analytically studied via multiple-scale analysis to determine the conditions double polarisation could occur. Relevant case studies are included and the finding is numerically validated. The chapter ends with a short excerpt on double polarisation that could be observed in a linear regime. The final chapter (i.e. Chapter 4) presents the experiments conducted, where various string properties such as the string polarisation angles and damping parameters are determined. These results pave the groundwork for the experimental validation of the finding in Chapter 3 as is presented in Section 4.4.
In Part II (named "Bridge"), the study of the coupling between the string and the bridge is presented over three chapters. In Chapter 5, several analytical coupled models are presented. The coupled models range from the simplest model where a single transversely vibrating string is coupled to a single oscillator to the most complex model where the string with 5 variables is coupled to 6 oscillators (three translations, three rotations). The eigenfrequencies of the models are derived and analyses are made as to how the coupling could affect the frequencies. Numerical schemes are subsequently devised and validated in Chapter 6. In Chapter 7, experiments are conducted on a simple single string and bridge setup to observe the double polarisation effect. Double decay is also observed and the results are supplemented by simulated data from numerical models where qualitative agreements between the experiments and simulations are achieved.
In Part III (named "Source identification of piano") which contains only Chapter 8, an experimental source identification investigation on the piano is presented. In conjunction with the submission to *Applied Acoustics*, the chapter presents the prepared manuscript complete with its own abstract and conclusion. The study is based on operational transfer path analysis (OTPA) which is a noise identification technique commonly used for automotive applications. The theory and experimental implementation of OTPA are introduced and the chapter is completed by presenting the findings.
At the end of the thesis, a conclusion is drawn along with some perspectives. Appendix and bibliography are also included at the end of the thesis for any interested readers.

Part I:

String

A wise man once said that to do a great and important work, two things are necessary: a definite plan, and not quite enough time.

R. C. Schafer, 1977

2

Modelling string vibration

The vibration of a string under tension is an important subject in musical acoustics as it forms the basis of the sound producing mechanism of numerous musical instruments like piano, cello and guitar. As with most physical systems, the vibration of the string can be studied and modelled with varying degrees of complexity. In this chapter, several equations governing the string vibration are derived, beginning with the most complex models before trickling down to simpler models. Attention has been given to nonlinear string models, as the nonlinearity is understood to have contributed to the double polarisation effect - a primary focus of this thesis.
The chapter begins with a derivation of the various string models in Section 2.1 and their energy conservation properties in Section 2.2. Modal solution of the simplest equation, i.e. the linear wave equation, is presented in the subsequent Section 2.3. Numerical schemes to solve the more complicated problems are proposed and investigated in Section 2.4.

2.1 Derivations of string models

In this section, the geometrically exact model is first derived based on physical laws. It is then simplified, with additional assumptions, to three other sets of equations, i.e.:

- third-order nonlinear string equations,
- Kirchhoff-Carrier nonlinear string equations,
- linear wave equations.

2.1.1 Geometrically exact string equations

The derivation of the geometrically exact string equations are based on the approaches found in several text books [73, 74]. To begin, consider a small element of

a string with a length dx as is shown in Figure 2.1. At the two ends of this element are two points, denoted F and G. When the string is subjected to a displacement, F and G are displaced to F^* and G^* respectively and the length of the element becomes ds. For the Cartesian coordinate system (x, y, z), unit vectors are defined as $\hat{\mathbf{i}}$, $\hat{\mathbf{j}}$ and $\hat{\mathbf{k}}$ respectively. The vector linking F and F^* is:

$$\mathbf{FF}^* = w\hat{\mathbf{i}} + u\hat{\mathbf{j}} + v\hat{\mathbf{k}}, \tag{2.1}$$

where u, v and w are the displacements in the two transverse and longitudinal directions respectively. For G and G^*, the finite length of the element dx induces a small perturbation in addition to the displacement of u, v and w. The vector linking G and G^* can be written as:

$$\mathbf{GG}^* = w(x + \mathrm{d}x)\hat{\mathbf{i}} + u(x + \mathrm{d}x)\hat{\mathbf{j}} + v(x + \mathrm{d}x)\hat{\mathbf{k}}. \tag{2.2}$$

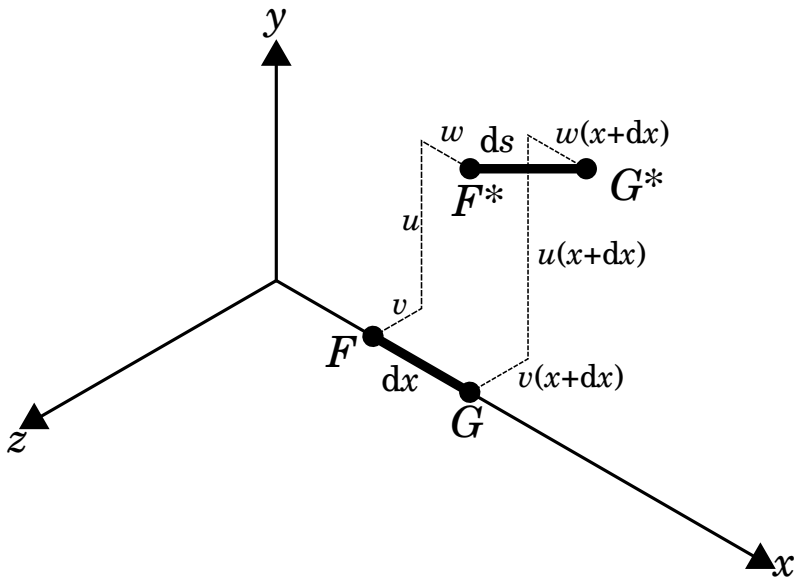

Figure 2.1: Element of a string in its original and displaced position.

For sufficiently small dx, $\mathbf{GG}^*$ can be rewritten as:

$$\mathbf{GG}^* = (w + w'\mathrm{d}x)\hat{\mathbf{i}} + (u + u'\mathrm{d}x)\hat{\mathbf{j}} + (v + v'\mathrm{d}x)\hat{\mathbf{k}}, \tag{2.3}$$

where the superscript $'$ indicates differentiation with respect to x. The vector linking F^* and G^* can thus be easily deduced by vectorial relations, where:

$$\mathbf{F}^*\mathbf{G}^* = -\mathbf{FF}^* + \mathrm{d}x\hat{\mathbf{i}} + \mathbf{GG}^* = \mathrm{d}x\left[(1 + w')\hat{\mathbf{i}} + u'\hat{\mathbf{j}} + v'\hat{\mathbf{k}})\right]. \tag{2.4}$$

The length of this vector is also ds, such that:

$$\mathrm{d}s = |\mathbf{F}^*\mathbf{G}^*| = \mathrm{d}x\sqrt{(1 + w')^2 + u'^2 + v'^2}. \tag{2.5}$$

The induced strain ε due to the displacement is simply:

$$\varepsilon = \frac{\mathrm{d}s - \mathrm{d}x}{\mathrm{d}x} = \sqrt{(1+w')^2 + u'^2 + v'^2} - 1. \tag{2.6}$$

Assuming that the behaviour of the material is elastic, from Hooke's law, the strain ε is proportional to the stress σ:

$$\sigma = \frac{F}{A} = E\varepsilon, \tag{2.7}$$

where E is the Young's modulus, A the cross-sectional area of the element and F the force applied to the element due to the strain that acts in the same direction. For a string at rest that is under a uniform tension T_0, a displaced string will thus have a variable tension T as described by :

$$T(x,t) = T_0 + EA\left(\sqrt{(1+w')^2 + u'^2 + v'^2} - 1\right). \tag{2.8}$$

By Newton's second law, the force balance of an infinitesimal string element at point x is:

$$\rho A\ddot{\mathbf{q}} = \frac{\partial}{\partial x}\left[T(x,t)\hat{\mathbf{n}}\right], \tag{2.9}$$

where ρA is the density per length of the string, $\ddot{\mathbf{q}}$ the vector of the acceleration of the string in three dimensions and $\hat{\mathbf{n}}$ the unit displacement vector at point x. They can be expressed as:

$$\ddot{\mathbf{q}} = \ddot{w}\hat{\mathbf{i}} + \ddot{u}\hat{\mathbf{j}} + \ddot{v}\hat{\mathbf{k}}, \tag{2.10}$$

and

$$\hat{\mathbf{n}} = \frac{\mathbf{F}'\mathbf{G}'}{|\mathbf{F}'\mathbf{G}'|} = \frac{(1+w')\hat{\mathbf{i}} + u'\hat{\mathbf{j}} + v'\hat{\mathbf{k}}}{\sqrt{(1+w')^2 + u'^2 + v'^2}}. \tag{2.11}$$

Substituting Equation (2.10), (2.8), and (2.11) into Equation (2.9), one can obtain the set of *geometrically exact string equations* [75]:

$$\rho A\ddot{u} - \frac{\partial}{\partial x}\left[EAu' - (EA - T_0)\frac{u'}{\sqrt{(1+w')^2 + u'^2 + v'^2}}\right] = 0, \tag{2.12a}$$

$$\rho A\ddot{v} - \frac{\partial}{\partial x}\left[EAv' - (EA - T_0)\frac{v'}{\sqrt{(1+w')^2 + u'^2 + v'^2}}\right] = 0, \tag{2.12b}$$

$$\rho A\ddot{w} - \frac{\partial}{\partial x}\left[EA(1+w') - (EA - T_0)\frac{1+w'}{\sqrt{(1+w')^2 + u'^2 + v'^2}}\right] = 0. \tag{2.12c}$$

To complete the equations, for a string with two fixed ends, a Dirichlet boundary conditions can be imposed such that:

$$u(0,t) = v(0,t) = w(0,t) = 0, \tag{2.13a}$$
$$u(L,t) = v(L,t) = w(L,t) = 0. \tag{2.13b}$$

The main feature of Equation (2.12) is that it not only describes the nonlinear interaction between the two transverse displacements, but also the coupling with the longitudinal displacement as well. The longitudinal displacement is responsible for the precursor signal in a piano tone and it is this nonlinear coupling that explains the origin of it from an excitation of hammer in a transverse direction.

2.1.2 Third-order nonlinear string equations

The geometrically exact equation (Equation (2.12)) is notoriously difficult to solve due to the square root terms at the numerator, i.e.

$$\left((1+w')^2 + u'^2 + v'^2\right)^{-\frac{1}{2}}. \tag{2.14}$$

Fortunately, it is possible to expand and truncate expression (2.14) to simplify the equation. Expression (2.14) can be expanded by binomial series, which is defined as:

$$(1+x)^\alpha = 1 + \alpha x + \frac{\alpha(\alpha-1)}{2!}x^2 + \cdots. \tag{2.15}$$

Truncating up to cubic terms, this will lead to:

$$\left((1+w')^2 + u'^2 + v'^2\right)^{-\frac{1}{2}} = 1 - w' + w'^2 + (\frac{3}{2}w' - \frac{1}{2})(u'^2 + v'^2) + \frac{3}{2}w'^3. \tag{2.16}$$

Substituting Equation (2.16) into (2.12), again truncating up to cubic terms, the equations can be rewritten as [73–75]:

$$\rho A\ddot{u} - T_0 u'' - (EA - T_0)\frac{\partial}{\partial x}\left[u'\left(w' - w'^2 + \frac{u'^2 + v'^2}{2}\right)\right] = 0, \tag{2.17a}$$
$$\rho A\ddot{v} - T_0 v'' - (EA - T_0)\frac{\partial}{\partial x}\left[v'\left(w' - w'^2 + \frac{u'^2 + v'^2}{2}\right)\right] = 0, \tag{2.17b}$$
$$\rho A\ddot{w} - EAw'' - (EA - T_0)\frac{\partial}{\partial x}\left[\left(\frac{1}{2} - w'\right)\left(u'^2 + v'^2\right)\right] = 0. \tag{2.17c}$$

A further reduction can be made. From Equation (2.17c), it can be deduced that w' is of the same order of magnitude as u'^2 and v'^2. For accuracy up until the order of magnitude of $O(u'^3)$ and $O(v'^3)$, the w'^2 term (in Equation (2.17a) and (2.17b)) and the product between w' and $u'^2 + v'^2$ (in Equation (2.17c)) are canceled as they

would otherwise be at the order of $O(u'^4)$. Equation (2.17) can then be simplified to:

$$\rho A\ddot{u} - T_0 u'' - (EA - T_0)\frac{\partial}{\partial x}\left[u'\left(w' + \frac{u'^2 + v'^2}{2}\right)\right] = 0, \tag{2.18a}$$

$$\rho A\ddot{v} - T_0 v'' - (EA - T_0)\frac{\partial}{\partial x}\left[v'\left(w' + \frac{u'^2 + v'^2}{2}\right)\right] = 0, \tag{2.18b}$$

$$\rho A\ddot{w} - EAw'' - (EA - T_0)\frac{\partial}{\partial x}\left[\frac{1}{2}\left(u'^2 + v'^2\right)\right] = 0. \tag{2.18c}$$

Equation (2.18) is known as the *third-order nonlinear string equations* and serve as an intermediate step in reducing the geometrically exact equation to Kirchhoff-Carrier equation. The third-order string equations are extensively studied, such as by [36] and [76], in which simpler planar version of Equation (2.18) where $v = 0$ is assumed.

2.1.3 Kirchhoff-Carrier nonlinear string equations

The third-order nonlinear string equations can be further reduced to the Kirchhoff-Carrier nonlinear string equations. The Kirchhoff-Carrier equations are simpler, yet retain the nonlinear coupling between the two transverse modes u and v and are also extensively studied ([73,74,77–79]). Despite needing a few assumptions to simplify the third-order nonlinear string equations to the Kirchhoff-Carrier equations, the main coupling of interest, i.e. between the two transverse modes, is retained and thus the use of it is justified.
The first assumption to be made is that the inertia of the longitudinal displacement is negligible. Nayfeh and Mook [74] reported that the n-th transverse mode interacts with the m-th longitudinal mode if the longitudinal frequency is approximately twice the transverse frequency. This gives a relation:

$$mc_L \approx 2nc_T, \tag{2.19}$$

where:

$$c_L = \sqrt{\frac{E}{\rho}}, \tag{2.20a}$$

$$c_T = \sqrt{\frac{T_0}{\rho A}}. \tag{2.20b}$$

The relation can be rewritten as:

$$n \approx \frac{m}{2}\sqrt{\frac{EA}{T_0}}. \tag{2.21}$$

Using nominal values for the physical parameters, the ratio n/m would be about 10 to 16[1]. This means that the first longitudinal mode will only have tangible interaction with the 10th or higher transverse mode. At the most extreme case, using the ultimate tensile strength (UTS) for a piano string, where $\mathrm{UTS} = T_0/A = 2,600\mathrm{MPa}$, the ratio $n/m = 4.4$. This means that the first longitudinal mode will only have tangible interaction with the 4th or higher transverse mode. In other words, under the most extreme condition, longitudinal inertia has no influence at all for the first three modes; under a nominal condition, longitudinal inertia has no influence at least on the first 10th or higher transverse modes.
Essentially, omitting the longitudinal inertia (i.e. $\ddot{w} = 0$) does not affect the nonlinear coupling between the first few transverse modes. This property thus allows analyses to be carried out on a set of Kirchhoff-Carrier equations that consider only the first few modes. From a simulation perspective though, it would mean that the higher modes would be modelled slightly less accurately with the absence of longitudinal modes.
The second assumption for the Kirchhoff-Carrier equation is that the ultimate tensile strength of the string is insignificant compared to its Young's modulus. The nominal value for the Young's modulus of a steel string is approximately 200GPa. This allows a simplification where:

$$EA - T_0 \approx EA. \tag{2.22}$$

This can be justified because even if UTS value is used where $T_0/A = 2,600\mathrm{MPa}$, it is still two orders of magnitude lower than Young's modulus.
With both assumptions, Equation (2.18) can be rewritten as:

$$\rho A\ddot{u} - T_0 u'' - EA\frac{\partial}{\partial x}\left[u'\left(w' + \frac{u'^2 + v'^2}{2}\right)\right] = 0, \tag{2.23a}$$

$$\rho A\ddot{v} - T_0 v'' - EA\frac{\partial}{\partial x}\left[v'\left(w' + \frac{u'^2 + v'^2}{2}\right)\right] = 0, \tag{2.23b}$$

$$-EAw'' - EA\frac{\partial}{\partial x}\left[\frac{1}{2}\left(u'^2 + v'^2\right)\right] = 0. \tag{2.23c}$$

Integrating Equation (2.23c) with respect to x once, one obtains the following equation:

$$w' + \frac{1}{2}\left(u'^2 + v'^2\right) = C(t). \tag{2.24}$$

Integrating Equation (2.24) again will yield:

$$w(L) - w(0) + \frac{1}{2}\int_0^L \left(u'^2 + v'^2\right)\mathrm{d}x = C(t)L. \tag{2.25}$$

[1]Nominal values for musical acoustics:E = 200GPa, A = $10^{-6}\mathrm{m}^2$, T_0 = 500N would yield $n/m = 10$.

Applying the boundary condition from Equation (2.13), one gets an expression for $C(t)$ and consequently, Equation (2.24) becomes

$$w' = \frac{1}{2L}\int_0^L \left(u'^2 + v'^2\right) \mathrm{d}x - \frac{1}{2}\left(u'^2 + v'^2\right). \tag{2.26}$$

Substituting Equation (2.26) into Equation (2.23a) and (2.23b), keeping up to order of magnitude of $O(u'^3)$ and $O(v'^3)$, one gets a standard form of the Kirchhoff-Carrier equations:

$$\rho A\ddot{u} - (T_0 + N)u'' = 0, \tag{2.27a}$$
$$\rho A\ddot{v} - (T_0 + N)v'' = 0, \tag{2.27b}$$

where

$$N = \frac{EA}{2L}\int_0^L \left(u'^2 + v'^2\right) \mathrm{d}x. \tag{2.28}$$

The boundary conditions for Equation (2.27), as simplified from Equation (2.13) by dropping the w terms, are:

$$u(0,t) = v(0,t) = 0, \tag{2.29a}$$
$$u(L,t) = v(L,t) = 0. \tag{2.29b}$$

2.1.4 Linear wave equation

In Equation (2.27), if the displacements u and v are small as compared to the diameter of the string, u' and v' are also very small such that:

$$u'^2 \approx v'^2 \approx 0, \tag{2.30}$$

thus $N = 0$ and one can recover the linearised vibrating string equation, more commonly known as the "wave equation":

$$\rho A\ddot{u} - T_0 u'' = 0. \tag{2.31}$$

The same equation can also be recovered from the geometrically exact string equations (2.12). Expanding the expression (2.14) and keeping only up to the linear term, one could invariably recover three uncoupled linear wave equations in the same form of Equation (2.31) (although the longitudinal equation would have different constants). To complete Equation (2.31), the boundary conditions at both ends are:

$$u(0,t) = 0, \tag{2.32a}$$
$$u(L,t) = 0. \tag{2.32b}$$

Due to its simplicity, the wave equation can be solved by various methods, such as by modal method (see Section 2.3), by d'Alembert method (see [73]) or numerically (see [60]).

2.1.5 Stiffness effect of a string

In Sections 2.1.2, 2.1.3 and 2.1.4, all of the models disregard the stiffness of the string, which can be easily observed in a piano string by bending it at its unstrung state. The stiffness causes inharmonicity in piano strings, where the partials are not an integer multiple of the fundamental frequency. Inharmonicity is an also important feature of the piano sound and it is modelled in this thesis by two stiffness models, namely the Euler-Bernoulli model and Timoshenko model.
A linear wave equation with stiffness modeled by Euler-Bernoulli theory can be written as [33]:

$$\rho A\ddot{u} - T_0 u'' + EIu'''' = 0, \tag{2.33}$$

where E is the Young's modulus and I is the area moment of inertia. The stiffness effect can be included by simply concatenating an extra term to the original string equation. On the other hand, the Timoshenko model is more complicated and can be written as an extension of the linear wave equation as [32]:

$$\rho A\ddot{u} - T_0 u'' + AG\kappa\frac{\partial}{\partial x}(\phi - u') = 0, \tag{2.34a}$$

$$\rho I\ddot{\phi} - EI\phi'' + AG\kappa(\phi - u') = 0, \tag{2.34b}$$

where κ is the shear coefficient, G is the shear modulus and ϕ is the rotational displacement of the cross-sectional area of the string at point x. The boundary conditions are given by:

$$u(0,t) = 0, \tag{2.35a}$$

$$u(L,t) = 0, \tag{2.35b}$$

$$\phi'(0,t) = 0, \tag{2.35c}$$

$$\phi'(L,t) = 0. \tag{2.35d}$$

Similar to Euler-Bernoulli model, Timoshenko model can essentially be a concatenation to existing string equation in addition to solving ϕ.
The two models are based on different assumptions and their derivations are out of the scope of this thesis[2]. However, it is important to highlight that Euler-Bernoulli model neglects the shear deformation of the string. As a result, plane sections remain planar and normal to the longitudinal axis. On the other hand, shear deformation is considered in the Timoshenko model and the shear angle $\phi - u'$ is solved. The Timoshenko model can be simplified to yield the Euler-Bernoulli model by means of nondimensional analysis and making the assumption that the ratio between the diameter and length of the string, i.e. d/L is small [68].
More practically, the phase and group velocities of the Euler-Bernoulli model are unbounded which could result in non-physical values at high frequencies [33]. In

[2] See [33] for derivations of the Timoshenko and Euler-Bernoulli models.

contrast, the Timoshenko model predicts finite velocities. Nevertheless, for the application of piano strings, the frequencies computed are very similar at low frequencies [33, 68]. The choice of the stiffness model is essentially somewhat arbitrary as despite the different assumptions, their differences are only noticeable at sufficiently high frequencies. Thus, for this thesis, the simpler Kirchhoff-Carrier nonlinear equations are paired with the simpler Euler-Bernoulli model and the geometrically exact nonlinear equations are enriched by the Timoshenko model.
The Kirchhoff-Carrier nonlinear stiff string equation can be written as:

$$\rho A\ddot{u} - (T_0 + N)u'' + EIu'''' = 0, \tag{2.36a}$$

$$\rho A\ddot{v} - (T_0 + N)v'' + EIv'''' = 0, \tag{2.36b}$$

where N is as defined in Equation (2.28) and the boundary conditions remain unchanged from Equation (2.29).
The geometrically exact nonlinear stiff string model can be written as:

$$\rho A\ddot{u} - \frac{\partial}{\partial x}\left[EAu' - (EA - T_0)\frac{u'}{\sqrt{(1+w')^2 + u'^2 + v'^2}}\right] + AG\kappa\frac{\partial}{\partial x}(\phi - u') = 0, \tag{2.37a}$$

$$\rho A\ddot{v} - \frac{\partial}{\partial x}\left[EAv' - (EA - T_0)\frac{v'}{\sqrt{(1+w')^2 + u'^2 + v'^2}}\right] + AG\kappa\frac{\partial}{\partial x}(\psi - v') = 0, \tag{2.37b}$$

$$\rho A\ddot{w} - \frac{\partial}{\partial x}\left[EA(1+w') - (EA - T_0)\frac{1+w'}{\sqrt{(1+w')^2 + u'^2 + v'^2}}\right] = 0, \tag{2.37c}$$

$$\rho I\ddot{\phi} - EI\phi'' + AG\kappa(\phi - u') = 0, \tag{2.37d}$$

$$\rho I\ddot{\psi} - EI\psi'' + AG\kappa(\psi - v') = 0, \tag{2.37e}$$

with its boundary conditions as:

$$u(0,t) = v(0,t) = w(0,t) = 0, \tag{2.38a}$$

$$u(L,t) = v(L,t) = w(L,t) = 0, \tag{2.38b}$$

$$\phi'(0,t) = \psi'(0,t) = 0, \tag{2.38c}$$

$$\phi'(L,t) = \psi'(L,t) = 0. \tag{2.38d}$$

2.2 Energy conservation of the string models

In this section, the derivation of the energy conservation properties of the three string models in Section 2.1 is presented. To demonstrate the steps, one can begin

with the simplest linear wave equation.
The linear wave equation is essentially a force equation over the string length. To obtain an energy expression, one can multiply the equation with velocity and integrate the whole equation over the string length. In doing so, an equation expressing power can be obtained. Power is the rate of change of energy. Energy is conserved if it can be shown that the energy is constant and positive.
Multiplying Equation (2.31) with $\dot{u}$ and integrating over the string length, one obtains:

$$\int_0^L \rho A \ddot{u} \dot{u} \mathrm{d}x - \int_0^L T_0 u'' \dot{u} \mathrm{d}x = 0. \tag{2.39}$$

Using integration by part to break down the second term in Equation (2.39) and knowing that:

$$\frac{\partial}{\partial t}\left(\dot{u}^2\right) = 2\dot{u}\ddot{u}, \tag{2.40a}$$

$$\frac{\partial}{\partial t}\left(u'^2\right) = 2u'\dot{u}', \tag{2.40b}$$

eventually, one will obtain that:

$$\frac{d}{dt}\left\{\frac{1}{2}\int_0^L \rho A\left(\dot{u}\right)^2 + \frac{1}{2}\int_0^L T_0\left(u'\right)^2\right\} = T_0\left[\dot{u}u'\right]_0^L. \tag{2.41}$$

On the left hand side (LHS), the first and second term of the equation represent the kinetic energy and potential energy respectively. On the right hand side (RHS) lies the boundary term. In the case of a string with two fixed ends, using boundary condition (2.32), the boundary terms vanish. Thus, the conservation of energy equation is written as:

$$\frac{d}{dt}\left\{\mathrm{KE_s} + \mathrm{PE_s}\right\} = 0, \tag{2.42}$$

where

$$\mathrm{KE_s} = \frac{1}{2}\int_0^L \rho A\left(\dot{u}\right)^2 \mathrm{d}x, \tag{2.43a}$$

$$\mathrm{PE_s} = \frac{1}{2}\int_0^L T_0\left(u'\right)^2 \mathrm{d}x. \tag{2.43b}$$

Each term is positive and the rate of change of energy equals to zero.
A similar strategy could be followed for subsequently more complicated equations with additional treatments given to the extra terms. In the linear Timoshenko string model, multiplying Equation (2.34a) and (2.34b) with $\dot{u}$ and $\dot{\phi}$ respectively

and integrating both of them over the string length L, one would obtain:

$$\frac{d}{dt}\left[\frac{1}{2}\int_0^L \rho A\left(\dot{u}\right)^2 \mathrm{d}x + \frac{1}{2}\int_0^L T_0\left(u'\right)^2 \mathrm{d}x\right] - AG\kappa\int_0^L \left(\phi - u'\right)\dot{u}'\mathrm{d}x = T_0\left[\dot{u}u'\right]_0^L - AG\kappa\left[\left(\phi - u'\right)\dot{u}\right]_0^L, \tag{2.44a}$$

$$\frac{d}{dt}\left[\frac{1}{2}\int_0^L \rho I\left(\dot{\phi}\right)^2 \mathrm{d}x + \frac{1}{2}\int_0^L EI\left(\phi'\right)^2 \mathrm{d}x\right] - AG\kappa\int_0^L \left(\phi - u'\right)\dot{\phi}\mathrm{d}x = EI\left[\dot{\phi}\phi'\right]_0^L. \tag{2.44b}$$

The boundary terms at RHS vanish when the boundary condition of Equation (2.35) is applied. Summing both equations and knowing that:

$$\frac{\partial}{\partial t}(\phi - u')^2 = 2(\phi - u')(\dot{\phi} - \dot{u}'), \tag{2.45}$$

one can arrive at the same form as Equation (2.42) with:

$$\mathrm{KE_s} = \frac{1}{2}\int_0^L \rho A\left(\dot{u}\right)^2 \mathrm{d}x + \frac{1}{2}\int_0^L \rho I\left(\dot{\phi}\right)^2 \mathrm{d}x, \tag{2.46a}$$

$$\mathrm{PE_s} = \frac{1}{2}\int_0^L T_0\left(u'\right)^2 \mathrm{d}x + \frac{1}{2}\int_0^L EI\left(\phi'\right)^2 \mathrm{d}x + \frac{1}{2}\int_0^L AG\kappa(\phi - u')^2\mathrm{d}x. \tag{2.46b}$$

All terms are positive and the sum of the rate of change is zero, indicating that energy is conserved.
Next is the Kirchhoff-Carrier nonlinear stiff string equation. Similar to the previous models, the two equations in Equation (2.36) can be multiplied by $\dot{u}$ and $\dot{v}$ respectively. The term $EIu''''\dot{u}$ can be integrated by parts twice to show:

$$\int_0^L EIu''\dot{u}''\mathrm{d}x = \left[u''''\dot{u} - u''\dot{u}'\right]_0^L, \tag{2.47}$$

and similarly for $EIv''''\dot{v}$. Again, from the boundary conditions, the boundary terms equate to zero. This leads to the energy conservation in the same form of Equation (2.42) where:

$$\mathrm{KE_s} = \frac{1}{2}\int_0^L \rho A\left(\dot{u}\right)^2 \mathrm{d}x + \frac{1}{2}\int_0^L \rho A\left(\dot{v}\right)^2 \mathrm{d}x,$$

$$\mathrm{PE_s} = \frac{1}{2}\int_0^L (T_0 + N)\left(u'\right)^2 \mathrm{d}x + \frac{1}{2}\int_0^L (T_0 + N)\left(v'\right)^2 \mathrm{d}x + \frac{1}{2}\int_0^L EI\left(u''\right)^2 \mathrm{d}x.$$

It is interesting to note that despite the nonlinear coupling in the term N, it is nonetheless obvious that PE_s is positive as N is always positive. Subsequently, it is elementary to show that the rest of the terms are positive to prove the conservation of energy.
The final string equation to prove the conservation of energy is the geometrically

exact nonlinear stiff string equation (i.e. Equation (2.37)). It is possible to rewrite the equation into a general form of matrix equations, as is done in Chabassier's thesis [75]. For $\mathbf{q} = [u, v, w, \phi, \psi]$, the equation can be written as:

$$\mathbf{M_s}\ddot{\mathbf{q}} - \frac{\partial}{\partial x}\left(\mathbf{A}\mathbf{q}' + \mathbf{B}\mathbf{q} + \nabla\mathbf{H}(\mathbf{q}')\right) + \mathbf{C}\mathbf{q} + \mathbf{B}^{\mathbf{T}}\mathbf{q}' = 0, \tag{2.49a}$$

$$q_k(0,t) = 0 \qquad \text{for} \qquad k = 1,2,3; \tag{2.49b}$$

$$q_k(L,t) = 0 \qquad \text{for} \qquad k = 1,2,3; \tag{2.49c}$$

$$q_k'(0,t) = 0 \qquad \text{for} \qquad k = 4,5; \tag{2.49d}$$

$$q_k'(L,t) = 0 \qquad \text{for} \qquad k = 4,5; \tag{2.49e}$$

where $\mathbf{A} = \mathbf{A_t} + \mathbf{A_r}$ and

$$\mathbf{M_s} = \begin{bmatrix} \rho A & 0 & 0 & 0 & 0 \\ 0 & \rho A & 0 & 0 & 0 \\ 0 & 0 & \rho A & 0 & 0 \\ 0 & 0 & 0 & \rho I & 0 \\ 0 & 0 & 0 & 0 & \rho I \end{bmatrix}, \mathbf{B} = \begin{bmatrix} 0 & 0 & 0 & -AG\kappa & 0 \\ 0 & 0 & 0 & 0 & -AG\kappa \\ 0 & 0 & 0 & 0 & 0 \\ 0 & 0 & 0 & 0 & 0 \\ 0 & 0 & 0 & 0 & 0 \end{bmatrix}, \mathbf{C} = \begin{bmatrix} 0 & 0 & 0 & 0 & 0 \\ 0 & 0 & 0 & 0 & 0 \\ 0 & 0 & 0 & 0 & 0 \\ 0 & 0 & 0 & AG\kappa & 0 \\ 0 & 0 & 0 & 0 & AG\kappa \end{bmatrix},$$

$$\mathbf{A_t} = \begin{bmatrix} T_0 & 0 & 0 & 0 & 0 \\ 0 & T_0 & 0 & 0 & 0 \\ 0 & 0 & EA & 0 & 0 \\ 0 & 0 & 0 & EI & 0 \\ 0 & 0 & 0 & 0 & EI \end{bmatrix} \quad \text{and} \quad \mathbf{A_r} = \begin{bmatrix} AG\kappa & 0 & 0 & 0 & 0 \\ 0 & AG\kappa & 0 & 0 & 0 \\ 0 & 0 & 0 & 0 & 0 \\ 0 & 0 & 0 & 0 & 0 \\ 0 & 0 & 0 & 0 & 0 \end{bmatrix}. \tag{2.50}$$

$\mathbf{H}$ is a functional and is defined as:

$$\mathbf{H}(u,v,w) = (EA - T_0)\left[\frac{1}{2}\left(u^2 + v^2\right) + (1+w) - \sqrt{u^2 + v^2 + (1+w)^2}\right]. \tag{2.51}$$

Equation (2.49) can also be used to recover earlier energy conservation properties, too. If functional $\mathbf{H} = 0$, $\mathbf{B} = \mathbf{C} = \mathbf{A_r} = 0$, one could recover the system of three uncoupled linear equations where $\mathbf{q} = [u, v, w]$. After multiplying Equation (2.49) with $\dot{\mathbf{q}}$, one could retrieve the energy conservation where:

$$\frac{d}{dt}\left\{\mathrm{KE_s} + \mathrm{PE_s}\right\} = 0, \tag{2.52}$$

such that:

$$\mathrm{KE_s} = \frac{1}{2}\int_0^L \mathbf{M_s}(\dot{\mathbf{q}})^2 \mathrm{d}x, \tag{2.53a}$$

$$\mathrm{PE_s} = \frac{1}{2}\int_0^L \mathbf{A}(\mathbf{q}')^2 \mathrm{d}x, \tag{2.53b}$$

which is analogous to Equation (2.43). However, setting only $\mathbf{H} = 0$, one could recover two pairs of Timoshenko stiff string equations (each associated with a transverse displacement) as well as a linear decoupled longitudinal wave equation, which

would give the conservation of energy equation for $\mathbf{q} = [u, v, w, \phi, \psi]$, such that:

$$\mathrm{KE_s} = \frac{1}{2}\int_0^L \mathbf{M_s}(\dot{\mathbf{q}})^2 \mathrm{d}x, \tag{2.54a}$$

$$\mathrm{PE_s} = \frac{1}{2}\int_0^L \mathbf{A_t}(\mathbf{q}')^2 \mathrm{d}x + \left(\frac{1}{2}\int_0^L \mathbf{A_r}(\mathbf{q}')^2 \mathrm{d}x \frac{1}{2}\int_0^L \mathbf{C}(\mathbf{q})^2 \mathrm{d}x + \frac{1}{2}\int_0^L \mathbf{B}\mathbf{q}\mathbf{q}' \mathrm{d}x + \frac{1}{2}\int_0^L \mathbf{B^T}\mathbf{q}'\mathbf{q} \mathrm{d}x\right), \tag{2.54b}$$

where the term in bracket in Equation (2.54b) is analogous to the last term of Equation (2.46b) such that the sum of all these terms will be positive.
Finally, if $\mathbf{H} \neq 0$ (i.e. geometrically exact nonlinear stiff string equation), one could show that:

$$-\int_0^L \frac{\partial}{\partial x}\left[\nabla \mathbf{H}(\mathbf{q}')\right]\dot{\mathbf{q}} = \int_0^L \frac{\partial}{\partial t}\mathbf{H}(\mathbf{q}') - \left[\nabla \mathbf{H}(\mathbf{q}')\dot{\mathbf{q}}\right]_0^L, \tag{2.55}$$

where the boundary terms will once more be equal to zero due to boundary conditions. The kinetic and potential energy of this particular system is thus [75]:

$$\mathrm{KE_s} = \frac{1}{2}\int_0^L \mathbf{M_s}(\dot{\mathbf{q}})^2 \mathrm{d}x, \tag{2.56a}$$

$$\begin{aligned}\mathrm{PE_s} = &\left(\frac{1}{2}\int_0^L \mathbf{A_r}(\mathbf{q}')^2 \mathrm{d}x + \frac{1}{2}\int_0^L \mathbf{C}(\mathbf{q})^2 \mathrm{d}x + \frac{1}{2}\int_0^L \mathbf{B}\mathbf{q}\mathbf{q}' \mathrm{d}x + \frac{1}{2}\int_0^L \mathbf{B^T}\mathbf{q}'\mathbf{q} \mathrm{d}x\right) \\ &+ \left(\frac{1}{2}\int_0^L \mathbf{A_t}(\mathbf{q}')^2 \mathrm{d}x + \frac{1}{2}\int_0^L \mathbf{H}(\mathbf{q}') \mathrm{d}x\right).\end{aligned} \tag{2.56b}$$

As is demonstrated in Chabassier's thesis [75], it can be proved that:

$$\frac{1}{2}\mathbf{A_t}(\mathbf{q}')^2 + \mathbf{H}(\mathbf{q}') \geq K|\mathbf{q}'|^2 \qquad \text{if} \qquad K = \min(T_0, EI)/2, \tag{2.57}$$

and thus Equation (2.56b) is positive and energy is conserved.

2.3 Modal solution of linear wave equation

The linear wave equation can be solved directly via modal method without the need of any numerical approximations. The solution, while simple, is in fact useful in demonstrating a lot of concepts in solving an eigenfrequency problem. It is thus presented here as a basis for more complex work in subsequent sections and chapters.
The wave equation, as rewritten here, is:

$$\rho A \ddot{u} - T_0 u'' = 0,$$

and it has a solution where the spatial and temporal terms can be separated such that:

$$u(x,t) = p(t)\xi(x). \tag{2.58}$$

Substituting Equation (2.58) into the wave equation, one would obtain:

$$\frac{\ddot{p}}{p} = \frac{T_0}{\rho A}\frac{\xi''}{\xi}. \tag{2.59}$$

By separation of variables, Equation (2.59) can be rewritten into two independent equations equating to a same constant $-\omega^2$. While the constant can be defined in any other way, it will be apparent that $-\omega^2$ is indeed a convenient choice in the development of the solution. The two independent equations are:

$$\frac{\ddot{p}}{p} = -\omega^2, \tag{2.60a}$$

$${c_T}^2\frac{\xi''}{\xi} = -\omega^2, \tag{2.60b}$$

where c_T is the phase speed of the transverse waves already introduced in Equation 2.20b and is given by:

$$c_T = \frac{\omega}{k} = \sqrt{\frac{T}{\rho A}}. \tag{2.61}$$

The boundary conditions of the system are thus:

$$u(0,t) = \xi(0)p(t) = 0, \tag{2.62a}$$

$$u(L,t) = \xi(L)p(t) = 0. \tag{2.62b}$$

The boundary condition $\xi(0) = \xi(L) = 0$ forms an eigenvalue problem together with Equation (2.60b) and is written as:

$$\begin{cases} \xi'' = -k^2\xi, \\ \xi(0) = \xi(L) = 0, \end{cases} \tag{2.63}$$

where k is the wavenumber and for $k \geq 0$, solution of Equation (2.63) can take the form below:

$$\xi(x) = C\cos(kx) + D\sin(kx), \tag{2.64}$$

where C and D are constants to be determined. Applying the boundary conditions in Equation (2.62) , the mode shape ξ can be written as:

$$\xi_n(x) = C_n\sin(k_n x) \qquad \text{with} \qquad k_n = \frac{n\pi}{L}, \tag{2.65}$$

where the subscript n indicates there are an infinite number of solutions to the eigenvalue problem (2.63) where the eigenvalues are k_n with eigenmodes $\xi_n(x)$. For each n, there is a corresponding ω_n given by the dispersion relation of Equation (2.61) and the solution of Equation (2.60a) is:

$$p_n(t) = P_n^1\cos(\omega_n t) + P_n^2\sin(\omega_n t). \tag{2.66}$$

The constants P_n^1 and P_n^2 can be solved with the knowledge of the initial conditions. Thus, for each n, there exists a solution of u_n where:

$$u_n = p_n(t)\xi_n(x). \tag{2.67}$$

Since the wave equation is linear, the solutions for the system can also be defined as any linear combination of u_n, i.e.:

$$u(x,t) = \sum_{n=1}^{N} \left[P_n^1 \cos(\omega_n t) + P_n^2 \sin(\omega_n t)\right] \sin(k_n x). \tag{2.68}$$

The constant C is no longer necessary as it can be solved together with P_n^1 and P_n^2. Suppose that the initial conditions can be defined as follows:

$$u_n(x,0) = U_0(x), \tag{2.69a}$$
$$\dot{u}_n(x,0) = U_1(x), \tag{2.69b}$$

from Equation (2.68):

$$U_0 = \sum_{n=1}^{N} P_n^1 \sin(k_n x), \tag{2.70a}$$
$$U_1 = \sum_{n=1}^{N} \omega_n P_n^2 \sin(k_n x). \tag{2.70b}$$

To solve for P_n^1 and P_n^2, the equations can be multiplied by another eigenmode ξ_m and be integrated over the string length, they then become:

$$\int_0^L U_0 \xi_m \mathrm{d}x = \sum_{n=1}^{N} P_n^1 \int_0^L \xi_n \xi_m \mathrm{d}x, \tag{2.71a}$$
$$\int_0^L U_1 \xi_m \mathrm{d}x = \sum_{n=1}^{N} P_n^2 \omega_n \int_0^L \xi_n \xi_m \mathrm{d}x. \tag{2.71b}$$

From the orthogonality properties of the eigenmodes:

$$\int_0^L \sin\left(\frac{n\pi x}{L}\right) \sin\left(\frac{m\pi x}{L}\right) \mathrm{d}x = \begin{cases} \frac{L}{2} & \text{for} \quad m = n, \\ 0 & \text{for} \quad m \neq n, \end{cases} \tag{2.72}$$

the solution for P_n^1 and P_n^2 can thus be written as:

$$P_n^1 = \frac{2}{L} \int_0^L \sin\left(\frac{n\pi x}{L}\right) U_0(x) \mathrm{d}x, \tag{2.73a}$$
$$\omega_n P_n^2 = \frac{2}{L} \int_0^L \sin\left(\frac{n\pi x}{L}\right) U_1(x) \mathrm{d}x. \tag{2.73b}$$

2.4 Numerical methods for string vibration

This section is devoted to the presentation of numerical solutions for the Kirchhoff-Carrier nonlinear equations and the geometrically exact nonlinear equations. To begin with the presentation, damping models are introduced in Section 2.4.1 as they will be used in the numerical simulations for accurate time-domain solutions. The damping models are:

- simple viscous damping model (SVM) [57],
- Valette & Cuesta damping model (VCM) [80].

The Kirchhoff-Carrier nonlinear stiff string equations are solved by a semi-implicit modal time-stepping scheme [60] as presented in Section 2.4.2 and the scheme is coded in MATLAB. On the other hand, the geometrically exact nonlinear stiff string equations are solved via finite element method as presented in Section 2.4.3 and the scheme is implemented in MONTJOIE, a high-order finite element solver developed in INRIA [81]. Convergence tests and comparisons between these two schemes are also carried out.

2.4.1 Damping models

Damping is an intrinsic properties that is present in all kinds of physical systems where the system loses energy in one way or another. In a vibrating string, the energy is lost internally through mechanisms like thermoelasticity, viscoelasticity or to the surroundings by air friction. The damping also displays a dependence on string's vibrating frequency where the higher the frequency, the higher the loss. An excellent model where the aforementioned losses (i.e. thermoelasticity, viscoelasticity and air friction) are considered is the Valette & Cuesta model (VCM) [80]. A simpler alternative is the simple viscous damping model (SVM) [57] where the frequency-dependent damping is modeled simply by two variables that are not associated to any physical meanings. The SVM is easily applied in both time and frequency domains, which is a justification of its wide use in simulations. However, it does not rely on physical arguments as compared to VCM. VCM is easily expressed in the frequency domain, but the complex frequency dependence makes it difficult to express in the time domain. A recent attempt is proposed in [82]. In what follows, the two models are presented and incorporated to the existing string equations.

Valette & Cuesta model (VCM) [80]

The Valette & Cuesta model (VCM) is a frequency-based damping model and can be added to a string equation in its modal form. Recall that Equation (2.60a) can be written in its modal form as:

$$\ddot{p}_n + {\omega_n}^2 p_n = 0 \qquad \text{for} \qquad n = 1, 2, 3... \tag{2.74}$$

where the subscript n indicates that there is an infinite number of solutions of the equation. When damping is added, a new term is appended to the equation:

$$\ddot{p}_n + {\omega_n}^2 p_n + 2\varsigma_n \dot{p_n} = 0, \tag{2.75}$$

with the damping constant ς_n:

$$\varsigma_n = \sigma_n, \tag{2.76}$$

and σ_n is the modal damping factor with a unit of s^{-1}. The concatenation of the damping term $2\varsigma_n \dot{p_n}$ can be applied to all string models expressed in modal form. The VCM damping parameter is associated to the quality factor by:

$$Q_n = \frac{\pi f_n}{\sigma_n}, \tag{2.77}$$

where for VCM [83]:

$$\frac{1}{Q_n} = \frac{1}{Q_{n,air}} + \frac{1}{Q_{n,vis}} + \frac{1}{Q_{ther}}, \tag{2.78}$$

and $f_n = \omega_n / 2\pi$. $Q_{n,air}$, $Q_{n,vis}$ and Q_{ther} are respectively the quality factors associated to losses due to air friction, viscoelasticity and thermoelasticity of the string. In particular, $Q_{n,air}$ and $Q_{n,vis}$ can be calculated by:

$$\frac{1}{Q_{n,air}} = \frac{2\pi\eta_{air} + 2\pi d\sqrt{\pi\eta_{air}\rho_{air} f_n}}{2\pi\rho A f_n}, \tag{2.79a}$$

$$\frac{1}{Q_{n,vis}} = \frac{4\pi^2 \rho A E I {f_n}^2}{{T_0}^2}\delta_{vis}, \tag{2.79b}$$

where η_{air} and ρ_{air} are the dynamic viscoscity and density of air respectively and nominal values can be chosen as $\eta_{air} = 1.8 \times 10^{-1} \mathrm{kgm}^{-1}\mathrm{s}^{-1}$ and $\rho_{air} = 1.2 \mathrm{kgm}^{-3}$ [83]. To completely determine Equation (2.78), it is necessary to obtain values for the viscoelastic loss angle δ_{vis} and the thermoelastic loss quality factor Q_{ther}. These values can be estimated by fitting experimental data to Equation (2.78) as detailed in Section 4.3.

Simple viscous damping model (SVM) [57]

In contrast to the VCM, the simple viscous damping model (SVM) adds the following terms to the string equations of motion:

$$2\mathbf{R}\rho A\dot{\mathbf{q}} - 2\boldsymbol{\zeta} T_0 \dot{\mathbf{q}}'', \tag{2.80}$$

where $\mathbf{R}$ and $\boldsymbol{\zeta}$ are the two damping constants vectors that fully describe the model and $\mathbf{q}$ is the string variable. The term $\mathbf{R}$ defines the constant losses while $\boldsymbol{\zeta}$ defines the frequency-dependent losses. To estimate these parameters, the damping terms are written in modal form. Appending SVM to the linear wave equation where $\mathbf{q} = [u]$, the modal form with temporal coordinate p_n can be written as:

$$\ddot{p}_n + {\omega_n}^2 p_n + 2(R_u + {\omega_n}^2 \zeta_u)\dot{p_n} = 0, \tag{2.81}$$

which is identical to Equation (2.75), by setting the damping constant ς_n:

$$\varsigma_n = R_u + {\omega_n}^2 \zeta_u. \tag{2.82}$$

Similar to VCM, the two unknowns R_u and ζ_u can be determined by fitting from experimental data as detailed in Section 4.3.
For the time domain simulation, it is also possible to append SVM to the geometrically exact nonlinear stiff string equations where $\mathbf{q} = [u, v, w, \phi, \psi]$. This would yield:

$$\rho A\ddot{u} - T_0 u'' - \frac{\partial}{\partial x}\left[EAu' - (EA - T_0)\frac{u'}{\sqrt{(1+w')^2 + u'^2 + v'^2}}\right] + AG\kappa\frac{\partial}{\partial x}(\phi - u') + 2R_u\rho A\dot{u} - 2\zeta_u T_0 \dot{u}'' = 0, \tag{2.83a}$$

$$\rho A\ddot{v} - T_0 v'' - \frac{\partial}{\partial x}\left[EAv' - (EA - T_0)\frac{v'}{\sqrt{(1+w')^2 + u'^2 + v'^2}}\right] + AG\kappa\frac{\partial}{\partial x}(\psi - v') + 2R_v\rho A\dot{v} - 2\zeta_v T_0 \dot{v}'' = 0, \tag{2.83b}$$

$$\rho A\ddot{w} - \frac{\partial}{\partial x}\left[EA(1+w') - (EA - T_0)\frac{1+w'}{\sqrt{(1+w')^2 + u'^2 + v'^2}}\right] + 2R_w\rho A\dot{w} - 2\zeta_w EA\dot{w}'' = 0, \tag{2.83c}$$

$$\rho I\ddot{\phi} - EI\phi'' + AG\kappa(\phi - u') + 2R_\phi\rho I\dot{\phi} - 2\zeta_\phi EI\dot{\phi}'' = 0, \tag{2.83d}$$

$$\rho I\ddot{\psi} - EI\psi'' + AG\kappa(\psi - v') + 2R_\psi\rho I\dot{\psi} - 2\zeta_\psi EI\dot{\psi}'' = 0, \tag{2.83e}$$

or in its compact form, as extended from Equation (2.49a):

$$\mathbf{M_s}\ddot{\mathbf{q}} - \frac{\partial}{\partial x}\left(\mathbf{A}\mathbf{q}' + \mathbf{B}\mathbf{q} + \nabla\mathbf{H}(\mathbf{q}')\right) + \mathbf{C}\mathbf{q} + \mathbf{B}^\mathbf{T}\mathbf{q}' + \mathbf{Y}\dot{\mathbf{q}} - \mathbf{Z}\dot{\mathbf{q}}'' = 0, \tag{2.84}$$

where

$$\mathbf{Y} = \begin{bmatrix} \rho AR_u & 0 & 0 & 0 & 0 \\ 0 & \rho AR_v & 0 & 0 & 0 \\ 0 & 0 & \rho AR_w & 0 & 0 \\ 0 & 0 & 0 & \rho IR_\phi & 0 \\ 0 & 0 & 0 & 0 & \rho IR_\psi \end{bmatrix}, \quad \mathbf{Z} = \begin{bmatrix} 2T_0\zeta_u & 0 & 0 & 0 & 0 \\ 0 & 2T_0\zeta_v & 0 & 0 & 0 \\ 0 & 0 & 2EA\zeta_w & 0 & 0 \\ 0 & 0 & 0 & 2EI\zeta_\phi & 0 \\ 0 & 0 & 0 & 0 & 2EI\zeta_\psi \end{bmatrix}. \tag{2.85}$$

2.4.2 Kirchhoff-Carrier damped nonlinear string model

Recalling from Equation (2.36), the Kirchhoff-Carrier stiff string equations can be written as:

$$\rho A\ddot{u} - (T_0 + N)u'' + EIu'''' = 0, \tag{2.86a}$$
$$\rho A\ddot{v} - (T_0 + N)v'' + EIv'''' = 0, \tag{2.86b}$$

where

$$N = \frac{EA}{2L}\int_0^L \left(u'^2 + v'^2\right) \mathrm{d}x,$$

and the boundary conditions are

$$u(0,t) = v(0,t) = 0,$$
$$u(L,t) = v(L,t) = 0.$$

Equation (2.86) can be approximated by Galerkin's formulation such that:

$$u(x,t) = \sum_{k=1}^{K} \xi_k(x)p_k(t), \qquad v(x,t) = \sum_{k=1}^{K} \xi_k(x)q_k(t), \tag{2.88}$$

and the eigenmodes ξ_k can be expressed as:

$$\xi_k(x) = \sin\left(\frac{k\pi x}{L}\right). \tag{2.89}$$

Substituting Equation (2.88) into (2.86), one can obtain:

$$\rho A\ddot{p_k}\xi_k + EIp_k{\xi_k}'''' - (T_0 + N)p_k{\xi_k}'' + 2\varsigma_k\dot{p}_k = 0, \tag{2.90a}$$
$$\rho A\ddot{q_k}\xi_k + EIq_k{\xi_k}'''' - (T_0 + N)q_k{\xi_k}'' + 2\varsigma_k\dot{q}_k = 0, \tag{2.90b}$$

and

$$N = \frac{EA}{2L}\int_0^L (p_m^2 + q_m^2){\xi_m'}^2 \mathrm{d}x, \tag{2.91}$$

where $2\varsigma_k\dot{p}_k$ and $2\varsigma_k\dot{q}_k$ are the damping terms appended for both displacements. Knowing that:

$$\int_0^L {\xi_m}'^2 \mathrm{d}x = L/2, \tag{2.92}$$

it is possible to eliminate all the terms associated to ξ_k and obtain:

$$\ddot{p_k} + \Omega_k^2\tilde{p}_k + D_k\dot{p_k} + N_kp_k\sum_{m=1}^{K}\left[m^2(p_m^2 + q_m^2)\right] = 0, \tag{2.93a}$$

$$\ddot{q_k} + \bar{\Omega}_k^2\tilde{q}_k + D_k\dot{q_k} + N_kq_k\sum_{m=1}^{K}\left[m^2(p_m^2 + q_m^2)\right] = 0, \tag{2.93b}$$

where

$$\Omega_k^2 = \bar{\Omega}_k^2 = \frac{EIk^4\pi^4}{\rho AL^4} + \frac{T_0k^2\pi^2}{\rho AL^2}, \tag{2.94a}$$

$$D_k = \frac{2\varsigma_k}{\rho A}, \tag{2.94b}$$

$$N_k = \frac{Ek^2\pi^4}{4\rho L^4}, \tag{2.94c}$$

and Ω_k^2 and $\bar{\Omega}_k^2$ are the eigenfrequencies of p_k and q_k respectively. In Chapter 3, it will be clear why a distinction is made between the two sets of eigenfrequencies. On the other hand, D_k and N_k represent the damping and nonlinear terms respectively.

The scheme at Equation 2.93 can be numerically integrated such that:

$$\ddot{p_k} = \frac{p_k^{n+1} - 2p^n + p_k^{n-1}}{\Delta t^2}, \tag{2.95a}$$

$$\dot{p_k} = \frac{p_k^{n+1} - p_k^{n-1}}{2\Delta t}, \tag{2.95b}$$

$$\tilde{p}_k = \alpha p_k^n + (1-\alpha)\frac{p_k^{n+1} + p_k^{n-1}}{2}. \tag{2.95c}$$

For $\ddot{p_k}$ and $\dot{p_k}$, a standard time-stepping scheme is proposed and for the term $\tilde{p}_k$, a family of scheme with α acting as an averaging parameter is introduced [60]. Such implementation allows the control of stability of the scheme, as will be evident later. The same treatments can be made similarly for $\ddot{q_k}$, $\dot{q_k}$ and $\tilde{q_k}$ and to ensure an energy conserving scheme, the nonlinear term in the summation sign is approximated by:

$$\sum_{m=1}^{K}(m^2(p_m^2 + q_m^2)) = \sum_{m=1}^{K} m^2\left[p_m^n\left(\frac{p_m^{n+1} + p_m^{n-1}}{2}\right) + q_m^n\left(\frac{q_m^{n+1} + q_m^{n-1}}{2}\right)\right]. \tag{2.96}$$

Substituting Equations (2.95) and (2.96) into (2.93), one could get a scheme for p

and q that writes as:

$$
\begin{aligned}
&\left(\frac{1}{\Delta t^2}+\Omega_k^2\frac{1-\alpha}{2}+\frac{D}{2\Delta t}\right){p_k}^{n+1}\\
&+(-\frac{2}{\Delta t^2}+\alpha\Omega_k^2+N_k\sum_{m=1}^{K}\left(\frac{m^2}{2}(p_m^{n+1}p_m^n+q_m^{n+1}q_m^n)\right){p_k}^n\\
&=-\left(-\frac{2}{\Delta t^2}\alpha\Omega_k^2+N_k\sum_{m=1}^{K}\left(\frac{m^2}{2}(p_m^{n-1}p_m^n+q_m^{n-1}q_m^n)\right)\right){p_k}^n\\
&\qquad-\left(\frac{1}{\Delta t^2}+\Omega_k^2\frac{1-\alpha}{2}-\frac{D}{2\Delta t}\right){p_k}^{n-1},
\end{aligned}
\tag{2.97a}
$$

$$
\begin{aligned}
&\left(\frac{1}{\Delta t^2}+\bar{\Omega}_k^2\frac{1-\alpha}{2}+\frac{D}{2\Delta t}\right){q_k}^{n+1}\\
&+(-\frac{2}{\Delta t^2}+\alpha\bar{\Omega}_k^2+N_k\sum_{m=1}^{K}\left(\frac{m^2}{2}(p_m^{n+1}p_m^n+q_m^{n+1}q_m^n)\right){q_k}^n\\
&=-\left(-\frac{2}{\Delta t^2}\alpha\bar{\Omega}_k^2+N_k\sum_{m=1}^{K}\left(\frac{m^2}{2}(p_m^{n-1}p_m^n+q_m^{n-1}q_m^n)\right)\right){q_k}^n\\
&\qquad-\left(\frac{1}{\Delta t^2}+\bar{\Omega}_k^2\frac{1-\alpha}{2}-\frac{D}{2\Delta t}\right){q_k}^{n-1}.
\end{aligned}
\tag{2.97b}
$$

At the LHS of Equation (2.97), the unknowns are all the terms with superscript $n+1$. This makes the scheme implicit as there are more than one term to be solved at the LHS. Fortunately, at each time step n, the scheme can be arranged in a matrix form and be solved as a system of linear equations, i.e. $\mathbb{AX}=\mathbb{B}$ such that for all $k=1,2,\cdots,K$ and all $m=1,2,\cdots,K$:

$$
\begin{bmatrix}
b_{11}+a_1 & b_{12} & \cdots & b_{1k} & c_{11} & c_{12} & \cdots & c_{1k}\\
b_{21} & b_{22}+a_2 & \cdots & b_{2k} & c_{21} & c_{22} & \cdots & c_{2k}\\
\vdots & \vdots & \ddots & \vdots & \vdots & \vdots & \ddots & \vdots\\
b_{k1} & b_{k2} & \cdots & b_{kk}+a_k & c_{k1} & c_{k2} & \cdots & c_{kk}\\
e_{11} & e_{12} & \cdots & e_{1k} & f_{11}+d_1 & f_{12} & \cdots & f_{1k}\\
e_{21} & e_{22} & \cdots & e_{2k} & f_{21} & f_{22}+d_2 & \cdots & f_{2k}\\
\vdots & \vdots & \ddots & \vdots & \vdots & \vdots & \ddots & \vdots\\
e_{k1} & e_{k2} & \cdots & e_{kk} & f_{k1} & f_{k2} & \cdots & f_{kk}+d_k
\end{bmatrix}
\begin{bmatrix}
p_1^{n+1}\\ p_2^{n+1}\\ \vdots\\ p_k^{n+1}\\ q_1^{n+1}\\ q_2^{n+1}\\ \vdots\\ q_k^{n+1}
\end{bmatrix}
=
\begin{bmatrix}
G_1\\ G_2\\ \vdots\\ G_k\\ H_1\\ H_2\\ \vdots\\ H_k
\end{bmatrix},
\tag{2.98}
$$

where

$$a_k = \frac{1}{\Delta t^2} + \Omega_k^2 \frac{1-\alpha}{2} + \frac{D_k}{2\Delta t}, \tag{2.99a}$$

$$b_{km} = N_k p_k^n \left[\frac{m^2}{2} p_m^n \right], \tag{2.99b}$$

$$c_{km} = N_k p_k^n \left[\frac{m^2}{2} q_m^n \right], \tag{2.99c}$$

$$d_k = \frac{1}{\Delta t^2} + \bar{\Omega}_k^2 \frac{1-\alpha}{2} + \frac{D_k}{2\Delta t}, \tag{2.99d}$$

$$e_{km} = N_k q_k^n \left[\frac{m^2}{2} p_m^n \right], \tag{2.99e}$$

$$f_{km} = N_k q_k^n \left[\frac{m^2}{2} q_m^n \right], \tag{2.99f}$$

and

$$\begin{aligned} G_k = &- \left(-\frac{2}{\Delta t^2}\alpha\Omega_k^2 + N_k \sum_{m=1}^{K} \left(\frac{m^2}{2} (p_m^{n-1} p_m^n + q_m^{n-1} q_m^n) \right) \right) p_k^n \\ &- \left(\frac{1}{\Delta t^2} + \Omega_k^2 \frac{1-\alpha}{2} - \frac{D}{2\Delta t} \right) p_k^{n-1}, \end{aligned} \tag{2.100a}$$

$$\begin{aligned} H_k = &- \left(-\frac{2}{\Delta t^2}\alpha\bar{\Omega}_k^2 + N_k \sum_{m=1}^{K} \left(\frac{m^2}{2} (p_m^{n-1} p_m^n + q_m^{n-1} q_m^n) \right) \right) q_k^n \\ &- \left(\frac{1}{\Delta t^2} + \bar{\Omega}_k^2 \frac{1-\alpha}{2} - \frac{D}{2\Delta t} \right) q_k^{n-1}. \end{aligned} \tag{2.100b}$$

$\mathbb{X}$ can thus be solved by taking:

$$\mathbb{X} = \mathbb{A}^{-1}\mathbb{B}. \tag{2.101}$$

The corresponding energy of the scheme at time step n, i.e. ϵ_n, with damping terms $D_k = 0$, is:

$$\begin{aligned} \epsilon_n = \sum_k^K \Bigg\{ &\left[1 + \left(\frac{1-2\alpha}{4} \right) \Omega_k^2 \Delta t^2 \right] \left(\frac{p_k^n - p_k^{n-1}}{\Delta t} \right)^2 + {\Omega_k}^2 \left(\frac{p_k^n + p_k^{n-1}}{2} \right)^2 \\ &+ \left[1 + \left(\frac{1-2\alpha}{4} \right) \bar{\Omega}_k^2 \Delta t^2 \right] \left(\frac{q_k^n - q_k^{n-1}}{\Delta t} \right)^2 + \bar{\Omega}_k^2 \left(\frac{q_k^n + q_k^{n-1}}{2} \right)^2 \\ &+ \frac{E\pi^4}{8\rho L^4} \left[k^2 (p_k^{n-1} p_k^n + q_k^{n-1} q_k^n) \right]^2 \Bigg\}, \end{aligned} \tag{2.102}$$

where conservation of energy can be shown such that:

$$\frac{1}{\Delta t} \left[\epsilon^{n+1} - \epsilon^n \right] = 0, \tag{2.103}$$

by multiplying both Equation (2.97a) and (2.97b) with the discrete velocity, i.e. $(p_k^{n+1} - p_k^{n-1})/2\Delta t$ and $(q_k^{n+1} - q_k^{n-1})/2\Delta t$ respectively. The proof is simply algebraic but tedious and is thus omitted for brevity.
Equation (2.4.2) is positive-definite when both:

$$\left[1 + \left(\frac{1-2\alpha}{4}\right)\Omega_k^2 \Delta t^2\right] > 0, \tag{2.104a}$$

$$\left[1 + \left(\frac{1-2\alpha}{4}\right)\bar{\Omega}_k^2 \Delta t^2\right] > 0, \tag{2.104b}$$

are satisfied. It is easy to infer that when:

$$\alpha \leq \frac{1}{2}, \tag{2.105}$$

Equation (2.104) is unconditionally satisfied and thus positive definiteness of Equation (2.4.2) and consequently the stability of the scheme can be guaranteed. Otherwise, as can be determined from Equation (2.104), the scheme is stable only when:

$$\Delta t < \frac{1}{\max([\Omega_K, \bar{\Omega}_K])} \sqrt{\frac{2}{\left(\alpha - \frac{1}{2}\right)}}. \tag{2.106}$$

The energy conservation property of the scheme can be demonstrated at Figure 2.2. A sample undamped simulation with $\alpha = 0.5$ is shown and it can be seen that the rate of change of numerical energy is at the vicinity of 10^{-12}J/s. The conservation properties could be further improved with fine tuning of simulation parameters α [60] but it is beyond the scope of the current work.

2.4.3 Geometrically exact damped nonlinear string model

Recalling that from Equation (2.49) and Equation (2.84), the geometrically exact nonlinear string model can be written as, for $\mathbf{q} = [u, v, w, \phi, \psi]$,

$$\mathbf{M_s}\ddot{\mathbf{q}} - \frac{\partial}{\partial x}\left(\mathbf{A}\mathbf{q}' + \mathbf{B}\mathbf{q} + \nabla\mathbf{H}(\mathbf{q}')\right) + \mathbf{C}\mathbf{q} + \mathbf{B}^{\mathbf{T}}\mathbf{q}' + \mathbf{Y}\dot{\mathbf{q}} - \mathbf{Z}\dot{\mathbf{q}}'' = 0, \tag{2.107a}$$

$$q_k(0,t) = 0 \qquad \text{for} \qquad k = 1,2,3; \tag{2.107b}$$

$$q_k(L,t) = 0 \qquad \text{for} \qquad k = 1,2,3; \tag{2.107c}$$

$$q_k'(0,t) = 0 \qquad \text{for} \qquad k = 4,5; \tag{2.107d}$$

$$q_k'(L,t) = 0 \qquad \text{for} \qquad k = 4,5; \tag{2.107e}$$

with the matrices and functional as defined in (2.50) and (2.51) respectively. The equation can be written in a variational form and thus be readily solved by finite-element method in the spatial domain. In the temporal domain, a ϑ-scheme, which is a class of the more general Newmark scheme, can be used to improve accuracy and ensure stability. Such approach has been attempted by Chabassier [63] and is

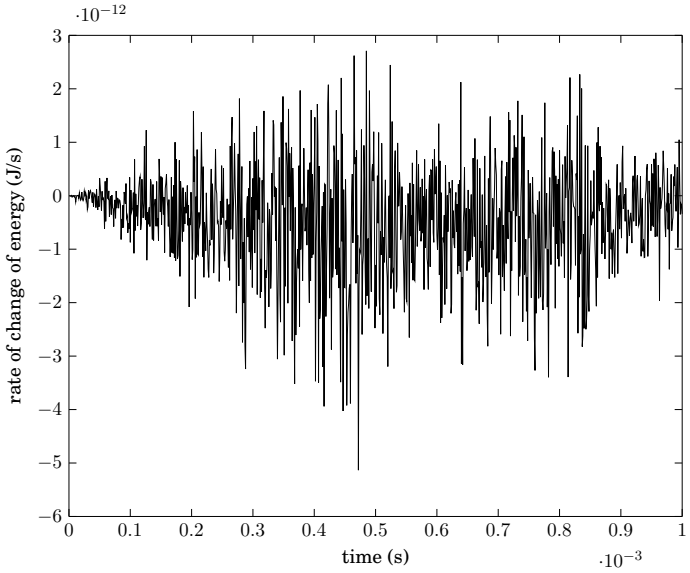

Figure 2.2: The computation simulates an undamped string subjected to a plucked initial condition (a.k.a triangle initial condition) with computational time steps, Δt = 10^{-6}s, total modes considered, $K = 40$ and $\alpha = 1/2$. String parameters: $T_0 = 895.3$N, $E = 190$GPa, $d = 1.3$mm, $\rho = 7,850$kg.m^{-3} and $L = 0.668$m.

implemented into MONTJOIE which is used in the current PhD work. MONTJOIE is a high-order finite element solver package developed Marc Duruflé in INRIA [81]. In this section, the finite element approach is briefly recapped while highlighting certain aspects of the problems faced and solutions proposed. However, to begin the explanation, it is useful to start with the linear wave equation, which can be retrieved from Equation (2.107a) by setting $\mathbf{B} = \mathbf{C} = \mathbf{A_r} = \mathbf{Y} = \mathbf{Z} = 0$ and $\mathbf{H} = 0$ with $\mathbf{q} = [u]$. One could obtain:

$$\ddot{\mathbf{q}} + {c_T}^2 \mathbf{q}'' = 0 \tag{2.108}$$

The solution begins with multiplying the wave equation with an arbitrary test function $\mathbf{q}^*(x)$ and integrating the whole equation over the length L. One obtains:

$$\int_0^L \ddot{\mathbf{q}}\mathbf{q}^* \mathrm{d}x - {c_T}^2 \int_0^L \mathbf{q}''\mathbf{q}^* \mathrm{d}x = 0. \tag{2.109}$$

After integrating the second term by part, one could recover the *variational formulation* (also known as "weak form") of the solution:

$$\int_0^L \ddot{\mathbf{q}}\mathbf{q}^* \mathrm{d}x + {c_T}^2 \int_0^L \mathbf{q}'\mathbf{q}^{*\prime} \mathrm{d}x = {c_T}^2 \left[\mathbf{q}'\mathbf{q}^*\right]_0^L. \tag{2.110}$$

Over the string length L, the string can be discretised into J number of nodes, with J-1 elements of a length h. The string variable x can thus be defined in a discretised

form:

$$x_j = jh \qquad \text{for} \qquad j = 1, 2, 3..., J, \tag{2.111}$$

such that $x_1 = 0$, and $x_J = L$. At each node j, the variable $\mathbf{q}$ or simply just u can be approximated as piecewise polynomial functions:

$$\mathbf{q}(x_j, t) = u(x_j, t) \approx \sum_{j=1}^{J} U_j(t)\chi_j(x_j), \tag{2.112}$$

with j being the node point number and χ_j is the basis function that takes the value of 1 at node j and 0 otherwise. In finite element method, the basis function is also known as the shape function. Next, the arbitrary test function $\mathbf{q}^*(x)$ or simply $u^*(x)$ can be chosen to be a basis function of index i, i.e. $\chi_i(x)$. Equation (2.109), after integration by part, can be written as:

$$\int_0^L \sum_{j=1}^{J} \ddot{U}_j \chi_j \chi_i \mathrm{d}x + {c_T}^2 \int_0^L \sum_{j=1}^{J} U_j {\chi_j}' {\chi_i}' \mathrm{d}x = {c_T}^2 \left[\sum_{j=1}^{J} U_j {\chi_j}' \chi_i \right]_0^L. \tag{2.113}$$

At the RHS, the boundary terms vanish after applying the boundary conditions and Equation (2.113) can thus be written in matrix form:

$$M_{ji}\ddot{U}_j + A_{ji}U_j = 0, \tag{2.114}$$

where

$$M_{ji} = \int_0^L \chi_j \chi_i \mathrm{d}x \qquad \text{and} \qquad A_{ji} = {c_T}^2 \int_0^L {\chi_j}' {\chi_i}' \mathrm{d}x. \tag{2.115}$$

M_{ji} and A_{ji} can be obtained if the basis function is defined. To solve both terms in discrete form, the integral can be approximated by various numerical integration methods, such as the rectangle or trapezoidal rule. The boundary conditions are also resolved such that:

$$u(0, t) = U_1 \chi_1 = 0, \tag{2.116a}$$

$$u(L, t) = U_J \chi_J = 0. \tag{2.116b}$$

With M_{ji} and A_{ji} known and the boundary condition resolved, U_j can then be solved by the time stepping method where:

$$\left\{ \ddot{U}_j \right\}^n = \frac{U_j^{n+1} - 2U_j^n + U_j^{n-1}}{\Delta t^2}, \tag{2.117a}$$

$$\{U_j\}^n = U_j^n. \tag{2.117b}$$

The subscript n indicates the time step point, such that for time t,

$$t_n = n\Delta t. \tag{2.118}$$

Substituting Equation (2.117) into (2.114), one then obtains an equation that is readily to be solved at every time step n:

$$M_{ji}\frac{U_j^{n+1}-2U_j^n+U_j^{n-1}}{\Delta t^2}+A_{ji}U_j^n=0. \tag{2.119}$$

For this example, the scheme in 2.119 can be solved explicitly such that:

$$U_j^{n+1}=(-M_{ji}^{-1}A_{ji}+2)U_j^n-U_j^{n-1} \tag{2.120}$$

For the geometrically exact nonlinear stiff string equation, i.e. Equation (2.107a), multiplying it with a test function $\mathbf{q}^*$ and integrating it over length L, performing integration by parts where necessary, the equation can be written as:

$$\begin{aligned}\int_0^L \mathbf{M_s}\ddot{\mathbf{q}}\mathbf{q}^* - \int_0^L \left(\mathbf{A}\mathbf{q}'+\mathbf{B}\mathbf{q}+\nabla\mathbf{H}(\mathbf{q}')\right)\mathbf{q}^{*\prime}+\int_0^L \mathbf{C}\mathbf{q}\mathbf{q}^*+\int_0^L \mathbf{B^T}\mathbf{q}'\mathbf{q}^*\\ +\int_0^L \mathbf{Y}\dot{\mathbf{q}}\mathbf{q}^{*\prime}+\int_0^L \mathbf{Z}\dot{\mathbf{q}}'\mathbf{q}^{*\prime}=\left[\mathbf{A}\mathbf{q}'+\mathbf{B}\mathbf{q}+\nabla\mathbf{H}(\mathbf{q}')+\mathbf{Z}\dot{\mathbf{q}}'\right]_0^L\mathbf{q}^*,\end{aligned} \tag{2.121}$$

Equation (2.121) can be written into semi-discrete form where the semi-discrete string variable, $\mathbf{q}_h$ can be given such that:

$$\text{for all } \mathbf{q_h}, \lim_{h\to 0}||\mathbf{q}-\mathbf{q}_h||=0, \tag{2.122}$$

for which the string of length L is discretised into elements of size h as is defined in Equation (2.111). It is then possible to write Equation (2.121) in its semi-discrete form:

$$\begin{aligned}\oint_0^L \mathbf{M_s}\ddot{\mathbf{q}}_h\mathbf{q}_h^* - \oint_0^L \left(\mathbf{A}\mathbf{q}_h'+\mathbf{B}\mathbf{q}_h+\nabla\mathbf{H}(\mathbf{q}_h')\right)\mathbf{q}_h^{*\prime}+\oint_0^L \mathbf{C}\mathbf{q}_h\mathbf{q}_h^*+\oint_0^L \mathbf{B^T}\mathbf{q}_h'\mathbf{q}_h^*\\ +\oint_0^L \mathbf{Y}\dot{\mathbf{q}}_h\mathbf{q}_h^{*\prime}+\oint_0^L \mathbf{Z}\dot{\mathbf{q}}_h'\mathbf{q}_h^{*\prime}=\left[\mathbf{A}\mathbf{q}_h'+\mathbf{B}\mathbf{q}_h+\nabla\mathbf{H}(\mathbf{q}_h')+\mathbf{Z}\dot{\mathbf{q}}_h'\right]_0^L\mathbf{q}_h^*,\end{aligned} \tag{2.123}$$

where the circular integral $\oint$ indicates a numerical integral via Gauss-Lobatto quadratures instead of a continuous integral. The advantage of using Gauss-Lobatto quadratures as a numerical integration method is to eliminate interpolation as the quadrature points can be defined to coincide with the nodal points of the elements. The semi-discrete variable $\mathbf{q}_h$ can be approximated by:

$$\mathbf{q}_h(x_j,t)\approx\sum_j^J \mathbf{Q}_h(t)\boldsymbol{\chi}_h(x_j), \tag{2.124}$$

which is analogous to Equation (2.112), where $\mathbf{Q}_h$ is a vector which represents the discrete form of $\mathbf{q}_h$ and $\boldsymbol{\chi}_h$ is the basis function. Using Equation (2.124) to write correspondingly $\mathbf{q}_h^*$, the fully discretised scheme for Equation (2.123) is:

$$M_h\ddot{\mathbf{Q}}_h+R_h\dot{\mathbf{Q}}_h+K_h\mathbf{Q}_h+\nabla\mathbf{H}^\circ(\mathbf{Q}_h)=0, \tag{2.125}$$

such that:

$$M_h \mathbf{Q}_h \mathbf{Q}_h^* = \oint_0^L \mathbf{M_s} \mathbf{q}_h \mathbf{q}_h^*, \tag{2.126a}$$

$$A_h \mathbf{Q}_h \mathbf{Q}_h^* = \oint_0^L \mathbf{A} \mathbf{q}_h' \mathbf{q}_h^{*\prime}, \tag{2.126b}$$

$$B_h \mathbf{Q}_h \mathbf{Q}_h^* = \oint_0^L \mathbf{B} \mathbf{q}_h \mathbf{q}_h^{*\prime}, \tag{2.126c}$$

$$C_h \mathbf{Q}_h \mathbf{Q}_h^* = \oint_0^L \mathbf{C} \mathbf{q}_h \mathbf{q}_h^*, \tag{2.126d}$$

$$R_h \mathbf{Q}_h \mathbf{Q}_h^* = \oint_0^L \mathbf{Y} \mathbf{q} \mathbf{q}^* + \oint_0^L \mathbf{Z} \mathbf{q}_h' \mathbf{q}_h^{*\prime}, \tag{2.126e}$$

$$\nabla \mathbf{H}^\circ(\mathbf{Q}_h)(\mathbf{Q}_h^*) = \oint_0^L \nabla \mathbf{H}(\mathbf{q}_h') \mathbf{q}_h^{*\prime}, \tag{2.126f}$$

where $K_h = A_h + B_h + C_h + {B_h}^T$. The RHS of Equation (2.123) vanishes when boundary conditions are applied. To solve Equation (2.125), it is necessary to obtain an energy conserving scheme where the energy is not only conserved but also positive-definite. For that, $\ddot{\mathbf{Q}}_h$ and $\dot{\mathbf{Q}}_h$ could take a form at time step n:

$$\left\{\ddot{\mathbf{Q}}_h\right\}^n = \frac{\mathbf{Q}_h^{n+1} - 2\mathbf{Q}_h^n + \mathbf{Q}_h^{n-1}}{\Delta t^2},$$
$$\left\{\dot{\mathbf{Q}}_h\right\}^n = \frac{\mathbf{Q}_h^{n+1} - \mathbf{Q}_h^{n-1}}{2\Delta t}.$$

For stability purposes, $\mathbf{Q}_h$ could be written in a ϑ-scheme where:

$$[\mathbf{Q}_h]_\vartheta^n = \vartheta \mathbf{Q}_h^{n+1} + (1 - 2\vartheta)\mathbf{Q}_h^n + \vartheta \mathbf{Q}_h^{n-1}, \tag{2.127}$$

for $\vartheta \in [0, 0.5]$ and acts like an averaging parameter.
To complete Equation (2.125), $\nabla \mathbf{H}^\circ(\mathbf{Q}_h)$ can be approximated in discrete form as:

$$\nabla \mathbf{H}^\circ(\mathbf{Q}_h) \approx \nabla_h \mathbf{H}^\circ(\mathbf{Q}_h^{n+\frac{1}{2}}, \mathbf{Q}_h^{n+\frac{1}{2}}), \tag{2.128}$$

and

$$\nabla_h \mathbf{H}^\circ(\mathbf{Q}_h^+, \mathbf{Q}_h^-).\mathbf{Q}_h^* = \frac{1}{6} \oint_0^L \sum_{\pi \in P} \sum_{k=1}^{3} \delta_k H(\mathbf{q}_k^{+\prime}, \mathbf{q}_k^{-\prime}, \mathbf{q}_{j \neq k}^{s(k,j)\prime}).\mathbf{q}_k{}', \tag{2.129}$$

where $s(k, j) = \text{sign}(j - k)$ and $\mathbf{q}^+$ and $\mathbf{q}^-$ relates respectively to $\mathbf{q}^{n+\frac{1}{2}}$ and $\mathbf{q}^{n-\frac{1}{2}}$ [68]. The δ_k operator is defined as below:

$$\delta_k H(a, b, c) = \begin{cases} \frac{H(a,c) - H(b,c)}{a-b} & \text{for } a \neq b, \\ \partial_k H(a, c) & \text{for } a = b, \end{cases} \tag{2.130}$$

and

$$H(a,b) = \frac{1}{2}(\mathbf{H}(a) + \mathbf{H}(b)). \tag{2.131}$$

The complete scheme in fully discrete form can thus be written as:

$$M_h \frac{\mathbf{Q}_h^{n+1} - 2\mathbf{Q}_h^n + \mathbf{Q}_h^{n-1}}{\Delta t^2} + R_h \frac{\mathbf{Q}_h^{n+1} - \mathbf{Q}_h^{n-1}}{2\Delta t} + K_h[\mathbf{Q}_h]_\vartheta^n + \nabla \mathbf{H}^\circ(\mathbf{Q}_h) = 0. \tag{2.132}$$

For more details including the derivation of the scheme and the proof of its energy conservation and positive definiteness (and thus stability), readers are advised to consult [37, 75]. The scheme presented has been implemented in MONTJOIE, a finite-element solver package with application to the modelling of piano. What has been contributed to MONTJOIE in this thesis is the implementation of the geometrically exact nonlinear stiff string equation where $\mathbf{q} = [u, v, w, \phi, \psi]$ (Equation (2.107a)), a variant of the equation without stiffness (i.e. $\mathbf{B} = \mathbf{C} = \mathbf{A_r} = 0$), and a pair of uncoupled linear wave equations (each representing u and v), all of which were previously not present in the solver.
From MONTJOIE, it is possible to calculate the discrete energy. The scheme is unconditionally stable when $\vartheta \geq 1/4$ [37]. Figure 2.3 shows the rate of change of numerical energy for a simulation of the geometrically exact nonlinear stiff string equation. As can be seen, the rate of change of the energy varies between three points ($\pm 1.10^{-7}$ and 0), which confirms the conservation of energy. It is possible to further reduce the variation of the numerical energy and improve the accuracy of the scheme by manipulating ϑ [37] but it is beyond the scope of the thesis.

2.4.4 Convergence tests

It is imperative to conduct convergence tests on numerical schemes to identify the suitable simulation parameters. Convergence tests offer insights on the trade-off between the accuracy and the computational efforts. Depending on the applications, different simulation parameters could be selected for performance optimisation. For the Kirchhoff-Carrier modal numerical scheme, there are three simulation parameters that can be manipulated. They are:

- averaging parameter α,
- number of modes K,
- time steps Δt.

As discussed earlier, the scheme is unconditionally stable when $\alpha \leq 1/2$. To ensure an unconditional stability with minimal dispersion,

$$\alpha = \frac{1}{2}, \tag{2.133}$$

is chosen. The number of modes K is highly dependent on the cases investigated and the choice of time steps. For instance, $\Delta t = 10^{-5}$s corresponds to a sampling

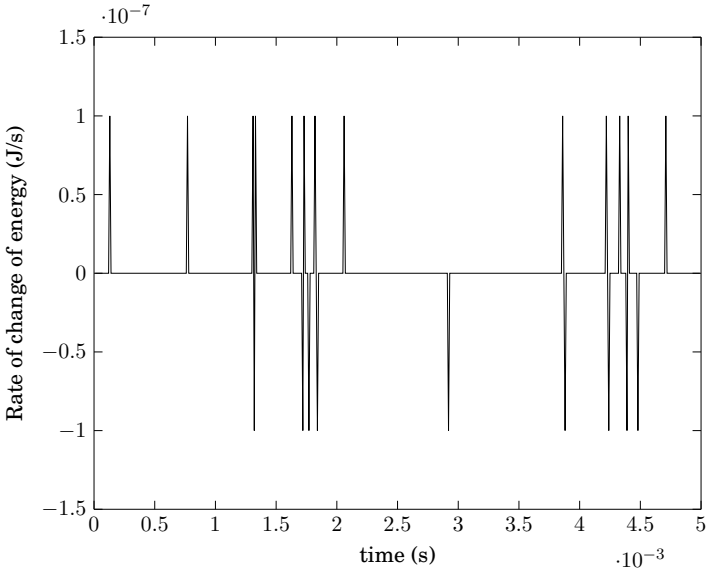

Figure 2.3: The computation simulates an undamped string subjected to a plucked initial condition (a.k.a triangle initial condition) with computational time steps, Δt = 10^{-6}s, 50 elements over the string length and $\vartheta = 1/4$. String parameters: $T_0 = 895.3$N, $E = 190$GPa, $d = 1.3$mm, $\rho = 7,850$kg.m^{-3} and $L = 0.668$m.

frequency of 100,000Hz and effectively the bandwidth of the simulation is up to 50,000Hz. Thus, it is not necessary to include any modes higher than 50,000Hz. To put it in a more general context, K can be chosen as long as:

$$\max\left(\frac{\Omega_K}{2\pi}\right) \leq \frac{1}{2\Delta t}, \tag{2.134}$$

where Ω_K is the eigenfrequencies of the string in rad/s as described in Equation (2.94a). However, practically, the system would have experienced numerical dispersion before hitting the limit imposed by Equation (2.134). Figure 2.4 show the differences in percentage between the first 40 theoretical eigenfrequencies and observed frequencies as obtained from the fast Fourier transform (FFT) algorithm when different values of time steps are used. The simulation parameters are summarised in Table 2.1. The undamped string is excited with a pluck initial condition with amplitude of 0.2mm at 0.3m from one end of the string and it is allowed to vibrate for 5s. For a time step of 10^{-4}s, dispersion is significantly more severe compared to the other results where 0.6% difference is observed at just 500Hz. Dispersion of up to 0.8% and 0.2% can be observed for the time step 10^{-5}s and 5.10^{-6}s at the theoretical eigenfrequency of 4,931Hz. Dispersion is virtually non-existent if a time step of 10^{-6}s is used (0.008% difference). Thus, for highly accurate simulation, the time step of 10^{-6}s is ideal and to complete a simulation that lasts 5s, it takes approximately 20 minutes by using one of the cores of the Intel Xeon CPU E5-2609 clocking at 2.50GHz. For simulation where only lower modes are of concern, using

a time step 10^{-5}s is sufficient to obtain accurate results which takes approximately 2 minutes.

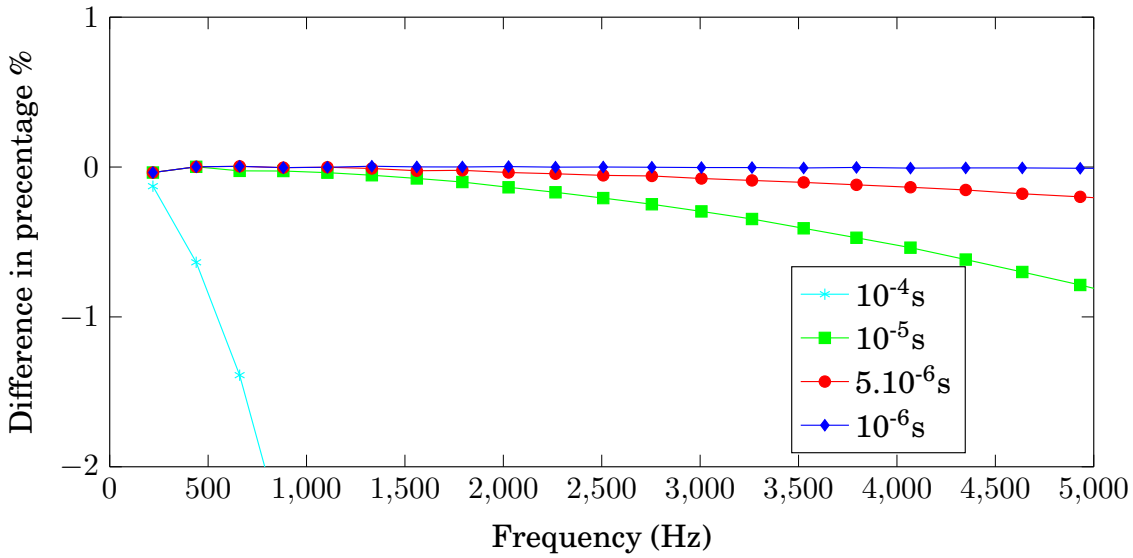

Figure 2.4: Difference in percentage between the theoretical eigenfrequencies and computed frequencies as observed from FFT plots when the simulations are done in time steps of 10^{-4}, 10^{-5}, 5.10^{-6} and 10^{-6} seconds.

Table 2.1: String parameters used for the convergence tests.

Parameter	Value
Density ρ	7850 kg.m^{-3}
diameter	0.0013m
Young's modulus	190GPa
Tension,T_0	895.3N
Length, L	0.668m

For the geometrically exact nonlinear stiff string finite element model, simulation parameters that can be varied are:

- averaging parameter ϑ,
- time step Δt,
- number of elements n_h.

Similar to the Kirchhoff-Carrier numerical scheme, the averaging parameter is set to:

$$\vartheta = \frac{1}{4} \tag{2.135}$$

where numerical stability is guaranteed.
The convergence test is performed by varying the time step Δt and the number of finite elements n_h. The simulation parameter is the same as in the Kirchhoff-Carrier numerical scheme (see Table 2.1) and the initial condition is also identical. The reference signal used is computed using $\Delta t = 10^{-7}$s and $n_h = 90$. Figure 2.5 shows the difference in percentage of the frequencies obtained from FFT plots against the frequency of the reference simulation. The time steps used are 10^{-4}, 10^{-5}, 5.10^{-6} and 10^{-6} seconds and all of them are computed with 90 finite elements, i.e. $n_h = 90$. Similar result compared to the Kirchhoff-Carrier numerical scheme is observed where dispersion is up to 0.8% and 0.2% for the time step 10^{-5}s and 5.10^{-6}s respectively at 4,927Hz. A 0.012% dispersion is observed for time step 10^{-6}s, which is slightly higher compared to the Kirchhoff-Carrier numerical scheme but is nonetheless a non-issue with such low dispersion. The slight difference is probably due to the use of different stiffness models. As such, similar recommendations can be made that for simulations concerning only the lower modes, a time step of 10^{-5}s is sufficient and for accurate simulation, a time step of time step 10^{-6}s can be used. Accuracy could be further improved by varying the simulation parameter ϑ but it is beyond the scope of this thesis.

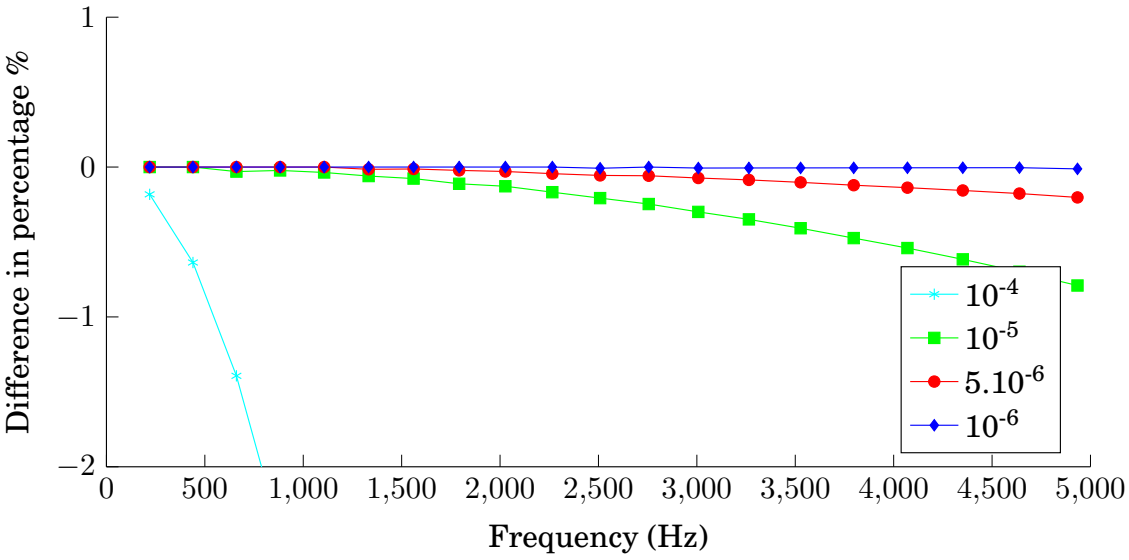

Figure 2.5: Differences in percentage of the frequencies compared to a reference simulation ($n_h = 90$, $\Delta t = 10^{-7}$s). The frequencies are extracted from FFT plots and the simulations are done in time steps of 10^{-4}, 10^{-5}, 5.10^{-6} and 10^{-6} seconds.

To investigate the influence of the number of elements, the simulations are repeated with 10, 30, 50, 70 and 90 elements and the results, plotted as difference in frequencies in percentage, are as shown in Figure 2.6. In both Figure 2.6a and 2.6b, using 10 elements yields poor performance and excellent agreements can be obtained by us-

Table 2.2: Time taken in hour:minute:second to complete a 5-second simulation with varying number of elements and time steps.

Number of elements	Time step (s)	
	10^{-6}	10^{-7}
10	00:19:17	
30	03:16:04	
50	04:22:30	
70	06:47:34	
90	08:11:48	49:30:35

ing 30 or more elements. Nonetheless, it appears that using 30 elements are prone to slightly more errors. Thus, a use of at least 50 elements across the string length is recommended. In this instance, the element size would correspond to 13.36mm and the solution is accurate up until 4927Hz (wavelength of 59mm) which suggests that it could cope with at least using only 4 elements per wavelength. The time taken to complete the reference signal and the simulations with a time step of 10^{-6}s for 5s using 8 cores of the Intel Xeon CPU E5-2609 clocking at 2.50GHz is also presented in Table 2.2.

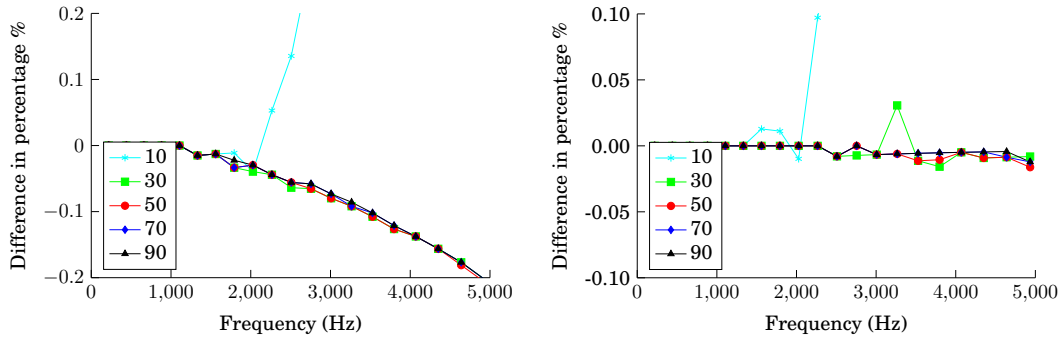

(a) $\Delta t = 5.10^{-6}$s. (b) $\Delta t = 10^{-6}$s.

Figure 2.6: Differences in percentage of the frequency compared to a reference simulation ($n_h = 90$, $\Delta t = 10^{-7}$s). The frequencies are extracted from FFT plots and the simulations are done with 10, 30, 50, 70 and 90 finite elements.

2.4.5 Comparison of numerical models

A comparison is performed to cross-verify the quality of the results provided by the two numerical models, using parameters that fit in the range consistent with the remainder of the study. It must be stressed that the comparison is not intended to test the assumption of the Kirchhoff-Carrier equation and in what cases it will differ from the geometrically exact equations.

To compare the two numerical models, the simple viscous damping model (SVM) is appended to both the Kirchhoff-Carrier equations and the geometrically exact equations. The damping coefficients used are:

$$R_u = R_v = 0.5067\mathrm{s}^{-1}, \tag{2.136a}$$

$$\zeta_u = \zeta_v = 3.8 \times 10^{-9} s, \tag{2.136b}$$

where these parameters are experimentally determined as will be detailed in Section 4.3. Additionally, to fully satisfy the geometrically exact equations,

$$R_\phi = R_\psi = 0.5067\mathrm{s}^{-1}, \tag{2.137a}$$

$$\zeta_\phi = \zeta_\psi = 3.8 \times 10^{-9} s, \tag{2.137b}$$

$$R_w = 0.5\mathrm{s}^{-1}, \tag{2.137c}$$

$$\zeta_w = 10^{-9} s, \tag{2.137d}$$

as per recommended by [84].
The simulation parameters used are as shown in Table 2.1 but the initial condition has changed. The string is plucked with a 33° offset from one polarisation at 0.3335m from one end with an amplitude of 0.33mm. To be in line with simulations done in Chapter 3, the frequency of the fundamental string mode u and v differ by 0.14Hz and the difference is accounted for by changing the density of the v string mode. Both models set their observation points at 0.638m from one string end, and for the Kirchhoff-Carrier numerical scheme:

$$K = 30, \tag{2.138a}$$

$$\alpha = 1/2, \tag{2.138b}$$

and for the geometrically exact finite element model, $\vartheta = 1/4$.
Figure 2.7 shows the wave envelopes of the displacements of the first 4 seconds of the simulations for both numerical models. The top plot shows the displacements in the plane of excitation (i.e at 33°) and the bottom plot shows the orthogonal out-of-plane displacement. Excellent agreements between the two models are observed. Zooming in to the first 20ms of the displacements (see Figure 2.8). the same excellent agreements are also observed. The discrepancy between the two models exists in their resonant frequencies as shown in Figure 2.9. At first glance, their frequencies are very close to each other. However, at closer look between 5,000Hz to 9,000Hz, the geometrically exact finite element models compute slightly lower frequencies compared to the Kirchhoff-Carrier numerical scheme. The discrepancy is not due to dispersion but rather to the difference of stiffness models used. As a reminder, the Kirchhoff-Carrier equations use the Euler-Bernoulli model while the geometrically exact equations use the Timoshenko model. It has been established that Euler-Bernoulli model would predict a comparatively higher frequency than the Timoshenko models at sufficiently high resonant frequencies [68]. Indeed, seeing that the difference is not really significant, it remains a debate whether Euler-Bernoulli model is necessarily inferior despite not being as enriched from a physical point of view.

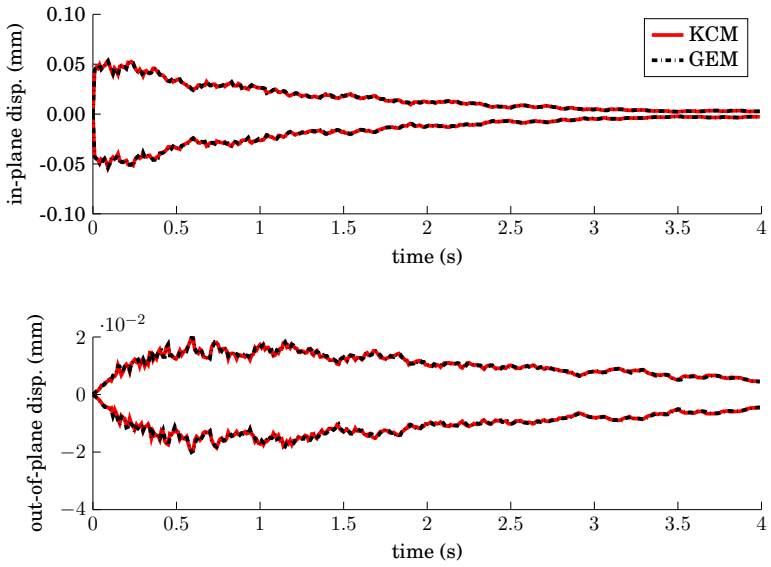

Figure 2.7: Comparison between the Kirchhoff-Carrier numerical scheme (KCM) and the geometrically exact finite element model (GEM), showing its wave envelope over the first 4s of the displacement-time plots. The top figure shows the dominant vertical displacement, the bottom shows the horizontal displacement.

2.5 Summary

In this chapter, the following string equations and their energy conservation properties are derived [73, 74]:

- geometrically exact nonlinear equations,
- Kirchhoff-Carrier nonlinear equations,
- linear wave equation.

The modal solution of undamped linear wave equation is shown. The nonlinear equations are solved numerically via a modal time-stepping method for the Kirchhoff-Carrier equations and a finite element method for the geometrically exact equations.
The following stiffness models are introduced [33, 68]:

- Euler-Bernoulli model (and is included in the Kirchhoff-Carrier equations),
- Timoshenko model (and is included in the geometrically exact equations),

and these damping models are presented:

- Valette & Cuesta model [80],

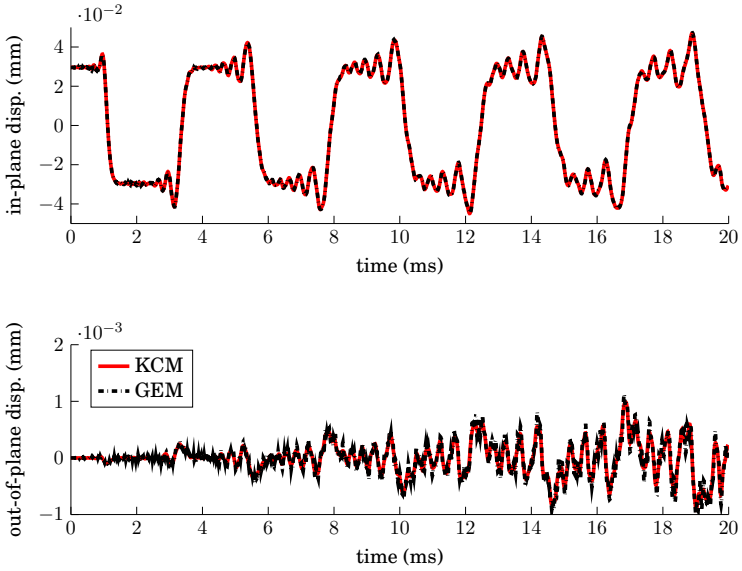

Figure 2.8: Comparison between the Kirchhoff-Carrier numerical scheme (KCM) and the geometrically exact finite element model (GEM), showing the first 20ms of the displacement-time plots. The top figure shows the dominant vertical displacement, the bottom shows the horizontal displacement.

- simple viscous damping model [57].

Convergence tests have been performed to identify the numerical parameters to use in the two models. A good agreement is also found between the comparison of the two models when the same damping model (SVM) is used.

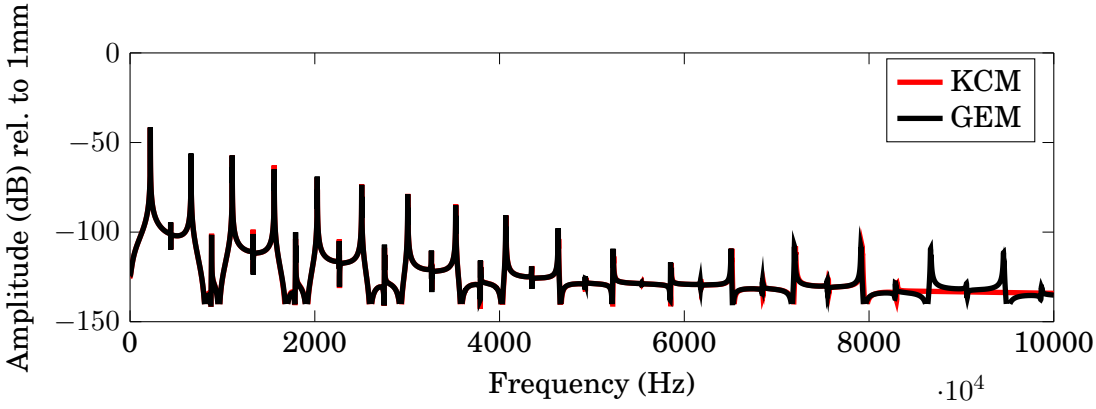

(a) 0 to 10,000Hz.

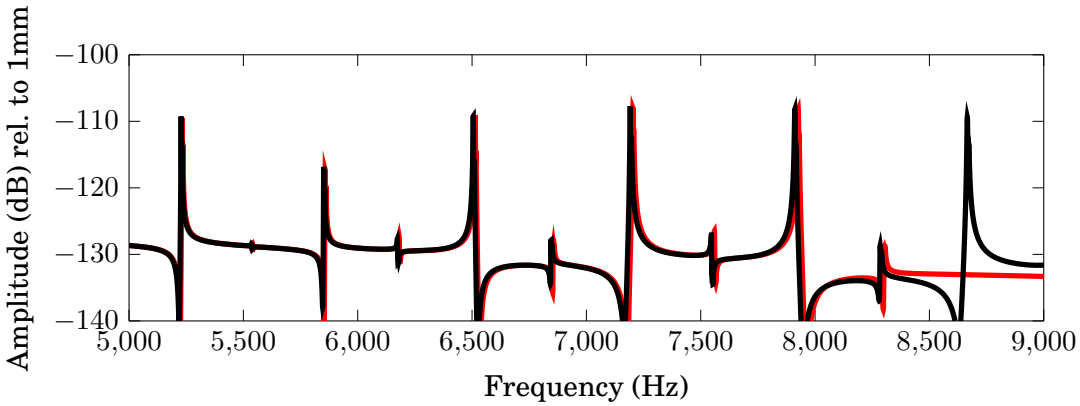

(b) 5,000 to 9,000Hz.

Figure 2.9: Frequencies of both Kirchhoff-Carrier numerical scheme (KCM) and the geometrically exact finite element model (GEM) as extracted from their respective FFT plots.

3

Nonlinear coupling of polarisation

As prefaced in the introduction (Chapter 1), one of the primary causes of the double polarisation is suspected to be the geometric nonlinearity in string when it is subjected to a large amplitude excitation, such as a strike by the piano hammer. This is especially intriguing as it is known that the two transverse modes, which form the two polarisations, have very close eigenfrequencies. When two eigenfrequencies are very close, 1:1 internal resonance could occur where energy can be exchanged between vibration modes [77]. This means that if the motion is initiated along one polarisation, the nonlinearity can make this motion unstable, so that eventually a coupled vibration arises with the two polarisations involved. The objective of this chapter is thus to clearly establish if the nonlinearity can be the cause of this coupling, as well as to highlight the main parameters governing the transfer of energy.

A conscious and deliberate choice is made to investigate strictly the nonlinear behaviour of the freely vibrating string bounded by two fixed ends. This is done so as not to be confused by the influence of other kinds of boundary conditions, such as a movable bridge (which is investigated in Part II instead). The freely vibrating strings with two fixed ends can be represented by the Kirchhoff-Carrier equations (see Section 2.1.3). The 1:1 internal resonance of such freely vibrating system was studied by Manevitch and Manevitch [79] although their study was not specific to string vibration. Investigation of similar systems have also been studied but under forced excitation [70, 71, 77, 78]. Inspired by these works, this chapter first presents a reduced and nondimensionalised form of the Kirchhoff-Carrier equations in Section 3.1. It then continues with a nonlinear study of the equation by multiple-scale analysis in Section 3.2 and presents some cases specific to the string in Section 3.3. These findings are numerically validated in Section 3.4 using methods presented in Section 2.4.2 and 2.4.3. Lastly, a simple demonstration of double polarisation on a linear string is presented in Section 3.5.

3.1 Reduced order model

The Kirchhoff-Carrier nonlinear equation for a freely vibrating string fixed at both ends with two polarised displacements u and v, as has been derived in Section 2.1.3, can be written as:

$$\rho A\ddot{u} - (T_0 + N)\, u'' = 0, \tag{3.1a}$$
$$\rho A\ddot{v} - (T_0 + N)\, v'' = 0, \tag{3.1b}$$

where

$$N = \frac{EA}{2L}\int_0^L \left(u'^2 + v'^2\right)\, \mathrm{d}x. \tag{3.2}$$

In Equation (3.1), damping and stiffness are ignored to simplify the analysis. Following [78], the equations can be made nondimensional for a more general treatment where:

$$\bar{x} = \frac{x}{L}, \qquad \bar{u} = \frac{u}{d}, \qquad \bar{v} = \frac{v}{d}, \qquad \bar{t} = \frac{t}{\bar{T}}, \qquad \bar{N} = \frac{N}{T_0}, \qquad \bar{f}_i = \frac{f_i}{f_0}, \qquad \bar{T} = \frac{L}{c_T^2}. \tag{3.3}$$

The new equations can be written as:

$$\ddot{u} - (1 + N)u'' = 0, \tag{3.4a}$$
$$\ddot{v} - (1 + N)v'' = 0, \tag{3.4b}$$

where

$$N = \frac{\varepsilon}{2}\int_0^1 (u'^2 + v'^2)\mathrm{d}x \qquad \text{and} \qquad \varepsilon = \frac{EAd^2}{T_0 L^2}, \tag{3.5}$$

where for clarity purposes, the overbars are dropped as all terms are now nondimensional. The solutions of the nondimensional equations can be expressed by Galerkin's approximations:

$$u(x,t) = \sum_{k=1}^{K} \xi_k(x) p_k(t), \qquad v(x,t) = \sum_{k=1}^{K} \xi_k(x) q_k(t), \tag{3.6}$$

where $\xi_k(x)$ are the eigenmodes, and $\{p_k(t), q_k(t)\}_{k\geq 1}$ the modal coordinates. Substituting Equation (3.6) into (3.4) and writing only the fundamental mode, i.e. $K = 1$, one could map the two modal coordinates p_1 and q_1 to p and q respectively and obtain the following nonlinear system:

$$\ddot{p} + \omega_1^2 p + \varepsilon\left[\Gamma_1 p^3 + C_1 p q^2\right] = 0, \tag{3.7a}$$
$$\ddot{q} + \omega_2^2 q + \varepsilon\left[\Gamma_2 q^3 + C_2 q p^2\right] = 0, \tag{3.7b}$$

where ε is the small parameter arising from the nondimensionalisation [78] as expressed in Equation (3.5). For a perfect string, the two eigenfrequencies are equal such that $\omega_2 = \omega_1 = \pi$ [78] and the nonlinear coefficients would be $\Gamma_1 = \Gamma_2 =$

$C_1 = C_2 = \pi^4/2$. However, such perfect string does not exist as imperfection such as variations in manufacturing and rusting would occur. To account for this imperfection, a detuning parameter σ_1 can be artificially introduced such that the two eigenfrequencies of the two modes are slightly different,

$$\omega_2 = \omega_1 + \varepsilon\sigma_1. \tag{3.8}$$

The detuning parameter σ_1 can be experimentally determined by measuring the difference in the two eigenfrequencies of the polarisation (see Section 4.4).

3.2 Multiple-scale analysis

A viable way to determine the nonlinear behaviour of the system in Equation (3.7) is by multiple-scale analysis, a pertubative method intended for finding solution for weakly nonlinear problems [74, 85, 86]. As its name suggests, the method introduces new time scales and describes the original system as a function of multiple independent time scales. For this study, the following time scales are introduced:

$$\mathcal{T}_0 = t, \tag{3.9a}$$
$$\mathcal{T}_1 = \varepsilon t, \tag{3.9b}$$

where $\mathcal{T}_0$ is the fast time scale in which most of the linear events take place. $\mathcal{T}_1$, on the other hand, is the slow time scale where nonlinear phenomenon could occur. From Equation (3.7), p and q can be approximated by:

$$p(t) = p_0(\mathcal{T}_0, \mathcal{T}_1) + \varepsilon p_1(\mathcal{T}_0, \mathcal{T}_1) + O(\varepsilon^2), \tag{3.10a}$$
$$q(t) = q_0(\mathcal{T}_0, \mathcal{T}_1) + \varepsilon q_1(\mathcal{T}_0, \mathcal{T}_1) + O(\varepsilon^2). \tag{3.10b}$$

Using $D_j = \partial/\partial\mathcal{T}_j$, Equation (3.7) can be expanded into terms of different orders of ε. Truncating the terms up to different order of ε would lead to different equations. At order ε^0:

$$D_0^2 p_0 + \omega_1^2 p_0 = 0, \tag{3.11a}$$
$$D_0^2 q_0 + \omega_2^2 q_0 = 0, \tag{3.11b}$$

and at order ε^1:

$$D_0^2 p_1 + \omega_1^2 p_1 = -2D_0 D_1 p_0 - \Gamma_1 p_0^3 - C_1 p_0 q_0^2, \tag{3.12a}$$
$$D_0^2 q_1 + \omega_2^2 q_1 = -2D_0 D_1 q_0 - \Gamma_2 q_0^3 - C_2 q_0 p_0^2. \tag{3.12b}$$

At order ε^0, the system is uncoupled and each equation corresponds to the case of a simple undamped harmonic linear oscillator. At order ε^1, the equations are nonlinearly coupled via a cubic order term. To solve for Equation (3.12), p_0 and q_0 can be defined as:

$$p_0 = A(\mathcal{T}_1)\exp(i\omega_1\mathcal{T}_0) + c.c, \tag{3.13a}$$
$$q_0 = B(\mathcal{T}_1)\exp(i\omega_2\mathcal{T}_0) + c.c, \tag{3.13b}$$

where $c.c$ stands for complex conjugate. Substituting Equation (3.13) into Equation (3.12), on the RHS, one would obtain terms associated with $\exp(i\omega_1\mathcal{T}_0)$, $\exp(i\omega_2\mathcal{T}_0)$, $\exp(3i\omega_1\mathcal{T}_0)$ and $\exp(3i\omega_2\mathcal{T}_0)$. Terms containing $\exp(i\omega_1\mathcal{T}_0)$ and $\exp(i\omega_2\mathcal{T}_0)$ are resonant terms and are to be eliminated to avoid secular terms. To achieve this, the coefficients associated to those terms are set to zero. This yields:

$$-2i\omega_1 A' - 3\Gamma_1 A^2\bar{A} - C_1 B\left[2A\bar{B} + \bar{A}B\exp(2i\sigma_1\mathcal{T}_1)\right] = 0, \tag{3.14a}$$

$$-2i\omega_2 B' - 3\Gamma_2 B^2\bar{B} - C_2 A\left[2B\bar{A} + \bar{B}A\exp(-2i\sigma_1\mathcal{T}_1)\right] = 0, \tag{3.14b}$$

where the operator $()' = \partial/\partial\mathcal{T}_1$ and the overbar indicates the respective complex conjugates. Equations (3.14) are the *solvability conditions* and can then be solved by writing A and B in polar form:

$$A(\mathcal{T}_1) = a(\mathcal{T}_1)\exp(i\alpha(\mathcal{T}_1)), \tag{3.15a}$$

$$B(\mathcal{T}_1) = b(\mathcal{T}_1)\exp(i\beta(\mathcal{T}_1)). \tag{3.15b}$$

Substituting Equation (3.15) into (3.14), the solvability conditions can be broken down into a set of four dynamical equations at the $\mathcal{T}_1$ time scale (two for amplitude a and b, two for their respective phases α and β):

$$a' = -\frac{C_1}{2\omega_1}ab^2\sin(\gamma_2 - \gamma_1), \tag{3.16a}$$

$$\gamma_1' = \frac{3\Gamma_1}{\omega_1}a^2 + \frac{C_1}{\omega_1}b^2\left[2 + \cos(\gamma_2 - \gamma_1)\right], \tag{3.16b}$$

$$b' = \frac{C_2}{2\omega_2}ba^2\sin(\gamma_2 - \gamma_1), \tag{3.16c}$$

$$\gamma_2' = \frac{3\Gamma_2}{\omega_2}b^2 + \frac{C_2}{\omega_2}a^2\left[2 + \cos(\gamma_2 - \gamma_1)\right] + 2\sigma_1. \tag{3.16d}$$

Note that the dynamical system in Equation (3.16) has been made autonomous by introducing the new angular variables γ_1 and γ_2, such that:

$$\gamma_1 = 2\alpha \qquad \text{and} \qquad \gamma_2 = 2\beta + 2\sigma_1\mathcal{T}_1. \tag{3.17}$$

3.2.1 Uncoupled solutions

While the main interest lies on the coupling between the two modal coordinates p and q (or their first order amplitude a and b), it is also important to first understand the uncoupled solutions. In this system, there are two uncoupled solutions, namely when $b = 0$ and $a = 0$ respectively. To facilitate upcoming discussions, the uncoupled mode $b = 0$ is called the "A-mode" (as $a \neq 0$) while the uncoupled mode $a = 0$ is called the "B-mode" (as $b \neq 0$).
The dynamical equations of the A-mode, which can be obtained by setting $b = 0$ in Equation (3.16) are:

$$a' = 0, \tag{3.18a}$$

$$\alpha' = \frac{3\Gamma_1}{2\omega_1}a^2. \tag{3.18b}$$

Solutions can be obtained by integrating both equations with respect to $\mathcal{T}_1$:

$$a = C_A, \tag{3.19a}$$

$$\alpha = \frac{3\Gamma_1}{2\omega_1} a^2 \mathcal{T}_1 + \alpha_A, \tag{3.19b}$$

where C_A and α_A are integration constants that do not depend on $\mathcal{T}_1$. It is then possible to express p_0 as an approximation to p:

$$p \approx p_0 = 2a \cos\left[\omega_{NL} t + \alpha_A\right], \tag{3.20}$$

where ω_{NL} denotes the nonlinear frequency and is given as:

$$\omega_{NL} = \omega_1 \left(1 + \varepsilon \frac{3\Gamma_1}{2{\omega_1}^2} a^2\right). \tag{3.21}$$

Equation (3.21) is known as a backbone curve. It expresses the dependency of the frequency of the uncoupled mode p on its amplitude a, a key feature of nonlinear oscillation. A similar exercise can be done for the B-mode, i.e. $a = 0$ and one would obtain:

$$q_0 = 2b \cos\left[\omega_{NL} t + \beta_B\right], \tag{3.22}$$

where

$$\omega_{NL} = \omega_2 \left(1 + \varepsilon \frac{3\Gamma_2}{2{\omega_2}^2} b^2\right), \tag{3.23}$$

where the frequency of the uncoupled mode q is dependent on its amplitude b. One can notice the similarity between the two solutions, coming from the fact that the uncoupled solutions are essentially the classical Duffing equations. The nonlinearity is completely governed by coefficients Γ_1 and Γ_2. Figure 3.1 shows the backbone curve (amplitude-frequency relationship, Equation (3.20) and (3.21)) for $\varepsilon = 0.001$. The value $\Gamma_1 = 0$ is used as an eyeguide to recall that for linear vibrations, the oscillation frequency is independent from the amplitude. The values $\Gamma_1 = \pi^4/2$, $\omega_1 = \pi$ are the standard values for perfect strings [78]. The figure allows one to estimate the deviation (in radian frequency) of the oscillations with respect to the linear eigenfrequency, as a function of the vibration amplitude.

3.2.2 Coupled solutions

In the coupled case, i.e. when both $a \neq 0, b \neq 0$, as inferred from Equation (3.16a), the fixed point solutions, i.e. when $a' = b' = \gamma_1' = \gamma_2' = 0$, for coupled stationary modes exist only if

$$\sin(\gamma_2 - \gamma_1) = 0. \tag{3.24}$$

This in turn indicates that $\cos(\gamma_2 - \gamma_1) = \pm 1$ with each case corresponding to a different coupled stationary mode.
For $\cos(\gamma_2 - \gamma_1) = +1$,

$$\gamma_2 - \gamma_1 = 2(\beta + \sigma_1 \mathcal{T}_1 - \alpha) = 2k\pi \quad \text{for} \quad k = 1, 2, 3... \tag{3.25}$$

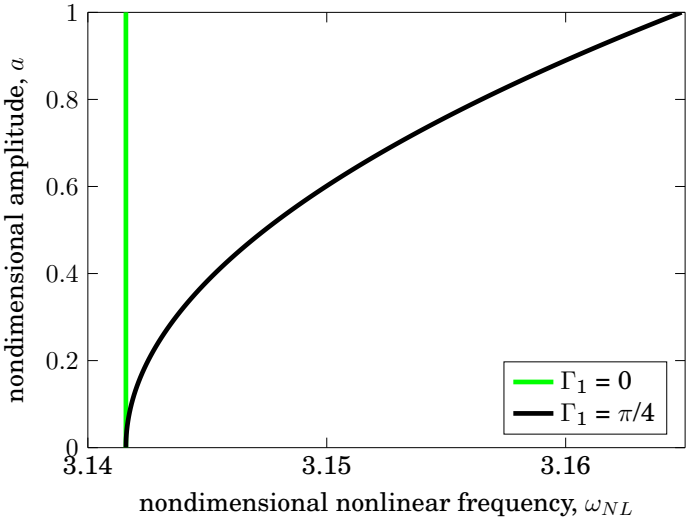

Figure 3.1: Backbone curve showing that the oscillation frequency of the uncoupled A-mode is dependent on its amplitude a. $\omega_1 = \pi$ and $\varepsilon = 10^{-3}$.

Assuming that the detuning between the two polarisations are insignificant, such that $\sigma_1 = 0$, one could obtain:

$$\beta = \alpha + k\pi \quad \text{for} \quad k= 1, 2, 3... \tag{3.26}$$

This would yield:

$$p = 2a\cos(\omega_1 \mathcal{T}_0 + \alpha), \tag{3.27a}$$
$$q = \pm 2b\cos(\omega_2 \mathcal{T}_0 + \alpha). \tag{3.27b}$$

Since $\sigma_1 = 0$, $\omega_1 = \omega_2$ and p and q can be related by:

$$\frac{q}{p} = \pm\frac{b}{a}. \tag{3.28}$$

Similarly, if $\cos(\gamma_2 - \gamma_1) = -1$ and again $\sigma_1 = 0$, one could obtain:

$$\beta = \alpha + (2k-1)\frac{\pi}{2} \quad \text{for} \quad k= 1, 2, 3... \tag{3.29}$$

which yields:

$$p = 2a\cos(\omega_1 \mathcal{T}_0 + \alpha), \tag{3.30a}$$
$$q = -2b\sin(\omega_2 \mathcal{T}_0 + \alpha). \tag{3.30b}$$

The relation between p and q is thus:

$$\frac{q^2}{4b^2} + \frac{p^2}{4a^2} = 1. \tag{3.31}$$

Equation (3.28) corresponds to a linear straight line relationship between the two displacements passing through the origins. On the other hand, Equation (3.31) corresponds to an elliptic motion around the origin. Following the study by Manevitch and Manevitch [79], the coupled modes of Equation (3.28) and (3.31) are thus referred to as the "normal mode" and "elliptic mode", as is illustrated in Figure 3.2.

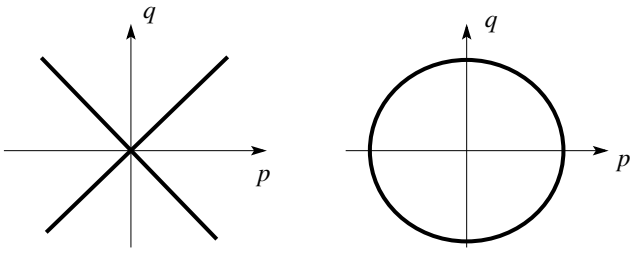

(a) normal mode (b) elliptic mode

Figure 3.2: Illustrations of the two modes of coupled solutions as inspired by [79].

From $\sin(\gamma_2 - \gamma_1) = 0$, one could infer that $\gamma_2 - \gamma_1 = n\pi$ and thus,

$$\gamma_2' - \gamma_1' = 0. \tag{3.32}$$

Substituting Equation (3.16b) and (3.16d) into (3.32), one could then obtain:

$$2\sigma_1 = \left(\frac{3\Gamma_1}{\omega_1} - \frac{C_2}{\omega_2}\left[2 + \cos(\gamma_2 - \gamma_1)\right]\right) a^2 + \left(\frac{C_1}{\omega_1}\left[2 + \cos(\gamma_2 - \gamma_1)\right] - \frac{3\Gamma_2}{\omega_2}\right) b^2. \tag{3.33}$$

For the normal mode where $\cos(\gamma_2 - \gamma_1) = +1$, this yields

$$2\sigma_1 = \left(\frac{3\Gamma_1}{\omega_1} - \frac{3C_2}{\omega_2}\right) a^2 + \left(\frac{3C_1}{\omega_1} - \frac{3\Gamma_2}{\omega_2}\right) b^2. \tag{3.34}$$

For this mode to branch off from A-mode (i.e. $b = 0$), the system must satisfy:

$$a^2 = \frac{2\sigma_1}{\frac{3\Gamma_1}{\omega_1} - \frac{3C_2}{\omega_2}}, \tag{3.35}$$

and to branch off from B-mode (i.e. $a = 0$), it would then have to satisfy:

$$b^2 = \frac{2\sigma_1}{\frac{3C_1}{\omega_1} - \frac{3\Gamma_2}{\omega_2}}. \tag{3.36}$$

For string vibrations where imperfection in the system is small where the detuning $\sigma_1 \neq 0$ and the nonlinear coefficients are similar, i.e. $\Gamma_1 \approx C_2$ or $C_1 \approx \Gamma_2$, the denominator for both Equations (3.35) and (3.36) will be very small. This suggests that the occurrence of coupled normal mode is practically unobservable for a system like string.

On the other hand, for elliptic mode where $\cos(\gamma_2 - \gamma_1) = -1$, Equation (3.33) yields:

$$2\sigma_1 = \left(\frac{3\Gamma_1}{\omega_1} - \frac{C_2}{\omega_2}\right) a^2 + \left(\frac{C_1}{\omega_1} - \frac{3\Gamma_2}{\omega_2}\right) b^2. \tag{3.37}$$

For this mode to appear from A-mode, the system must satisfy:

$$a^2 = \frac{2\sigma_1}{\frac{3\Gamma_1}{\omega_1} - \frac{C_2}{\omega_2}}, \tag{3.38}$$

and to appear from B-mode, it must satisfy

$$b^2 = \frac{2\sigma_1}{\frac{C_1}{\omega_1} - \frac{3\Gamma_2}{\omega_2}}. \tag{3.39}$$

Elliptic mode cannot develop from the uncoupled B-mode unless $\frac{C_1}{\omega_1} - \frac{3\Gamma_2}{\omega_2} > 0$. In the case of a slightly imperfect string where the nonlinear coefficients are similar, if not identical, it is then impossible to see the uncoupled B-mode to branch off into coupled elliptic mode. As a result, the most possible coupled modes that are physically possible for a string would be the elliptic mode that branches off from uncoupled A-mode as dictated by Equation (3.38).

3.2.3 Stability analysis

The analysis is followed by examining the stability of the uncoupled and coupled solutions. One of the methods to determine the stability of a dynamical system is to evaluate the eigenvalues of its Jacobian matrix. For the dynamical system of Equation (3.16), the Jacobian matrix of the coupled solutions $\mathbf{J}$ is:

$$\mathbf{J} = \begin{bmatrix} 0 & \frac{C_1}{2\omega_1} ab^2\gamma_c & 0 & -\frac{C_1}{2\omega_1} ab^2\gamma_c \\ \frac{6\Gamma_1}{\omega_1} a & 0 & 2\frac{C_1}{\omega_1} b(2+\gamma_c) & 0 \\ 0 & -\frac{C_2}{2\omega_2} ba^2\gamma_c & 0 & \frac{C_2}{2\omega_2} ba^2\gamma_c \\ 2\frac{C_2}{\omega_2} a(2+\gamma_c) & 0 & \frac{6\Gamma_2}{\omega_2} b & 0 \end{bmatrix}. \tag{3.40}$$

where $\gamma_c = \cos(\gamma_2 - \gamma_1)$. The eigenvalues λ can be obtained by solving the determinants of $\mathbf{J} - \mathbf{I}\lambda$, which yields four eigenvalues, with two of them equal to zero. The other pair, after setting $\cos(\gamma_2 - \gamma_1)$ to either +1 or -1, is:

$$\lambda_{NM}^2 = 3a^2b^2 \left[\frac{C_1}{\omega_1}\left(\frac{\Gamma_1}{\omega_1} - \frac{C_2}{\omega_2}\right) + \frac{C_2}{\omega_2}\left(\frac{\Gamma_2}{\omega_2} - \frac{C_1}{\omega_1}\right)\right], \tag{3.41a}$$

$$\lambda_{EM}^2 = a^2b^2 \left[-\frac{C_1}{\omega_1}\left(\frac{3\Gamma_1}{\omega_1} - \frac{C_2}{\omega_2}\right) - \frac{C_2}{\omega_2}\left(\frac{3\Gamma_2}{\omega_2} - \frac{C_1}{\omega_1}\right)\right], \tag{3.41b}$$

where the subscript NM indicates normal mode ($\gamma_c = +1$) and EM the elliptic mode ($\gamma_c = -1$). Stability is guaranteed if the terms in square brackets are less than zero. After simplifying, the following stability condition can be obtained:

$$\frac{\omega_2\Gamma_1}{C_2\omega_1} + \frac{\Gamma_2\omega_1}{C_1\omega_2} < 2 \qquad \text{for normal modes,} \tag{3.42a}$$

$$\frac{\omega_2\Gamma_1}{C_2\omega_1} + \frac{\Gamma_2\omega_1}{C_1\omega_2} > \frac{2}{3} \qquad \text{for elliptic modes.} \tag{3.42b}$$

It is interesting to see that the stability of the coupled solutions does not depend on the energy but rather on the physical parameters of the system (i.e. eigenfrequencies and nonlinear constants). It also means that regardless of the level of excitation, exhibition of stable normal or elliptic modes are already pre-determined.

To complete the analysis, the stability condition of the uncoupled modes is determined. As noted by Manevitch and Manevitch [79], the stability of the uncoupled solutions is determined by the energy of the system. Using the same approach as for the coupled case (i.e. by determining the eigenvalues of the Jacobian matrix) does unfortunately not give a useful criteria for the stability of uncoupled solutions. Furthermore, Manevitch and Manevitch do not demonstrate an explicit proof of the stability of uncoupled solutions in [79]. The underlying problem is that when setting either $b = 0$ or $a = 0$ in the system, the degeneracy is ill-conditioned so that the phase space shrinks down to a two DOFs system where the perturbation brought by the other oscillators are not defined and thus cannot be studied.

Fortunately, the solution can be found from the forced and damped vibration case by canceling the damping terms and identifying the external excitation frequency to the nonlinear oscillation frequency ω_{NL}. Using the existence conditions derived in [77] from a geometric analysis in phase space, one can obtain the following inequality relations for the uncoupled solutions that define the *instability regions*:
For A-mode:

$$\left[\omega_2 + \varepsilon\frac{C_2}{2\omega_2}a^2\right] < \omega_{NL} < \left[\omega_2 + \varepsilon\frac{3C_2}{2\omega_2}a^2\right], \tag{3.43}$$

and for B-mode:

$$\left[\omega_1 + \varepsilon\frac{C_1}{2\omega_1}b^2\right] < \omega_{NL} < \left[\omega_1 + \varepsilon\frac{3C_1}{2\omega_1}b^2\right]. \tag{3.44}$$

The instability affecting the A-mode originates from the eigenfrequency of the other uncoupled mode, ω_2 and vice versa. This is because the existence of the B-mode upsets the stability of the original uncoupled solution. It is also interesting to note that the point where the uncoupled solution changes its stability (either in losing or restoring it) is also the point where the uncoupled solution branches into a coupled solution (or a coupled solution leaves and enters the uncoupled solution) as defined by Equations (3.35), (3.36), (3.38) and (3.39).

3.3 Case study

In this section, several case studies are made to demonstrate the properties of the system. Firstly, a perfect string is considered (i.e. $\sigma_1 = 0$, $C_1 = C_2 = \Gamma_1 = \Gamma_2$). For this case, the two amplitude-frequency relationships for uncoupled solutions given by Equation (3.21) and (3.23) are exactly the same but lie on different planes as shown in Figure 3.3a. For the coupled solutions, Equation (3.42a) dictates that the normal mode is unstable and thus no normal modes can be observed in the perfect case. On the other hand, elliptic modes do exist, and Equation (3.37) shows that they have the same amplitude : $a = b$ as shown by the translucent red plane in Figure 3.3a. Also from Equation (3.37), one obtains the backbone curve for the coupled, elliptic modes in the perfect case as:

$$\omega_{NL} = \omega_1 \left(1 + 2\varepsilon \frac{\Gamma_1}{\omega_1^2} a^2\right). \tag{3.45}$$

This shows that coupled solutions have a stronger hardening behaviour than uncoupled modes (see Equation (3.21)), as shown in Figure 3.3b, a 2D version of Figure 3.3a.

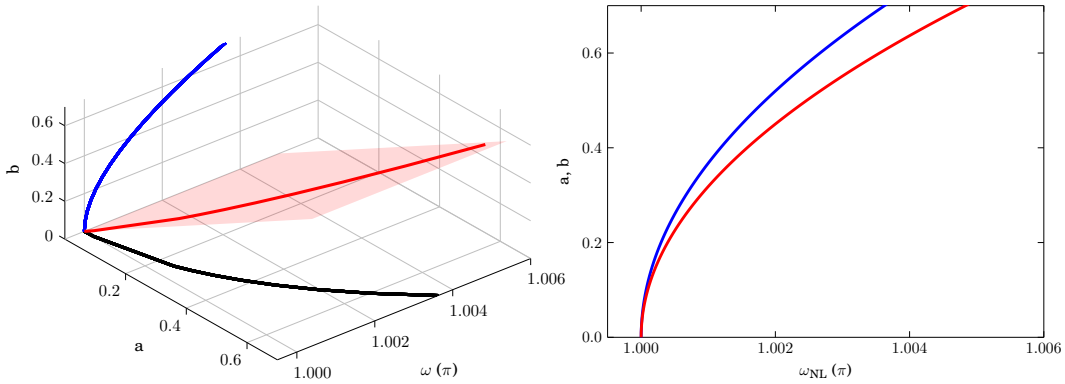

(a) 3-dimensional view.

(b) 2-dimensional view.

Figure 3.3: Backbone curves for the string, perfect case with $\omega_1 = \omega_2 = \pi$ (no detuning: $\sigma_1 = 0$), and equal nonlinear coefficients $C_1 = C_2 = \Gamma_1 = \Gamma_2 = \pi^4/2$. The black — and blue — lines indicate the two uncoupled modes while the red — line indicates the elliptic mode. $\varepsilon = 10^{-3}$. For the 2-dimensional view, the (ω_{NL}, a) plane and (ω_{NL}, b) are plotted on top of one another.

Finally, it is possible to show that the uncoupled solutions are bounded by Equation (3.43) and (3.44) respectively while the elliptic mode satisfies (3.42b). This leads to the conclusion that all the solutions shown in Figure 3.3a are stable. This means that if the motion is excited on a given polarization, then it will stay on it all the time such that there will no branching off into the elliptic mode. The coupled elliptic solutions could only be excited and observed if very specific initial conditions are given to the string such that the motion is initiated along this mode.

The next case to be investigated is the more realistic imperfect string. A detuning $\sigma_1 = 1$ between the two eigenfrequencies of the polarisation is introduced and all the nonlinear coupling coefficients are assumed to be equal and perfect, such that

$$C_1 = C_2 = \Gamma_1 = \Gamma_2 = \frac{\pi^4}{2}. \tag{3.46}$$

The backbone curves are represented in Figure 3.4, where now the two uncoupled solutions (black and blue lines) are different and originates respectively from ω_1 and $\omega_2 = \omega_1 + \varepsilon\sigma_1$. Equation (3.42a) reveals that the normal mode is always unstable in this configuration while the elliptic mode is stable as dictated by Equation (3.42b). On the other hand, the instability conditions for uncoupled solutions (Equation (3.43) and (3.44)) show that:

- B-mode is always stable. The uncoupled solution does not enter the instability region as defined by Equation (3.44) (bounded by cyan lines in Figure 3.4).
- A-mode becomes unstable as it enters the instability region as defined by Equation (3.43) (bounded by grey lines in Figure 3.4).

The crossing between the A-mode and its instability limit occurs exactly when condition (3.38) is fulfilled. From this point, the uncoupled solution becomes unstable, and it branches into the elliptic mode (red line).
The important conclusion that can be drawn from this study is that as soon as an imperfection is taken into account, i.e. when $\sigma_1 \neq 0$, an unstable region for uncoupled modes exists. Once the amplitude limit is exceeded, uncoupled solution becomes unstable so that even though an initial condition is given for that polarisation, an energy transfer will occur so that eventually the system would settle on the stable elliptic mode. A numerical validation of this phenomenon is presented in the following section with experimental validation being presented in Chapter 4.

3.4 Numerical validation

The reduced Kirchhoff-Carrier nonlinear equation that was introduced in Equation (3.1) can be numerically integrated in time by the modal approach as introduced in Section 2.4.2. It is then possible to simulate the equations with increasing amplitude of initial conditions to validate the existence condition of coupled modes. The system in interest is a string and it is assumed that the nonlinear coefficients are equal, such that:

$$C_1 = C_2 = \Gamma_1 = \Gamma_2 = \frac{\pi^4}{2},$$

and there is detuning between the two eigenfrequencies, such that:

$$\omega_2 = \omega_1 + \varepsilon\sigma_1,$$

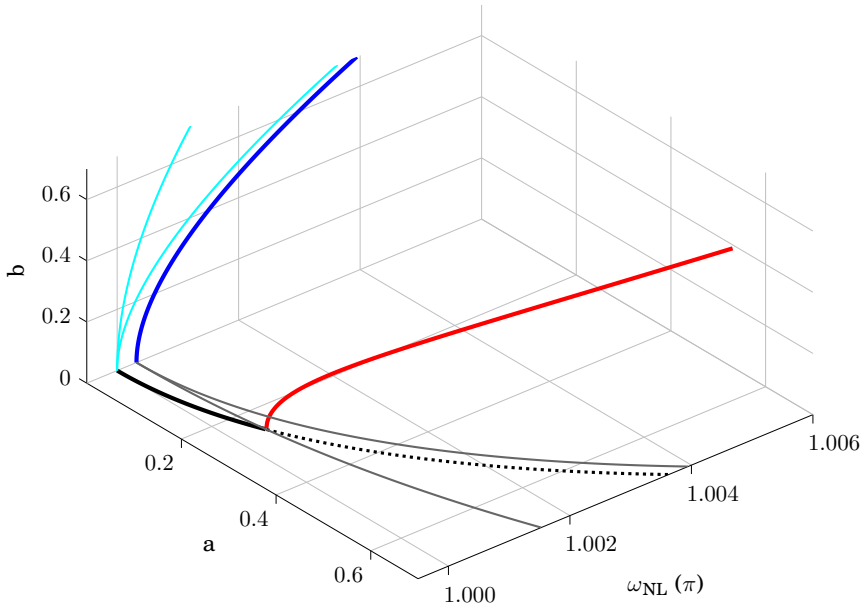

Figure 3.4: Amplitude-frequency relationships for periodic solutions of the nonlinear string, imperfect case with $\sigma_1 = 1$, all other coefficients being the same as in Figure 3.3a: $C_1 = C_2 = \Gamma_1 = \Gamma_2 = \pi^4/2$, $\omega_1 = \pi$, $\varepsilon = 10^{-3}$. Black — : uncoupled solution $a \neq 0$, blue — uncoupled solution $b \neq 0$, red — coupled elliptic mode. Dashed lines - - indicates instability. In grey and cyan lines are the instability limits predicted by Eq. (3.43) and (3.44) respectively.

as previously defined in Equation (3.8). The nonlinear phenomenon that can be observed is the transition of uncoupled A-mode into the elliptic mode when Equation (3.38) is satisfied, as rewritten here:

$$a^2 = \frac{2\sigma_1}{\frac{3\Gamma_1}{\omega_1} - \frac{C_2}{\omega_2}}.$$

Using $\sigma_1 = 6.1372$, $\varepsilon = 3.3905 \times 10^{-4}$ and the physical parameters outlined in Table 3.1, A-mode can branch into elliptic mode if the following condition is satisfied:

$$u_{init} \geq 1.64\mathrm{mm}, \tag{3.47}$$

where u_{init} indicates the initial amplitude of the first mode of the u (or p or a) polarisation. To prescribe a different frequency between the u and v polarisation, they are both given slightly different density, i.e. ρ and $\tilde{\rho}$ respectively for Equation (3.1a) and (3.1b). The simulations are made with a time step of $\Delta t = 10^{-5}$s as only the first mode is being solved.
Figure 3.5 shows the maximum amplitude achieved by the two polarisations when an undamped string is excited with a half-sine wave (i.e. first mode shape) of increasing initial displacement using the Kirchhoff-Carrier numerical scheme. Only

Table 3.1: Simulation parameters used for the simulation.

Parameters	Values
Tension, T_0	895.2N
Young's modulus, E	189.7 GPa
diameter, d	1.3mm
length, L	0.668m
density for u polarisation, ρ	7850kg.m^{-3}
density for v polarisation, $\tilde{\rho}$	7840kg.m^{-3}

the first mode of each polarisation is considered (i.e. total number of modes, $K = 1$) such that it would resemble the reduced order model as presented in Equation (3.7). The excitation is made such that the u polarisation (A-mode) is always 16 order of magnitude larger than the v polarisation (B-mode) so that B-mode would be very lightly excited. This is necessary for numerical purposes as the B-mode would otherwise always remain as 0 and exchange of energy would not have occurred.

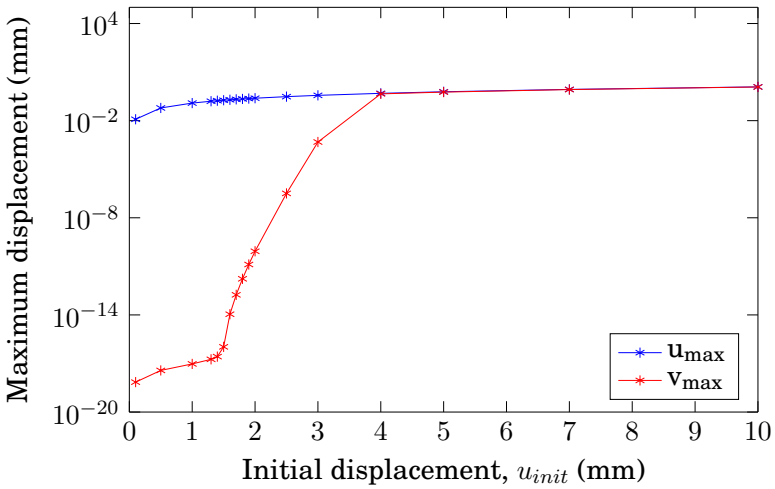

Figure 3.5: Maximum amplitude achieved by the two polarisations when an undamped string is excited with a half-sine wave (i.e. first mode shape) of increasing initial displacement when solving the reduced order Kirchhoff-Carrier equation. Observed point is at 30mm from one end of the string.

At low excitations, v increases at the same rate as u. However, as it approaches the threshold as defined in Equation (3.47), the maximum amplitude of v increases much more rapidly compared to the increase of u. This is because as the threshold is exceeded, 1:1 internal resonance condition is met and there is an energy exchange from the u polarisation to the v polarisation. At sufficiently high initial displace-

ment level ($u_{init} > 4$mm), energy exchange occurred in a way that v would achieve the same maximum amplitude as u as is shown in Figure 3.6. At that point, the energy remaining at the u polarisation would be minimal before it regains the energy from v. This is followed by an exchange of energy back to the u polarisation. In an undamped system, this nonlinear exchange of energy between u and v occurs repetitively (not shown in Figure 3.6).

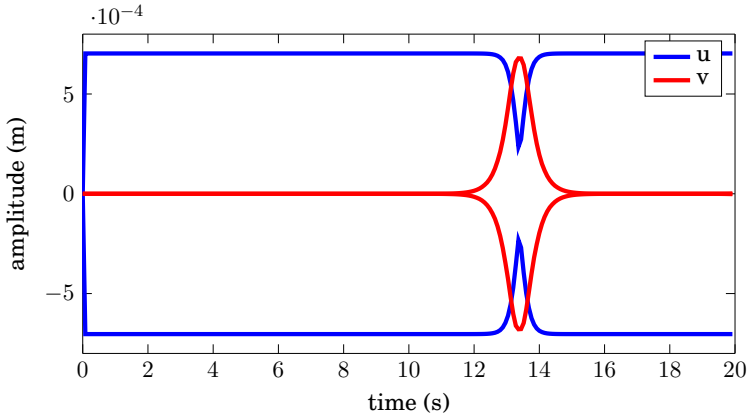

Figure 3.6: Wave envelopes of the displacement-time plot of the nonlinear Kirchhoff-Carrier equation when it is subjected to an initial condition of a half-sine wave at an amplitude of 5mm. Observed point is at 30mm from one end of string and the amplitude is thus approximately 0.14 times of the initial condition amplitude.

A similar numerical experiment is re-conducted but instead of solving only the reduced order model, the geometrically exact nonlinear string model is solved instead using MONTJOIE finite-element solver. The time step used is 10^{-6}s and 50 finite elements are used over the string length. The string remains undamped.

Figure 3.7a shows the maximum displacement of the u and v polarisations with increasing amplitude of a half-sine wave initial condition at u. A small difference as compared to previous simulations on the reduced order Kirchhoff-Carrier equations is that the v polarisation is given a constant half-sine wave initial condition with amplitude of 10^{-16}m and does not scale with u. Similar result compared to Figure 3.5 is observed but the energy gain of the v polarisation occurs at smaller initial amplitude. At the initial amplitude of 1.5mm, the finite-element model already predicts a maximum displacement of v at the order of 10^{-10}m but it was still at the order of 10^{-16}m for the Kirchhoff-Carrier reduced order model. The difference could be due to the development of other nonlinear phenomenon that was not modeled by the Kirchhoff-Carrier model.

To testify that elliptic mode cannot be originated from B-mode as defined in Equation (3.39) and that there is also no stable normal modes, a similar numerical experiment, is conducted using MONTJOIE for the geometrically exact string model.

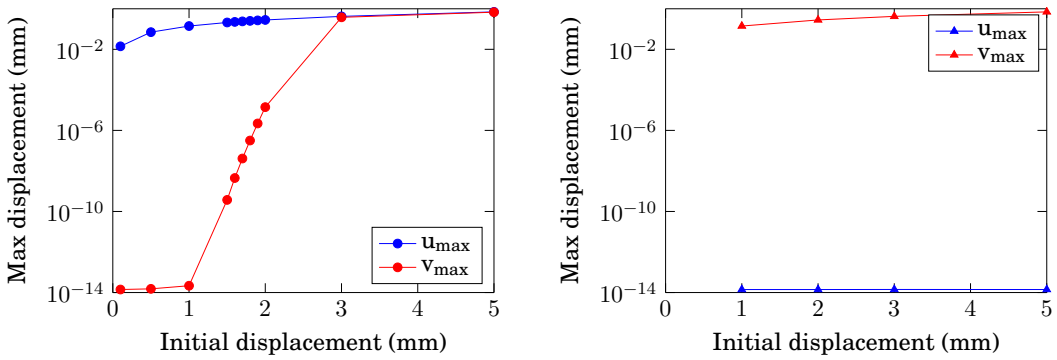

(a) Excitation at u polarisation.

(b) Excitation at v polarisation.

Figure 3.7: Maximum amplitude achieved by the two polarisations when an undamped string is excited with a half-sine wave (i.e. first mode shape) of increasing initial displacement at the (a) u polarisaion and (b) v polarisation respectively when solving the geometrically exact equation via the MONTJOIE finite-element solver. Observed point is at 30mm from one end of the string.

The difference compared to the previous MONTJOIE simulation is that instead of exciting the u polarisation with increasing amplitude, the v polarisation is excited. Figure 3.7b shows the maximum displacement of both the v and u polarisations. Despite increasing initial displacement of v, u remains at the order of 10^{-14}m, which invariably confirms that there are no coupled modes that could originate from the B-mode.

To further understand the nonlinear phenomenon, two more numerical experiments are conducted using the MONTJOIE finite-element solver. The viscous damping model [57] is prescribed to the string equation and the same experiment where the u polarisation is excited with increasing amplitude is repeated. The experiments are repeated twice, with different initial amplitude of the v polarisation at 10^{-6}m and 10^{-9}m respectively. The idea here is to obtain a basic understanding on the influence of damping on the geometrically exact string model, which is a more accurate representation of a physical string. The two new sets of data are plotted together with the undamped data in Figure 3.8. $v_{max,damped1}$ and $v_{max,damped2}$ indicate that the v polarisations are initialised at 10^{-6}m and 10^{-9}m respectively. The maximum amplitude of the u polarisation, as indicated by $u_{max,all}$ remains unchanged for all undamped and damped cases as it is the amplitude of the initial conditions. Both the damped v polarisations responded in a similar fashion. There is no increment in its maximum amplitude until an initial displacement of 2mm. In comparison, in the undamped case, increase would have been observed at least from 1.5mm. Such difference is expected; as damping is present in the system, energy is dissipated and thus more initial energy is required to trigger the nonlinear phenomenon of 1:1 internal resonance.

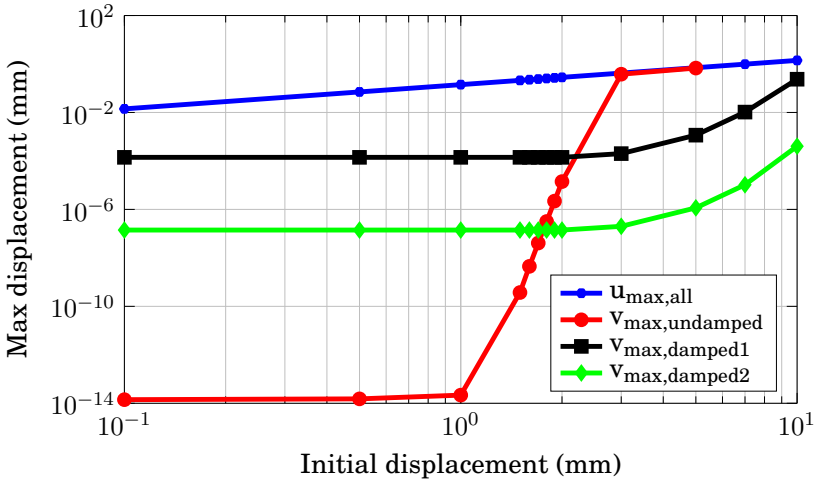

Figure 3.8: Maximum amplitude achieved by the two polarisations when undamped and damped strings are excited with a half-sine wave (i.e. first mode shape) of increasing initial displacement at the u polarisation when solving the geometrically exact equation via MONTJOIE finite-element solver. Observed point is at 30mm from one end of the string.

3.5 Double polarisation in linear wave equation

In Section 3.2 and 3.3, it has been shown that if a threshold amplitude is exceeded, double polarisation would occur due to the nonlinearity of the string. The string enters the coupled elliptic mode and energy is exchanged between the two modes of the string. However, double polarisation could also occur even if the string is being excited linearly with small amplitude. Such non-planar motion is distinctively different from the aforementioned phenomenon as there is no energy exchange between the two polarisations at all. For the linear double polarisation to occur, the following conditions must be met:

- the two polarisations must be slightly detuned from one another,
- the two polarisations are excited at the same time.

It is intuitive to acknowledge that these conditions can easily be met. On one hand, string is prone to imperfection with variability in manufacturing or by natural rusting in metallic objects. The imperfection would invariably introduce detuning between the two polarisations of the string. On the other hand, it is very easy to excite both polarisations, albeit at different amplitudes. Given that both polarisations are at right angle between each other, chances are an excitation could trigger both modes with non-negligible amplitudes. To demonstrate the non-planar motion, one can write two linear wave equations for two transverse displacements u and v

where:

$$\rho A\ddot{u} - T_0 u'' = 0, \tag{3.48a}$$
$$\rho A\ddot{v} - T_0 v'' = 0, \tag{3.48b}$$

with a boundary condition where the string is fixed at both ends:

$$u(0,t) = v(0,t) = 0, \tag{3.49a}$$
$$u(L,t) = v(L,t) = 0. \tag{3.49b}$$

For simplicity purposes, only the first mode is considered and the string is excited with an initial displacement and has no initial velocity. Under these assumptions, the solution to the two wave equations are:

$$u(x,t) = \sin\left(\frac{\pi x}{L}\right) P\cos(\omega_u t), \tag{3.50a}$$
$$v(x,t) = \sin\left(\frac{\pi x}{L}\right) Q\cos(\omega_v t), \tag{3.50b}$$

where ω_u and ω_v are the two fundamental frequencies of the two transverse modes respectively. If $\omega_u = \omega_v$, Equation (3.50) can be transformed into polar coordinates (r, θ) where:

$$r(x,t) = \sqrt{1+R^2}P\sin\left(\frac{n\pi x}{L}\right)\cos(\omega_u t), \tag{3.51a}$$
$$\theta(x,t) = \arctan(R), \tag{3.51b}$$

where $R = Q/P$. From Equation (3.51), it can be seen that θ is constant and is dependent on the ratio between the excited amplitude of the two displacements. If only either mode is excited, R will either be 0 or very large where θ will either be at 0 or $\pi/2$ rad. On the other hand, the radius r is determined entirely by the initial displacement condition of the two modes and oscillates at the rate of ω_u. For example, if $R = 1$, the string oscillates at $\pi/4$ rad and remains in the same plane all the time.
If the two fundamental frequencies are slightly different either in the form of slight variation in tension or density, ω_u and ω_v can be defined such that:

$$\omega_v = \omega_u + \delta, \tag{3.52}$$

where δ is a detuning between the two frequencies. The radius r and angle θ in polar coordinates thus become:

$$r(x,t) = \sin\left(\frac{n\pi x}{L}\right)\sqrt{u^2 + R^2\Delta^2(u - \eta/(R\Delta))}, \tag{3.53a}$$
$$\theta(x,t) = \arctan(R\Delta(1 - \tan(\omega_u t)\tan(\delta t))), \tag{3.53b}$$

where $\Delta = \cos(\delta t)$ and $\eta = Q\sin(\omega_u t)\sin(\delta t)$. One could see that the angle is no longer constant and is a function of time. This invariably confirms that if there is a

detuning between the two fundamental frequencies, the oscillation no longer stays planar but follows a path. This is because as the two wave equations are oscillating at different frequencies, they will eventually go out of phase and thus they do not remain in the same plane. Depending on the parameters, this non-planar motion can thus be observable and complicate the readings from experiment.
Figure 3.9 shows a few examples of the trajectories as predicted by Equation (3.50) for a string where $\omega_u = 13,786\text{rad/s}$ at $x = L/2$.

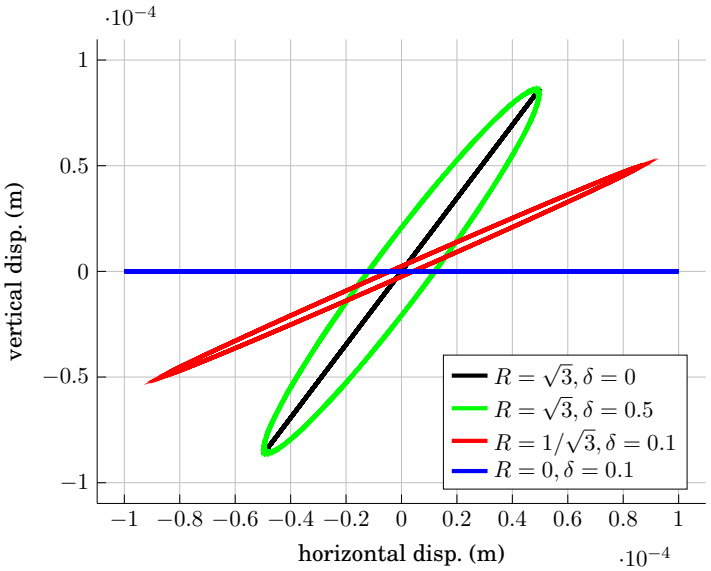

Figure 3.9: Sample trajectories based on Equation (3.50) under different conditions for a string where $\omega_u = 13,786\text{rad/s}$ at $x = L/2$.

The blue (—) line shown is for $R = 0$ (i.e. $P = 1, Q = 0$), $\delta = 0.1$. This shows that even if there is a detuning between the two modes, both modes need to be excited. In this case, $Q = 0$ and thus only a straight line trajectory is observed instead. The red (—) line shown is for $R = 1/\sqrt{3}, \delta = 0.1$. The ratio $R = 1/\sqrt{3}$ results in a 30° counter-clockwise rotation from the horizon and both modes are being excited. Under the presence of a small detuning of $\delta = 0.1$, an elliptical non-planar trajectory can be seen. The (—) line shown is for $R = \sqrt{3}, \delta = 0.5$. The ratio $R = \sqrt{3}$ corresponds to a 60° counter-clockwise rotation from the horizon and under a bigger detuning at $\delta = 0.5$, the elliptical non-planar trajectory is more pronounced. Finally, at the same angle, the black (—) line shown is for $R = \sqrt{3}$ but it is defined such that there is no detuning between the mode, i.e. $\delta = 0$. When there is no longer any detuning, the modes do not go out-of-phase and thus no double polarisation can be observed. In short, the examples demonstrate that the two following criteria:

- the two polarisations must be slightly detuned from one another,
- the two polarisations are excited at the same time,

must be met before double polarisation can be observed in linear string vibrations.

3.6 Summary

In this chapter, the condition where nonlinear strings can exhibit double polarisation is determined by multiple-scale analysis. For a string with two slightly detuned modes, as an initial amplitude threshold is exceeded, nonlinear elliptic coupled mode could occur where the in-plane polarisation could exchange energy with the out-of-plane polarisation. The situation where this could arise is first studied by theoretical case studies and is also numerically validated. Lastly, it is also demonstrated that double polarisation could occur in a linear string.

4

Experiments on string

In Chapter 2, string equations and their numerical models are introduced. In Chapter 3, the double polarisation as caused by the string's nonlinearity is studied. The idea of detuning is also introduced. In this final chapter of Part I, several experiments are conducted to demonstrate the presence of detuning and nonlinearity in a piano string. In what follows, the experimental setup will be presented in Section 4.1 followed by the introduction and identification of the polarisation angle, a physical parameter that is closely related to the detuning of the string in Section 4.2. String's material parameters are then identified in Section 4.3 and the chapter closes by demonstrating the nonlinear behaviour of the piano string in Section 4.4.

4.1 Experimental setup

To validate the analytical findings in Section 3.2, A monochord experimental rig is built as shown in Figure 4.1. A great deal of attention has been given to set up the experiment so that accurate results can be extracted. The following items have been used to ensure the accuracy of the experiment:

- **Measuring device** (green arrow): A KEYENCE 9030-D optical micrometer is being used as it allows the measurement of the two transverse displacements of a string at a single point. This is achieved by placing two orthogonal optical micrometers, H1 and H2, where the shadow casted by the string is tracked independently for both micrometers. The evolution of the double polarisation can thus be accurately captured. In addition to that, the device can sample up to 16,000Hz with $\pm 2\mu\mathrm{m}$ accuracy and does not require calibration between its voltage output and actual displacement.

- **String** (blue arrow): The string of choice is a piano string manufactured by French piano maker Stephen Paulello [87]. The string is tin-plated and classified as type M by the manufacturer and has a diameter of 1.3mm. While the

string is plated by tin to minimise rusting, it still suffers from rusting that can be considered as a source of imperfection.

- **Boundary condition** (red arrows): A pair of custom-made clamps that imitate the clamping mechanism of a collet is being used as the boundary condition of the string. The motivation behind the use of such clamps is to be as close to an actual fixed-fixed boundary condition as possible. A quick check of the boundary condition can be performed by exciting the string right in the middle. If a fixed-fixed boundary condition is ensured, any even numbers of modes will not be observed in the frequency responses of the displacement [80].

- **Initial condition**: The string is excited via the use of thin copper wire. Thin copper wire is passed over the string and pulled to form a triangular shape initial condition. As the pulling force increases, the copper wire will break and thus triggering the free vibration of the piano string. The excitation method is highly repeatable and consistent [83]. If a higher initial displacement is needed, a thicker copper wire can be used instead so that the string can be displaced more before the copper wire breaks. The use of copper wire also allows the excitation of the string at different angles.

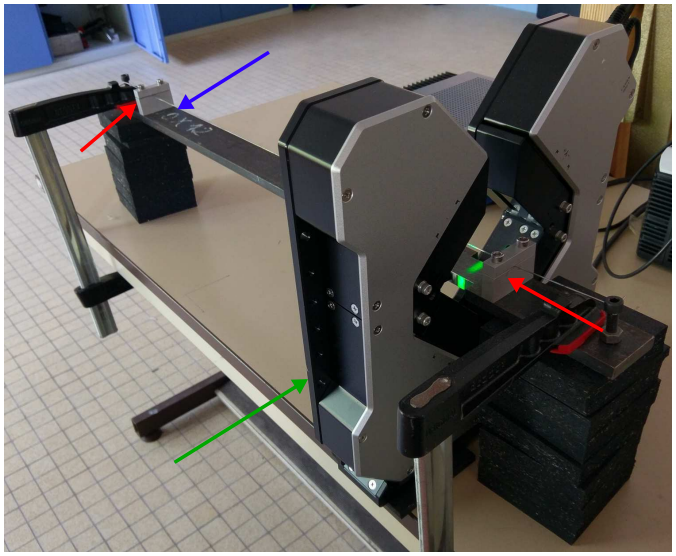

Figure 4.1: Actual experimental setup. The green, blue and red arrows show the Keyence 9030-D, piano string and the boundary conditions respectively.

Figure 4.2 shows the schematic diagram of the experiment. The string is fixed onto a bolt at each end and is screwed onto a steel plate. It is then stretched under tension by tightening the bolts. The custom clamps are then used to fix its vibrating length

to $L = 0.668$m and the Keyence 9030-D is placed at 0.03m from one end (marked K in Figure 4.2) to measure the string vibrations.

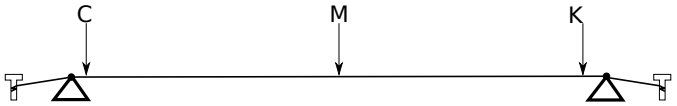

Figure 4.2: Simplified diagram of the experimental setup.

4.2 Identification of polarisation angle

The first experiment to be conducted for the validation purpose is to identify the natural polarisation angles of the string. In an analytical or numerical context, it is convenient, albeit arbitrarily, to define that the polarisations lie on the vertical or horizontal plane. However, this is not necessarily the case for a string in the experiment. Intrinsic material properties in the string have already defined its own natural polarisation angles that are to be discovered. In addition to that, the natural polarisation of each eigenmode may not be identical as well. However, for the context of this thesis, only the first mode is of concern to validate the analytical finding as presented in Chapter 3, where nonlinear energy exchange between the two polarisations are expected.

To determine the polarisation angles, the string is lightly excited using 0.07mm-thick copper wire at its midpoint (marked M in Figure 4.2) so that most of the energy is concentrated on the first mode. The 0.07mm copper wire will displace the string by about 0.55mm before it breaks and set it to vibrate freely and linearly. This excitation is repeated multiple times, each time pulling at a different angle and the vibration is recorded for 5 seconds. For reference, 0° is defined at the measurement axis of the H2 optical micrometer. Correspondingly, the measurement axis of the H1 optical micrometer is thus +90°.

In most cases, both string modes will be excited as the string's natural polarisation angle falls on a very specific angle. If both string modes are slightly different from one another in terms of frequency, both of them will be present in the displacement signals. A way to observe them is to rotate all signals that are excited in different angles to have their maximum amplitudes at the H2 axis, with an example as shown in Figure 4.3. The signal at H2 is then named as the "dominant" mode and the corresponding orthogonal signal at H1 as "orthogonal". Theoretically speaking, if the string is excited over 180°, there will be two angles for which the dominant signal contains only one mode and there is no orthogonal displacement at all. At each of these angles, the single mode observed in the dominant signal is different from one another. In practice, this is virtually impossible to achieve. Instead, it is possible to observe a very strong mode in the dominant signal accompanied by a very weak mode in the orthogonal signal at certain angles. When this is observed,

that angle is then identified as the natural polarisation angle of the specific mode observed in the dominant signal.

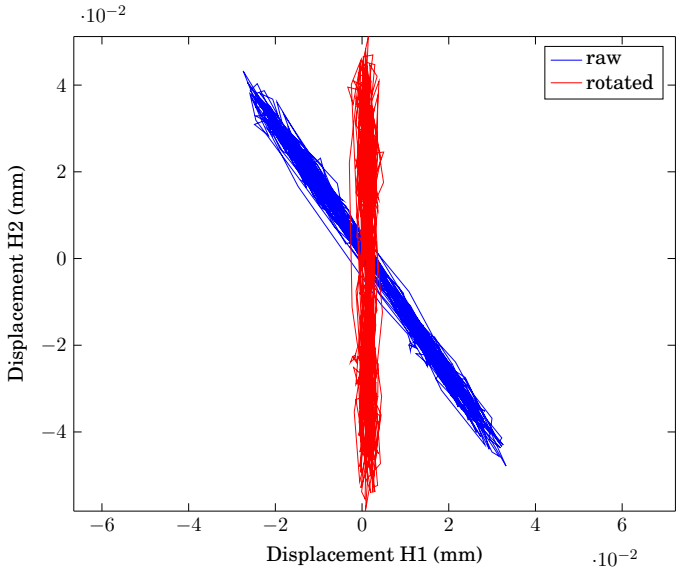

Figure 4.3: Comparison of raw signal and rotated signal. This particular raw signal was rotated by -33°. The "dominant" and "orthogonal" signal are the vertical and horizontal displacements of the rotated signal respectively.

To identify the frequency of the dominant and orthogonal signals, a high-resolution parameter identification method is necessary due to the small detuning in the string. It would be very difficult to obtain linear displacement signals that are long enough to have the frequency resolution that can identify clearly the difference between the two string's frequencies. Thus, the ESPRIT method is employed where a signal, $u(t)$ can be decomposed into:

$$u(t) = \sum_{k=1}^{K} a_k e^{\varsigma_k t} e^{j(2\pi f_k + \varphi_k)}, \tag{4.1}$$

where a_k, ς_k, f_k and φ_k are the amplitude, damping constant, frequency and phase of the k-th identified mode up to a maximum of K modes [88, 89]. For the purpose of this set of data, only the first mode is consider and thus $K = 1$. To optimise the processing requirement of the ESPRIT method, only a 0.3s-long signal is processed. The time t_0 when the orthogonal displacement is the largest is first identified and a 0.3s-long signal centered at t_0 is then extracted and analysed by ESPRIT algorithm. This allows accurate identification of the orthogonal mode as the signal is usually very weak.
Figure 4.4 shows the amplitude of the dominant and orthogonal modes at each transformed angle. The top figure shows its absolute amplitude while the bottom

figure displays the relative ratio between the dominant and orthogonal mode. At around -85° and +5°, the orthogonal mode is at its weakest and the dominant mode is the strongest. As mentioned before, these two angles can be identified as the string's natural polarisation angles. This is because when the string is excited along this angle, one polarisation is very strongly excited and the other very weakly excited. These excitations would be analogous to exciting the uncoupled system in the (ω_{NL}, a) plane or the (ω_{NL}, b) plane in Figure 3.4. At sections around -40° and +50°, it can be seen that both the dominant and orthogonal modes are equally strong. This is because they are both similarly excited in strength.

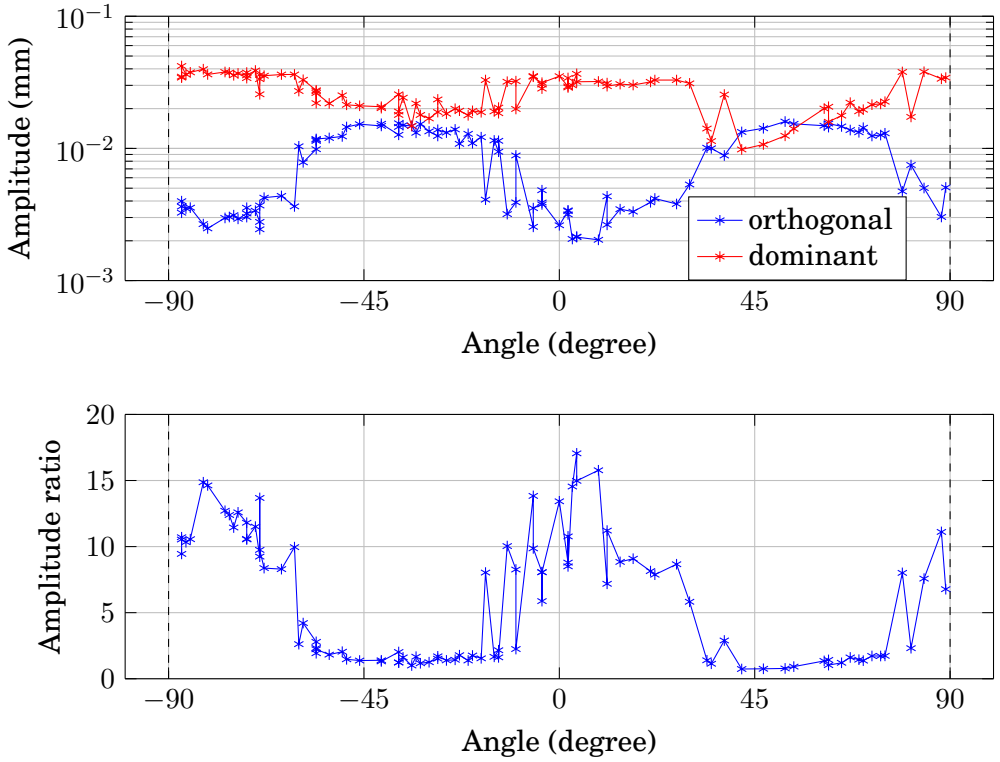

Figure 4.4: Amplitude of dominant and orthogonal modes from -90° to +90°.

Figure 4.5 shows the frequency of both the dominant and orthogonal modes as predicted by ESPRIT algorithm. On the top figure, the actual frequency of the modes are shown and the difference between these modes are shown at the bottom. It can be seen that the difference between the two modes are about 0.1Hz at most. At -85°, the dominant mode is about 0.1Hz higher than the orthogonal mode and vice versa at +5°. This suggests that the two eigenfrequencies of the string are 0.1Hz apart. However, the absolute dominant frequency is approximately 219.8Hz at -85° but 219.6Hz at +5°, which would otherwise suggests that the two eigenfrequencies are 0.2Hz different. It is inconclusive to suggest which theory is valid and thus a further study is required to determine the detuning between the two eigenfrequencies.

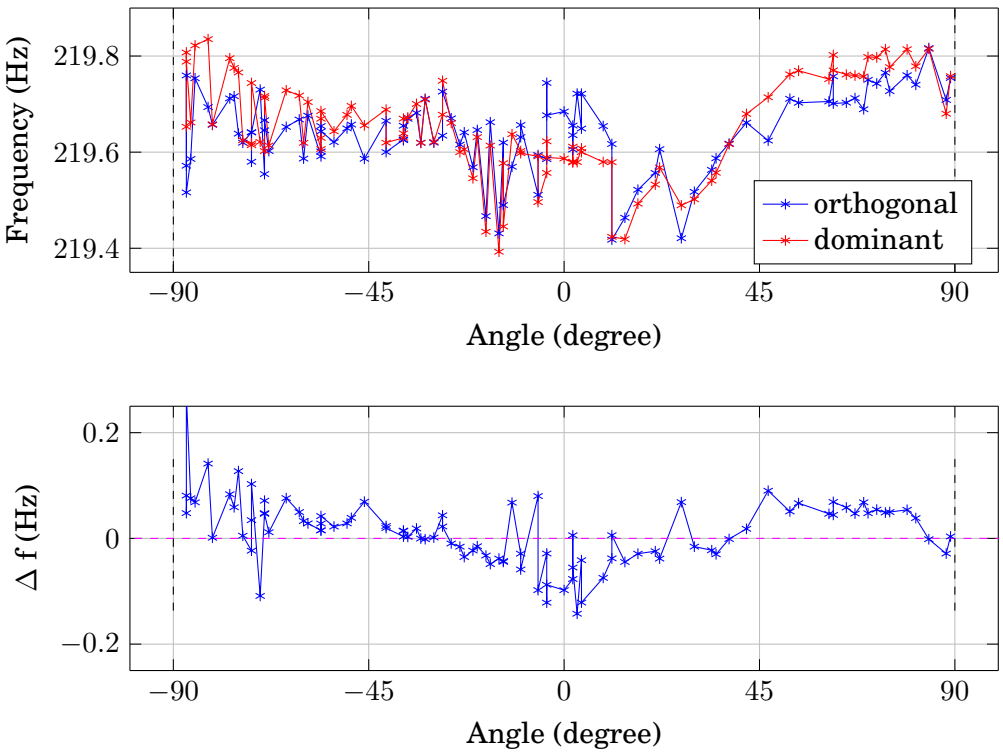

Figure 4.5: Frequency of dominant and orthogonal modes across the tested angle range.

A similar experiment is being conducted numerically in the finite-element solver MONTJOIE and the result is being shown in Figure 4.6. Simulations are run for different angles and they are passed to ESPRIT for extraction of frequency and amplitude of the fundamental mode. The top plot shows the amplitude as extracted while the bottom plot shows frequency. Since it is a numerical simulation, the default polarisations are at 0° (or +180°) and +90°. First, it is reassuring to see the resemblance between the top amplitude plot and Figure 4.4 where the dominant polarisation is shown to be the highest at its natural polarisation (i.e. at 0° and +90°). At the midpoint between the two polarisations, i.e. at +45°, it can be seen that the strengths are comparable, which is consistent to the experimental finding.

As for the frequency, it is artificially implemented that the two eigenfrequencies are separated by 0.07Hz and this difference is clearly shown. At 0° (or +180°), the lower eigenfrequency mode, ω_1 sits at 223.02Hz and at +90°, the eigenfrequency ω_2 is 223.78Hz. As one sweeps from +0° to +90°, it can be seen that several orthogonal modes are detected at the vicinity of the two eigenfrequencies and are increasing in strength. At +45°, the dominant mode swaps to the higher eigenfrequency ω_2, while the lower eigenfrequency ω_1 decreases in strength until it becomes non-existent at +90°. The same phenomenon is then mirrored from +90° to +180° where ω_1 regains

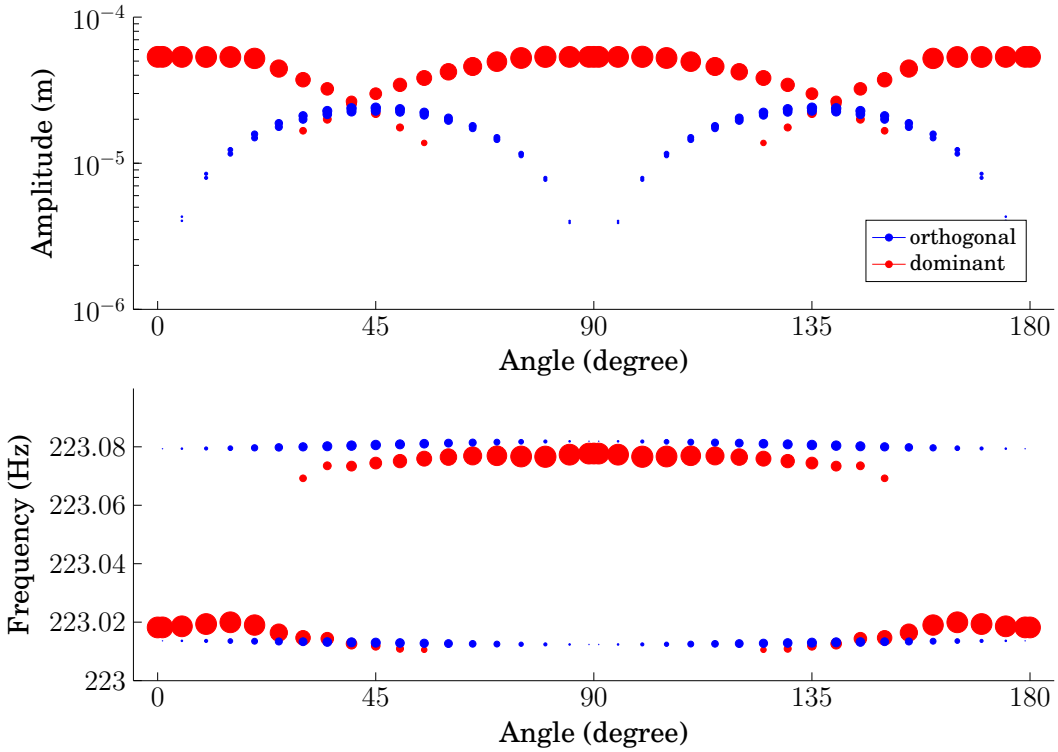

Figure 4.6: Amplitude(top) and frequency(bottom) of dominant and orthogonal modes across the tested angle range in MONTJOIE. In both plots, the marker size also indicates the amplitude level, with bigger marker indicating higher amplitude level. In instances where more than one dominant or orthogonal modes are reported (with slightly lesser amplitudes), the second dominant or orthogonal modes are also shown.

the strength. In this plot, the two eigenfrequencies do not shift around and stay mostly at its own value. It makes it easy to identify the detuning. The difference between the two frequencies are the same value across the whole angle range. This is in contrast with the experimental data where there is a noticeable shift with no clear indication of the detuning difference.

In short, while the simulation result does not give a hint on identifying the detuning between the two experimental eigenfrequencies, it does cross-validate the amplitude result obtained from the experiment. With that, the natural polarisation is identified to be at +5° and -85° for the string inspected. Despite the fact that the detuning difference is not clearly determined, it is important to note that the mode at +5° has a lower frequency compared to the one at -85° and their difference is less than 0.2Hz. The eigenfrequency +5° corresponds to the lower eigenfrequency mode ω_1 in Equation (3.8), i.e. the black curve in Figure 3.4 while the one at -85° corresponds to ω_2, the blue curve in Figure 3.4.

4.3 Identification of string parameters

Tension and Young's modulus

After identifying the natural polarisation of the first eigenmode of each transverse displacement, the string can be further characterised. Using the data from the multi-angle excitations is not suitable as they were done at the midpoint on the string, thus missing out information on every even modes. To mitigate this, a new set of experiments are done with an excitation near the boundary of the string, specifically 19mm from the end of the string (marked C in Figure 4.2). This is a strategic location as it is only a nodal point for multiple of the 35th mode, which has an eigenfrequency that exceeds 8,000Hz, the half of the sampling frequency. The excitation is made along the natural polarisation at +5°. The measurement is repeated 6 times and the signals are passed to an ESPRIT algorithm to extract information on its frequencies and damping constants.
The tension and the Young's modulus of the string can be identified by experimentally determining the eigenfrequencies of the string. As derived by Chabassier for a linear Timoshenko stiff string equation [75], the eigenfrequency equation can be approximated by:

$$f_n = nf_0 + Bn^3, \tag{4.2}$$

where

$$f_0 = \frac{1}{2L}\sqrt{\frac{T_0}{\rho A}} \qquad \text{and} \qquad B = \frac{\pi^2 EI}{4L^3}\sqrt{\frac{T_0}{\rho A}}\left[1 - \frac{T_0}{EA}\right].$$

The two unknowns (f_0 and B) in Equation (4.2) can be completely determined if $n = 2$. If $n > 2$, it becomes an overdetermined system and a matrix equation can be constructed for Equation (4.2) such that:

$$\begin{bmatrix} f_1 \\ f_2 \\ f_3 \\ \vdots \\ f_n \end{bmatrix} = \begin{bmatrix} 1 & 1 \\ 2 & 8 \\ 3 & 9 \\ \vdots & \vdots \\ n & n^3 \end{bmatrix} \begin{bmatrix} f_0 \\ B \end{bmatrix}. \tag{4.3}$$

The two unknowns f_0 and B can thus be determined by fitting the data via the least-square method. The least-square method minimises the squared residual, $\mathcal{S}$ between the fitted and experimental data and $\mathcal{S}$ defined as:

$$\mathcal{S} = \sum_{n=1}^{N} \left(f_{n,exp} - f_{n,fit}\right)^2, \tag{4.4}$$

where $f_{n,exp}$ and $f_{n,fit}$ are the experimental and fitted eigenfrequencies from a data set with N entries. The least-square fit method can be performed in MATLAB by the "\" (blackslash) operator.

In this experiment, up to 22 eigenfrequencies are identified consistently in 6 sets of measurement data by ESPRIT with a standard deviation of less than 0.8Hz as shown in table 4.1. Taking the average of each eigenfrequency and performing a least-square fit, f_0 and B can be determined. Subsequently the two material parameters T_0 and E can be calculated and they are presented in table 4.2.

Table 4.1: Averaged eigenfrequencies as extracted by ESPRIT and their standard deviation (STD).

n	Average frequency, f_n (Hz)	STD (Hz)
1	187.54	0.05
2	375.51	0.10
3	564.52	0.15
4	879.25	0.19
5	1102.57	0.23
6	1328.61	0.28
7	1556.60	0.33
8	1788.28	0.41
9	2023.71	0.28
10	2262.33	0.73
11	2507.24	0.51
12	2754.25	0.53
13	3007.90	0.60
14	3267.32	0.64
15	3530.87	0.65
16	3802.52	0.60
17	4080.50	0.65
18	4364.43	0.72
19	4655.34	0.74
20	4954.45	0.77
21	5259.43	0.71
22	5572.88	0.80

Table 4.2: Model parameters obtained from experimental data.

Parameter	Value
T_0 (N)	895.2
E (GPa)	189.7

Damping parameters

A similar strategy can be followed to obtain the damping parameters. Frequency-dependent damping constants, ς_n can be extracted by ESPRIT algorithm. They are

then substituted into Equation (2.76) and (2.82). For convenience, they are being rewritten below. For the Valette & Cuesta models (VCM) models [80], Equation (2.76) is:

$$\varsigma_n = \sigma_n, \tag{4.5}$$

where

$$\frac{\sigma_n}{\pi f_n} = \frac{1}{Q_{n,air}} + \frac{1}{Q_{n,vis}} + \frac{1}{Q_{ther}},$$

and

$$\frac{1}{Q_{n,air}} = \frac{2\pi\eta_{air} + 2\pi d\sqrt{\pi\eta_{air}\rho_{air} f_n}}{2\pi\rho A f_n},$$
$$\frac{1}{Q_{n,vis}} = \frac{4\pi^2 \rho A E I {f_n}^2}{{T_0}^2}\delta_{vis}.$$

The unknowns to be solved in Equation (4.5) is viscoelastic loss angle δ_{vis} and the thermoelastic loss quality factor Q_{ther}. Meanwhile, for the simple viscous damping model (SVM) [57], Equation (2.82) is:

$$\varsigma_n = R_u + {\omega_n}^2 \zeta_u, \tag{4.7}$$

where R_u and ζ_u are two unknowns that characterise the damping models. Both Equation (4.5) and (4.7) are written in frequency-dependent forms and as such, they can be written as an overdetermined system like Equation (4.3) and have the unknowns be determined by fitting the data via least-square method.
Figure 4.7 shows the 22 extracted experimental damping constants and two different VCMs that are obtained based on the fitting of those data. The first VCM model, as shown as grey curve, is obtained by fitting Equation (4.5) using all 22 experimental damping constants, i.e. $n = 22$. However, that results in a negative δ_{vis} which is not realistic. If δ_{vis} is negative, it would have meant that the string is gaining energy rather than losing it. Thus, this model cannot be used and must be discarded. An alternative is to use less modes, i.e. reducing n. When $n = 16$, by least-square method, the fitted δ_{vis} is positive. The VCM obtained using this value and the corresponding Q_{ther} is as shown as the black curve in Figure 4.7. One can argue that the 16-mode VCM is more realistic even though it uses less data points. Indeed, considering only the first 16 modes, the 16-mode VCM does not differ greatly from the 22-mode VCM. From mode 17 and above, the 16-mode VCM fits the experimental values poorly. In spite of that, for most purposes, the lower modes are usually more strongly excited and the higher modes are more strongly attenuated. Thus, between having unrealistic damping constant and a poor fit at higher modes, it is more appropriate to opt for the latter and adopt the 16-mode VCM.
Figure 4.8 shows again the 22 extracted experimental damping constants and two different SVMs that are obtained based on the fitting of those experimental data. The two SVMs that are shown are obtained by considering all 22 modes or the first 16 modes. As can be seen, the 22-mode model is also suboptimal with strong

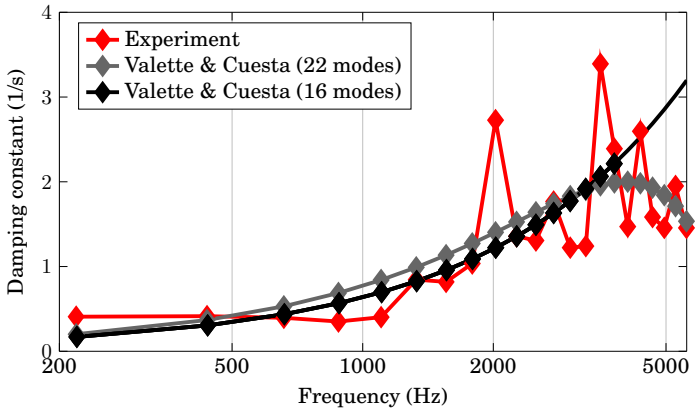

Figure 4.7: Comparison between the 22-mode and 16-mode estimation of Valette & Cuesta model against the experimental data.

overestimation (by a factor of 2) for the first 5 modes. In contrast, the 16-mode SVM models the lower modes more accurately and is thus preferred.
All the determined damping parameters are as shown in Table 4.3. When SVM is being used for the geometrically exact finite-element model in MONTJOIE, the other damping parameters are chosen as:

$$R_\phi = R_\psi = R_v = R_u = 0.5067\text{s}^{-1}, \tag{4.8a}$$

$$\zeta_\phi = \zeta_\psi = \zeta_v = \zeta_u = 3.8 \times 10^{-9}\text{s}, \tag{4.8b}$$

$$R_w = 0.5\text{s}^{-1}, \tag{4.8c}$$

$$\zeta_w = 10^{-9}\text{s}, \tag{4.8d}$$

as per recommended by [84].

Table 4.3: Damping parameters of SVM and VCM.

Parameter	Value
δ_{vis}	1.2208e-4
Q_{ther}	5941
R_u	0.5067 1/s$^-$1
ζ_u	3.800e-9 s

Since VCM is used exclusively for the Kirchhoff-Carrier numerical scheme (see Section 2.4.2), it is possible to further improve the modelling of the damping phenomenon using a "hybrid VCM". For the first 22 modes, experimental damping constants are used and if modelling of the 23rd mode and above is necessary, the 16-mode VCM is used instead. An example of the hybrid VCM is as shown alongside with the 16-mode SVM in Figure 4.9 up until the audible limit of 20kHz.
The hybrid VCM and SVM can both be used in the Kirchhoff-Carrier numerical scheme. The same simulation performed in Section 2.4.5 is repeated for the scheme

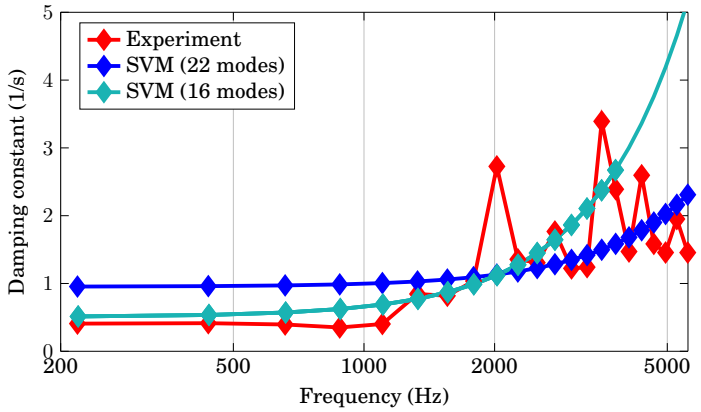

Figure 4.8: Comparison between the 22-mode and 16-mode estimation of the simple viscous damping model against the experimental data.

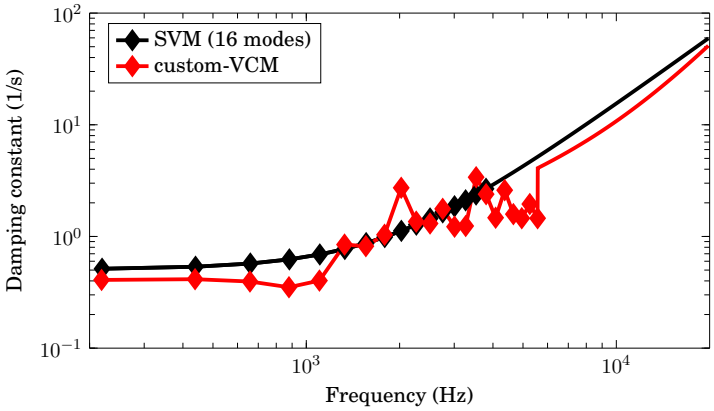

Figure 4.9: Comparison between the hybrid Valette & Cuesta model and 16-mode the simple viscous damping model within the audible frequency range.

with hybrid VCM. To recap, the simulation parameters used are as shown in Table 2.1 and the string is plucked with a 33° offset from one polarisation at 0.3335m from one end with an amplitude of 0.33mm. A detuning between the two fundamental frequencies of the string polarisation u and v is given at 0.14Hz and the difference is accounted for by changing the density of the v string mode. Observation point is at 0.638m from one end of the string.

The simulation is configured to match an experimental measurement that are conducted under very similar condition. The simulated displacements for both damping models are as shown together with the experimental data. The top plot shows the displacements in the plane of excitation (i.e at 33°) and the bottom plot shows the orthogonal out-of-plane displacement. Comparing between hybrid VCM and SVM, the string is more strongly damped by SVM which is not surprising as SVM has

consistently higher damping constants than hybrid VCM as is shown in Figure 4.9. Comparing between the simulation done with hybrid VCM and the experimental data, the numerical simulation exhibits a stronger attenuation which is perplexing as the hybrid VCM uses experimental damping constants for the first 16 modes. Since the string is only lightly excited, it is not expected that the discrepancy originates from the high frequency modes. The discrepancy between the simulations using the hybrid VCM and the measurements could be attributed to experimental errors of inaccuracy in extracting the damping constants using ESPRIT algorithm.

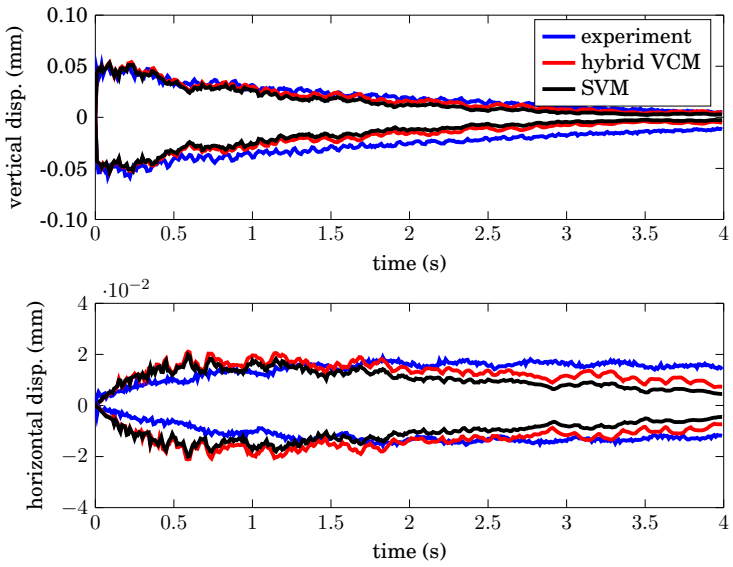

Figure 4.10: Comparison between the experimental data (labeled 'experiment'), the Kirchhoff-Carrier numerical scheme with hybrid VCM and with SVM, showing its wave envelope over the first 4 seconds after excitation. The envelope is obtained by determining the maximum and minimum displacements over a short time sample of 10ms.

4.4 Nonlinear effect and detuning identification

From the findings of Section 3.2 via multiple-scale analysis, if the two eigenfrequencies of a string are slightly detuned from each other, it is possible that an uncoupled polarisation can lose its stability due to 1:1 internal resonance if it is being excited above a threshold amplitude as is defined in Equations (3.43) and (3.44). As the uncoupled polarisation loses its stability, it could then branch into a stable coupled mode as dictated by Equations (3.38), (3.39), (3.35) and (3.36). From earlier analysis, it can be understood that for a coupled system like the two string polarisations, Equations (3.39), (3.35) and (3.36) could not be satisfied. Thus, from Equation (3.38), only the polarisation u, with dimensionless eigenfrequency ω_1 and

amplitude $2a$, can branch into a stable elliptic mode. The stability of the elliptic mode is guaranteed as is defined in Equation (3.42b). Rewriting Equation (3.38):

$$a^2 = \frac{2\sigma_1}{\frac{3\Gamma_1}{\omega_1} - \frac{C_2}{\omega_2}}, \tag{4.9}$$

where Γ_1 and C_2 are the two nonlinear coefficients and can be assumed to be $\pi^4/2$; σ_1 is the detuning parameter that relates the two polarisations' frequency by $\omega_2 = \omega_1 + \varepsilon\sigma_1$, and ε is a small parameter as defined in Equation (3.5).
A closer look at Equation (4.9) reveals that the RHS is entirely dependent on σ_1. As such, theoretically speaking, if the minimum a where elliptic mode could occur is found, it is thus possible to determine σ_1 and consequently the difference between the two polarisations' frequency. To obtain a, the string needs to be excited with increasing initial amplitude until vibration of the second polarisation is observed. This is achieved by pulling the string with copper wire of increasing thickness, or with multiple copper wires so that the string would be displaced more before the copper wires break and send the string free to vibrate.
Figure 4.11a shows the amplitude spectral density of the fundamental frequency of both the dominant and orthogonal modes when the string is excited at +5° with variable initial amplitudes. It is imperative to excite at +5° (with tolerance of $\pm 1°$) instead of -85° because the elliptic mode originates only from the uncoupled mode with lower eigenfrequency, as is shown in Equation (4.9). The data are plotted on the x-axis based on the initial excited amplitude of each measurement, similar to the numerical experiments performed in Section 3.4. On the y-axis, the amplitude spectral densities (ASD) of the fundamental mode are plotted instead. To obtain ASD over the full frequency spectrum, two different 0.1s signals are then obtained for both the in-plane dominant signal and out-of-plane orthogonal signal, for when their amplitudes are the largest. For the dominant signal, this corresponds to the beginning of the signal. The ASD of these signals are then estimated using the following equation:

$$\mathrm{ASD} = \sqrt{\frac{|\mathrm{FFT}|^2 \Delta t^2}{T}}, \tag{4.10}$$

where FFT represents the Fourier transform of the signals using the fast Fourier-Transform algorithm, Δt the time resolution of the signal (1/16000s) and T the length of the signal (0.1s). Finally, the ASD of fundamental modes are extracted and plotted. The main advantage of using amplitude spectral density instead of simply a Fourier transform is to obtain results that are independent from influence of frequency resolution.
At low initial excited amplitude (i.e. <0.6mm), the dominant and orthogonal components are at least an order of magnitude apart from each other. This is because it is impossible to completely isolate the orthogonal mode. As such, the orthogonal mode is always very lightly excited. When the string is strongly excited (i.e. >1.3mm), orthogonal modes vibrate in the same order of magnitude as the initial dominant modes and confirm the findings where nonlinear exchange of energy between the

two polarisations could occur if the string is excited beyond a certain amplitude threshold. At moderate excitation (between 0.7mm and 1.0mm), an intermediate regime is observed where the difference in magnitude has reduced, suggesting that nonlinear exchange of energy took place but is not strong enough to develop fully. This observation could be due to the influence of string's damping. As such, it is difficult to recommend the usage of these data to obtain the detuning parameters as shown in Equation (4.9).

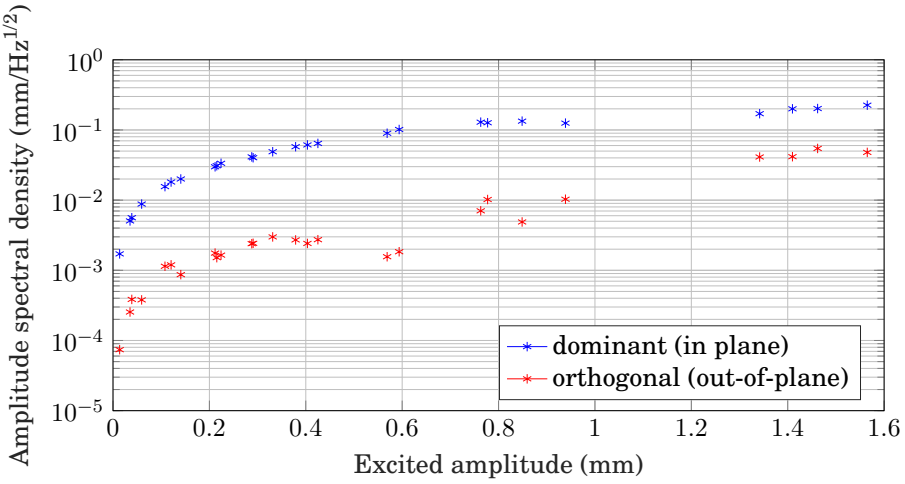

(a) Excitation at +5°.

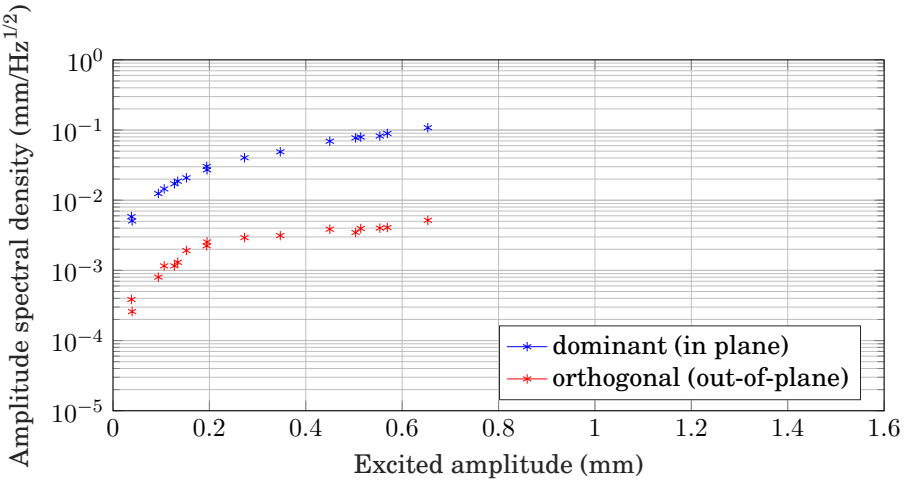

(b) Excitation at -85°.

Figure 4.11: Dominant and orthogonal amplitude spectral densities, plotted against increasing initial amplitudes.

To further validate the finding from multiple-scale analysis, the other polarisation is also excited with increasing initial amplitude. As has been discussed ear-

lier, from Equations (3.36) and (3.39), when one excites the other polarisation v with frequency ω_2 and amplitude $2b$, neither elliptic nor normal mode could occur. Figure 4.11b shows the amplitude of the fundamental frequency of both the dominant and orthogonal modes when the string is excited at -85° with variable initial amplitude. These amplitudes are extracted based on the same methods as in Figure 4.11a. Unfortunately, only data up to 0.7mm are shown. Higher excitation data for this polarisation is not available due to difficulty in exciting the string as it requires pulling the string with a downward motion at a slightly awkward angle. It also requires the use of multiple copper wire which further reduces the precision of the pulling action. As a result, several sets of data obtained for the higher excitation are not satisfactory as they are not excited within the tolerance of the angle and are thus not included.

4.5 Summary

In this chapter, experiments are conducted on a monochord test bench. An original method is proposed to identify the natural polarisation angles of the string's fundamental mode. The two identified polarisation angles are +5° and -85° respectively. The detuning between the two modes is found to be between 0.1Hz and 0.2Hz. The material and damping parameters of the string are also identified. Lastly, the findings from Chapter 3 is experimentally validated where double polarisation is observed once an amplitude threshold is exceeded.

Part II:

Bridge

> Your problem is to bridge the gap which exists between where you are now and the goal you intend to reach.
>
> Earl Nightingale

5

Modelling the coupling between the string and a lumped bridge

In most pianos, strings are strung over the bridge in a horizontal zig-zag configuration. Weinreich [27] noted that when a string is excited vertically by a hammer, energy in the vertical direction decays and is transferred through the bridge to the soundboard more rapidly compared to the energy in the horizontal direction. Consequently, despite being a weaker polarisation in the beginning, the horizontal vibration becomes dominant and provides the characteristic double decay of a piano. In Chabassier et al.'s work [63, 75], both the string and bridge are only allowed to move in the vertical plane. One of the main idea of the thesis is to extend the work by considering vibrations in the horizontal plane. The horizontal vibration of the string was studied in Part I and in this part, the focus is on the bridge and its coupling with the string.
In this chapter, a bottom-up approach is adopted where the coupling between the string and a lumped bridge is built from the simplest model to the most complicated in Section 5.1. As a reminder, the lumped bridge is considered as a set of oscillators in different directions that are all in the same point. A modal approach is taken where the eigenfrequencies of these models are determined in Section 5.2. For the simplest cases, the exact modal solutions are also proposed.

5.1 Derivation of coupled models of the string and a lumped bridge

To facilitate the identification of the various models of varying degree-of-freedom (DOF) used throughout the chapter, a unique naming scheme is proposed with a format of:

$$\mathrm{ST_1L_1R_1\text{-}BT_2L_2R_2} \tag{5.1}$$

where $\mathrm{T}_1, \mathrm{T}_2, \mathrm{L}_1, \mathrm{L}_2, \mathrm{R}_1$ and R_2 are integers between 0 and 2. The prefixes S and B indicate the string and bridge subsystem respectively and the three digits that

follow after the alphabet indicate the number of DOF in transverse motion, longitudinal motion and rotational motion respectively. For example, the most complex coupled model built in this thesis, S212-B213 would consider all 2 transverse, 1 longitudinal and 2 rotational displacements of the strings coupled to a bridge with freedom to move in all 3 translational and 3 rotational directions.

5.1.1 S100-B100: Linear wave equation coupled to a single-oscillator lumped bridge

The simplest possible case involving the string and bridge is when both of them only have a single displacement in the same direction, e.g. in the vertical direction. The string has its transverse displacement described by the linear wave equation (Equation (2.31)) while the bridge can be described as a simple harmonic oscillator with an external force from the string. If the string is attached to the bridge at $x = L$ as illustrated in Figure 5.1, the equation of the coupled system is thus [90]:

$$\rho A\ddot{u} - T_0 u'' = 0, \tag{5.2a}$$

$$M_1\ddot{\lambda}_1 + S_1\dot{\lambda}_1 + K_1\lambda_1 = -T_0 u'(L,t), \tag{5.2b}$$

where u is the transverse displacement of the string and λ_1 is the vertical displacement of the bridge oscillator. M_1, S_1 and K_1 are the bridge's mass, damping coefficient and stiffness coefficient respectively. The subscript 1 is appended to all the oscillators' terms so as to be consistent with models proposed later in this section.

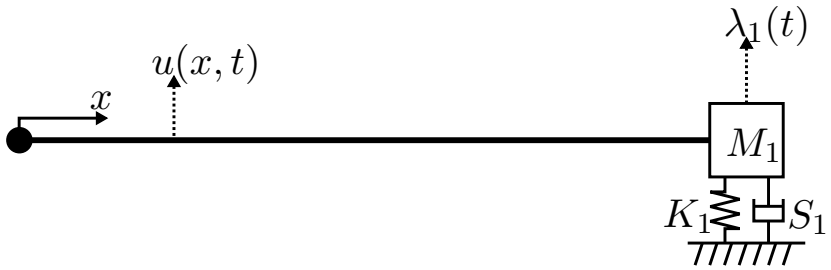

Figure 5.1: Illustration of the coupling between a transversely vibrating string and its bridge (S100-B100).

At $x = 0$, the string is fixed and thus its boundary condition can be written as:

$$u(0,t) = 0. \tag{5.3}$$

At $x = L$, the string is attached to the bridge. The boundary condition can be obtained by writing the energy equation of the system. To obtain an energy expression, the same approach as in Chapter 2 is used here as well. Equation (5.2a) is first multiplied by $\dot{u}$ and then integrated over the string length. For Equation (5.2b), it is only necessary to multiply the equation by $\dot{\lambda}_1$ and set $S_1 = 0$ for a conservative

system. The equations become

$$\frac{d}{dt}\left[\frac{1}{2}\int_0^L \rho A\left(\dot{u}\right)^2 + \frac{1}{2}\int_0^L T_0\left(u'\right)^2\right] = T_0\left[\dot{u}u'\right]_0^L, \tag{5.4a}$$

$$\frac{d}{dt}\left[\frac{1}{2}M_1(\dot{\lambda}_1)^2 + \frac{1}{2}K_1\left(\lambda_1\right)^2\right] = -T_0u'(L,t)\dot{\lambda}_1. \tag{5.4b}$$

It is useful to recall that in a string with both fixed ends, the boundary terms at the RHS of Equation (5.4a) go to zero due to the boundary conditions. In a coupled system, the sum of all the terms at the RHS of both equations (5.4a) and (5.4b) go to zero. This yields:

$$\dot{u}(L,t) = \dot{\lambda}_1, \tag{5.5}$$

which corresponds to the continuity of velocity and the boundary condition at $x = L$. The energy of this system can thus be written as:

$$\frac{d}{dt}\left[\mathrm{KE_s} + \mathrm{PE_s} + \mathrm{KE_b} + \mathrm{PE_b}\right] = 0, \tag{5.6}$$

where

$$\mathrm{KE_s} = \frac{1}{2}\int_0^L \rho A\left(\dot{u}\right)^2 \mathrm{d}x, \tag{5.7a}$$

$$\mathrm{PE_s} = \frac{1}{2}\int_0^L T_0\left(u'\right)^2 \mathrm{d}x, \tag{5.7b}$$

$$\mathrm{KE_b} = \frac{1}{2}M_1\dot{\lambda}_1^2, \tag{5.7c}$$

$$\mathrm{PE_b} = \frac{1}{2}K_1\lambda_1^2. \tag{5.7d}$$

5.1.2 S100-B101: Linear wave equation coupled to a two-oscillator lumped bridge

It is possible to extend the 1DOF bridge model slightly by including an offset between the attachment point of the string and the mass centre of the bridge. The offset forms a rigid link between the two points and allows the lumped bridge to rotate as it is subjected to a moment induced by the offset and string force. The system is illustrated in Figure 5.2 and its equation is written as:

$$\rho A\ddot{u} - T_0u'' = 0, \tag{5.8a}$$

$$M_1\ddot{\lambda}_1 + S_1\dot{\lambda}_1 + K_1\lambda_1 = -T_0u'(L,t), \tag{5.8b}$$

$$I_2\ddot{\theta}_2 + R_2\dot{\theta}_2 + J_2\theta_2 = -T_0u'(L,t)(-h_3). \tag{5.8c}$$

In Equation (5.8c), the offset h_3 is preceded with a negative sign. This is done so that it would be consistent with models that are derived subsequently. Compared to S100-B100, it is obvious that the same boundary condition remains at $x = 0$

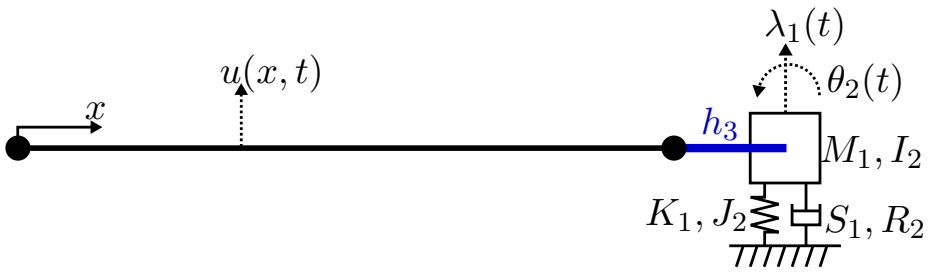

Figure 5.2: S100-B101 model

where $u(0,t) = 0$. At $x = L$, the boundary condition can be similarly obtained by writing the energy equations. Multiplying Equation (5.8a), (5.8b) and (5.8c) with $\dot{u}$, $\dot{\lambda}_1$ and $\dot{\theta}_2$ respectively, integrating only Equation (5.8a) over length L and setting $S_1 = R_2 = 0$, one would obtain:

$$\frac{d}{dt}\left[\frac{1}{2}\int_0^L \rho A\left(\dot{u}\right)^2 + \frac{1}{2}\int_0^L T_0\left(u'\right)^2\right] = T_0\left[\dot{u}u'\right]_0^L, \tag{5.9a}$$

$$\frac{d}{dt}\left[\frac{1}{2}M_1(\dot{\lambda}_1)^2 + \frac{1}{2}K_1(\lambda_1)^2\right] = -T_0u'(L,t)\dot{\lambda}_1, \tag{5.9b}$$

$$\frac{d}{dt}\left[\frac{1}{2}I_2(\dot{\theta}_2)^2 + \frac{1}{2}J_2(\theta_2)^2\right] = -T_0u'(L,t)(-h_3)\dot{\theta}_2. \tag{5.9c}$$

The LHS and RHS define the energy of the system and boundary terms respectively. For conservation of energy, the sum of all RHS terms equate to zero and this yields the boundary condition:

$$\dot{u}(L,t) = \dot{\lambda}_1 + (-h_3)\dot{\theta}_2, \tag{5.10}$$

and the energy of the system is the same as Equation (5.6) where $\mathrm{KE_s}$ and $\mathrm{PE_s}$ are as expressed in Equation (5.7) and:

$$\mathrm{KE_b} = \frac{1}{2}M_1{\dot{\lambda}_1}^2 + \frac{1}{2}I_2\dot{\theta}_2^2,$$
$$\mathrm{PE_b} = \frac{1}{2}K_1{\lambda_1}^2 + \frac{1}{2}J_2\theta_2^2.$$

5.1.3 S101-B101: Linear Timoshenko string equation coupled to a two-oscillator lumped bridge

Another factor that could induce a rotation in the lumped bridge is the rotation of the string cross-sectional area. The rotation of the string arises when the Timoshenko string is considered. Coupling a Timoshenko string model to a lumped bridge with one translational and rotational oscillator, the system as illustrated in

Figure 5.3 have the following equations of motion:

$$\rho A\ddot{u} - T_0 u'' + AG\kappa\frac{\partial}{\partial x}(\phi - u') = 0, \tag{5.12a}$$

$$\rho I\ddot{\phi} - EI\phi'' + AG\kappa(\phi - u') = 0, \tag{5.12b}$$

$$M_1\ddot{\lambda}_1 + S_1\dot{\lambda}_1 + K_1\lambda_1 = -T_0 u'(L,t) + AG\kappa\left[\phi(L,t) - u'(L,t)\right], \tag{5.12c}$$

$$I_2\ddot{\theta}_2 + R_2\dot{\theta}_2 + J_2\theta_2 = -EI\phi'(L,t) + \left[-T_0 u'(L,t) + AG\kappa(\phi(L,t) - u'(L,t))\right](-h_3), \tag{5.12d}$$

with boundary conditions:

$$u(0,t) = 0, \tag{5.13a}$$

$$\phi'(0,t) = 0 \tag{5.13b}$$

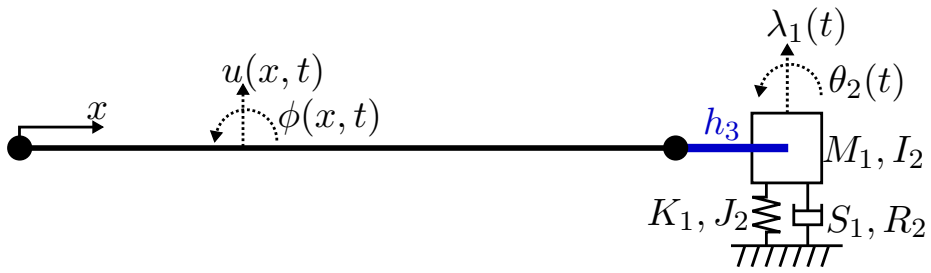

Figure 5.3: S101-B101 model.

Writing the same energy equation, one would obtain the boundary condition:

$$\dot{u}(L,t) = \dot{\lambda}_1 + (-h_3)\dot{\theta}_2, \tag{5.14a}$$

$$\dot{\phi}(L,t) = \dot{\theta}_2. \tag{5.14b}$$

The energy of the system has the same form as Equation (5.6) where

$$\mathrm{KE_s} = \frac{1}{2}\int_0^L \rho A\left(\dot{u}\right)^2 \mathrm{d}x + \frac{1}{2}\int_0^L \rho I\left(\dot{\phi}\right)^2 \mathrm{d}x, \tag{5.15a}$$

$$\mathrm{PE_s} = \frac{1}{2}\int_0^L T_0\left(u'\right)^2 \mathrm{d}x + \frac{1}{2}\int_0^L EI\left(\phi'\right)^2 \mathrm{d}x + \frac{1}{2}\int_0^L AG\kappa(\phi - u')^2 \mathrm{d}x, \tag{5.15b}$$

$$\mathrm{KE_b} = \frac{1}{2}M_1\dot{\lambda}_1{}^2 + \frac{1}{2}I_2\dot{\theta}_2^2, \tag{5.15c}$$

$$\mathrm{PE_b} = \frac{1}{2}K_1\lambda_1{}^2 + \frac{1}{2}J_2\theta_2^2. \tag{5.15d}$$

5.1.4 S200-B201: Non-planar linear string coupled to a three-oscillator lumped bridge

The coupling case can be extended to include non-planar motion of the string. The simplest non-planar string equation considered is a pair of uncoupled linear wave

equation that are coupled at $x = L$ to two translational oscillators respectively, forming effectively two uncoupled S100-B100 systems. Given an offset between the attachment point and mass centre of the bridge as is shown in Figure 5.4, the two uncoupled S100-B100 system can be coupled by the additional rotational oscillator with the following equations of motion:

$$\rho A\ddot{u} - T_0 u'' = 0, \tag{5.16a}$$
$$\rho A\ddot{v} - T_0 v'' = 0, \tag{5.16b}$$
$$M_1\ddot{\lambda}_1 + S_1\dot{\lambda}_1 + K_1\lambda_1 = -T_0 u'(L,t), \tag{5.16c}$$
$$M_2\ddot{\lambda}_2 + S_2\dot{\lambda}_2 + K_2\lambda_2 = -T_0 v'(L,t), \tag{5.16d}$$
$$I_3\ddot{\theta}_3 + R_3\dot{\theta}_3 + J_3\theta_3 = T_0 u'(L,t)h_2 - T_0 v'(L,t)h_1. \tag{5.16e}$$

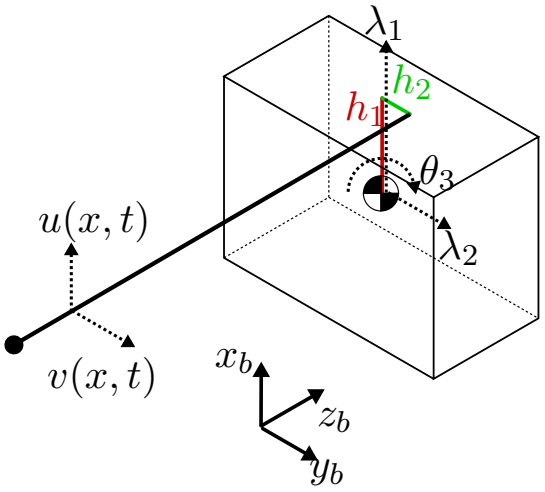

Figure 5.4: S200-B201 model.

To facilitate subsequent discussion, the coordinate system of the lumped bridge is finally introduced (see Figure 5.4) where the direction z_b coincides with the axial direction of the string, i.e. x.
Similar to earlier case, a fixed boundary condition can be imposed at $x = 0$ where:

$$u(0,t) = v(0,t) = 0. \tag{5.17}$$

The boundary condition at $x = L$ can be similarly recovered from the energy equations, and is written as:

$$\dot{u}(L,t) = \dot{\lambda}_1 - h_2\dot{\theta}_3, \tag{5.18a}$$
$$\dot{v}(L,t) = \dot{\lambda}_2 + h_1\dot{\theta}_3. \tag{5.18b}$$

For a conservative system where $S_1 = S_2 = R_3 = 0$, the energy equation retains the same form as Equation (5.6) where:

$$\mathrm{KE_s} = \frac{1}{2}\int_0^L \rho A \left(\dot{u}\right)^2 \mathrm{d}x + \frac{1}{2}\int_0^L \rho A \left(\dot{v}\right)^2 \mathrm{d}x, \tag{5.19a}$$

$$\mathrm{PE_s} = \frac{1}{2}\int_0^L T_0 \left(u'\right)^2 \mathrm{d}x + \frac{1}{2}\int_0^L T_0 \left(v'\right)^2 \mathrm{d}x, \tag{5.19b}$$

$$\mathrm{KE_b} = \frac{1}{2}M_2\dot{\lambda_2}^2 + \frac{1}{2}M_1\dot{\lambda_1}^2 + \frac{1}{2}I_3\dot{\theta}_3^2, \tag{5.19c}$$

$$\mathrm{PE_b} = \frac{1}{2}K_2\lambda_2^2 + \frac{1}{2}K_1\lambda_1^2 + \frac{1}{2}J_3\theta_3^2. \tag{5.19d}$$

5.1.5 S212-B213: 5DOF string coupled to a lumped bridge with three translational and three rotational oscillators

In earlier subsections, various models have been built to understand how the coupled string and bridge model varies in different situations. They can be summarised as follows:

- In Section 5.1.1, the simplest model is built with only one transverse displacement on the string and the bridge. The boundary condition is:

$$\dot{u}(L,t) = \dot{\lambda}_1.$$

- In Section 5.1.2, an offset between the string attachment point and centre of bridge mass is introduced. This induces a torque on the bridge and allows the bridge to rotate by an θ_2 about the y_b-axis. The boundary condition, after accounting for the offset h_3, is:

$$\dot{u}(L,t) = \dot{\lambda}_1 + (-h_3)\dot{\theta}_2.$$

- In 5.1.3, string vibrates transversely and also rotates along its cross-sectional area. The rotational displacement of the string is coupled to the rotational displacement of the bridge. The boundary conditions are:

$$\dot{u}(L,t) = \dot{\lambda} + (-h_3)\dot{\theta}_2,$$
$$\dot{\phi}(L,t) = \dot{\theta}.$$

- In Section 5.1.4, string vibrates in both transverse directions and each transverse displacement is coupled to a translational oscillator, essentially forming two S100-B100 systems. The two systems are coupled together by the rotational oscillator when there is an offset between the string attachment point and the bridge mass centre. The boundary conditions become:

$$\dot{u}(L,t) = \dot{\lambda_1} - h_2\dot{\theta}_3,$$
$$\dot{v}(L,t) = \dot{\lambda_2} + h_1\dot{\theta}_3.$$

Inferring from all of the results above, it is possible to build a model where the string is attached to a lumped bridge in 3D as is shown in Figure 5.5. The horizontal, vertical and longitudinal offsets are shown in blue, red and green lines respectively. The equations of motion, for a geometrically exact nonlinear stiff string equation coupled to the said lumped bridge, are:

$$\mathbf{M_s}\ddot{\mathbf{q}} - \frac{\partial}{\partial x}\left(\mathbf{A}\mathbf{q}' + \mathbf{B}\mathbf{q} + \nabla\mathbf{H}(\mathbf{q}')\right) + \mathbf{C}\mathbf{q} + \mathbf{B^T}\mathbf{q}' + \mathbf{Y}\dot{\mathbf{q}} - \mathbf{Z}\dot{\mathbf{q}}'' = 0, \tag{5.22a}$$

$$\mathbf{M_b}\ddot{\boldsymbol{\lambda}} + \mathbf{S_b}\dot{\boldsymbol{\lambda}} + \mathbf{K_b}\boldsymbol{\lambda} = -\mathcal{F}_\mathcal{B}, \tag{5.22b}$$

$$\mathbf{I_b}\ddot{\boldsymbol{\theta}} + \mathbf{R_b}\dot{\boldsymbol{\theta}} + \mathbf{J_b}\boldsymbol{\theta} = -\mathcal{M}_\mathcal{B} + \mathbf{h} \times (-\mathcal{F}_\mathcal{B}), \tag{5.22c}$$

where $\mathbf{q} = [u, v, w, \phi, \psi]$, and $\mathbf{M_s}$, $\mathbf{A}$, $\mathbf{B}$, $\mathbf{C}$, $\mathbf{Y}$, $\mathbf{Z}$ and $\nabla\mathbf{H}$ remain the same as described in the Chapter 2 (see Equation (2.50)). The other matrices are:

$$\mathbf{M_b} = \begin{bmatrix} M_1 & 0 & 0 \\ 0 & M_2 & 0 \\ 0 & 0 & M_3 \end{bmatrix}, \quad \mathbf{S_b} = \begin{bmatrix} S_1 & 0 & 0 \\ 0 & S_2 & 0 \\ 0 & 0 & S_3 \end{bmatrix}, \quad \mathbf{K_b} = \begin{bmatrix} K_1 & 0 & 0 \\ 0 & K_2 & 0 \\ 0 & 0 & K_3 \end{bmatrix}$$

$$\mathbf{I_b} = \begin{bmatrix} I_1 & 0 & 0 \\ 0 & I_2 & 0 \\ 0 & 0 & I_3 \end{bmatrix}, \quad \mathbf{R_b} = \begin{bmatrix} R_1 & 0 & 0 \\ 0 & R_2 & 0 \\ 0 & 0 & R_3 \end{bmatrix}, \quad \mathbf{J_b} = \begin{bmatrix} J_1 & 0 & 0 \\ 0 & J_2 & 0 \\ 0 & 0 & J_3 \end{bmatrix}, \quad \mathbf{h} = \begin{bmatrix} h_1 \\ h_2 \\ h_3 \end{bmatrix}, \tag{5.23}$$

and

$$\mathcal{F}_\mathcal{B} = [F_1 \quad F_2 \quad F_3]^T, \tag{5.24a}$$

$$\mathcal{M}_\mathcal{B} = [F_5 \quad F_4 \quad 0]^T, \tag{5.24b}$$

where

$$\mathbf{F} = [\mathbf{A}\mathbf{q}' + \mathbf{B}\mathbf{q} + \nabla\mathbf{H}(\mathbf{q}') + \mathbf{Z}\dot{\mathbf{q}}']_{x=L}. \tag{5.25}$$

Note that the third term of $\mathcal{M}_\mathcal{B}$ is zero. This is because the rotation about the string's axial axis is not considered and thus there is no corresponding moment for θ_3. The boundary condition at $x = 0$ is:

$$u(0,t) = v(0,t) = w(0,t) = 0, \tag{5.26a}$$

$$\phi'(0,t) = \psi'(0,t) = 0. \tag{5.26b}$$

It is possible to recover the boundary condition at $x = L$ by writing out the energy equation and equating all the boundary terms to zero. This would yield the

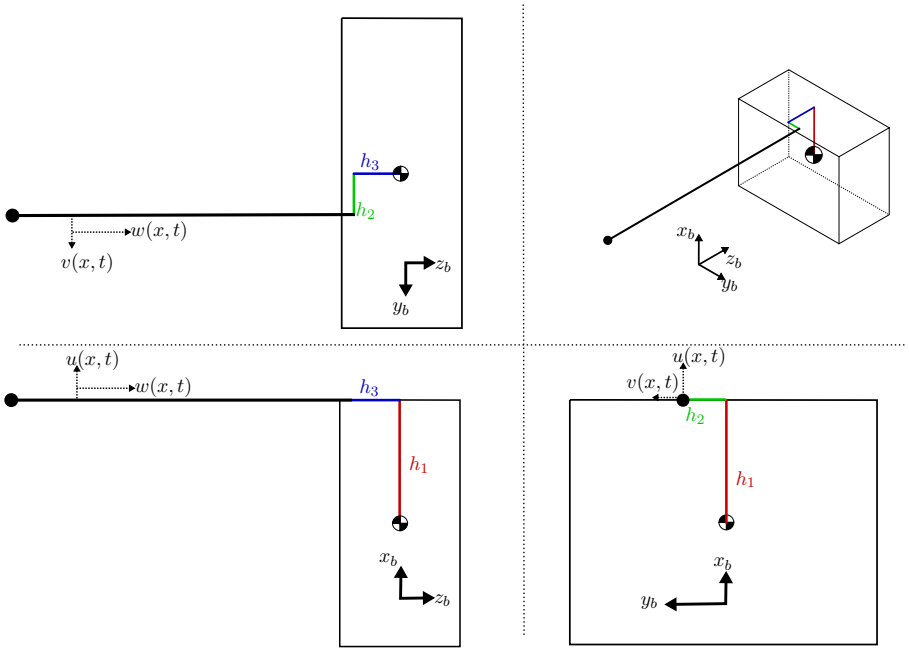

Figure 5.5: From top left, counter-clockwise: Top view, side view, front view and isometric overview. Isometric view is not to scale to the orthographic figures. Note that h_3 would have a negative value but h_1 and h_2 would be positive in this configuration.

following boundary conditions:

$$\dot{u}(L,t) = \dot{\lambda}_1 + h_3\dot{\theta}_2 - h_2\dot{\theta}_3, \tag{5.27a}$$
$$\dot{v}(L,t) = \dot{\lambda}_2 + h_1\dot{\theta}_3 - h_3\dot{\theta}_1, \tag{5.27b}$$
$$\dot{w}(L,t) = \dot{\lambda}_3 + h_2\dot{\theta}_1 - h_1\dot{\theta}_2, \tag{5.27c}$$
$$\dot{\phi}(L,t) = \dot{\theta}_2, \tag{5.27d}$$
$$\dot{\psi}(L,t) = \dot{\theta}_1. \tag{5.27e}$$

Equation (5.22) and boundary condition (5.27) are actually a general form for all the previous cases when different $\mathbf{h}$, $\mathbf{q}$, $\boldsymbol{\lambda}$ and $\boldsymbol{\theta}$ values are considered as summarised in Table 5.1.

Up until this point, all the models are derived based on the assumption that the coordinate axis of the string coincides with the coordinate axis of the bridge. However, it can be inferred from a piano that the string does not terminate at the bridge at such perfection but at certain incident angles. The incident angles α and β can be observed when seen from the side or from the top respectively as shown in Figure 5.6. Angle α is present in the piano so that the string could exert its downbearing forces to transmit its energy to the soundboard. Angle β can be most easily seen from triplets of string. At one end, all the strings terminate at the tuning pins

Table 5.1: Various cases with different $\mathbf{h}$, $\mathbf{q}$, $\boldsymbol{\lambda}$ and $\boldsymbol{\theta}$ values.

Case	$\mathbf{h}$	$\mathbf{q}$	$\boldsymbol{\lambda}$	$\boldsymbol{\theta}$
S100-B100	$[0, 0, 0]$	$[u, 0, 0, 0, 0]$	$[\lambda_1, 0, 0]$	$[0, 0, 0]$
S100-B101	$[0, 0, h_3]$	$[u, 0, 0, 0, 0]$	$[\lambda_1, 0, 0]$	$[0, \theta_2, 0]$
S101-B101	$[0, 0, h_3]$	$[u, 0, 0, \phi, 0]$	$[\lambda_1, 0, 0]$	$[0, \theta_2, 0]$
S200-B201	$[h_1, h_2, 0]$	$[u, v, 0, 0, 0]$	$[\lambda_1, \lambda_2, 0]$	$[0, 0, \theta_3]$
S212-B213	$[h_1, h_2, h_3]$	$[u, v, w, \phi, \psi]$	$[\lambda_1, \lambda_2, \lambda_3]$	$[\theta_1, \theta_2, \theta_3]$

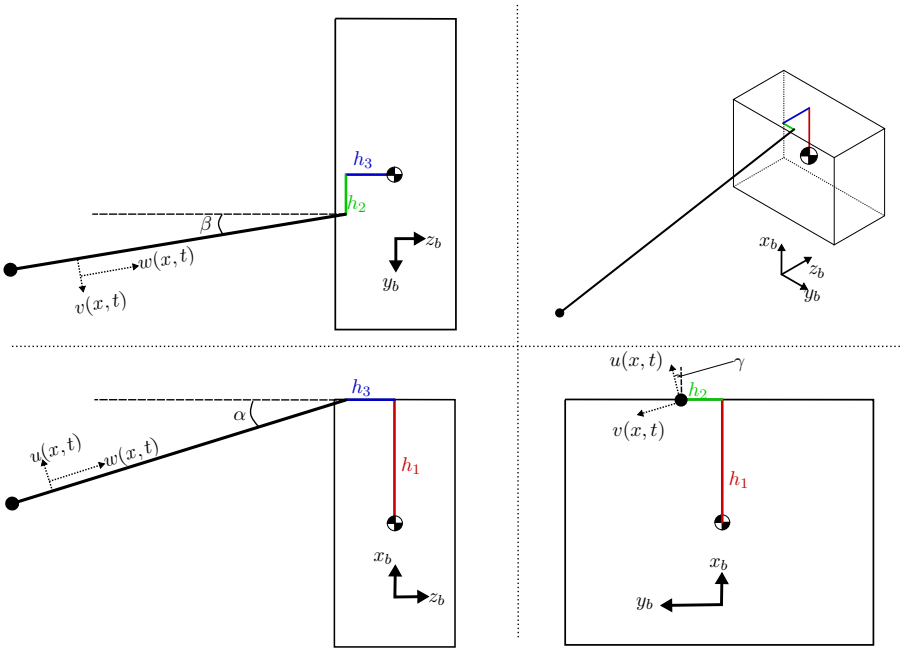

Figure 5.6: From top left, counter-clockwise: Top view, side view, front view and isometric overview. Isometric view is not to scale to the orthographic figures. Note that h_3 would have a negative value but h_1 and h_2 would be positive in this configuration.

fastened to the pinblock and each of these pins are closely placed together. As the strings terminate at the other end, i.e. at the bridge, each of the string terminates more widely apart from each other, and thus all the strings would have a slightly different incident angle β. Last but not least, from result obtained in Section 4.2, it is unlikely that the string natural polarisation would match the bridge horizontal and vertical axis perfectly. Thus, an angular offset of γ is needed to properly describe the interaction between these polarisations and the bridge.

Considering each offset angle individually, the transformation matrix, writing only

the translational displacements, are:

$$\begin{bmatrix}\dot{\lambda}_1\\ \dot{\lambda}_2\\ \dot{\lambda}_3\end{bmatrix} = \begin{bmatrix}\cos(\alpha) & 0 & \sin(\alpha)\\ 0 & 1 & 0\\ -\sin(\alpha) & 0 & \cos(\alpha)\end{bmatrix}\begin{bmatrix}\dot{u}\\ \dot{v}\\ \dot{w}\end{bmatrix}, \tag{5.28a}$$

$$\begin{bmatrix}\dot{\lambda}_1\\ \dot{\lambda}_2\\ \dot{\lambda}_3\end{bmatrix} = \begin{bmatrix}1 & 0 & 0\\ 0 & \cos(\beta) & -\sin(\beta)\\ 0 & \sin(\beta) & \cos(\beta)\end{bmatrix}\begin{bmatrix}\dot{u}\\ \dot{v}\\ \dot{w}\end{bmatrix}, \tag{5.28b}$$

$$\begin{bmatrix}\dot{\lambda}_1\\ \dot{\lambda}_2\\ \dot{\lambda}_3\end{bmatrix} = \begin{bmatrix}\cos(\gamma) & -\sin(\gamma) & 0\\ \sin(\gamma) & \cos(\gamma) & 0\\ 0 & 0 & 1\end{bmatrix}\begin{bmatrix}\dot{u}\\ \dot{v}\\ \dot{w}\end{bmatrix}. \tag{5.28c}$$

These transformations are first introduced by Euler with the angles α, β and γ known as the Euler angles. It is tempting to simply multiply all three transformation matrix together to describe the angular transformation from the string variables $[u, v, w]$ to the bridge variables $[\lambda_1, \lambda_2, \lambda_3]$ axis. However, since these matrix are not commutative, the order of multiplication of the transformation matrices would affect the final transformation matrix. For the context of the transformation from string axis to bridge axis, all angles ought to be transformed simultaneously. Describing the transformations via Euler angle formulations is unfortunately not sufficient as each of the transformation matrix do not share the same eigenvectors (in a 2D transformation, the rotation eigenvectors are $\pm i$).

In the context of this PhD work, the interest is on the double polarisation of the string. It can also be learned from Section 4.2 that γ can take any value as the string natural polarisation is not necessarily horizontal and vertical. It can also be deduced that α and β are usually very small and thus one can neglect their influence by setting the values to be zero. Thus, the full coupling conditions at $x = L$, after taking into account only the transformation angle γ is:

$$\underbrace{\begin{bmatrix}\cos(\gamma) & -\sin(\gamma) & 0 & -h_3 & 0\\ \sin(\gamma) & \cos(\gamma) & 0 & 0 & h_3\\ 0 & 0 & 1 & h_1\cos(\gamma) - h_2\sin(\gamma) & -h_2\cos(\gamma) - h_1\sin(\gamma)\\ 0 & 0 & 0 & \sin(\gamma) & \cos(\gamma)\\ 0 & 0 & 0 & \cos(\gamma) & -\sin(\gamma)\end{bmatrix}}_{\tau}\begin{bmatrix}\dot{u}\\ \dot{v}\\ \dot{w}\\ \dot{\phi}\\ \dot{\psi}\end{bmatrix} = \begin{bmatrix}\dot{\lambda}_1\\ \dot{\lambda}_2\\ \dot{\lambda}_3\\ \dot{\theta}_1\\ \dot{\theta}_2\end{bmatrix} + \begin{bmatrix}-h_2\dot{\theta}_3\\ h_1\dot{\theta}_3\\ 0\\ 0\\ 0\end{bmatrix}. \tag{5.29}$$

It is possible to redefine the equations of motion in Equation (5.22) to also consider the angle γ. For the lumped bridge, instead of expressing them as two vectors in $\boldsymbol{\lambda}$

and $\boldsymbol{\theta}$, one could express them in a vector $\boldsymbol{\Upsilon}$ and a variable θ_3:

$$\mathbf{M_s}\ddot{\mathbf{q}} - \frac{\partial}{\partial x}\left(\mathbf{A}\mathbf{q}' + \mathbf{B}\mathbf{q} + \nabla\mathbf{H}(\mathbf{q}')\right) + \mathbf{C}\mathbf{q} + \mathbf{B^T}\mathbf{q}' + \mathbf{Y}\dot{\mathbf{q}} - \mathbf{Z}\dot{\mathbf{q}}'' = 0, \tag{5.30a}$$

$$\mathcal{M}_b\ddot{\boldsymbol{\Upsilon}} + \mathcal{S}_b\dot{\boldsymbol{\Upsilon}} + \mathcal{K}_b\boldsymbol{\Upsilon} = -\mathbf{F}^{\mathcal{R}}, \tag{5.30b}$$

$$I_3\ddot{\theta}_3 + R_3\dot{\theta}_3 + J_3\theta_3 = F_1^{\mathcal{R}}h_2 - F_2^{\mathcal{R}}h_1, \tag{5.30c}$$

where:

$$\boldsymbol{\Upsilon} = [\lambda_1 \quad \lambda_2 \quad \lambda_3 \quad \theta_1 \quad \theta_2]^T, \tag{5.31}$$

and

$$\mathcal{M}_b = \begin{bmatrix} M_1 & 0 & 0 & 0 & 0 \\ 0 & M_2 & 0 & 0 & 0 \\ 0 & 0 & M_3 & 0 & 0 \\ 0 & 0 & 0 & I_1 & 0 \\ 0 & 0 & 0 & 0 & I_2 \end{bmatrix}, \quad \mathcal{S}_b = \begin{bmatrix} S_1 & 0 & 0 & 0 & 0 \\ 0 & S_2 & 0 & 0 & 0 \\ 0 & 0 & S_3 & 0 & 0 \\ 0 & 0 & 0 & R_1 & 0 \\ 0 & 0 & 0 & 0 & R_2 \end{bmatrix}, \quad \mathcal{K}_b = \begin{bmatrix} K_1 & 0 & 0 & 0 & 0 \\ 0 & K_2 & 0 & 0 & 0 \\ 0 & 0 & K_3 & 0 & 0 \\ 0 & 0 & 0 & J_1 & 0 \\ 0 & 0 & 0 & 0 & J_2 \end{bmatrix}. \tag{5.32}$$

$\mathbf{F}^{\mathcal{R}}$ is the resolved string forces or moments onto the bridge and is given by:

$$\mathbf{F}^{\mathcal{R}} = \boldsymbol{\tau}\mathbf{F} \tag{5.33}$$

The reason why the lumped bridge unknowns are rewritten from $\boldsymbol{\lambda}$ and $\boldsymbol{\theta}$ to $\boldsymbol{\Upsilon}$ and θ_3 is to facilitate the explanation of its numerical schemes in Chapter 6. In this form, θ_3 can be viewed as an extra oscillator in the coupled system between $\mathbf{q}$ and $\boldsymbol{\Upsilon}$.

The energy of the conservative system (i.e. $\mathbf{Y} = 0$, $\mathbf{Z} = 0$, $\mathcal{S}_b$ = 0, R_3 = 0) can be defined as:

$$\frac{d}{dt}\left[\mathrm{KE_s} + \mathrm{PE_s} + \mathrm{KE_b} + \mathrm{PE_b}\right] = 0, \tag{5.34}$$

where

$$\begin{aligned}
\mathrm{KE_s} &= \frac{1}{2}\int_0^L \mathbf{M}(\dot{\mathbf{q}})^2 \mathrm{d}x, \\
\mathrm{PE_s} &= \left(\frac{1}{2}\int_0^L \mathbf{A_r}(\mathbf{q}')^2 \mathrm{d}x + \frac{1}{2}\int_0^L \mathbf{C}(\mathbf{q})^2 \mathrm{d}x + \frac{1}{2}\int_0^L \mathbf{B}\mathbf{q}\mathbf{q}' \mathrm{d}x + \frac{1}{2}\int_0^L \mathbf{B^T}\mathbf{q}'\mathbf{q} \mathrm{d}x\right) \\
&\quad + \left(\frac{1}{2}\int_0^L \mathbf{A_t}(\mathbf{q}')^2 \mathrm{d}x + \frac{1}{2}\int_0^L \mathbf{H}(\mathbf{q}') \mathrm{d}x\right). \\
\mathrm{KE_b} &= \frac{1}{2}\mathcal{M}_b\dot{\boldsymbol{\Upsilon}}^2 + \frac{1}{2}I_3\dot{\theta}_3^2, \\
\mathrm{PE_b} &= \frac{1}{2}\mathcal{K}_b\boldsymbol{\Upsilon}^2 + \frac{1}{2}J_3\theta_3^2.
\end{aligned}$$

5.2 Eigenfrequencies and analysis

In this section, the eigenfrequency equations of the presented models in Section 5.1 are derived, and the modal solutions are obtained where practically possible. The idea of this section is to establish the changes brought by the addition of lumped bridge models to the vibrating strings on their eigenfrequencies. The eigenfrequencies obtained are also used to validate numerical schemes that are proposed in Section 6.1. To ease the derivation and analysis, only conservative models are considered, i.e. damping is ignored.

5.2.1 S100-B100: Linear wave equation coupled to a single-oscillator lumped bridge

Eigenfrequency and modal solution

Equation (5.2) can be solved completely by modal method where u and λ_1 can be defined as:

$$\begin{bmatrix} u(x,t) \\ \lambda_1(t) \end{bmatrix} = p(t) \begin{bmatrix} \xi(x) \\ \Lambda_1 \end{bmatrix}. \tag{5.36}$$

Following the steps in Section 2.3, one can recover the mode shape:

$$\xi(x) = \sin(k_T x), \tag{5.37}$$

where k_T is the wavenumber and is defined as:

$$k_T = \frac{\omega}{c_T} \qquad \text{with} \qquad c_T = \sqrt{\frac{T_0}{\rho A}}. \tag{5.38}$$

Applying the boundary condition (5.5), one can easily get:

$$\Lambda_1 = \xi(L). \tag{5.39}$$

Substituting these relations into Equation (5.2), one could reach:

$$-\omega^2 M_1 + K_1 = -T_0 \frac{\xi'(L)}{\xi(L)} \tag{5.40}$$

with can be further simplified into the eigenfrequency equation:

$$\tan\left(\frac{\omega_n L}{c_T}\right) = \frac{T_0 \omega_n}{c_T(M_1\omega_n^2 - K_1)}, \tag{5.41}$$

where the subscript n indicates that there are infinite numbers of eigenfrequencies ω_n that satisfies the equation. The corresponding eigenmodes for the string are thus:

$$\xi_n(x) = \sin(k_{T,n} x), \tag{5.42}$$

and the modal coordinates are

$$p_n(t) = P_n^1 \cos(\omega_n t) + P_n^2 \sin(\omega_n t). \tag{5.43}$$

Considering only the first N modes, solutions for u and λ can thus be written as:

$$u(x,t) = \sum_{n=1}^{N} \left[P_n^1 \cos(\omega_n t) + P_n^2 \sin(\omega_n t)\right] \sin(k_n x), \tag{5.44a}$$

$$\lambda_1(t) = \sum_{n=1}^{N} \left[P_n^1 \cos(\omega_n t) + P_n^2 \sin(\omega_n t)\right] \sin(k_n L). \tag{5.44b}$$

To solve for P_n^1 and P_n^2, initial conditions are needed. For this case, the initial conditions can be defined as:

$$u(x,0) = U_0, \tag{5.45a}$$

$$\lambda_1(0) = V_0, \tag{5.45b}$$

$$\dot{u}(x,0) = U_1, \tag{5.45c}$$

$$\dot{\lambda}_1(0) = B_1. \tag{5.45d}$$

This gives:

$$U_0 = \sum_{n=1}^{N} P_n^1 \sin(k_n x), \tag{5.46a}$$

$$B_0 = \sum_{n=1}^{N} P_n^1 \sin(k_n L), \tag{5.46b}$$

$$U_1 = \sum_{n=1}^{N} \omega_n P_n^2 \sin(k_n x), \tag{5.46c}$$

$$B_1 = \sum_{n=1}^{N} \omega_n P_n^2 \sin(k_n L). \tag{5.46d}$$

Multiplying the first and third equations with another eigenmode ξ_m and integrating over the string length, and multiplying second and fourth equations with $\xi_m(L)$,

they become:

$$\int_0^L U_0 \xi_m \mathrm{d}x = \sum_{n=1}^{N} P_n^1 \int_0^L \xi_n \xi_m \mathrm{d}x, \tag{5.47a}$$

$$B_0 \xi_m(L) = \sum_{n=1}^{N} P_n^1 \xi_n(L) \xi_m(L), \tag{5.47b}$$

$$\int_0^L U_1 \xi_m \mathrm{d}x = \sum_{n=1}^{N} P_n^2 \omega_n \int_0^L \xi_n \xi_m \mathrm{d}x, \tag{5.47c}$$

$$B_1 \xi_m(L) = \sum_{n=1}^{N} \omega_n P_n^2 \xi_n(L) \xi_m(L). \tag{5.47d}$$

To solve for P_n^1 and P_n^2, it is necessary to obtain the orthogonality properties of the modes so that $\int_0^L \xi_n \xi_m \mathrm{d}x$ and $\xi_n(L)\xi_m(L)$ are defined. Thus, using Equation (5.44), Equation (5.2a) can be written in ξ_n as:

$$-\omega_n^2 \rho A \xi_n - T_0 \xi_n'' = 0. \tag{5.48}$$

Multiplying Equation (5.48) with ξ_m and integrating over the length, one obtains:

$$-\omega_n^2 \int_0^L \rho A \xi_n \xi_m \mathrm{d}x - T_0 \int_0^L \xi_n'' \xi_m \mathrm{d}x = 0. \tag{5.49}$$

The equation can be decomposed by integration by part:

$$\omega_n^2 \int_0^L \rho A \xi_n \xi_m \mathrm{d}x - T_0 \int_0^L \xi_n' \xi_m' \mathrm{d}x = -T_0 [\xi_n' \xi_m]_0^L, \tag{5.50}$$

where the boundary term at RHS can be written as:

$$-T_0 \xi_n'(L)\xi_m(L) + \cancelto{0}{T_0 \xi_n'(0)\xi_m(0)} = (-\omega_n^2 M_1 + K_1)\xi_n(L)\xi_m(L), \tag{5.51}$$

as inferred from Equation (5.40). Rearranging, one can write:

$$\omega_n^2 \mathcal{P}_{\mathcal{M}} - \mathcal{P}_{\mathcal{T}} = 0, \tag{5.52}$$

where the following orthogonality products are introduced [90]:

$$\mathcal{P}_{\mathcal{M}}(m,n) = \int_0^L \rho A \xi_n \xi_m \mathrm{d}x + M_1 \xi_n(L)\xi_m(L), \tag{5.53a}$$

$$\mathcal{P}_{\mathcal{T}}(m,n) = \int_0^L T_0 \xi_n' \xi_m' \mathrm{d}x + K_1 \xi_n(L)\xi_m(L). \tag{5.53b}$$

Rewriting Equation (5.52) for index m, it can be shown that:

$$(\omega_n^2 - \omega_m^2)\mathcal{P}_{\mathcal{M}} = 0, \tag{5.54}$$

where for $n \neq m$,

$$\mathcal{P}_{\mathcal{M}} = 0, \tag{5.55}$$

and for $n = m$,

$$\mathcal{P}_{\mathcal{M}}(m) = \int_0^L \rho A {\xi_m}^2 \mathrm{d}x + M_1 {\xi_m}^2(L). \tag{5.56}$$

This shows that the modes are orthogonal with respect to the mass. Similarly, rewriting Equation (5.52) in index m can also yield:

$$(\omega_m^2 - \omega_n^2)\mathcal{P}_{\mathcal{T}} = 0, \tag{5.57}$$

where for $n \neq m$,

$$\mathcal{P}_{\mathcal{T}} = 0, \tag{5.58}$$

and for $n = m$,

$$\mathcal{P}_{\mathcal{T}}(m) = \int_0^L T_0 {\xi_m'}^2 \mathrm{d}x + K_1 {\xi_m}^2(L). \tag{5.59}$$

This shows that the modes are orthogonal to each other with respect to stiffness. With these orthogonality relations, it is now possible to solve Equation (5.47). Multiplying Equation (5.47a) with ρA and Equation (5.47b) with M and summing them together, it yields:

$$\rho A \int_0^L U_0 \xi_m(x) \mathrm{d}x + M_1 B_0 \xi_m(L) = P_m^1 \left[\int_0^L \rho A {\xi_m}^2 \mathrm{d}x + M_1 {\xi_m}^2(L) \right], \tag{5.60}$$

where P_m^1 can be solved, for each index m, by:

$$P_m^1 = \frac{\rho A \int_0^L U_0 \xi_m(x) \mathrm{d}x + M_1 B_0 \xi_m(L)}{\mathcal{P}_{\mathcal{M}}}. \tag{5.61}$$

Similarly, P_m^2 can be solved by:

$$\omega_m P_m^2 = \frac{\rho A \int_0^L U_1 \xi_m(x) \mathrm{d}x + M_1 B_1 \xi_m(L)}{\mathcal{P}_{\mathcal{M}}}. \tag{5.62}$$

Substituting both Equations (5.61) and (5.62) into Equation (5.44), one could thus obtain the modal solutions of the S100-B100 system.

Analysis

It is useful to recall that for a fixed-fixed string, the eigenfrequencies can be found from:

$$\sin\left(\frac{\omega_n L}{c_t}\right) = 0, \tag{5.63}$$

which gives:

$$\omega_n = \frac{n\pi c_T}{L}. \tag{5.64}$$

Equation (5.64) is also recoverable if RHS of Equation (5.41) equals to zero, i.e.:

$$\tan\left(\frac{\omega_n L}{c_T}\right) = 0. \tag{5.65}$$

The case in which this happens is when either K_1 or M_1 is infinitely large. Intuitively, if a string is attached to an extremely stiff or massive end, that end could be considered fixed.
Before proceeding further, it is useful to first define the fundamental frequency of the string in a fixed-fixed case, f_s:

$$f_s = \frac{1}{2L}\sqrt{\frac{T_0}{\rho A}}. \tag{5.66}$$

In the coupled system, the RHS of Equation (5.41) is not zero. However, since a tangent function always have asymptotes, it can be inferred that *between the asymptotes, there will always be a solution to Equation* (5.41). In this case, a solution is present between $(n-1/2)f_s$ and $(n+1/2)f_s$.
A sample case is presented in Figure 5.7 with the used parameters shown in Table 5.2. The values of M_1 and K_1 may not necessarily be realistic but are exaggerated to demonstrate their influences to the system. When $M_1 = 0$, the RHS of Equation (5.41) becomes $-\omega c_T T_0/K_1$ and this is plotted as the green line in Figure 5.7 where the x-axis is defined in multiples of f_s. As the green line intersects the tangent curves below the x-axis, it will always reduce the eigenfrequencies as compared to a fixed-fixed case. Physically, introducing a finite stiffness essentially introduces more flexibility and the whole system becomes less stiff, thus reduces the eigenfrequencies. It can be verified that as K_1 increases, the slope becomes less steep and the intersection occurs closer to $\frac{n\pi c_T}{L}$ and as K approaches infinity, $-\omega c_T T_0/K_1$ tends to zero and Equation (5.65) is recovered.

Table 5.2: Physical parameters used for the analysis of S100-B100 system.

Parameter	Value
T_0	880 N
ρ	7,850 kg.m^{-3}
A	9.7993.10^{-7} m^2
M_1	0.001 kg
K_1	4,500 kg.s^{-2}
L	1.05 m

When $K_1 = 0$, the RHS of Equation (5.41) becomes $\rho A c_T/M_1\omega$ and this is represented as the red curve in Figure 5.7. Interestingly, when a mass is introduced to a system, a new eigenfrequency is found between 0 and $\frac{1}{2}\frac{\pi c_T}{L}$ as the red curve first intersects it. At higher frequencies, the curve will always intersect above the x-axis and thus introducing a finite mass increases the eigenfrequencies when compared

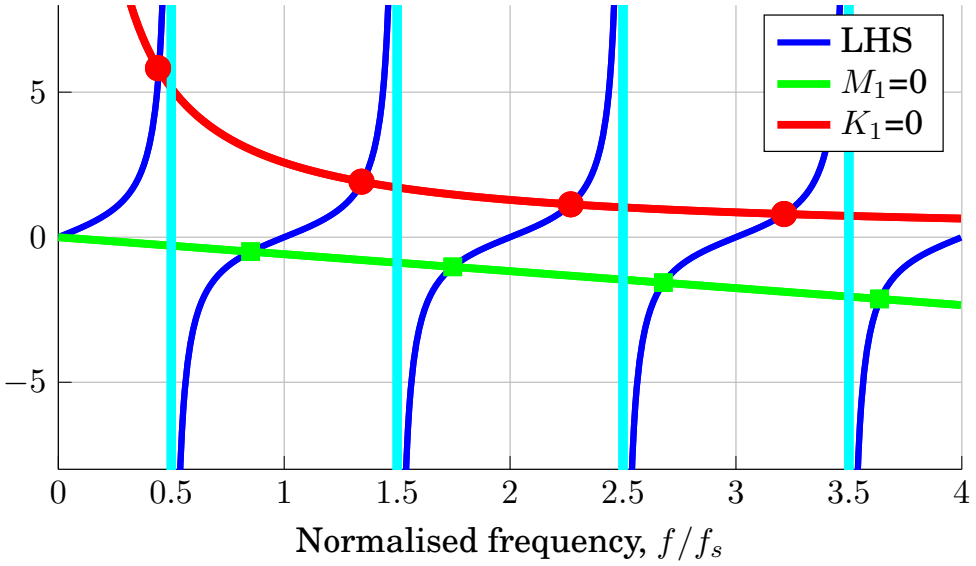

Figure 5.7: Eigenfrequency analysis. Blue represents the tangent function at LHS of Equation (5.41) and green represents the RHS when $M = 0$ and red for $K = 0$. The cyan line is the asymptote of the tangent function.

to a fixed-fixed case. As M_1 approaches infinity, $\rho A c_T / M_1 \omega$ tends to zero and Equation (5.65) is recovered.
Lastly, for an oscillator with a finite mass and stiffness, i.e. $K_1 \neq 0, M_1 \neq 0$, the RHS becomes a rational function with a vertical asymptote at $f = f_*$ where

$$f_* = \frac{1}{2\pi}\sqrt{\frac{K_1}{M_1}}, \tag{5.67}$$

is the eigenfrequency of the harmonic oscillator as shown in Figure 5.8 where $f_* = 2.1 f_s$. The addition of an oscillator brings the following changes:

1. All eigenfrequencies of the string that are smaller than f_* are reduced.
2. All eigenfrequencies of the string that are larger than f_* are increased.
3. For sufficiently large n, the RHS of Equation (5.41) tends to zero and the eigenfrequencies converge to the eigenfrequencies of a fixed-fixed string.
4. For any n, if f_* falls between $(n - 1/2)f_s$ and $(n + 1/2)f_s$, there exists an additional eigenfrequency in that range.
5. If f_* falls exactly on $(n - 1/2)f_s$ or $(n + 1/2)f_s$, this additional eigenfrequency then would not exist.

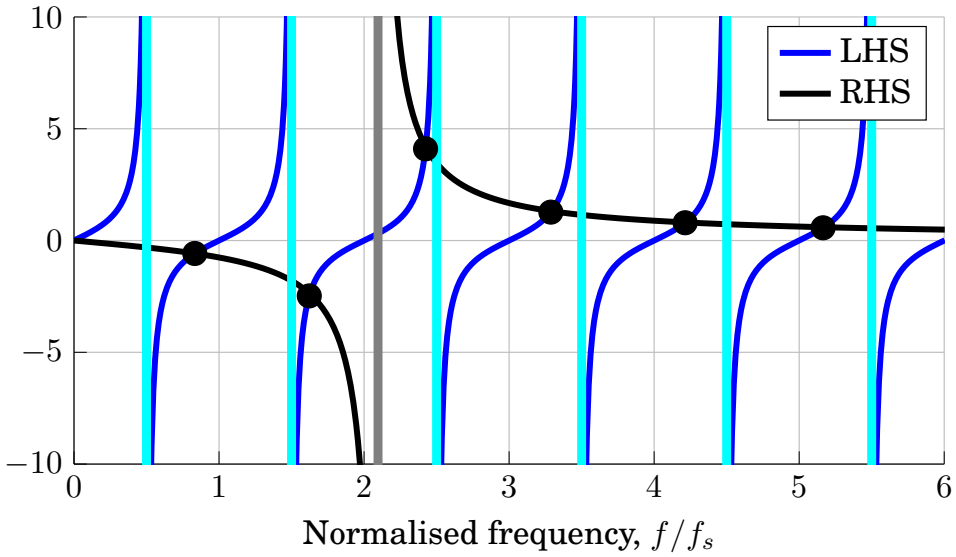

Figure 5.8: Graphical plot for Equation (5.41) using parameters from Table 5.2. Blue and black curves represent the LHS and RHS respectively. The intersections between the two curves are solutions to Equation (5.41), marked with black circles. Asymptotes of LHS and RHS are shown as cyan and grey lines respectively.

Using the same parameter in Table 5.2 except that M_1 and K_1 are both increased by a factor of 10 to 0.01kg and 45,000kg/s^2 respectively, the graphical plot for the LHS and RHS of Equation (5.41) is shown in Figure 5.9. Since both M_1 and K_1 are increased by the same factor, the oscillator frequency does not change. Comparing it to Figure 5.8, one could see that the eigenfrequencies of the system are much closer to multiples of the string's frequency, f_s. This is because as the oscillator becomes more massive and stiff, it resembles more closely as a fixed boundary condition. As such, the perturbation introduced by the oscillator onto the string's eigenfrequencies becomes less significant.

5.2.2 S100-B101: Linear wave equation coupled to a two-oscillator lumped bridge

Eigenfrequency and modal solution

Defining that:

$$\begin{bmatrix} u \\ \lambda_1 \\ \theta_2 \end{bmatrix} = p(t) \begin{bmatrix} \xi(x) \\ \Lambda_1 \\ \Theta_2 \end{bmatrix}, \tag{5.68}$$

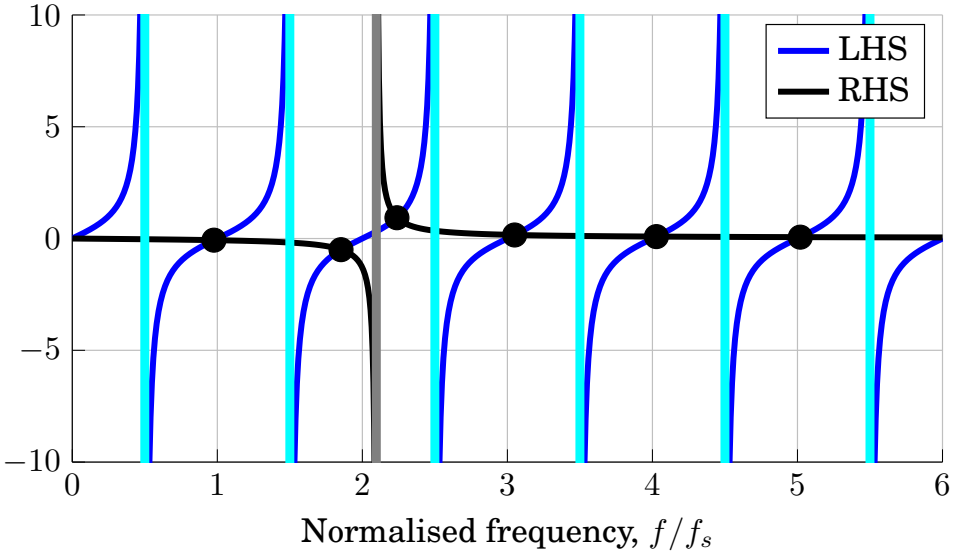

Figure 5.9: Graphical plot for Equation (5.41) using parameters from Table 5.2 except that M_1 and K_1 are 0.01kg and 45,000kg/s^2 respectively. Blue and black curves represent the LHS and RHS respectively. The intersections between the two curves are solutions to Equation (5.41), marked with black circles. Asymptotes of LHS and RHS are shown as cyan and grey lines respectively.

one can follow the same strategy as in Section 5.2.1 and obtain the eigenfrequency equation for Equation (5.8):

$$\tan\left(\frac{\omega_n L}{c_T}\right) = \frac{T_0 \omega_n}{c_T}\left(\frac{1}{\omega_n^2 M_1 - K_1} + \frac{{h_3}^2}{\omega_n^2 I_2 - J_2}\right), \tag{5.69}$$

where the subscript n indicates that there is an infinite number of solutions to the equation, just like Equation (5.41). The expressions for Λ_1 and Θ_2 are:

$$\Lambda_1 = \frac{-T_0 \xi'(L)}{-\omega^2 M_1 + K_1}, \tag{5.70a}$$

$$\Theta_2 = \frac{-h_3 T_0 \xi'(L)}{-\omega^2 I_2 + J_2}, \tag{5.70b}$$

$$\xi(L) = \Lambda_1 + h_3 \Theta_2. \tag{5.70c}$$

Similarly, one would obtain the solutions for u, λ_1 and θ_2 in the following form:

$$u(x,t) = \sum_{n=1}^{N} \left[P_n^1 \cos(\omega_n t) + P_n^2 \sin(\omega_n t)\right] \sin(k_n x), \tag{5.71a}$$

$$\lambda_1(t) = \sum_{n=1}^{N} \left[P_n^1 \cos(\omega_n t) + P_n^2 \sin(\omega_n t)\right] \frac{-T_0 k_n \cos(k_n L)}{-\omega_n^2 M_1 + K_1}, \tag{5.71b}$$

$$\theta_2(t) = \sum_{n=1}^{N} \left[P_n^1 \cos(\omega_n t) + P_n^2 \sin(\omega_n t)\right] \frac{-h_3 T_0 k_n \cos(k_n L)}{-\omega_n^2 I_2 + J_2}. \tag{5.71c}$$

Compared to Equation (5.44), the expression of u is the same but it differs for λ_1. This is because the boundary condition has changed from $u(L,t) = \lambda_1(t)$ to $u(L,t) = \lambda_1(t) + h_3\theta_2(t)$. To solve for P_n^1 and P_n^2, initial conditions are needed. For this case, the initial conditions are:

$$u(x,0) = U_0, \tag{5.72a}$$

$$\lambda_1(0) = B_1^0, \tag{5.72b}$$

$$\theta_2(0) = \Theta_2^0, \tag{5.72c}$$

$$\dot{u}(x,0) = U_1, \tag{5.72d}$$

$$\dot{\lambda}_1(0) = B_1^1, \tag{5.72e}$$

$$\dot{\theta}_2(0) = \Theta_2^1. \tag{5.72f}$$

The approach is essentially the same as in previous section. However, it is necessary to obtain the expression of $\mathcal{P}_\mathcal{T}$ and $\mathcal{P}_\mathcal{M}$. Rewriting Equation (5.50)

$$\omega_n^2 \int_0^L \rho A \xi_n \xi_m \mathrm{d}x - T_0 \int_0^L \xi_n' \xi_m' \mathrm{d}x = -T_0 [\xi_n' \xi_m]_0^L, \tag{5.73}$$

and rewriting Equation (5.70c) into an indexable form such that:

$$\xi_m(L) = \Lambda_{1,m} + h_3 \Theta_{2,m}, \tag{5.74}$$

the boundary terms on the RHS then become:

$$T_0 \xi_n'(L)\xi_m(L) - \cancelto{0}{T_0 \xi_n'(0)\xi_m(0)} = T_0 \xi_n'(L)\Lambda_{1,m} + h_3 T_0 \xi_n'(L)\Theta_{2,m}. \tag{5.75}$$

From Equation (5.70a) and (5.70b), Equation (5.75) becomes:

$$\begin{aligned} &T_0 \xi_n'(L)\Lambda_{1,m} + h_3 T_0 \xi_n'(L)\Theta_{2,m} \\ &\qquad = \left[\Lambda_{1,n}(-\omega_n^2 M_1 + K_1)\right] \Lambda_{1,m} + \left[\Theta_{2,n}(-\omega_n^2 I_2 + J_2)\right] \Theta_{2,m}. \end{aligned} \tag{5.76}$$

Equation (5.73) can then be written as:

$$\omega_n^2 \mathcal{P}_\mathcal{M} = \mathcal{P}_\mathcal{T}, \tag{5.77}$$

where

$$\mathcal{P}_{\mathcal{M}}(m,n) = \int_0^L \rho A \xi_n \xi_m \mathrm{d}x + M_2 \xi_n(L)\xi_m(L) + I_2 \Theta_{2,m}\Theta_{2,n}, \tag{5.78a}$$

$$\mathcal{P}_{\mathcal{T}}(m,n) = \int_0^L T_0 \xi_n' \xi_m' \mathrm{d}x + K_1 \xi_n(L)\xi_m(L) + J_2 \Theta_{2,m}\Theta_{2,n}. \tag{5.78b}$$

Since Equation (5.77) is the same as Equation (5.52), similar orthogonality relations can be obtained, such that for $n = m$:

$$\mathcal{P}_{\mathcal{M}}(m) = \int_0^L \rho A {\xi_m}^2 \mathrm{d}x + M_1 {\Lambda_{1,m}}^2 + I_2 {\Theta_{2,m}}^2, \tag{5.79a}$$

$$\mathcal{P}_{\mathcal{T}}(m) = \int_0^L T_0 {\xi_m'}^2 \mathrm{d}x + K_1 {\Lambda_{1,m}}^2 + J_2 {\Theta_{2,m}}^2, \tag{5.79b}$$

and for $n \neq m$:

$$\mathcal{P}_{\mathcal{M}} = 0, \tag{5.80a}$$

$$\mathcal{P}_{\mathcal{T}} = 0. \tag{5.80b}$$

These relations are then applied to obtain P_m^1 and P_m^2, where:

$$P_m^1 = \frac{\rho A \int_0^L U_0 \xi_m(x)\mathrm{d}x + M_1 B_1^0 \Lambda_{1,m} + I_2 \Theta_2^0 \Theta_{2,m}}{\mathcal{P}_{\mathcal{M}}}, \tag{5.81a}$$

$$\omega_m P_m^2 = \frac{\rho A \int_0^L U_1 \xi_m(x)\mathrm{d}x + M_1 B_1^1 \Lambda_{1,m} + I_2 \Theta_2^1 \Theta_{2,m}}{\mathcal{P}_{\mathcal{M}}}. \tag{5.81b}$$

Equation (5.71) is thus fully defined with the eigenfrequencies given by Equation (5.69).

Analysis

Qualitatively, the addition of the rotational oscillator affects the eigenfrequencies in a similar manner as with the translational oscillator. For convenience, one can define the eigenfrequency of the rotational oscillator as:

$$f_*^r = \frac{1}{2\pi}\sqrt{\frac{I_2}{J_2}}. \tag{5.82}$$

As shown in Figure 5.10 with $f_* = 2.1 f_s$ and $f_*^r = 3.8 f_s$, the addition of rotational oscillator brings the following changes:

1. There exists only one solution bounded between $(n - 1/2)f_s$ and $(n + 1/2)f_s$ except when the "oscillator frequencies" f_* or f_*^r falls in the same range. In that case, there will be three solutions if both f_* and f_*^r fall in the same range, or two if they are not in the same range.

2. If the string frequencies are less than the smallest frequency between the two oscillators, they will be reduced.

3. If the string frequencies are greater than the largest frequency between the two oscillators, they will be increased.

4. If the string frequencies are between the two oscillator frequencies, it may increase or decrease when compared to the fixed-fixed case.

5. If f_*^r falls on exactly $(n-1/2)f_s$ or $(n+1/2)f_s$ or on f_*, there will not be any additional eigenfrequency.

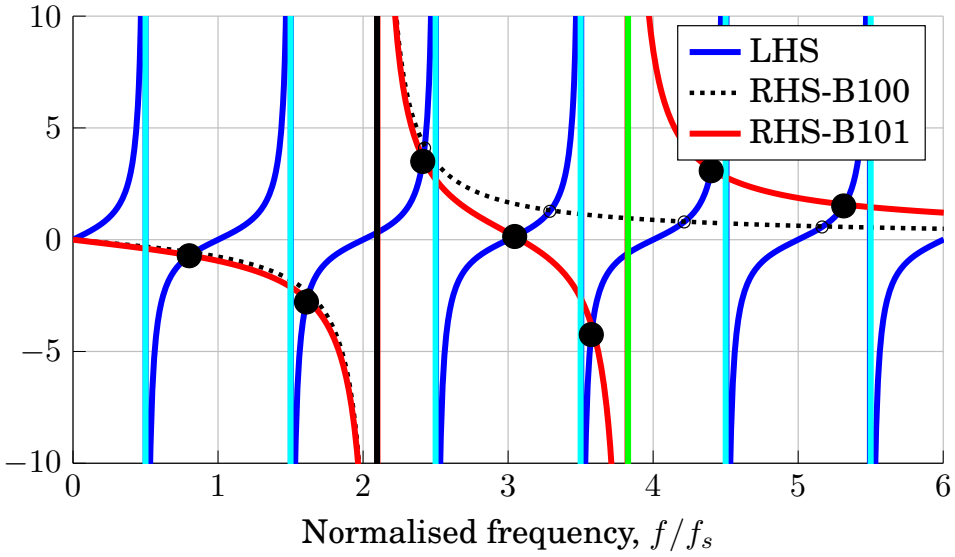

Figure 5.10: Graphical plot for Equation (5.69). The LHS and RHS (labeled as RHS-B101) are represented by blue and red curves respectively. The solutions of Equation (5.69) are marked as black circles. The black curve of Figure 5.8 (i.e. the RHS of Equation (5.41)) is also shown as dotted black curves (labeled RHS-B100) to highlight the effect of the additional rotational oscillator.. The paramaters are outlined in Table 5.3 as Case 1.

Figure 5.11 shows an example of when there are two oscillators' frequencies bounded within $(n-1/2)f_s$ and $(n+1/2)f_s$. The parameters of this particular example are presented as Case 2 in Table 5.2. Between $1.5f_s$ and $2.5f_s$, there are now three solutions to Equation (5.69). One of it belongs originally to the string, and the other two are the oscillators. The other features of such system are also retained outside of that range, i.e. string frequencies reduce if they are smaller than the oscillators' frequencies and increase if larger.

Table 5.3: Physical parameters used for the analysis of S100-B101 system.

Parameter	Case 1	Case 2
T_0	880 N	
ρ	7,850 kg.m^{-3}	
A	9.7993.10^{-7} m^2	
M_1	0.001 kg	
K_1	4,500 kg.s^{-2}	
L	1.05 m	
I_2	0.001 kg.m^2	
J_2	15,000 kgm^2.s^{-2}	3,000 kgm^2.s^{-2}
h_3	1m	

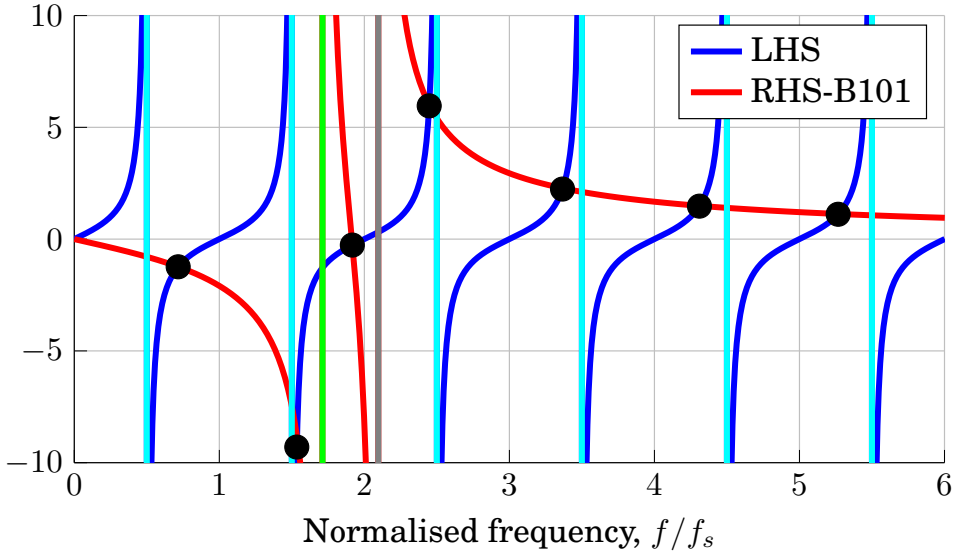

Figure 5.11: Graphical plot for Equation (5.69) for a special case when $J_2 = 3,000$ kgm^2. The LHS and RHS are represented by blue and red curves respectively. The solutions of Equation (5.69) are marked as black circles. As can be seen, there are three solutions bounded between $1.5f_s$ and $2.5f_s$. The parameters are outlined in Table 5.3 as Case 2.

5.2.3 S200-B201: Non-planar linear string coupled to a three-oscillator lumped bridge

The S200-B201 is perhaps the most interesting case to be investigated as it involves the two polarisations, one of the main focuses of the thesis.

Eigenfrequencies

The general solutions of the system can be written as:

$$\begin{bmatrix} u \\ v \\ \lambda_1 \\ \lambda_2 \\ \theta_3 \end{bmatrix} = q(t) \begin{bmatrix} \xi_u(x) \\ \xi_v(x) \\ \Lambda_1 \\ \Lambda_3 \\ \Theta \end{bmatrix}, \tag{5.83}$$

where

$$\xi_u(x) = \sin(k_u x), \tag{5.84a}$$
$$\xi_v(x) = \Xi \sin(k_v x), \tag{5.84b}$$

after applying the boundary condition at $x = 0$. For ξ_u, the constant term is omitted. Instead, a constant Ξ is defined to relate the amplitude between ξ_u and ξ_v that can be complex to include any phase. The use of two different mode shapes for the two different polarisations result in two different wavenumbers k_u and k_v related to the angular frequencies ω by the following dispersion relations:

$$c_{T,u} = \frac{\omega}{k_u} = \sqrt{\frac{T_0}{\rho A}}, \tag{5.85a}$$
$$c_{T,v} = \frac{\omega}{k_v} = \sqrt{\frac{T_0}{\tilde{\rho} A}}, \tag{5.85b}$$

where the v polarisation is prescribed with a slightly different density $\tilde{\rho}$ which results in different velocity compared to the u polarisation.
Substituting Equation (5.83) into (5.16c), (5.16d), (5.16e) and (5.18), it yields:

$$\Lambda_1 = -\frac{T_0 \cos(k_u L) k_u}{K_1 - \omega^2 M_1}, \tag{5.86a}$$
$$\Lambda_2^* = -\frac{T_0 \cos(k_v L) k_v}{K_2 - \omega^2 M_2}, \tag{5.86b}$$
$$(-\omega^2 I_3 + J_3) = \Lambda_1 (K_1 - \omega^2 M_1) h_2 - \Lambda_2^* (K_2 - \omega^2 M_2) h_1, \tag{5.86c}$$
$$\Theta = \frac{\sin(k_u L) - \Lambda_1}{h_2}, \tag{5.86d}$$
$$\Xi = \frac{h_1}{h_2} \frac{\sin(k_u L - \Lambda_1)}{\Lambda_2^* - \sin(k_v L)}, \tag{5.86e}$$

where:

$$\Lambda_2^* = \frac{\Lambda_2}{\Xi}. \tag{5.87}$$

The introduction of Λ_2^* is essentially for simplification purposes as the derivation would otherwise be more tedious. It is possible to substitute Equation (5.86a), (5.86b),

(5.86d) and (5.86e) into (5.86c), and by further simplification and rearranging, to obtain the eigenfrequency equation:

$$1 = -h_2^2 \frac{T_0 k_{u,n}}{(J_3 - \omega_n^2 I_3)\mathcal{F}(k_{u,n})} - h_1^2 \frac{T_0 k_{v,n}}{(J_3 - \omega_n^2 I_3)\mathcal{G}(k_{v,n})}, \tag{5.88}$$

where:

$$\mathcal{F}(k_{u,n}) = \tan(k_{u,n}L) + \frac{T_0 k_{u,n}}{K_1 - \omega_n^2 M_1}, \tag{5.89a}$$

$$\mathcal{G}(k_{v,n}) = \tan(k_{v,n}L) + \frac{T_0 k_{v,n}}{K_2 - \omega_n^2 M_2}. \tag{5.89b}$$

The addition of the subscript n indicates that there is an infinite number of solutions for Equation (5.88). Setting either h_1 or h_2 to zero yields two decoupled systems, each representing a case of S100-B100 (see Equation (5.41)) and S100-B101 (see Equation (5.69)). For instance, if $h_2 = 0$, one could recover the two equations:

$$\tan\left(\frac{\omega_n L}{c_{T,u}}\right) = \frac{T_0 \omega_n}{c_{T,u}(M_1\omega_n^2 - K_1)}, \tag{5.90a}$$

$$\tan\left(\frac{\omega_n L}{c_{T,v}}\right) = \frac{T_0 \omega_n}{c_{T,v}} \left(\frac{1}{\omega_n^2 M_2 - K_2} + \frac{{h_1}^2}{\omega_n^2 I_3 - J_3}\right), \tag{5.90b}$$

and if $h_1 = 0$:

$$\tan\left(\frac{\omega_n L}{c_{T,v}}\right) = \frac{T_0 \omega_n}{c_{T,v}(M_2\omega_n^2 - K_2)}, \tag{5.91a}$$

$$\tan\left(\frac{\omega_n L}{c_{T,u}}\right) = \frac{T_0 \omega_n}{c_{T,u}} \left(\frac{1}{\omega_n^2 M_1 - K_1} + \frac{{h_2}^2}{\omega_n^2 I_3 - J_3}\right). \tag{5.91b}$$

Analysis

In this section, as the system becomes more complex, instead of presenting graphical plots (such as Figure 5.8), the solutions for the eigenfrequencies are presented in number lines instead. To bridge the differences between the two types of presentation, the example of Figure 5.11 is repeated in Figure 5.12 where both methods are shown top and bottom. For the number line, from left to right, each increasing number represents a multiple of f_s, the string eigenfrequencies. The eigenfrequencies will be marked using black circular markers on the line. Notable other features like the oscillator frequencies will be shown as well in green and gray lines.
Due to the complexity of the system, five different cases of increasing complexities are analysed.

I. Both polarisations have the same eigenfrequencies and both the translational oscillators have the same parameters. Essentially, this is a pair of identical S100-B100 systems being coupled by the rotational oscillator.

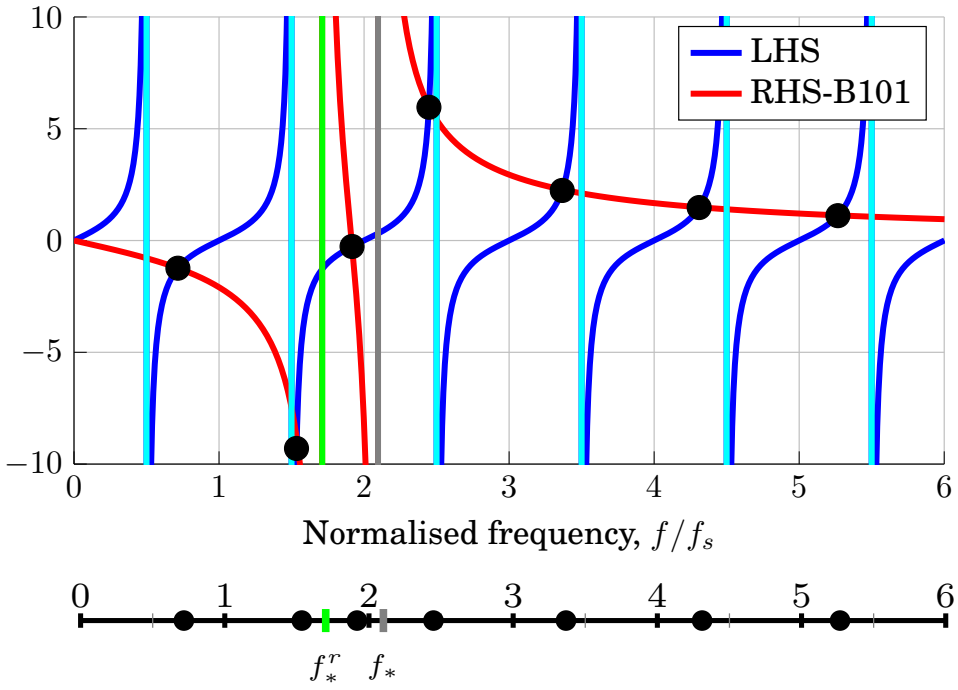

Figure 5.12: Comparison between the graphical plot of Figure 5.11 and its frequency number line counterpart.

II. Case I is repeated but with $\rho \neq \tilde{\rho}$. This would introduce a difference of eigenfrequencies between the two string's polarisation even in a fixed-fixed case. In essence, this represents a case of two S100-B100 systems being coupled by the rotational oscillator.

III. Case I is repeated but the parameters of the translational oscillators have been varied.

IV. Case III is repeated but the parameters of the two translational and one rotational oscillators have been varied to be of higher frequencies. The rational of this case will be justified as it is discussed.

V. Case IV is repeated but with $\rho \neq \tilde{\rho}$. In this case, the polarisations and the oscillators all have different parameters.

All of the physical parameters used to complete the five cases are presented in Table 5.4. Some of these values are not physical such as the exaggerated values for the offset h_1 and h_2. They are chosen simply to "amplify" its effect on the system. The most important outcome of the analysis is to identify the general changes the system brings as compared to a fixed-fixed string, rather than finding the exact eigenfrequency for an arbitrarily defined system.

Table 5.4: Physical parameters used for the analysis of S200-B201 systems, all five cases.

	Case				
Parameter	I	II	III	IV	V
T_0 (N)	880				
ρ (kg.m^{-3})	7850				
$\tilde{\rho}$ (kg.m^{-3})	7850	7457	7850		7457
A (m^2)	9.7993×10^{-7}				
L (m)	0.61				
M_1 (kg)	0.003735				
K_1 (kg.s^{-2})	5607			56070	
M_2 (kg)	0.003735				
K_2 (kg.s^{-2})	5607		3917	33300	
I_3 (kgm^2)	0.001				
J_3 (kgm^2.s^{-2})	4888			48888	
h_1 (m)	1				
h_2 (m)	1				

Case I The parameters used are presented as Case I in Table 5.4. In Figure 5.13, three sets of eigenfrequencies are shown on the number line with their exact values (in Hz) shown in Table 5.5. The blue and red markers represent the eigenfrequencies as determined from Equations (5.90b) and (5.91b) respectively while the black markers display the eigenfrequencies for the complete system, i.e. from Equation (5.88). Equations (5.90a) and (5.91a) are not shown as they represent the S100-B100 case which have been fully decoupled from the system when h_2 or h_1 is zero. To ease any further discussion, the blue and red markers will represent the "v-λ_2" and "u-λ_1" system while the black markers would represent the "complete" system.

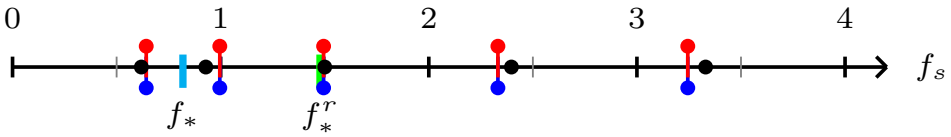

Figure 5.13: Eigenfrequencies plotted on a number line for Case I in units of the fundamental string mode, f_s =238.2Hz. The blue and red markers represent the eigenfrequencies as determined from Equation (5.90b) and (5.91b) respectively while the black markers display the eigenfrequencies for the complete system, i.e. from Equation (5.88).

Since all other parameters are the same, both "v-λ_2" and "u-λ_1" system have the same eigenfrequencies. When both h_2 and h_1 are not zero, i.e. the complete system,

Table 5.5: Eigenfrequencies for Case I and as plotted in Figure 5.13. f_s = 238.2Hz.

	Eigenfrequency (Hz)				
n	1	2	3	4	5
complete	147.4	221.2	356.6	571	793.1
v-λ_2	153	237.2	356	555.5	772.9
u-λ_1	153	237.2	356	555.5	772.9

both $\mathcal{F}$ and $\mathcal{G}$ as defined in Equation (5.88) become the same and the equation becomes essentially the same as Equation (5.69) for a S100-B101 system, such that:

$$\tan\left(\frac{\omega_n L}{c_T}\right) = \frac{T_0\omega_n}{c_T}\left(\frac{1}{\omega_n^2 M_1 - K_1} + \frac{h_1^2 + h_2^2}{\omega_n^2 I_3 - J_3}\right). \tag{5.92}$$

Thus, the system is just another case of S100-B101 system where the eigenfrequencies would increase if they are above the rotational oscillators f_*^r or decrease otherwise. The extent of these adjustments are then influenced by the combined offset $h_1^2 + h_2^2$ and the rotational oscillator's parameters.

Case II The second case looks at the influence of a detuning between the two strings' polarisations on the eigenfrequencies of the system. All of the parameters are presented as Case II in Table 5.4. The only change from Case I is that $\tilde{\rho} = 0.95\rho = 7,457\text{kgm}^{-3}$. The effect of the artificial difference of density between the two polarisations cause the second polarisation v to have a higher eigenfrequency, increasing from 238.2Hz to 244.4Hz. Such difference is again exaggerated so as to easily capture and present the changes a detuning could bring.
Figure 5.14 presents the number line with the respective eigenfrequencies tabulated in Table 5.6. The identical translational oscillators are shown as a cyan line. In this case, the v-λ_2 and u-λ_1 systems are no longer identical, as the strings have different eigenfrequencies despite being coupled to oscillators with the same parameters. When the complete system is considered, the modes from one decoupled system (for example, the v-λ_2 system) perturb the other decoupled system (u-λ_1). As a result, the modes appear to "repel" each other and cause the eigenfrequencies of the complete system to be further apart. A clear example is marked with a overhead square bracket between $2f_s$ and $2.5f_s$ where independently the uncoupled systems have modes at $2.33f_s$ and $2.38f_s$ (see the red and blue lollipops) but once they are coupled, they become further apart at $2.11f_s$ and $2.42f_s$ (see the black dots) respectively (see $n = 6, 7$ in Table 5.6). However, there is an exception for the rotational oscillator. Since both decoupled systems "share" the same mode, and as such the complete system only have one mode (see $n = 5$ in Table 5.6).

Case III The parameters used are presented in Table 5.4 as Case III. Compared to Case II, Case III reverts back to $\rho = \tilde{\rho}$ but changes the stiffness for one of the two oscillators. Specifically, $K_2 = 3,917\text{kgs}^{-2}$. Essentially, Case III is similar to Case

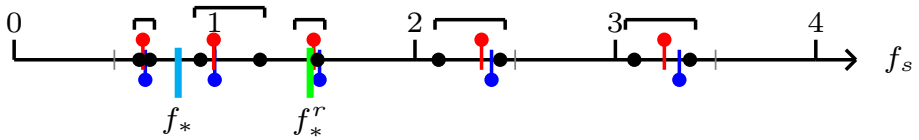

Figure 5.14: Eigenfrequencies plotted on a number line for Case II in units of the fundamental string mode for polarisation u, f_s =238.2Hz.

Table 5.6: Eigenfrequencies for Case II and as plotted in Figure 5.14.

	Eigenfrequency (Hz)								
n	1	2	3	4	5	6	7	8	9
complete	148.8	161.4	221.5	292.4	360.6	504.5	577.7	737.1	803.3
u-λ_1	153		237.2		356	555.5		772.9	
v-λ_2		155.9		238.4	363		567.4		790.6

II where two different uncoupled systems (v-λ_2 and u-λ_1) are coupled by the rotational oscillator. Thus, the same repelling phenomenon can be expected. As shown in Figure 5.15 and Table 5.7, the modes from one uncoupled system perturb the modes from the other system and cause them to "repel" each other. A clear example is marked with an overhead square bracket between $2f_s$ and $2.5f_s$ where independently the uncoupled systems have a mode at $2.3f_s$ (see the red and blue lollipops) but once they are coupled, they become further apart at $2.1f_s$ and $2.4f_s$ (see the black dots) respectively.

In Case II and III, it can be inferred that as n increases, the frequency pairs (6,7) and (8,9) are getting closer. This is logical as they move away from the oscillators, the perturbation brought by the oscillators become less significant. This prompts an interesting question as to how the fundamental modes would detune from each other if the oscillators are at higher frequencies. The is because the addition of oscillators can be seen as essentially a source of detuning which will cause double polarisation as discussed extensively in Chapter 3. A high frequency pair of oscillators are thus studied in Case IV.

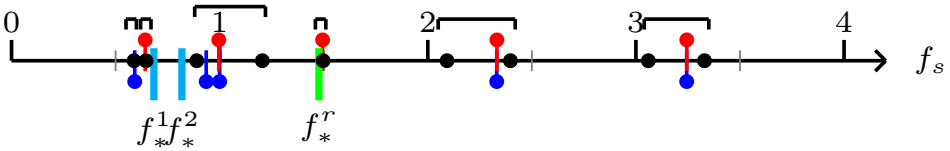

Figure 5.15: Eigenfrequencies plotted on a number line for Case III in units of the fundamental string mode for polarisation u, f_s =238.2Hz.

Table 5.7: Eigenfrequencies for Case III and as plotted in Figure 5.15.

	Eigenfrequency (Hz)								
n	1	2	3	4	5	6	7	8	9
complete	140.2	153.9	212.0	287	356.6	498.4	570.9	728.8	793.1
v-λ_2	141.0		222.8		356	555.3		772.7	
u-λ_1		153		237.2	356		555.5		772.8

Case IV Figure 5.16 and Table 5.8 show the eigenfrequencies when two identical string polarisations are coupled to three (two translational, one rotational) different high-frequency oscillators. The parameters used are presented as Case IV in Table 5.4. The two translational oscillators are marked in Figure 5.16 with $f_*^1 = 6.3 f_s$ and $f_*^2 = 8.2 f_s$ while the rotational oscillator is marked as $f_*^r = 4.7 f_s$. The repelling pairs of eigenfrequencies are as expectedly observed but notably, at lower frequencies, the gap of the pairs are pretty small. This in turn means that the detuning effect caused by the oscillators onto the string modes are reduced when they are further away.

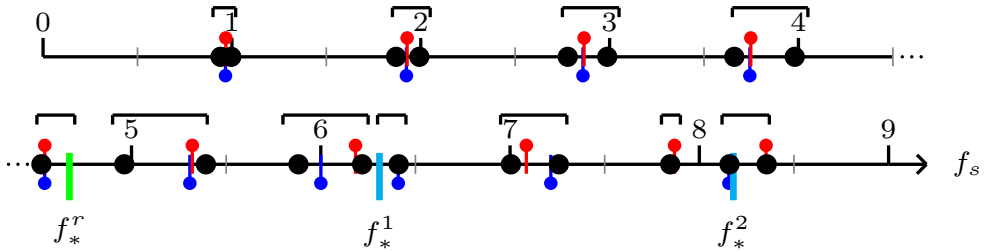

Figure 5.16: Eigenfrequencies plotted on a number line for Case IV in units of the fundamental string mode for polarisation u, f_s =238.2Hz.

Table 5.8: Eigenfrequencies for Case IV and as plotted in Figure 5.16.

	Eigenfrequency (Hz)									
n	1	2	3	4	5	6	7	8	9	10
complete	223.8	237.4	445.3	474.6	661.9	711.6	871.9	947.8	1077.5	1181.9
v-λ_2	230.1		458.3		681		891.5		1081.7	1264.4
u-λ_1		230.5		459.2		682.4		892.7	1081.8	

n	11	12	13	14	15	16	17	18	19
complete	1284.5	1401.1	1481.1	1527.2	1668.5	1728.8	1869.1	1943.6	1990.3
v-λ_2		1429.3		1526.7		1718.7		1942.8	
u-λ_1	1267.5		1472.9		1687.9		1874.4		1989.6

Case V The last case to be investigated is an extension of Case IV where a detuning between the strings' eigenfrequencies are also considered, i.e. $\tilde{\rho} = 0.95\rho = 7,457\text{kgm}^{-3}$. The eigenfrequencies are as shown in Figure 5.17 and Table 5.9. The complete lists of parameters are presented as Case V in Table 5.4. In general, Case V behaves similarly with IV where the lower pairs of eigenfrequencies have smaller gaps as they are further away from the oscillators' frequencies.

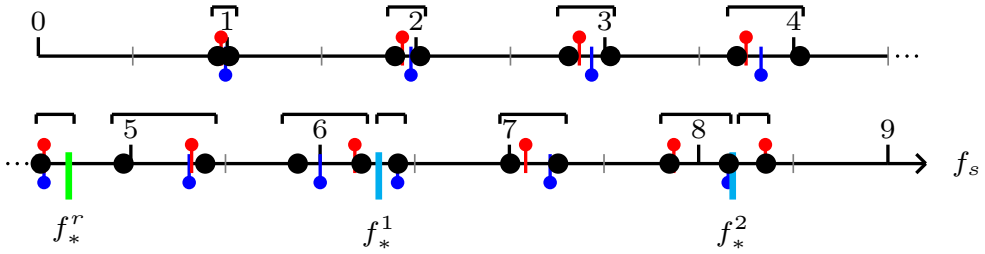

Figure 5.17: Eigenfrequencies plotted on a number line for Case V in units of the fundamental string mode for polarisation u, f_s =238.2Hz.

Table 5.9: Eigenfrequencies for Case V and as plotted in Figure 5.17.

	Eigenfrequency (Hz)									
n	1	2	3	4	5	6	7	8	9	10
complete	226.2	241	450.1	481.7	669	721.8	881.2	960.7	1089.1	1197.1
v-λ_2		236.1		470		697.9		911.6	1103.1	
u-λ_1	230.5		459.2		682.4		892.7		1081.8	1267.5
n	11	12	13	14	15	16	17	18	19	
complete	1297.9	1419	1482.2	1551.3	1675.7	1762.1	1872	1981.5	1997.7	
v-λ_2	1288.9	1445.5		1551.5		1758.9			1990.7	
u-λ_1			1472.9		1687.9		1874.4	1989.6		

In short, the analysis for all the five cases of the S200-B201 system can be summarised as follows:

- The S200-B201 system can be viewed as a coupling between two S100-B101 system that shares the same rotational oscillator.
- Each decoupled system, if non-identical, views another as a source of perturbation and as such, pairs of eigenfrequencies can be found that pertains to each of their original string modes.
- If the decoupled systems are identical, the system simplifies to a S100-B101 system with a combined offset $h_1^2 + h_2^2$.

- If the oscillators' frequencies are much further away from the string's modes, the detuning introduced by the oscillators are less significant (Case IV and V) compared to when the oscillators have similar frequencies as the string's modes (Case III).

5.3 Summary

In this chapter, several coupled systems between a string and a lumped bridge are proposed. Most notably, a S212-B213 system is presented where a string with 5 variables (2 transverse polarisations, 1 longitudinal vibration, 2 rotations) is coupled to a bridge with 6 oscillators (3 translations, 3 rotations). In addition to that, an angular offset, γ between the string's polarisation and the bridge's vertical and horizontal displacements is prescribed. The eigenfrequency equations of some of the simpler systems are derived, specifically the S100-B100, S100-B101 and S200-B201. These will be used in Section 6.2 later for validation of the numerical schemes. Graphical analyses were performed to describe the perturbation the oscillators bring to the string's eigenfrequencies.

6

Numerical schemes of the coupled string-bridge system

In this chapter, numerical schemes are introduced to solve the coupled systems between a string and a lumped bridge as introduced in Chapter 5. Specifically, these systems will be solved via finite element method using the MONTJOIE finite-element package [81]. There are two main advantages using this approach:

- Complex cases like the S212-B213 system can be solved. It is also possible to solve other lumped bridge that was not defined, such as the S111-B111 model.
- Different string models can be used. In Chapter 5, proposed lumped bridge models are coupled to linear strings. In MONTJOIE, it is possible to select stiff string or nonlinear models, including the geometrically exact nonlinear stiff string model defined in Chapter 2.
- Complex coupling conditions can be specified. For example, the angular offset between the string's polarisation and bridge displacement, γ, as proposed in Section 5.1.5, can be included.

In the following Section 6.1, numerical schemes to solve the coupling problem are proposed. They include the "general scheme" that is originally proposed by Chabassier [75] as presented in Section 6.1.1 and the "extended scheme" that is newly proposed in Section 6.1.2. As its name suggests, extended scheme is an extension of the general scheme in which it allows the solution of additional oscillator vibrating in the direction that is not solved in the string. In Section 6.2, these schemes are validated against the eigenfrequencies as obtained from Section 5.2.

6.1 Numerical scheme

It could be prohibitively difficult to solve the equations presented in Section 5.1 directly if nonlinear strings are used to couple the lumped bridge. A viable approach

is to solve these subsystems independently and couple them by means of Lagrange multipliers. A convenient choice for the Lagrange multipliers is the string forces and moments at $x = L$ that allow solving the bridge and string variables at interleaved time steps. This approach is efficient as it avoids the difficulty of solving the whole coupled system implicitly.

6.1.1 General scheme

Recalling that the equations of motion for a complete coupled system of nonlinear string and lumped bridge model can be written as (as copied from Equation (5.30) to (5.33)):

$$\mathbf{M_s}\ddot{\mathbf{q}} - \frac{\partial}{\partial x}\left(\mathbf{A}\mathbf{q}' + \mathbf{B}\mathbf{q} + \nabla\mathbf{H}(\mathbf{q}')\right) + \mathbf{C}\mathbf{q} + \mathbf{B^T}\mathbf{q}' + \mathbf{Y}\dot{\mathbf{q}} - \mathbf{Z}\dot{\mathbf{q}}'' = 0, \tag{6.1a}$$

$$\mathcal{M}_b\ddot{\boldsymbol{\Upsilon}} + \mathcal{S}_b\dot{\boldsymbol{\Upsilon}} + \mathcal{K}_b\boldsymbol{\Upsilon} = -\mathbf{F}^{\mathcal{R}}, \tag{6.1b}$$

$$I_3\ddot{\theta}_3 + R_3\dot{\theta}_3 + J_3\theta_3 = F_1^{\mathcal{R}}h_2 - F_2^{\mathcal{R}}h_1, \tag{6.1c}$$

where:

$$\mathbf{q} = [u \quad v \quad w \quad \phi \quad \psi]^T, \tag{6.2a}$$

$$\boldsymbol{\Upsilon} = [\lambda_1 \quad \lambda_2 \quad \lambda_3 \quad \theta_1 \quad \theta_2]^T, \tag{6.2b}$$

and

$$\mathcal{M}_b = \begin{bmatrix} M_1 & 0 & 0 & 0 & 0 \\ 0 & M_2 & 0 & 0 & 0 \\ 0 & 0 & M_3 & 0 & 0 \\ 0 & 0 & 0 & I_1 & 0 \\ 0 & 0 & 0 & 0 & I_2 \end{bmatrix}, \quad \mathcal{S}_b = \begin{bmatrix} S_1 & 0 & 0 & 0 & 0 \\ 0 & S_2 & 0 & 0 & 0 \\ 0 & 0 & S_3 & 0 & 0 \\ 0 & 0 & 0 & R_1 & 0 \\ 0 & 0 & 0 & 0 & R_2 \end{bmatrix}, \quad \mathcal{K}_b = \begin{bmatrix} K_1 & 0 & 0 & 0 & 0 \\ 0 & K_2 & 0 & 0 & 0 \\ 0 & 0 & K_3 & 0 & 0 \\ 0 & 0 & 0 & J_1 & 0 \\ 0 & 0 & 0 & 0 & J_2 \end{bmatrix}. \tag{6.3}$$

The matrices $\mathbf{M_s}$, $\mathbf{A}$, $\mathbf{B}$, $\mathbf{C}$, $\mathbf{Y}$, $\mathbf{Z}$ and functional $\mathbf{H}$ are from Equation (2.50) and (2.51). The coupling conditions between the bridge and the string are given by:

$$\boldsymbol{\tau}\dot{\mathbf{q}} = \dot{\boldsymbol{\Upsilon}}, \tag{6.4}$$

where $\boldsymbol{\tau}$ is as expressed in Equation (5.29). Meanwhile, $\mathbf{F}^{\mathcal{R}}$ are the resolved string forces onto the bridge and is given by:

$$\mathbf{F}^{\mathcal{R}} = \boldsymbol{\tau}\mathbf{F}, \tag{6.5}$$

where $\mathbf{F}$ is described by Equation (5.25):

$$\mathbf{F} = [\mathbf{A}\mathbf{q}' + \mathbf{B}\mathbf{q} + \nabla\mathbf{H}(\mathbf{q}') + \mathbf{Z}\dot{\mathbf{q}}']_{x=L}. \tag{6.6}$$

To recap, Equation (6.1a) and (6.1b) represent the string and the lumped bridge respectively. For the scheme discussed in this section, only these two equations

are solved. Equation (6.1c), which represents the extra rotational oscillator in the lumped bridge, is omitted. The scheme where Equation (6.1c) is included will be presented in Section 6.1.2 instead.
The variational form of Equation (6.1a) can be written as (see Equation (2.121)):

$$\int_0^L \mathbf{M}\ddot{\mathbf{q}}\mathbf{q}^* - \int_0^L \left(\mathbf{A}\mathbf{q}' + \mathbf{B}\mathbf{q} + \nabla\mathbf{H}(\mathbf{q}')\right)\mathbf{q}^{*\prime} + \int_0^L \mathbf{C}\mathbf{q}\mathbf{q}^* + \int_0^L \mathbf{B}^\mathbf{T}\mathbf{q}'\mathbf{q}^* + \int_0^L \mathbf{Y}\dot{\mathbf{q}}\mathbf{q}^{*\prime} + \int_0^L \mathbf{Z}\dot{\mathbf{q}}'\mathbf{q}^{*\prime} = \left[\mathbf{A}\mathbf{q}' + \mathbf{B}\mathbf{q} + \nabla\mathbf{H}(\mathbf{q}') + \mathbf{Z}\dot{\mathbf{q}}'\right]_0^L \mathbf{q}^*, \quad (6.7)$$

and for the lumped bridge:

$$\mathcal{M}_b\ddot{\boldsymbol{\Upsilon}}\boldsymbol{\Upsilon}^* + \mathcal{S}_b\dot{\boldsymbol{\Upsilon}}\boldsymbol{\Upsilon}^* + \mathcal{K}_b\boldsymbol{\Upsilon}\boldsymbol{\Upsilon}^* = -\mathbf{F}^\mathcal{R}\boldsymbol{\Upsilon}^*, \quad (6.8)$$

where $\mathbf{q}^*$ and $\boldsymbol{\Upsilon}^*$ are the test functions for the string and lumped bridge respectively. Substituting $\mathbf{q}^* = \dot{\mathbf{q}}$ and $\boldsymbol{\Upsilon}^* = \dot{\boldsymbol{\Upsilon}}$, one could yield the conservation of energy as in Equation (5.34) where the following condition needs to be satisfied:

$$\left[\mathbf{A}\mathbf{q}' + \mathbf{B}\mathbf{q} + \nabla\mathbf{H}(\mathbf{q}') + \mathbf{Z}\dot{\mathbf{q}}'\right]_{x=L}\dot{\mathbf{q}} = \mathbf{F}^\mathcal{R}\dot{\boldsymbol{\Upsilon}}. \quad (6.9)$$

It is then possible to rewrite the RHS of Equation (6.7):

$$\int_0^L \mathbf{M}\ddot{\mathbf{q}}\mathbf{q}^* - \int_0^L \left(\mathbf{A}\mathbf{q}' + \mathbf{B}\mathbf{q} + \nabla\mathbf{H}(\mathbf{q}')\right)\mathbf{q}^{*\prime} + \int_0^L \mathbf{C}\mathbf{q}\mathbf{q}^* + \int_0^L \mathbf{B}^\mathbf{T}\mathbf{q}'\mathbf{q}^* + \int_0^L \mathbf{Y}\dot{\mathbf{q}}\mathbf{q}^{*\prime} + \int_0^L \mathbf{Z}\dot{\mathbf{q}}'\mathbf{q}^{*\prime} = \mathbf{F}^\mathcal{R}\boldsymbol{\tau}\mathbf{q}^*, \quad (6.10)$$

and as per presented in Section 2.4.3, into a discrete form where:

$$M_h\ddot{\mathbf{Q}}_h + R_h\dot{\mathbf{Q}}_h + K_h\mathbf{Q}_h + \nabla\mathbf{H}^\circ(\mathbf{Q}_h) = \mathbf{F}_\mathbf{h}^\mathcal{R}\boldsymbol{\tau}, \quad (6.11)$$

with $\mathbf{F}_\mathbf{h}^\mathcal{R}$ being the discrete form of $\mathbf{F}^\mathcal{R}$ as indicated by the subscript h.
For Equation (6.8), the lumped bridge is essentially a single point and thus the basis function to be substituted into the test function $\boldsymbol{\Upsilon}^*$ is simply an identity matrix:

$$\boldsymbol{\Upsilon}^* = \mathbf{I}. \quad (6.12)$$

A conversion matrix $\mathbb{P}_h$ can also be introduced such that [75]:

$$\mathbb{P}_h^T\mathcal{M}_b\mathbb{P}_h = \mathbf{I}, \quad (6.13a)$$
$$\mathbb{P}_h^T\mathcal{S}_b\mathbb{P}_h = \mathbb{S}_h, \quad (6.13b)$$
$$\mathbb{P}_h^T\mathcal{K}_b\mathbb{P}_h = \mathbb{K}_h, \quad (6.13c)$$
$$\mathbb{P}_h\boldsymbol{\Upsilon} = \boldsymbol{\Upsilon}_h, \quad (6.13d)$$
$$\mathbb{P}_h^T\mathcal{M}_b\boldsymbol{\Upsilon}_h = \boldsymbol{\Upsilon}. \quad (6.13e)$$

Using both Equation (6.12) and (6.13), Equation (6.8) can thus be written as:

$$\ddot{\boldsymbol{\Upsilon}}_h + \mathbb{S}_h \dot{\boldsymbol{\Upsilon}}_h + \mathbb{K}_h \boldsymbol{\Upsilon}_h = \mathbb{P}^T \mathbf{F}_{\mathbf{h}}^{\mathcal{R}}. \tag{6.14}$$

From Equation (6.4), the discrete boundary conditions between the string (Equation (6.11)) and lumped bridge (Equation (6.14)) are thus:

$$\boldsymbol{\tau} \dot{\mathbf{Q}}_h = \mathbb{P}_h^T \dot{\boldsymbol{\Upsilon}}_h, \tag{6.15}$$

A convenient method to solve the system of Equation (6.11) and (6.14) efficiently is to couple the two equations by Lagrange multipliers and solve them at interleaved time steps. A suitable candidate for this is the projected string forces on the lumped bridge $\mathbf{F}_{\mathbf{h}}^{\mathcal{R}}$ as it appears in both equations. Discretising both equations and their corresponding boundary conditions in time, the general scheme can be presented as:

$$M_h \frac{\mathbf{Q}_h^{n+1} - 2\mathbf{Q}_h^n + \mathbf{Q}_h^{n-1}}{\Delta t^2} + R_h \frac{\mathbf{Q_h}^{n+1} - \mathbf{Q}_h^{n-1}}{2\Delta t} + K_h [\mathbf{Q}_h]_\vartheta^n + \nabla \mathbf{H}^\circ(\mathbf{Q}_h) = \mathbf{F}_{\mathbf{h}}^{\mathcal{R}} \boldsymbol{\tau}, \tag{6.16a}$$

$$\ddot{\boldsymbol{\Upsilon}}_h + \mathbb{S}_h \dot{\boldsymbol{\Upsilon}}_h + \mathbb{K}_h \boldsymbol{\Upsilon}_h = \mathbb{P}^T \mathbf{F}_{\mathbf{h}}^{\mathcal{R}}, \tag{6.16b}$$

$$\boldsymbol{\tau} \frac{\mathbf{Q}_h^{n+1} - \mathbf{Q}_h^{n-1}}{2\Delta t} = \mathbb{P}_h^T \frac{\boldsymbol{\Upsilon}_{\boldsymbol{h}}^{\boldsymbol{n+1/2}} - \boldsymbol{\Upsilon}_{\boldsymbol{h}}^{\boldsymbol{n-1/2}}}{\Delta t}, \tag{6.16c}$$

Equation (6.16b) can be solved analytically at time step $n + 1/2$ where:

$$\boldsymbol{\Upsilon}_h^{n+1/2} = \mathcal{S}_{\Delta t}^0 \boldsymbol{\Upsilon}_h^{n-1/2} + \mathcal{S}_{\Delta t}^1 \dot{\boldsymbol{\Upsilon}}_h^{n-1/2} + (-\mathbb{P}_h^T \mathbf{F}_{\mathbf{h}}^{\mathcal{R}}) \mathcal{R}_{\Delta t}, \tag{6.17a}$$

$$\dot{\boldsymbol{\Upsilon}}_h^{n+1/2} = \dot{\mathcal{S}}_{\Delta t}^0 \boldsymbol{\Upsilon}_h^{n-1/2} + \dot{\mathcal{S}}_{\Delta t}^1 \dot{\boldsymbol{\Upsilon}}_h^{n-1/2} + (-\mathbb{P}_h^T \mathbf{F}_{\mathbf{h}}^{\mathcal{R}}) \dot{\mathcal{R}}_{\Delta t}, \tag{6.17b}$$

where expression of $\mathcal{S}_{\Delta t}^0$, $\mathcal{S}_{\Delta t}^1$, $\mathcal{R}_{\Delta t}$, $\dot{\mathcal{S}}_{\Delta t}^0$, $\dot{\mathcal{S}}_{\Delta t}^1$ and $\dot{\mathcal{R}}_{\Delta t}$, as derived and presented by Derveaux [91] and later by Chabassier [75], can be found in Appendix A.
It is possible to rewrite Equation (6.16c) into:

$$\boldsymbol{\tau} \frac{\mathbf{Q}_h^{n+1} - \mathbf{Q}_h^{n-1}}{2\Delta t} = \mathbb{P}_h^T \frac{\mathcal{S}_{\Delta t}^0 \boldsymbol{\Upsilon}_h^{n-1/2} + \mathcal{S}_{\Delta t}^1 \dot{\boldsymbol{\Upsilon}}_h^{\,n-1/2} + \mathbb{P}_h^T (-\mathbf{F}_{\mathbf{k}}^{\mathcal{R}}) \mathcal{R}_{\Delta t} - \boldsymbol{\Upsilon}_h^{n-1/2}}{\Delta t}, \tag{6.18}$$

and subsequently as:

$$\boldsymbol{\tau} \frac{\mathbf{Q}_h^{n+1} - \mathbf{Q}_h^{n-1}}{2\Delta t} = \mathcal{A} + (-\mathbf{F}_{\mathbf{h}}^{\mathcal{R}}) \mathcal{B}, \tag{6.19}$$

where

$$\mathcal{A} = \frac{1}{\Delta t} \mathbb{P}_h^T (\mathcal{S}_{\Delta t}^0 \boldsymbol{\Upsilon}_h^{n-1/2} + \mathcal{S}_{\Delta t}^1 \dot{\boldsymbol{\Upsilon}}_h^{\,n-1/2} - \boldsymbol{\Upsilon}_h^{n-1/2}), \tag{6.20a}$$

$$\mathcal{B} = \frac{1}{\Delta t} \mathbb{P}_h^T \mathcal{R}_{\Delta t}. \tag{6.20b}$$

When the scheme is in the form of Equation (6.19), $\mathcal{B}$ is only required to be solved at the first time step where $\mathcal{A}$ will be updated at every time step.

Example: S100-B100

The scheme proposed in Equation (6.16) can be demonstrated in the simplest case of S100-B100 where $\mathbf{Q}_h = [u_h]$ and $\boldsymbol{\Upsilon}_h = [\lambda_{1,h}]$. Equation (6.16) can be rewritten into:

$$M_h \frac{u_h^{n+1} - 2u_h^n + u_h^{n-1}}{\Delta t^2} + R_h \frac{u_h^{n+1} - u_h^{n-1}}{2\Delta t} + K_h [u_h]_\vartheta^n + \nabla \mathbf{H}^\circ(u_h) = F_{1,h}^{\mathcal{R}}, \tag{6.21a}$$

$$\ddot{\boldsymbol{\Upsilon}}_h + \mathbb{S}_h \dot{\boldsymbol{\Upsilon}}_h + \mathbb{K}_h \boldsymbol{\Upsilon}_h = \mathbb{P}^T \mathbf{F}_{\mathbf{h}}^{\mathcal{R}}, \tag{6.21b}$$

$$\mathbf{I} \frac{u_h^{n+1} - u_h^{n-1}}{2\Delta t} = \mathbb{P}_h^T \frac{\lambda_{1,h}^{n+1/2} - \lambda_{1,h}^{n-1/2}}{\Delta t}, \tag{6.21c}$$

where the transformation matrix $\boldsymbol{\tau}$ is simply an identity matrix of $\mathbf{I} = [1]$. The term $\nabla \mathbf{H}^\circ(u_h)$ could be dropped for a linear problem. Equation (6.21c) could be rewritten into:

$$\frac{u_h^{n+1} - u_h^{n-1}}{2\Delta t} = \mathcal{A} + (-F_{1,h}^{\mathcal{R}})\mathcal{B}, \tag{6.22}$$

where

$$\mathcal{A} = \frac{1}{\Delta t} \mathbb{P}_h^T (\mathcal{S}_{\Delta t}^0 \lambda_{1,h}^{n-1/2} + \mathcal{S}_{\Delta t}^1 \dot{\lambda}_{1,h}^{n-1/2} - \lambda_{1,h}^{n-1/2}), \tag{6.23a}$$

$$\mathcal{B} = \frac{1}{\Delta t} \mathbb{P}_h^T \mathcal{R}_{\Delta t}. \tag{6.23b}$$

Other systems: S101-B101

The same scheme proposed in Equation (6.16) can also be applied to a S101-B101 system, where a linear Timoshenko string equation is coupled to a two-oscillator lumped bridge model. In that case,

$$\mathbf{Q}_h = [u_h, \phi_h], \tag{6.24a}$$

$$\boldsymbol{\Upsilon}_{\boldsymbol{h}} = [\lambda_{1,h}, \theta_{2,h}], \tag{6.24b}$$

and the transformation matrix, $\boldsymbol{\nu}$ would correspond to the boundary condition in Equation (5.14), where:

$$\boldsymbol{\tau} = \begin{bmatrix} 1 & -(-h_3) \\ 0 & 1 \end{bmatrix}. \tag{6.25}$$

6.1.2 Extended Scheme

In Section 6.1.1, the scheme proposed is suitable only for systems where the lumped bridge only contains variables that corresponds to the string variables. For instance, a S100-B100 only has λ_1 as the lumped bridge and it corresponds to the transverse displacement u of the string. However, as have been presented in Section 5.1, there are a few models that have an additional rotational oscillator, such as in the form

of Equation (6.1c). To solve for these systems, the General Scheme proposed in Section 6.1.1 needs to be further extended to what will be known as the Extended Scheme.
The variational form of Equation (6.1a) and (6.1b) are the same as Equation (6.10) and (6.8) respectively. On the other hand, the variational form of (6.1c) can be written as:

$$I_3\ddot{\theta}_3\theta_3^* + R_3\dot{\theta}_3\theta_3^* + J_3\theta_3\theta_3^* = \left[F_1^{\mathcal{R}}h_2 - F_2^{\mathcal{R}}h_1\right]\theta_3^*, \tag{6.26}$$

where θ_3^* is the test function. Substituting $\theta_3^* = \dot{\theta}_3$ as the test function, one can recover the energy conservation in Equation (5.34) if the following relations are satisfied:

$$\left[\mathbf{A}\mathbf{q}' + \mathbf{B}\mathbf{q} + \nabla\mathbf{H}(\mathbf{q}') + \mathbf{Z}\dot{\mathbf{q}}'\right]_{x=L}\dot{\mathbf{q}} = \mathbf{F}_{\mathbf{k}}^{\mathcal{R}}\dot{\boldsymbol{\Upsilon}} + \left[F_1^{\mathcal{R}}h_2 - F_2^{\mathcal{R}}h_1\right]\dot{\theta}_3. \tag{6.27}$$

Using the coupling conditions of Equation (5.29)(rewritten here for convenience):

$$\underbrace{\begin{bmatrix} \cos(\gamma) & -\sin(\gamma) & 0 & -h_3 & 0 \\ \sin(\gamma) & \cos(\gamma) & 0 & 0 & h_3 \\ 0 & 0 & 1 & h_1\cos(\gamma) - h_2\sin(\gamma) & -(h_2\cos(\gamma) + h_1\sin(\gamma)) \\ 0 & 0 & 0 & \sin(\gamma) & \cos(\gamma) \\ 0 & 0 & 0 & \cos(\gamma) & -\sin(\gamma) \end{bmatrix}}_{\boldsymbol{\tau}} \begin{bmatrix} \dot{u} \\ \dot{v} \\ \dot{w} \\ \dot{\phi} \\ \dot{\psi} \end{bmatrix} = \begin{bmatrix} \dot{\lambda}_1 \\ \dot{\lambda}_2 \\ \dot{\lambda}_3 \\ \dot{\theta}_1 \\ \dot{\theta}_2 \end{bmatrix} + \begin{bmatrix} -h_2\dot{\theta}_3 \\ h_1\dot{\theta}_3 \\ 0 \\ 0 \\ 0 \end{bmatrix}, \tag{6.28}$$

one recovers Equation (6.10) and subsequently (6.16a) for the string part. For the original oscillators that are also present in the general scheme, it is natural that Equation (6.16b) can be recovered. Lastly, the extra oscillator has the basis function:

$$\theta_3^* = 1, \tag{6.29}$$

and Equation (6.26) can be solved analytically in a similar manner as the original oscillators. However, since it is just an equation, it can be simply divided by I_3 to obtain a form that can be solved analytically via the method of Derveaux [91] (see Appendix A). The complete scheme, taking into consideration of the coupling conditions of Equation (6.28), can be written as:

$$M_h\frac{\mathbf{Q}_h^{n+1} - 2\mathbf{Q}_h^n + \mathbf{Q}_h^{n-1}}{\Delta t^2} + R_h\frac{\mathbf{Q_h}^{n+1} - \mathbf{Q}_h^{n-1}}{2\Delta t} + K_h[\mathbf{Q}_h]_\vartheta^n + \nabla\mathbf{H}^\circ(\mathbf{Q}_h) = \mathbf{F}_{\mathbf{h}}^{\mathcal{R}}\boldsymbol{\tau}, \tag{6.30a}$$

$$\ddot{\boldsymbol{\Upsilon}}_h + \mathbb{S}_h\dot{\boldsymbol{\Upsilon}}_h + \mathbb{K}_h\boldsymbol{\Upsilon}_h = \mathbb{P}^T\mathbf{F}_{\mathbf{h}}^{\mathcal{R}}, \tag{6.30b}$$

$$\ddot{\theta}_{3,h} + R_3I_3^{-1}\dot{\theta}_{3,h} + J_3I_3^{-1}\theta_{3,h} = I_3^{-1}\left[F_{1,h}^{\mathcal{R}}h_2 - F_{2,h}^{\mathcal{R}}h_1\right], \tag{6.30c}$$

$$\boldsymbol{\tau}\frac{\mathbf{Q}_h^{n+1} - \mathbf{Q}_h^{n-1}}{2\Delta t} = \mathbb{P}_h^T\frac{\boldsymbol{\Upsilon}_{\boldsymbol{h}}^{\boldsymbol{n+1/2}} - \boldsymbol{\Upsilon}_{\boldsymbol{h}}^{\boldsymbol{n-1/2}}}{\Delta t} + \hbar\frac{{\theta_{3,h}}^{n+1/2} - {\theta_{3,h}}^{n-1/2}}{\Delta t}, \tag{6.30d}$$

where a subscript h is appended to Equation (6.30c) and $\theta_3 = \theta_{3,h}$. The vector $\hbar$ is expressed as:

$$\hbar^T = \begin{bmatrix} -h_2 & h_1 & 0 & 0 & 0 \end{bmatrix} \tag{6.31}$$

Note that due to the addition of extra oscillator, the coupling condition in Equation (6.30d) is updated compared to Equation (6.16c). Solutions of Equation (6.30b) are given in Equation (6.17) and the solutions of Equation (6.30c) are written in a similar form:

$$\theta_{3,h}^{n+1/2} = \mathcal{S}_{\Delta t}^0 \theta_{3,h}^{n-1/2} + \mathcal{S}_{\Delta t}^1 \dot{\theta}_{3,h}^{n-1/2} + I_3^{-1}(h_2 F_{1,h}^{\mathcal{R}} - h_1 F_{2,h}^{\mathcal{R}})\mathcal{R}_{\Delta t}, \tag{6.32a}$$

$$\dot{\theta}_{3,h}^{n+1/2} = \dot{\mathcal{S}}_{\Delta t}^0 \theta_{3,h}^{n-1/2} + \dot{\mathcal{S}}_{\Delta t}^1 \dot{\theta}_{3,h}^{n-1/2} + I_3^{-1}(h_2 F_{1,h}^{\mathcal{R}} - h_1 F_{2,h}^{\mathcal{R}})\dot{\mathcal{R}}_{\Delta t}. \tag{6.32b}$$

It is thus possible to rewrite Equation (6.30d) as:

$$\boldsymbol{\tau}\frac{\mathbf{Q}_h^{n+1} - \mathbf{Q}_h^{n-1}}{2\Delta t} = \left[\mathcal{A} + \mathbb{P}_h^T(-\mathbf{F}_{\mathbf{h}}^{\mathcal{R}})\mathcal{B}\right] + \hbar\left[\mathcal{C} + I_3^{-1}(h_2 F_{1,h}^{\mathcal{R}} - h_1 F_{2,h}^{\mathcal{R}})\mathcal{D}\right], \tag{6.33}$$

where $\mathcal{A}$ and $\mathcal{B}$ are as defined in Equation (6.20); $\mathcal{C}$ and $\mathcal{D}$ are:

$$\mathcal{C} = \frac{1}{\Delta t}\mathbb{P}_h^T(\mathcal{S}_{\Delta t}^0 \theta_{3,h}^{n-1/2} + \mathcal{S}_{\Delta t}^1 \dot{\theta}_{3,h}^{n-1/2} - \theta_{3,h}^{n-1/2}), \tag{6.34a}$$

$$\mathcal{D} = \frac{1}{\Delta t} I_3^{-1}\mathcal{R}_{\Delta t}. \tag{6.34b}$$

Example: S200-B201

The schemes in Equation (6.30) can be easily adapted for other coupled string-bridge system that uses θ_3 as the extra oscillator, such as the S200-B201 system. This system has the following coupling conditions:

$$\dot{u}(L,t) = \dot{\lambda}_1 - h_2\dot{\theta}_3, \tag{6.35a}$$

$$\dot{v}(L,t) = \dot{\lambda}_2 + h_1\dot{\theta}_3. \tag{6.35b}$$

The variables to use in the scheme of Equation (6.30) become:

$$\mathbf{Q}_h = [u_h \quad v_h], \tag{6.36a}$$

$$\boldsymbol{\Upsilon}_h = [\lambda_{1,h} \quad \lambda_{2,h}], \tag{6.36b}$$

$$\boldsymbol{\tau} = \mathbf{I}, \tag{6.36c}$$

$$\hbar^T = [-h2 \quad h1], \tag{6.36d}$$

where $\boldsymbol{\tau}$ is a 2-by-2 matrix and if it is linear (as is the case shown in Section 5.1.4),

$$\nabla\mathbf{H}^\circ = 0. \tag{6.37}$$

Example: S100-B101

For systems where the extra oscillator is not θ_3, the scheme will have to be reconstructed but the strategy is the same. For a S100-B101 system (see Section 5.1.2), the scheme could be written as:

$$M_h \frac{\mathbf{Q}_h^{n+1} - 2\mathbf{Q}_h^n + \mathbf{Q}_h^{n-1}}{\Delta t^2} + R_h \frac{\mathbf{Q_h}^{n+1} - \mathbf{Q}_h^{n-1}}{2\Delta t} + K_h[\mathbf{Q}_h]_\vartheta^n = \mathbf{F}_\mathbf{h}^\mathcal{R}\boldsymbol{\tau}, \tag{6.38a}$$

$$\ddot{\boldsymbol{\Upsilon}}_h + \mathbb{S}_h\dot{\boldsymbol{\Upsilon}}_h + \mathbb{K}_h\boldsymbol{\Upsilon}_h = \mathbb{P}^T\mathbf{F}_\mathbf{h}^\mathcal{R}, \tag{6.38b}$$

$$\ddot{\theta}_{2,h} + R_2 I_2^{-1}\dot{\theta}_{2,h} + J_2 I_2^{-1}\theta_{2,h} = I_2^{-1}\left[F_{1,h}^\mathcal{R}(-h_3)\right], \tag{6.38c}$$

$$\boldsymbol{\tau}\frac{\mathbf{Q}_h^{n+1} - \mathbf{Q}_h^{n-1}}{2\Delta t} = \mathbb{P}_h^T \frac{\boldsymbol{\Upsilon}_\boldsymbol{h}^{\boldsymbol{n+1/2}} - \boldsymbol{\Upsilon}_\boldsymbol{h}^{\boldsymbol{n-1/2}}}{\Delta t} + \hbar\frac{{\theta_{2,h}}^{n+1/2} - {\theta_{2,h}}^{n-1/2}}{\Delta t}, \tag{6.38d}$$

where

$$\mathbf{Q}_h = [u_h], \tag{6.39a}$$

$$\boldsymbol{\Upsilon}_h = [\lambda_{1,h}], \tag{6.39b}$$

$$\boldsymbol{\tau} = \mathbf{I}, \tag{6.39c}$$

$$\hbar = [(-h_3)], \tag{6.39d}$$

and solutions of $\theta_{2,h}$ are:

$$\theta_{2,h}^{n+1/2} = \mathcal{S}_{\Delta t}^0\theta_{2,h}^{n-1/2} + \mathcal{S}_{\Delta t}^1\dot{\theta}_{2,h}^{n-1/2} + (-I_2^{-1}(-h_3)F_{1,h}^\mathcal{R})\mathcal{R}_{\Delta t}, \tag{6.40a}$$

$$\dot{\theta}_{2,h}^{n+1/2} = \dot{\mathcal{S}}_{\Delta t}^0\theta_{2,h}^{n-1/2} + \dot{\mathcal{S}}_{\Delta t}^1\dot{\theta}_{2,h}^{n-1/2} + (-I_2^{-1}(-h_3)F_{1,h}^\mathcal{R})\dot{\mathcal{R}}_{\Delta t}. \tag{6.40b}$$

6.2 Validation of the numerical schemes

A validation of the numerical schemes is essential to confirm that they are correctly implemented in the finite-element solver MONTJOIE. To begin, the simplest scheme is first validated, followed by more complicated cases. To validate the scheme, results from Section 5.2 are used. Specifically, the validation is achieved by comparing the eigenfrequencies calculated analytically from the modal approach against the frequencies obtained from the simulated time-domain displacement signals via Fast Fourier Tranform (FFT).

6.2.1 S100-B100: Linear wave equation coupled to a single-oscillator lumped bridge

The numerical scheme of a S100-B100 system is the general scheme as expressed in Equation (6.21). Recalling from Section 5.2.1, the eigenfrequencies of the system can be obtained by solving for Equation (5.41), rewritten here for convenience:

$$\tan\left(\frac{\omega_n L}{c_T}\right) = \frac{T_0\omega_n}{c_T(M_1\omega_n^2 - K_1)}. \tag{6.41}$$

The material parameters used for both the computation of the frequencies from Equation (6.41) and from the numerical scheme in Equation (6.21) are as shown in Table 6.1.

Table 6.1: Physical parameters used for the analysis for S100-B100 system.

Parameter	Value
T_0	880 N
ρ	7,850 kg.m^{-3}
A	9.7993.10^{-7} m^2
M_1	0.001 kg
K_1	4,500 kg.s^{-2}
L	1.05 m

In the MONTJOIE simulation, the string is excited by a half-sine wave for $x = [0, L]$ at an amplitude of 10^{-5}m. Even though a half-sine wave is used, it excites all other frequencies as well because the half-sine wave corresponds to the first mode of the uncoupled string, not the frequency of the coupled system. The other numerical parameters used are as shown in Table 6.2.

Table 6.2: Simulation parameters used for the S100-B100 system.

Parameter	Value
Time step, Δt	10^{-6}s
total time	10 s
Number of elements	50
ϑ	0.25
Observed point	0.5m from one end

The first ten frequencies as obtained from Equation (6.41) and MONTJOIE simulation are as shown in Table 6.3. The resonant frequencies of the simulation are obtained by identifying the peaks in the frequency response of the displacement signal. The frequency response is computed by performing fast Fourier transform (FFT) on the time-domain signal. Since the total simulated time is 10s, this would yield a frequency resolution of 0.1Hz. Comparing between the analytical eigenfrequencies and frequencies from the MONTJOIE simulations, they agree completely for all the frequencies observed. Such result indicates that the MONTJOIE simulations are accurate.

6.2.2 S100-B101: Linear wave equation coupled to a two-oscillator lumped bridge

For a S100-B101 system, the numerical scheme is extended as expressed in Equation (6.38). The eigenfrequencies of this system can be obtained by solving for Equa-

Table 6.3: The first ten frequencies as obtained from Equation (6.41) and MONTJOIE for S100-B100 system.

	Frequency (Hz)									
n	1	2	3	4	5	6	7	8	9	10
Equation (6.41)	134.2	261.9	390.6	530.3	679.1	832.8	989.1	1146.7	1305.3	1464.4
MONTJOIE	134.2	261.9	390.6	530.3	679.1	832.8	989.1	1146.7	1305.3	1464.4

tion (5.69), repeated here for convenience:

$$\tan\left(\frac{\omega_n L}{c_T}\right) = \frac{T_0\omega_n}{c_T}\left(\frac{1}{\omega_n^2 M_1 - K_1} + \frac{{h_3}^2}{\omega_n^2 I_2 - J_2}\right). \tag{6.42}$$

The material parameters used to compute the eigenfrequencies are presented in Table 6.1 with additional new parameters shown in Table 6.4. The numerical simulation parameters are kept the same from the previous case, i.e. the same as Table 6.2. The same initial condition is also used.

Table 6.4: Additional parameters used for the validation of S100-B101 scheme.

Parameter	Value
I_2	0.001 kgm^2
J_2	15,000 kgm^2.s^{-2}
h_3	1m

The first ten frequencies as obtained from Equation (6.42) and MONTJOIE are as shown in Table 6.5. Once again, MONTJOIE simulations agree completely for all the eigenfrequencies observed.

Table 6.5: The first ten frequencies as obtained from Equation (6.41) and MONTJOIE for S100-B100 system.

	Frequency (Hz)									
n	1	2	3	4	5	6	7	8	9	10
Equation (6.42)	129.7	260.0	388.8	490.6	576.5	709.0	856.8	1009.4	1164.5	1321.0
MONTJOIE	129.7	260.0	388.8	490.6	576.5	709.0	856.8	1009.4	1164.5	1321.0

To further validate the scheme of Equation (6.38), a set of simulations with different values of h_3 are performed. The material parameters used in the simulations are different from before and are shown in Table (6.6). The numerical simulation parameters are the same as Table 6.2 except that the time step has been reduced to 10^{-5}s to reduce the overall time needed to compute all the cases.
The frequencies computed from Equation (6.42) and obtained from the frequency responses of the displacement signals from MONTJOIE simulations are shown in

Table 6.6: Physical parameters used for further validation of S100-B101 scheme.

Parameter	Value
T_0	880 N
ρ	7850 kg.m^{-3}
A	9.7993e-7 m^2
M_1	0.01 kg
K_1	986.96 kg.s^{-2}
I_2	0.0001 kgm^2
J_2	3397.75 kgm^2.s^{-2}
L	1.05 m

Tables 6.7 and 6.8 respectively. Note that the values used for h_3 may not necessarily be realistic. Due to the use of a larger time step, there are numerical dispersions in the MONTJOIE data for frequencies from around 550Hz and above. With increasing frequencies, the differences between the two sets of data also increase. Regardless of the numerical dispersion, the trends of how the frequencies change with increasing h_3 are correctly captured by the simulations of MONTJOIE. Thus, in addition to the excellent agreement from earlier result in Table 6.3, the numerical scheme in Equation (6.38) can be considered to have been successfully validated.

Table 6.7: Eigenfrequencies as obtained from Equation (6.42) using different values of h_3.

h_3 (m)	Frequency (Hz) from Equation (6.42)									
0.1	59.7	173.5	290.9	331.5	488.2	647.9	808.2	968.8	1129.5	1290.3
0.5	59.5	161.3	267.9	361.3	502.5	657.3	815.3	974.5	1134.3	1294.4
1	58.9	137.3	252.7	384.4	528.3	679.2	833.6	990.1	1147.9	1306.4
1.5	58.0	118.3	247.2	393.3	544.1	697.3	852.0	1007.9	1164.7	1322.2
2	57.0	106.0	244.9	397.1	551.9	707.7	864.1	1021.0	1178.3	1336.0

Table 6.8: Frequencies obtained from MONTJOIE-simulated time signals using different values of h_3.

h_3 (m)	Frequency (Hz) from MONTJOIE									
0.1	59.7	173.5	290.9	331.5	488.2	647.9	808.1	968.5	1129.0	1290.0
0.5	59.5	161.3	267.9	361.3	502.5	657.2	815.1	974.2	1133.8	1293.7
1	58.9	137.3	252.7	384.4	528.3	679.1	833.4	989.8	1147.4	1305.7
1.5	58.0	118.3	247.2	393.3	544.1	679.2	851.8	1007.6	1164.2	1321.4
2	57.0	106.0	244.9	397.1	551.8	707.6	863.9	1020.7	1177.8	1335.2

6.2.3 S200-B201: Non-planar linear string coupled to a three-oscillator lumped bridge

The third case to be conducted is to validate the extended numerical scheme presented in Equation (6.30) for a S200-B201 system. The scheme for S200-B201, although similar in principle, is different from a S100-B101 system as it solves for θ_3 instead of θ_2. As far as the numerical scheme is concerned, the S200-B201 scheme is essentially a reduced version of the complete S212-B213 system. Both systems solve for the same extra oscillator, i.e. θ_3, albeit the S212-B213 system also computes for extra unknowns in the other two rotations and the longitudinal displacement of the string and bridge. Since only the theoretical eigenfrequencies for S200-B201 system are known, validating a S200-B201 scheme can also be viewed as a validation for the S212-B213 scheme as well since both employ the same approach and solve for the same extra oscillators.
To comprehensively validate the S200-B201 scheme in Equation (6.30), the five cases that were first presented in Section 5.2.3 are being simulated in MONTJOIE. FFT results of the displacement time signals are analysed and the frequencies of the systems are extracted to compare against theoretical eigenfrequencies obtained from Equation (5.88), which is rewritten as Equation (6.43) for easy reference.

$$1 = -h_2^2 \frac{T_0 k_{u,n}}{(J_3 - \omega_n^2 I_3)\mathcal{F}(k_{u,n})} - h_1^2 \frac{T_0 k_{v,n}}{(J_3 - \omega_n^2 I_3)\mathcal{G}(k_{v,n})}, \tag{6.43}$$

where:

$$\mathcal{F}(k_{u,n}) = \tan(k_{u,n}L) + \frac{T_0 k_{u,n}}{K_1 - \omega_n^2 M_1},$$
$$\mathcal{G}(k_{v,n}) = \tan(k_{v,n}L) + \frac{T_0 k_{v,n}}{K_2 - \omega_n^2 M_2}.$$

In what follows, the eigenfrequencies that were first presented in Tables 5.5, 5.6, 5.7, 5.8 and 5.9, each representing Cases I, II, III, IV and V respectively are shown again in Tables 6.10, 6.11, 6.12, 6.13 and 6.14. For each case, the frequencies as obtained from the MONTJOIE simulations are also shown in the same table. To recap, the physical parameters used for each case are shown in Table 5.4, and is reproduced here in Table 6.9 to remind the readers the differences between each cases.
All simulations are run for 10s with a time step of 10^{-6}s, yielding a frequency resolution of 0.1Hz. For Cases II to V, each simulation begins with an initial condition of a half-sine wave with an amplitude of 10^{-5}m for both the strings. For Case I, the two strings have slightly different initial amplitudes of 1.5×10^{-5}m and 10^{-5}m. This is because if the same initial condition is given to both the strings, the two string forces applied to the rotational oscillator of the bridge would simply cancel out each other. This causes the system to degenerates into two uncoupled S100-B100 systems which gives an entirely different set of frequencies.

Table 6.9: Physical parameters used for the analysis of S200-B201 systems, all five cases.

	Case				
Parameter	I	II	III	IV	V
T_0 (N)	880				
ρ (kg.m^{-3})	7850				
$\tilde{\rho}$ (kg.m^{-3})	7850	7457	7850		7457
A (m^2)	9.7993×10^{-7}				
L (m)	0.61				
M_1 (kg)	0.003735				
K_1 (kg.s^{-2})	5607			56070	
M_2 (kg)	0.003735				
K_2 (kg.s^{-2})	5607		3917	33300	
I_3 (kgm^2)	0.001				
J_3 (kgm^2.s^{-2})	4888			48888	
h_1 (m)	1				
h_2 (m)	1				

It is perhaps easier to begin the discussion by ignoring first the result from Table 6.10 for Case I. Looking at the results in Tables 6.11, 6.12, 6.13 and 6.14, the frequencies extracted from MONTJOIE simulations are identical to the accuracy of 0.1Hz with the sole exception of the 4th frequency for Case IV in Table 6.13 (see the value in bold) where it is 0.1Hz higher than is computed by Equation (6.43).
The big elephant in the room is the result from Table 6.10. On one hand, all the frequencies computed by Equation (6.43) are correctly simulated in MONTJOIE. On the other hand, there are also additional frequencies (in bold) that show up in the FFT plot of the displacement signal. These extra frequencies could be due to limited accuracy of the numerical scheme where the two string modes are actually not exactly identical. Indeed, it is possible to identify these extra modes using the eigenfrequency equation (i.e. Equation (6.43)) if one assigns:

$$\tilde{\rho} = 7849.9\text{kg.m}^{-3}. \tag{6.45}$$

In other words, there is a finite detuning between the frequencies of the two string's modes that are inherent in the simulation. This detuning is only noticeable in the most perfect case. Admittedly, this represents a flaw of the numerical scheme but in practice, such system is highly unprobable and would simply be restricted to theoretical studies. It would require not only the same string's parameter, but the corresponding oscillators as well. For the purpose of this thesis, where the detuning between the string's modes is a main subject of study, the flaw of this scheme is not a concern. Detuning would have been artificially introduced anyway, as it is discovered to be present in a physical system (see Chapter 4.4).

Table 6.10: Frequencies for Case I as obtained from Equation (6.43) and MONTJOIE.

	Frequency (Hz)								
Equation (6.43)	147.4		221.2		356.6		571.0		793.1
MONTJOIE	147.4	**160.1**	221.2	**289.9**	356.6	**489.9**	57.01	**728.9**	793.1

Table 6.11: Frequencies for Case II as obtained from Equation (6.43) and MONTJOIE.

	Frequency (Hz)								
Equation (6.43)	148.8	161.4	221.5	292.3	360.6	504.5	577.7	737.1	803.3
MONTJOIE	148.8	161.4	221.5	292.3	360.6	504.5	577.7	737.1	803.3

Table 6.12: Frequencies for Case III as obtained from Equation (6.43) and MONTJOIE.

	Frequency (Hz)								
Equation (6.43)	140.2	153.9	212.0	287.0	356.6	498.4	570.9	728.8	793.1
MONTJOIE	140.2	153.9	212.0	287.0	356.6	498.4	570.9	728.8	793.1

Table 6.13: Frequencies for Case IV as obtained from Equation (6.43) and MONTJOIE.

	Frequency (Hz)									
Equation (6.43)	223.8	237.4	445.3	474.6	661.9	711.6	871.9	947.8	1077.5	1181.9
MONTJOIE	223.8	237.4	445.3	**474.7**	661.9	711.6	871.9	947.8	1077.5	1181.9
Equation (6.43)	1284.5	1401.1	1481.1	1527.2	1668.5	1728.8	1869.1	1943.6	1990.3	
MONTJOIE	1284.5	1401.1	1481.1	1527.2	1668.5	1728.8	1869.1	1943.6	1990.3	

Table 6.14: Frequencies for Case V as obtained from Equation (6.43) and MONTJOIE.

	Frequency (Hz)									
Equation (6.43)	226.2	241.0	450.1	481.7	669.0	721.8	881.2	960.7	1089.1	1197.1
MONTJOIE	226.2	241.0	450.1	481.7	669.0	721.8	881.2	960.7	1089.1	1197.1
Equation (6.43)	1297.9	1419.0	1482.2	1551.3	1675.7	1762.1	1872.0	1981.5	1997.7	
MONTJOIE	1297.9	1419.0	1482.2	1551.3	1675.7	1762.1	1872.0	1981.5	1997.7	

6.3 Summary

In this chapter, two numerical schemes implemented in MONTJOIE are presented. The general scheme that was proposed by Chabassier [75] is used for systems that do not include an additional oscillator, such as a simple S100-B100 and S101-B101

system. On the other hand, the extended scheme that is proposed in this PhD thesis is used for systems that solve for an additional rotational oscillator. Examples of them include the S100-B101, S200-B201 and the most complex S212-B213 system. The schemes written for S100-B100, S100-B101 and S200-B201 are all successfully validated by comparing the frequencies extracted from the displacement signals against theoretical eigenfrequencies obtained from Section 5.2.
A short manual intended for MONTJOIE users is also included as Appendix B.

7

Measurements and simulations of a lumped bridge coupled to a string

In Chapter 5, various models coupling a lumped bridge to a string are proposed and they are numerically validated in Chapter 6. The idea is to develop a numerical model that can be used to compare against experimental findings *qualitatively* so as to understand the mechanism behind any observed phenomenon. The chapter begins with the presentation of the experimental setup in Section 7.1, followed by the necessary identification of modelling parameters in Section 7.2 and concludes with the findings from experiments and numerical simulations in Section 7.3.

7.1 Experimental setup

The experimental test bench, as shown in Figure 7.1, is based on earlier string's experiment which was previously detailed in Chapter 4 where the string was terminated by the collet-imitating clamps at both end to imitate fixed-fixed boundary conditions. For the lumped bridge experiment, the string is strung over a bass bridge cutout in a zig-zag pattern. The bass bridge is 51mm wide, 30mm tall and 20mm deep. The string's vibrating length is reduced as compared to the fixed-fixed configuration. It also changes its boundary condition at one end from a fixed boundary condition (see Figure 7.2a) to a more complicated zig-zag boundary condition (see Figure 7.2b). In a fixed boundary condition, vibration of the string is restricted in all directions as it is held in place by the clamp. On the other hand, the zig-zag pattern is a common method used to couple strings to the bridge in a piano. In such configuration, the string is restricted by two angled bridge pins. To further imitate the setup of a piano, the string is slightly elevated by the lumped bridge, resulting in a vertical downbearing force applied onto the bridge. Due to the downbearing force, the string is no longer coupled to just the lumped bridge, but also the steel

plate. The implication of such setup will be discussed further in Section 7.2.2.

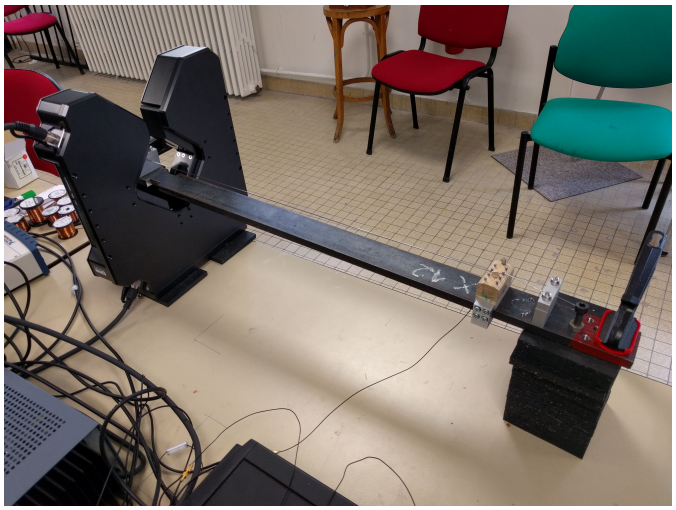

Figure 7.1: Actual experimental setup of a string coupled to a lumped bridge.

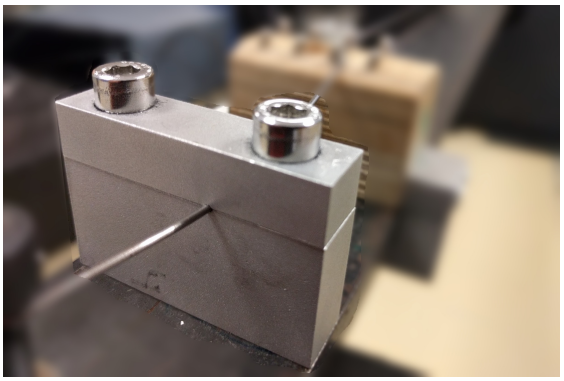

(a) Fixed boundary condition using a clamp.

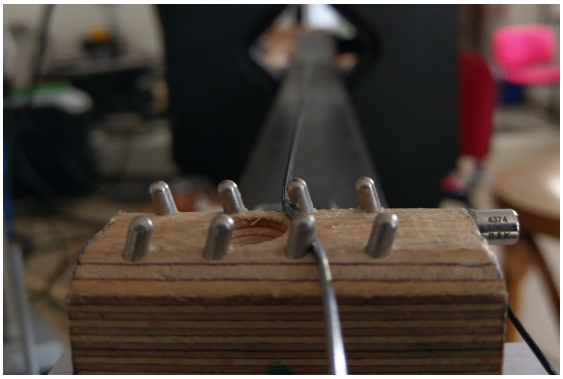

(b) Zig-zag boundary condition.

Figure 7.2: Boundary conditions (a) before and (b) after the bridge is mounted.

The lumped bridge used (see Figure 7.3) is originally part of the bass bridge of a dismantled Pleyel P-131 upright piano. A screw that attaches the lumped bridge to the rest of the soundboard assembly was removed, leaving a cavity in the middle of the lumped bridge. The bridge pins, however, was not removed. As the string was strung over in a zig-zag pattern, the lumped bridge is prone to being rotated around a vertical axis. To fix the lumped bridge in place, a custom-made G-clamp is fabricated such that the lumped bridge is snugly fitted between the clamp without any rotation. The bridge is further secured by tightening the bolts against itself carefully without permanently damaging it. The clamp is also made to have minimal

contact with the bridge so that the bridge is more freely to vibrate both translationally and rotationally.

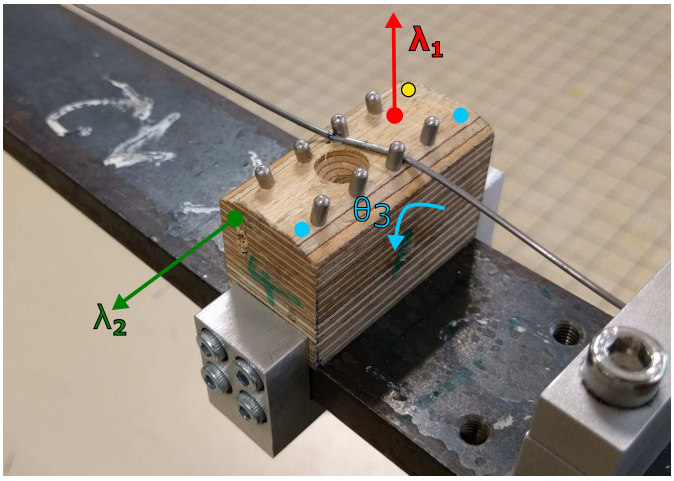

Figure 7.3: Close-up look of the lumped bridge. The bridge is further secured by tightening the bolts on the clamp. The top two bolts seen are pushed onto the bridge and the bottom two bolts are pushed onto the steel plate. Also shown are the two translational displacements of the bridge, λ_1, λ_2 and the respective in-plane rotational displacement θ_3.

Lastly, it is worth pointing out that the Keyence-9030D is set up such that the two measuring axes are 45° off the horizontal and vertical datums as shown in Figure 7.4. Thus the two measuring axes, named "H2" and "H1" are denoted as 0° and +90° respectively (see dashed lines in Figure 7.4). As a result, the vertical and horizontal datums (solid lines in Figure 7.4) are at +45° and -45° respectively. From Section 5.1.5, one could prescribe an angular offset γ between the string's polarisations and the bridge's axes (which is defined to be the vertical and horizontal datums). An example of this γ is also shown in Figure 7.4 and defined as the angle between the solid line (i.e. datum) and the dashed line (i.e. string's polarisation). As a reminder, the orientation of the angles can literally be mirrored, depending on which side it is being viewed on.

7.2 Parameter identification

To reconstruct the numerical model presented in Chapter 5, it is necessary to obtain the input parameters for the string and the lumped bridge. For the string, it is important to determine its material parameters, i.e. viscous damping parameters and Young's modulus. Some parameters specific to the set up are also determined, such as the string tension and most importantly its polarisation angle. The polarisation angle will determine the angular offset γ between the string's axes and the bridge's axes (see Figure 7.4). On the other hand, the lumped bridge is modelled as

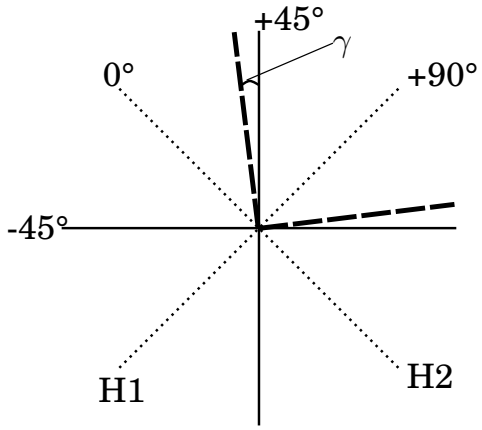

Figure 7.4: Illustration of the various angles in the experimental set up. The measuring axes H2 and H1 lie on 0° and +90° (dotted lines). The vertical and horizontal datums are +45° and -45° respectively (solid lines). Also shown is an example of angular offset γ between the string's polarisations (shown as dashed lines) and the bridge's axes (vertical and horizontal datums).

simple harmonic oscillators of different directions. Thus, its modal mass, damping and stiffness will have to be determined experimentally as well.

7.2.1 String

As some of the string characteristics could differ with and without the presence of the lumped bridge, careful choice needs to be made when selecting the string parameters for simulation. For instance, due to additional damping that will be introduced by the lumped bridge, the identification of the string's damping parameter needs to be performed for the string before the lumped bridge is mounted. After the string is mounted, the frequency of the string would increase due to decrease of string vibrating length. Thus, the tension value to be input into the numerical model needs to be based on the data after the bridge has already been mounted. For both instances, the string's polarisation angles are also identified.
To begin, a new set of string of the same type (1.3mm diameter, Stephen Paulello's string Type M [87]) used in Chapter 4 was mounted onto the setup with lower tension and are fixed at both ends without the bridge. To identify the damping parameter, it is first necessary to identify the natural polarisation of the string using the same technique discussed in Section 4.2. To briefly summarise the technique, the string is lightly pulled using thin copper wire of diameter 0.05mm at one-third of the string length until the wire breaks and the string starts vibrating. A quick check of the linearity of the string vibration can thus be performed by observing the absence of modes of multiple of 3. Next, the string displacement is rotated to an angle such that the initial displacement is maximised in measuring axis H2 as is shown in Figure 4.3. The H2 and H1 displacements are then termed the "dominant"

and "orthogonal" signals and are analysed by the ESPRIT algorithm [88, 89]. At a certain angle, one of the modes will be strongly observed with high amplitude while the other mode will only be weakly excited. The angle when this is observed is thus the string polarisation angle and two of these angles will be observed in a string.

Figure 7.5 shows the amplitude plot of the two dominant and orthogonal modes, similar to Figure 4.4. The top plot shows the absolute displacement as extracted by ESPRIT and the bottom plot shows the ratio between the dominant and the orthogonal signals. The string polarisation angle corresponds to the angle where the ratio is the largest , i.e. when only one mode is very strongly excited with the other mode mostly negligible. It is found that the two polarisation angles are at -70° and +20° respectively, and they are different from what is observed in Section 4.2 which is at -85° and +5°. Both strings are being inspected on the same test bench using the same clamps as the fixed boundary conditions and the difference between the two test cases suggest that the polarisation angle of the string is indeed an intrinsic properties and is not influenced by the experimental setup.

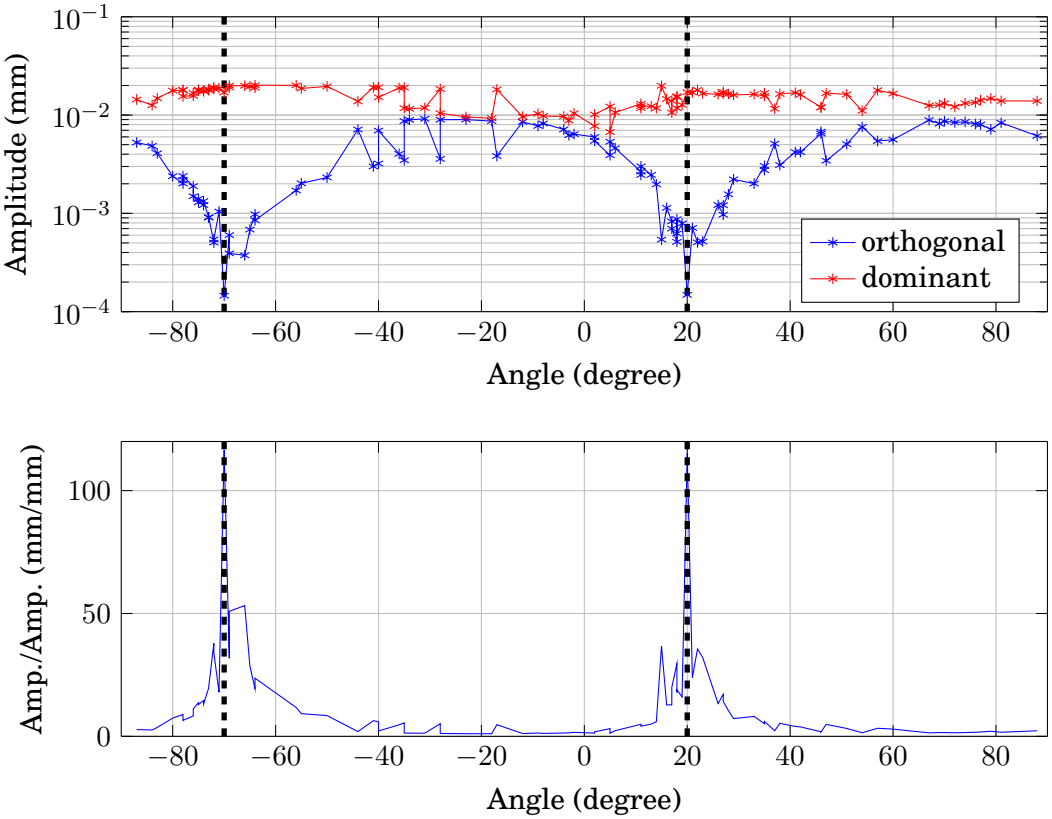

Figure 7.5: Amplitude of dominant and orthogonal modes from -90° to +90°. The top plot shows the absolute amplitudes and the bottom plot shows the ratio between dominant and orthogonal amplitudes.

Figure 7.6 shows the frequency extracted by ESPRIT algorithm, with the top showing the absolute frequency and the bottom the difference between both of them. Similar to Figure 4.5, there are fluctuations across the different angles excited but it can be observed that the difference between the two frequencies are the largest at their natural polarisation angles. Specifically, at +20°, the dominant mode is about 0.2Hz lower than the orthogonal mode. As such, at this angle, this polarisation is identified to be the lower fundamental mode of the string (u in Chapter 3) and the other the slightly perturbed mode (v in Chapter 3).

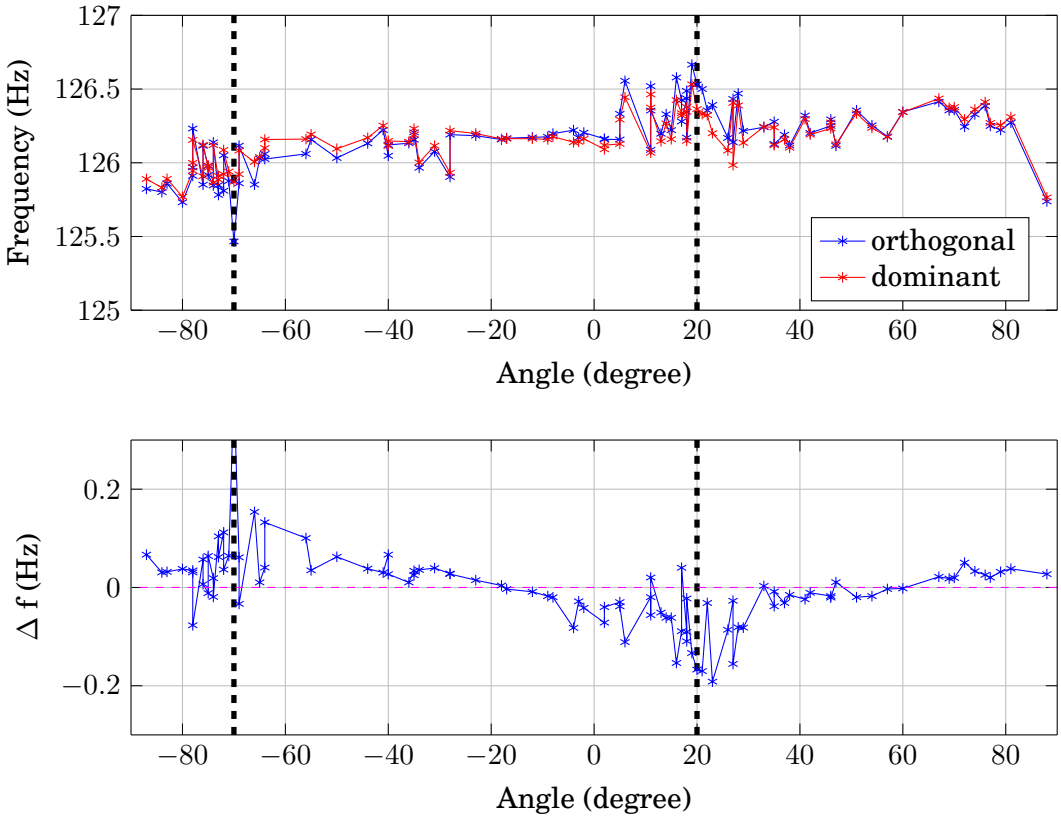

Figure 7.6: Frequency of dominant and orthogonal modes from -90° to +90°. The top plot shows the absolute frequencies extracted and the bottom plot shows the differences between dominant and orthogonal frequencies.

With the lower fundamental mode identified, it is then possible to identify the string's resonant frequencies and damping parameters. The string is plucked using the copper wire of 0.05mm at 20mm from one end of the string at +20° for 5 times. 16 string's resonant frequencies and corresponding damping constants are extracted using ESPRIT algorithm. The averaged experimental damping constants are shown in Figure 7.7 alongside with two fitted simple viscous damping models (SVM) as described by Equation (2.82). The model produced by least square fit

overestimates the damping of the lowest mode by a factor of three. Given that the accuracy of the lower modes are more important as these modes are more strongly excited, a custom fit model is proposed and used instead where the lower modes are more accurately modeled with overestimation only at higher modes. The custom fit model uses the following damping parameters:

$$R_u = R = v = R_\phi = R_\psi = 0.0957\text{s}^-1, \tag{7.1a}$$
$$R_w = 0.5\text{s}^-1, \tag{7.1b}$$
$$\zeta_u = \zeta_v = \zeta_\phi = \zeta_\psi = 7.10^{-9}\text{s}, \tag{7.1c}$$
$$\zeta_w = 10^{-9}\text{s}, \tag{7.1d}$$

with R_w and ζ_w as recommended in [84]. Using the same set of frequencies, one could also obtain the Young's modulus to be 185GPa, lower from nominal values of 200GPa for steel.

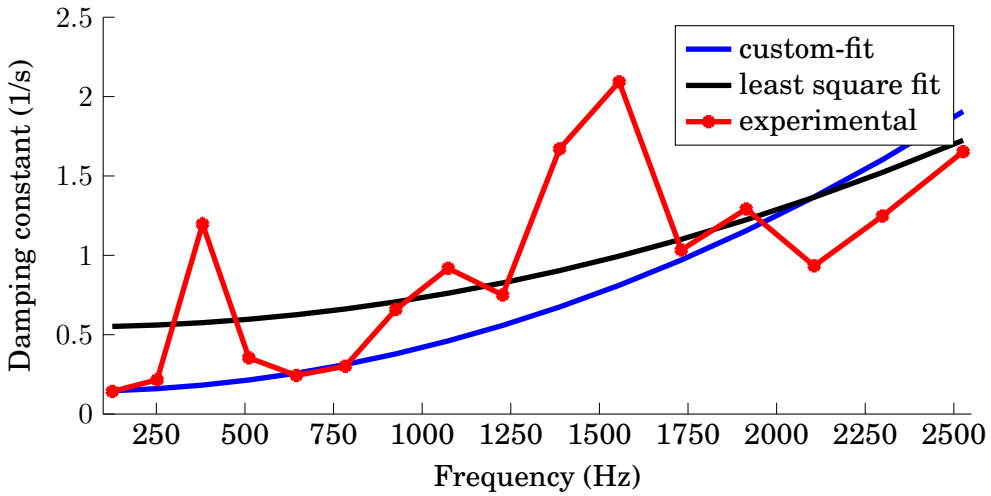

Figure 7.7: Comparison between experimental, least square fit and custom-fit damping constants.

As the string is fully characterised in a fixed-fixed condition, the bridge is mounted. To install the bridge, the string is slightly loosen before it is tighten again when the bridge is in place. As the bridge is designated to be placed near one end of the string, there is a safety concern that the shorter end of the string could snap due to excessive tension. Another reason to loosen the string is that the zig-zag pattern of the bridge inflicts a permanent distortion on the string and a failure of installation (such as bridge gets dislodged before it is secured in the clamp) would mean redoing the experiment with a new set of string.
After the bridge is installed, the polarisation angle experiment and post-processing are repeated. Figure 7.8 and 7.9 show the amplitudes and frequencies of the dominant and orthogonal signals similar to what is shown in Figure 7.5 and 7.6. Im-

mediately, one can point out from the amplitude plot that the string polarisation angles have changed to +38° and -53 ° respectively. In other word, there is a 7-8° difference between the axes of the string polarisation and the axes of the lumped bridge which are in the vertical (+45°) and horizontal (-45°) plane. This difference is thus the angular offset γ that appears in the S212-B213 model of Equation (5.30) and is shown in Figure 7.4. Certainly, the introduction of the lumped bridge has brought a change to the string polarisation angle. However, it is not established if the change is relative where the lumped bridge will always offset the string polarisation angle by approximately +18° or the change is absolute where it would disregard any original string polarisation angle and fix the new angle to be in the vicinity of +38° and -53°. Additional experiments would need to be repeated several times to properly investigate and answer the question.

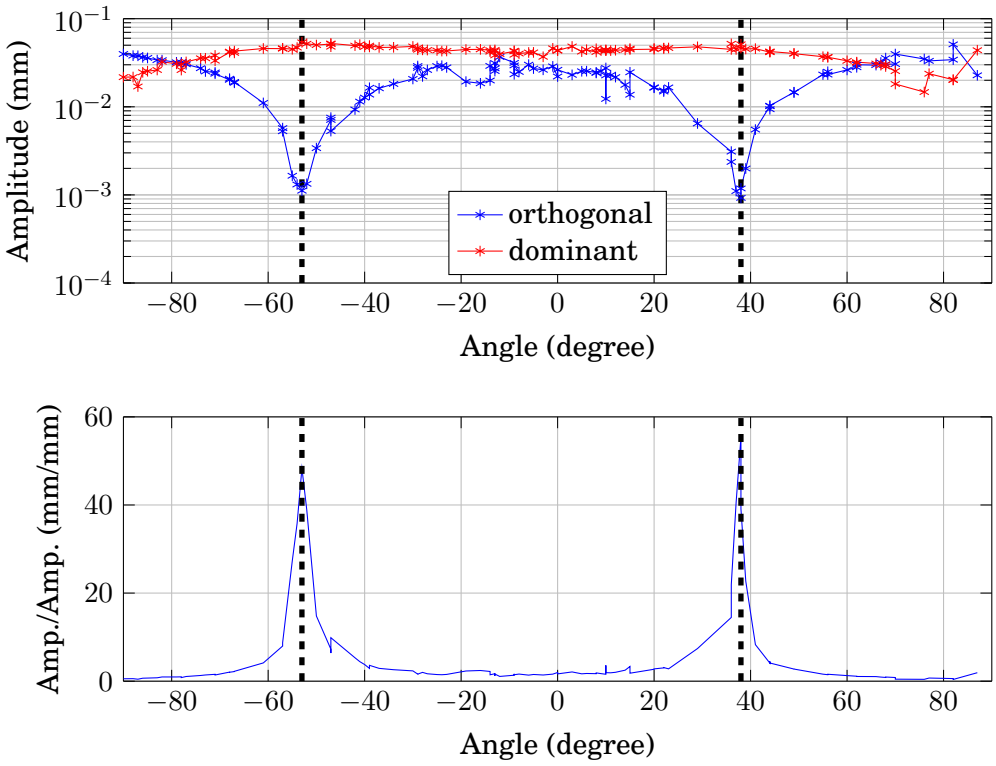

Figure 7.8: Amplitude of dominant and orthogonal modes from -90° to +90°. The top plot shows the absolute amplitudes and the bottom plot shows the ratio between dominant and orthogonal amplitudes.

In addition to the change in polarisation angle, there are also a few differences when the pair of Figure 7.8 and 7.9 (i.e. after the bridge is mounted) is compared to Figure 7.5 and 7.6 (i.e. before the bridge is mounted). In Figure 7.8, at +70° to +90° and from -90° to -80°, the recorded orthogonal amplitudes exceed the dominant amplitudes. The two regimes are essentially continuous, as anything outside of -90° and

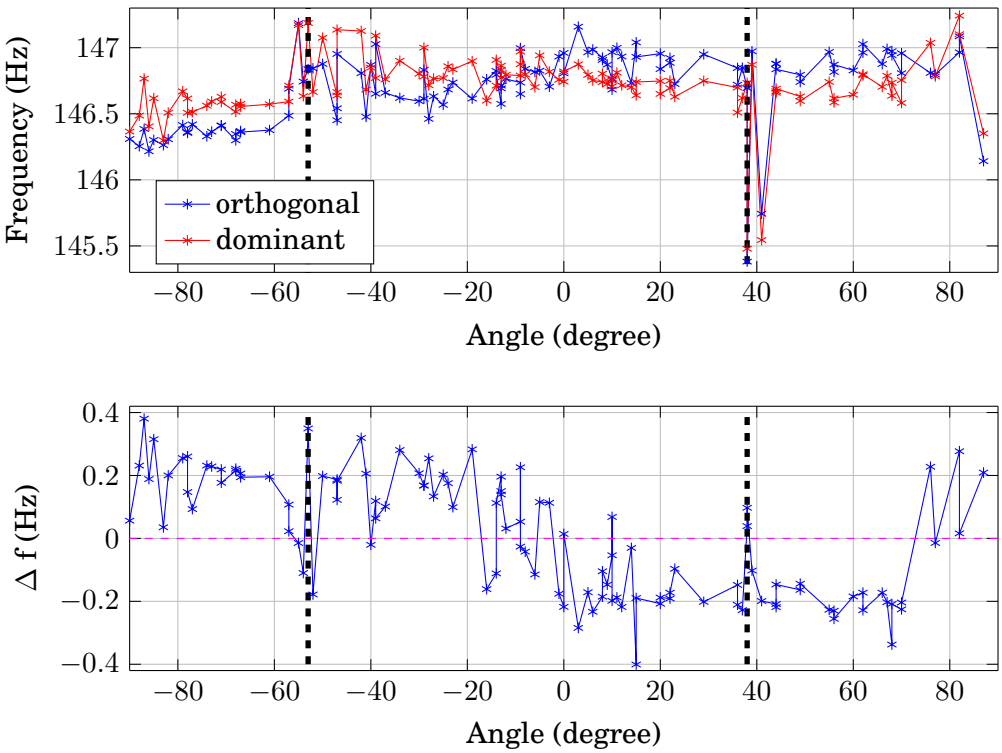

Figure 7.9: Frequency of dominant and orthogonal modes from -90° to +90°. The top plot shows the absolute frequencies extracted and the bottom plot shows the differences between dominant and orthogonal frequencies.

+90° can be projected inside this range but with a negative initial amplitude. The reason why the orthogonal amplitudes would record larger dominant amplitudes are down to the method used to obtain the plot. As explained in Section 4.2, the ESPRIT alrogithm is only fed with a short 0.3s signal. For consistency purposes, this is taken to be when the orthogonal signal has the largest amplitude. This method ultimately works fine for a fixed-fixed string scenario as the orthogonal amplitude is always small. When the bridge is coupled to the string, the double polarisation phenomenon is much more pronounced such that even though the excitation begins in the -90° plane, the out-of-plane displacement can sometimes be larger than the in-plane displacement as is shown in Figure 7.10. In essence, this shows that the introduction of the bridge would encourage a stronger development of the double polarisation effect as such crossovers were not presented in Figure 7.5.

Another observed difference is between Figure 7.6 and 7.9. In Figure 7.6, the largest difference between the two frequencies of the dominant and orthogonal modes is observed in the vicinity of the string polarisation angle (+20° and -70°) as a peak. However, in Figure 7.9, the largest difference between the two frequencies exist over a wider range that roughly centers around its polarisation angle (+38° and

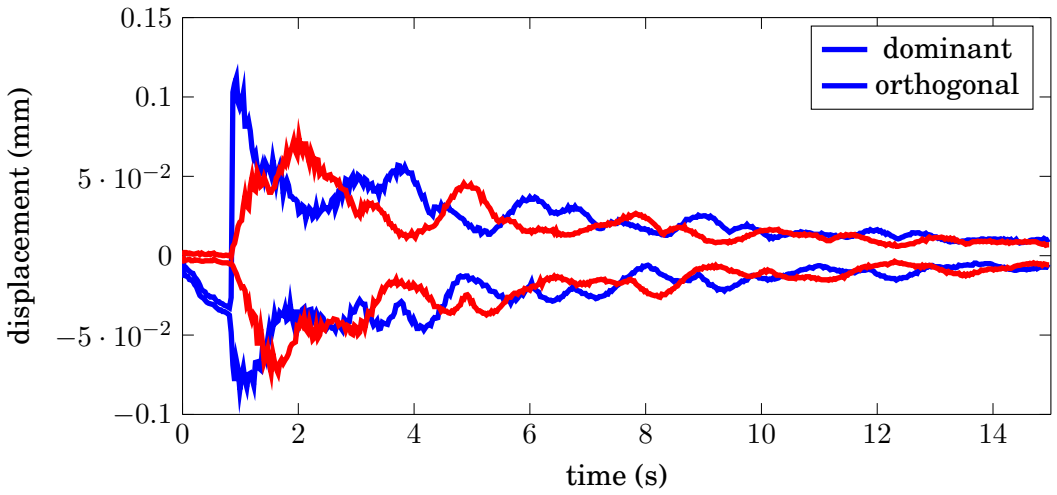

Figure 7.10: Wave envelope of the displacement-time signal for the dominant and orthogonal modes with excitation beginning in the -90° plane with a temporal resolution of 0.03s.

-53°)). Instead of a peak, a plateau is observed, notably between 0° to +70°[1]. Using the same angular reference in Figure 7.4, the string would come into contact with the top surface of the bridge at approximately -135° (or in other word, +45°). As the contact surface is more regular, it is perhaps why the plateau in that vicinity (+20° to +70°) is more flat compared to the one between -90° and -20°. Nonetheless, since the plateau only appears after the bridge is mounted (as it is not observed in Figure 4.5), a further study using similar experimental techniques could be warranted to further understand the zig-zag boundary condition.

Lastly, the introduction of the lumped bridge introduces a strongly observed detuning of 0.2Hz between the string modes, in which this frequency difference is adopted for subsequent numerical simulations. The choice of detuning is a dilemma where it could be defined in as the differences between the dominant and orthogonal frequencies at the polarisation angles (in which it would be +0.2Hz at -53° and -0.2Hz at +38°) or the differences between the absolute frequencies of the dominant mode at both -53° and +38°. Using the latter definition, the detuning could range between 0.2Hz to 0.4Hz if averaged frequencies around the polarisation angles are used for the calculation. As a first assumption, the minimum detuning value of 0.2Hz is adopted.

Using the same method in Section 4.3, the tension and the Young's modulus of the string are also determined. Up to 16 averaged frequencies are identified over 5 sets of data and a tension of 330.161N is identified with a corresponding Young's

[1]Essentially, what is observed between 0° to +70° is an "anti-plateau", like a flat seabed. The term "plateau" is used simply to mean a flat region rather than an elevated region, as is its definition as a geographic feature.

modulus of 181GPa.
To summarise, in this section, the following string parameters are identified:

- Angular offset between string and bridge, γ: +7°,
- String tension: 330.161N,
- String damping: see Equation (7.1) and Figure 7.7,
- Young's modulus: 181GPa but not used in simulation.

7.2.2 Oscillators

In Section 5.1.5, a complete S212-B213 system has been proposed where a string with 5 variables (2 translationals, 1 longitudinal, 2 rotationals) is coupled to a lumped bridge consisting of 6 oscillators (2 translationals, 1 longitudinal, 3 rotationals). There is an angular offset, γ between the two string polarisations (i.e. translational displacements) and the two translational oscillators (see Figure 5.6). However, to study the double polarisation of the string, the model can be simplified to a S200-B201 system, such as those described in Section 5.1.4 yet retaining the angular offset. Essentially, the general form of Equation (5.30) remains identical but the number of variables is reduced, such that for the string variables $\mathbf{q} = [u \quad v]^T$ and for the lumped bridge variables $\boldsymbol{\Upsilon} = [\lambda_1 \quad \lambda_2]^T$ and θ_3. The equations of motion become:

$$\mathbf{M_s}\ddot{\mathbf{q}} - \frac{\partial}{\partial x}\left(\mathbf{A}\mathbf{q}' + \mathbf{B}\mathbf{q} + \nabla\mathbf{H}(\mathbf{q}')\right) + \mathbf{C}\mathbf{q} + \mathbf{B^T}\mathbf{q}' + \mathbf{Y}\dot{\mathbf{q}} - \mathbf{Z}\dot{\mathbf{q}}'' = 0, \tag{7.2a}$$

$$\mathcal{M}_b\ddot{\boldsymbol{\Upsilon}} + \mathcal{S}_b\dot{\boldsymbol{\Upsilon}} + \mathcal{K}_b\boldsymbol{\Upsilon} = -\mathbf{F}_\mathbf{k}^\mathcal{R}, \tag{7.2b}$$

$$I_3\ddot{\theta}_3 + R_3\dot{\theta}_3 + J_3\theta_3 = F_1^\mathcal{R}h_2 - F_2^\mathcal{R}h_1, \tag{7.2c}$$

where:

$$\mathbf{M_s} = \begin{bmatrix}\rho A & 0\\ 0 & \tilde{\rho}A\end{bmatrix}, \quad \mathbf{A} = \begin{bmatrix}T_0 & 0\\ 0 & T_0\end{bmatrix}, \quad \mathbf{Y} = \begin{bmatrix}2\rho A R_u & 0\\ 0 & 2\tilde{\rho}A R_v\end{bmatrix}, \quad \mathbf{Z} = \begin{bmatrix}2T_0\zeta_u & 0\\ 0 & 2T_0\zeta_v\end{bmatrix},$$
$$\mathbf{B} = \mathbf{C} = \mathbf{0}, \quad \mathbf{H} = 0, \quad \mathcal{M}_b = \begin{bmatrix}M_1 & 0\\ 0 & M_2\end{bmatrix}, \quad \mathcal{S}_b = \begin{bmatrix}S_1 & 0\\ 0 & S_2\end{bmatrix}, \quad \mathcal{K}_b = \begin{bmatrix}K_1 & 0\\ 0 & K_2\end{bmatrix}. \tag{7.3}$$

The reduced coupling conditions as simplified from Equation (5.29) are:

$$\underbrace{\begin{bmatrix}\cos(\gamma) & -\sin(\gamma)\\ \sin(\gamma) & \cos(\gamma)\end{bmatrix}}_{\boldsymbol{\tau}}\begin{bmatrix}\dot{u}\\ \dot{v}\end{bmatrix} = \begin{bmatrix}\dot{\lambda}_1\\ \dot{\lambda}_2\end{bmatrix} + \begin{bmatrix}-h_2\dot{\theta}_3\\ h_1\dot{\theta}_3\end{bmatrix}, \tag{7.4}$$

and the resolved string forces onto the bridge are:

$$\mathbf{F}_\mathbf{k}^\mathcal{R} = \boldsymbol{\tau}[\mathbf{A}\mathbf{q}' + \mathbf{B}\mathbf{q} + \nabla\mathbf{H}(\mathbf{q}') + \mathbf{Z}\dot{\mathbf{q}}']_{x=L}. \tag{7.5}$$

For the study of double polarisation, the reduced S200-B201 system is chosen because it includes all the main oscillators the string polarisations can exchange energy with. The string is modeled as a pair of linear wave equations, each for one polarisation. The nonlinearity and stiffness effects of the string are not in consideration.
The oscillators' parameters that need to be identified are essentially its mass (or mass moment of inertia), damping and stiffness, i.e. $\mathcal{M}_b$, $\mathcal{S}_b$, $\mathcal{K}_b$, I_3, R_3 and J_3. To achieve that, the lumped bridge is struck with a PCB 086C04 impact hammer and the bridge's acceleration is measured by Brüel & Kjær charge accelerometers type 4374. Referring to Figure 7.3, a single accelerometer is placed at the base of the red and green arrows to measure the vertical and horizontal motion of the bridge respectively.
For the rotational motions, two accelerometers are placed at the two end of the bridge (shown as blue dots in Figure 7.3) and the hammer is struck at the yellow dot. The relative difference between the two accelerations at both ends thus constitute a net rotation experienced by the bridge as inferred from Figure 7.11. The rotational acceleration can thus be deduced by:

$$\theta_3(t) = \frac{a_1(t) - a_2(t)}{L_{acc}}. \tag{7.6}$$

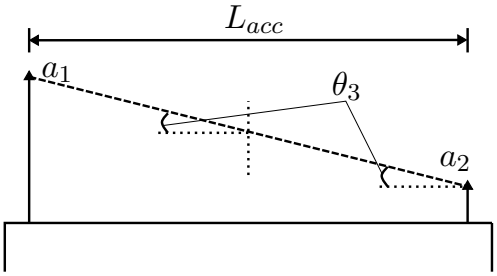

Figure 7.11: Illustration on how the rotational displacement of the bridge can be estimated from measuring the acceleration at two extreme points. The diagram shows only the top surface of the bridge.

For the vertical λ_1 and horizontal λ_2 motion, the hammer is struck as close to the accelerometer as possible (within 10mm from the accelerometer). Assuming that the force and acceleration measured act through the same point, the mobility of the bridge in these directions can be computed by:

$$Y_{ad}(j\omega) = \frac{a(j\omega)}{j\omega F_h(j\omega)}, \tag{7.7}$$

where Y_{ad}, a and F_h represent the mobility, accelerometer signal and hammer force respectively. Figure 7.12 shows the mobility for both the vertical and horizontal motions averaged over 4 sets of data. At very low frequencies, there are rigid body

motions for both motions. However, there is a resonant frequency at about 58Hz that is only observed in the vertical mobility. This is the fundamental frequency of the steel beam under the bridge, f_{sb}, as it can be approximated by the eigenfrequency equation for a simply-support beam:

$$2\pi f_{sb} = \pi^2 \sqrt{\frac{E_{sb} I_{sb}}{\rho_{sb} A_{sb} L_{sb}}}, \tag{7.8}$$

where E_{sb}, I_{sb}, ρ_{sb}, A_{sb}, L_{sb}^5 are the Young's modulus, second moment of area, density, area and approximate vibrating length of the steel beam respectively. Given that the beam has a width of 51mm, a height of 30mm and an approximate vibrating length of 0.7m, using nominal values where $E_{sb} = 200GPa$ and $\rho_{sb} = 8000kg/m^3$, the fundamental frequency of the steel beam f_{sb} can be identified to be 60.8Hz, which is very close to the 58Hz observed. As a result, the peak observed at 175Hz is identified as first the vertical bridge mode instead. As for the horizontal mobility, there are no obvious peaks. Ignoring the first 100Hz, there are three peaks identified at about 200Hz, 550Hz and 670Hz. It is plausible that the 200Hz peak originates from the vertical mode that is accidentally excited. Out of the 4 measurements taken, it is only detected in one of them. Thus, this peak is ignored and the horizontal bridge mode is identified at the next peak, i.e. at 551Hz.

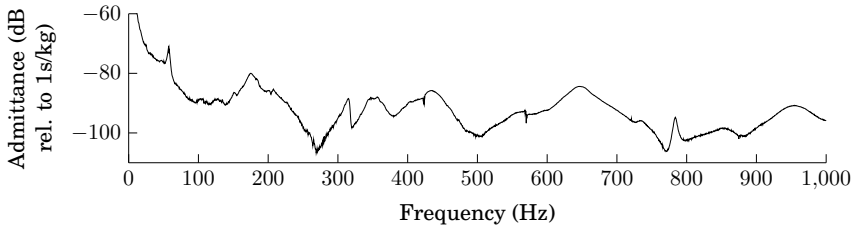

(a) Vertical motion.

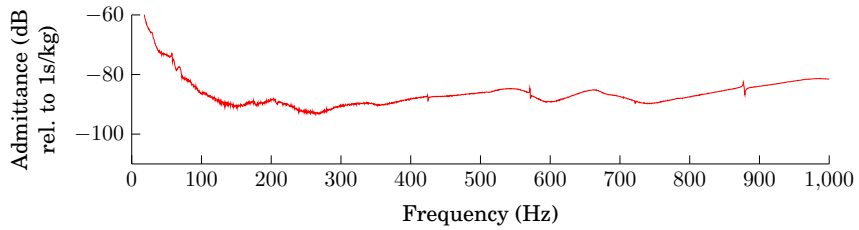

(b) Horizontal motion.

Figure 7.12: Admittance data for (a) vertical and (b) horizontal motion.

Figure 7.13 shows the averaged frequency responses of the estimated rotational accelerations for two different sets of data with each set of data containing 5 measurements. In the set of Data 1, two clear peaks are observed at 424Hz and 560Hz

respectively. However, they seem to be aligned with the string partials. To establish if it is a coincidence or whether the rotational modes could be influenced by the string's partials, the string is slightly tightened and the same procedure is carried out to measure the frequency responses again, and is labeled Data 2. Both data agreement very closely from one another, thus rejecting the hypothesis that the string's partials have an influence on the bridge modes. Even though there are two clear peaks defined, only the first one, i.e. at 424Hz is used as the rotational oscillator.

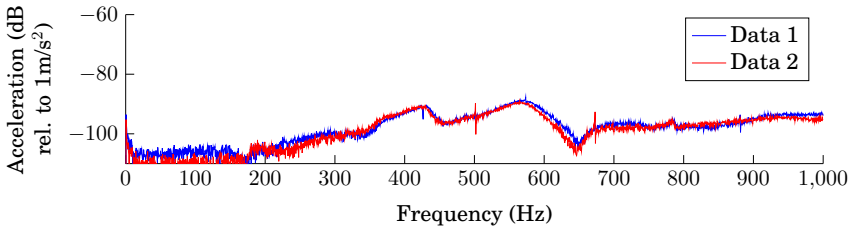

Figure 7.13: Frequency responses of the difference between two accelerometers, each with slightly different tension on the string.

An oscillator's frequency can be estimated by taking the square root of the quotient between the stiffness and the mass. For instance, the oscillator's frequency of λ_i can be computed by:

$$f_{osc,i} = \frac{1}{2\pi}\sqrt{\frac{K_i}{M_i}}, \quad \text{for } i = 1, 2. \tag{7.9}$$

However, knowing only the frequency is not sufficient as one can only know the ratio between the modal mass and stiffness. Fortunately, at first order, the modal mass can be estimated to be the actual mass of the system. The bridge itself weighs only 37g while the beam weights approximately 3kg. Since the beam modes are visible in the mobility data of the bridge motions, the mass of the system is chosen to be the mass of the beam, i.e. 3kg. The choice is further supported from the analysis in Section 5.2 where a low mass could cause a shift of the string's frequencies. This is not strongly observed in the experiment, thus further supporting the choice of 3kg over 37g. Consequently, as a first approximation, the mass of both vertical and horizontal oscillators are identified as 3kg and the corresponding stiffness can be estimated from Equation (7.9). Similarly, the mass moment of inertia of the rotational motion, I_3 can be computed by:

$$I_3 = \frac{M_{1,2}}{12}\left(L_x^2 + L_y^2\right), \tag{7.10}$$

where L_x and L_y are the height and width of the lumped bridge, which are 51mm and 30mm respectively. With I_3 known, the rotational stiffness J_3 can also be de-

termined by:

$$f_{osc}^{r} = \frac{1}{2\pi}\sqrt{\frac{J_3}{I_3}}. \tag{7.11}$$

Last but not least, the damping of the oscillators need to be identified. This is achieved by using the half power method. The method computes the difference between the two frequencies at 3dB below the peak of the mode in a power spectrum. Using that difference, Δf_i, the damping coefficients (in kg.s^{-1}) can be determined as [89]:

$$S_i = 2\pi M_1 \Delta f_i \quad \text{for} \quad i = 1, 2. \tag{7.12}$$

While the half power method is intended for mobility data, it is also used for the frequency responses of the rotational displacement. This is because at up to 1,000Hz, the force spectrum from the hammer is flat. As such, whether including the force spectrum or not would not have made much difference. Thus, the same method is also applied to the rotational data, where the damping R_3 can be obtained by:

$$R_3 = 2\pi I_3 \Delta f_r, \tag{7.13}$$

where Δf_r is the difference of the two frequencies at 3dB below the peak of 424Hz in Figure 7.13.
The identified oscillator's parameters are summarised in Table 7.1:

Table 7.1: Experimentally identified oscillators' parameters.

	Vertical	Horizontal	Rotational
Frequency	175.2 Hz	551.2 Hz	423.7 Hz
Mass	$M_1 = 3$ kg	$M_2 =$3 kg	$I_3 = 7.25\times10^{-4}$ kgm^2
Damping	$S_1 = 343.06$ kg/s	$S_2 =$1975 kg/s	$R_3 =$0.2118 kgm^2/s
Stiffness	$K_1 = 3.635 \times 10^7$ kg/s^2	$K_2 = 3.598 \times 10^7$ kg/s^2	$J_3 =$5138 kgm^2/s^2

7.3 Results and discussion

7.3.1 Experiment on the coupled string-bridge system

The main idea of conducting the experiment is to observe the double polarisation and identify the cause behind it. The system is excited by plucking the string using the copper wire method where a thin wire of 0.07mm is pulled until it breaks at 168mm from the bridge end. The use of a thin copper wire would ensure the string vibration stays in the linear regime. Two types of excitations are made, one vertically and one horizontally. The vertical excitation would be similar to how a hammer strikes the string in a piano where most energy is concentrated in this direction. The horizontal excitation would act as an opposite case where most energy would be input at an orthogonal plane to the vertical plane. Figure 7.14 shows the root-mean squared (RMS) displacements of the string at 0.03m from the fixed

end. The RMS displacements u_{rms} are sampled over a windows of 50ms where the signals are calculated by:

$$u_{rms} = \sqrt{\frac{1}{N}\sum_{n=1}^{N} u_n^2}, \tag{7.14}$$

where N is the total number of data points in the 50ms window.

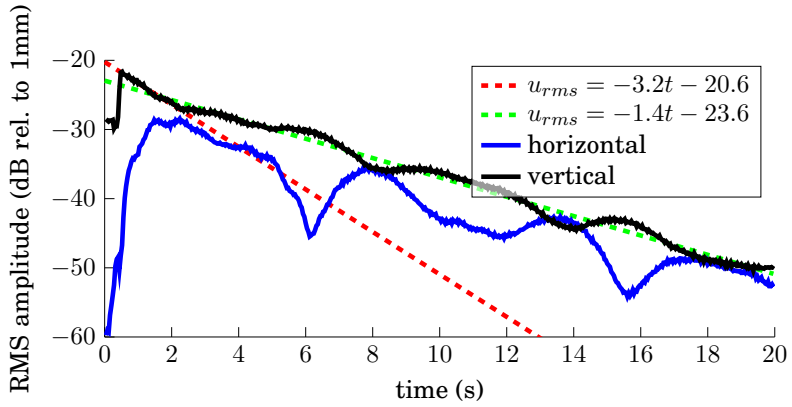

(a) Vertical excitation.

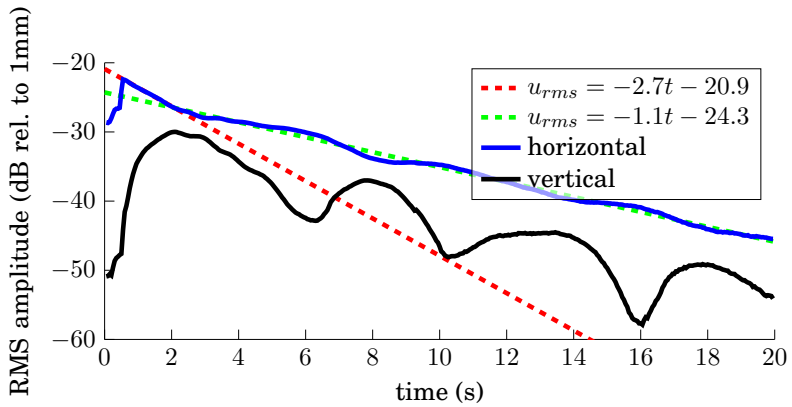

(b) Horizontal excitation.

Figure 7.14: RMS displacements of (a) vertical and (b) horizontal excitation. The RMS displacement is sampled over a window of 50ms.

In both cases, double polarisation is clearly observed. In Figure 7.14a where the string is excited vertically, horizontal displacement is initially very small but subsequently gains in amplitude until it is in the same order of magnitude as the vertical displacement. Similarly, as the string is pulled horizontally (see Figure 7.14b), the vertical displacement gains in amplitude but only within about 3dB of the horizontal amplitude. Such phenomenon is not surprising as from the study in Section 3.5, it is indeed possible to have double polarisation in the linear string motion as long

as there is a detuning between the two string's modes and they are both excited. However, the double polarisation effect is also further augmented by the addition of the bridge.

Figure 7.15 shows the RMS displacement of the string when it is excited at +27° before the bridge is mounted. From the result obtained in Section 7.2.1, the string had a natural polarisation angle at +20° and the excitation is essentially very similar as they are both excited at +7° from their natural polarisation. As a reminder, the string's natural polarisation angle after the bridge is mounted is +38° and pulling the string vertically would be exciting it at +45°. In Figure 7.15, the dominant signal represents the displacement in the plane where the excitation is made and the orthogonal signal represents the out-of-plane displacement. Comparing it to Figure 7.14a where both vertical and horizontal displacements are comparable, the orthogonal out-of-plane displacement still remains at least 3dB less than the dominant in-plane displacement. While the excitation is on a different string position, with a different string length and initial amplitude, it is nonetheless clear that qualitatively the addition of lumped bridge has introduced an extra path for the energy to be exchanged between the modes of the string.

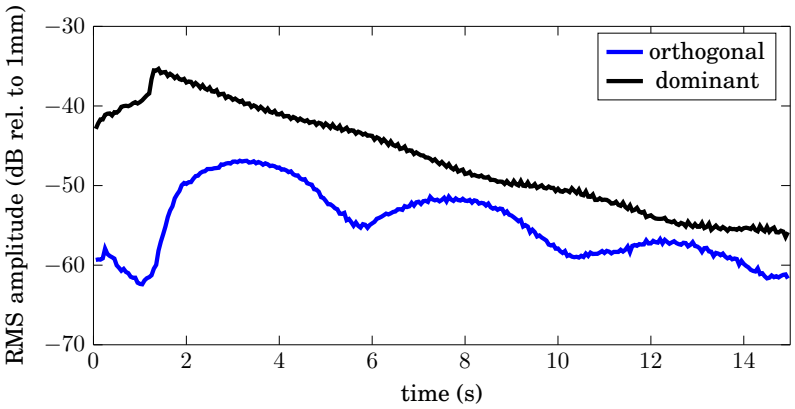

Figure 7.15: RMS displacements of a string with fixed-fixed boundary condition when excited at +27°, when the string natural polarisation falls on +20°. RMS value is sampled over a window of 50ms.

In addition to the double polarisation effect, double decay can also be observed in the two plots of Figure 7.14. In both figures, two straight line fit of the signals are obtained, one within the first 1.5s after the string starts vibrating (dashed red line), and one from after 1.5s of excitation until the 20th second of signal acquisition (dashed green line). The equations for these straight lines are shown respectively in the legend of the figures. For both cases, the string experiences a larger decay at the initial 1.5 seconds than during the subsequent signal, as indicated with a steeper gradient of the straight line. This is consistent with observation on a piano even for a single string struck by a hammer [28]. However, in Giordano's book [28], beats are

only observed for a multi-string setup where duplets or triplets of slightly detuned strings are struck at the same time. In Figure 7.14, beats are both observed on the vertical and horizontal excitation of a single string.

Weinreich attributed the double decay phenomenon of a vertically struck string to the presence of horizontal displacement [27]. Initial vertical displacement is transmitted to the bridge quickly forming the first sharp decay before the vertical displacement becomes comparable to the horizontal displacement and decays slowly. Giordano echoed this explanation and suggested that the horizontal displacement could be due to the movement of the bridge and soundboard [28]. Weinreich also made an analysis to demonstrate that double decay is present if there are two strings vibrating vertically at slightly detuned frquencies from one another [27]. This is because the two vertical string forces would eventually go out-of-phase and reduce the net energy transfer to the bridge, thus forming two different decay characteristics and beating. The same analysis involving two strings are also performed in more details by Chaigne and Kergomard [90].

This begs the question of why double decay and beats are both observed on the single string setup in Figure 7.14. The two-string analysis is actually applicable for a single string as well. A single string contains two oscillating modes and unless they are aligned perfectly with the bridge vertically and horizontally, there will always be two different string forces acting vertically onto the bridge. The string forces exerted vertically, like their corresponding string's polarisation, would be slightly detuned from one another, thereby achieving the beating and double decay characteristic proposed by Weinreich [27].

The double decay phenomenon is also contributed by the presence of lower oscillator modes in the vertical direction. As determined earlier in Section 7.2.2, the vertical oscillation of the lumped bridge can be represented by a harmonic oscillator with resonant frequency of 175.2Hz. On the other hand, the horizontal harmonic oscillator has a resonant frequency of 551.2Hz. Figure 7.16 shows the frequency responses of the two displacements when excited horizontally. It can be seen that most of the energy is concentrated on the first two modes (139.6Hz and 280Hz) whose resonant frequencies are close to the vertical oscillator's frequency of 175.2Hz. In contrast, the string mode closest to the horizontal oscillator's frequency is the fifth mode (568.4Hz) and it is almost 30dB less than the first two modes. Thus, the energy transfer to the bridge is also much less significant.

The presence of lower vertical oscillator mode also explains why a double decay can be observed even if the string is initially horizontally excited. Due to detuning, even if the string is horizontally excited, it would demonstrate double polarisation where vertical displacement gains in amplitude. It can be thought that the initial energy gained in the vertical displacement is subsequently leaked to the vertical oscillator, thereby constituting a higher decay, before transitioning to slower decay like the case of a vertical excitation. Since the energy is initiated in the horizontal plane, less energy would eventually be transferred to the lumped bridge compared to the vertically excited case, as evident from the higher amplitudes after 20 seconds. It

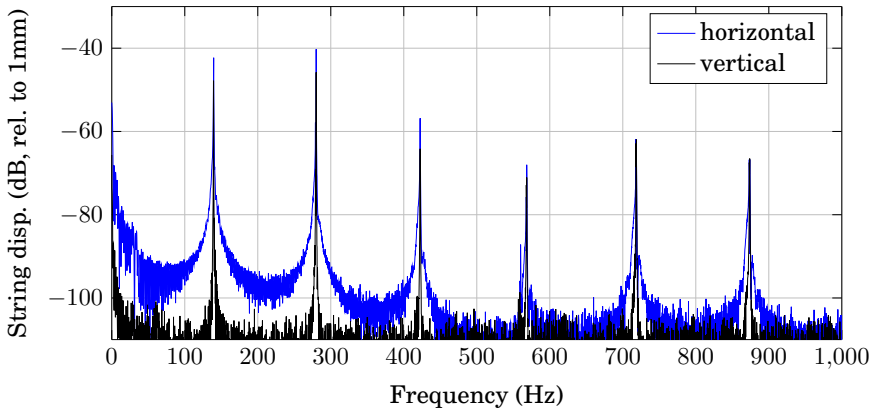

Figure 7.16: Frequency responses of the string displacements when it is excited horizontally.

can also be inferred from the overall lower decay rates as demonstrated by the less steep slope of both the straight lines depicting the decay rates in Figure 7.14b compared to Figure 7.14a.

7.3.2 Numerical simulations of the coupled string-bridge system

In Section 7.3.1, the double polarisation and double decay phenomena have been observed experimentally. The idea of this section is to conduct a series of numerical simulations to confirm that:

Observation I A single string with two slightly detuned fundamental modes can induce double decay with beatings if there is an angular offset between the string's natural polarisation and the bridge's oscillating direction. This angular offset can be described by the variable γ that appears in Equation (7.4).

Observation II Even if the string is excited horizontally, the energy of the string principally leaks through the vertical oscillator.

The simulation parameters used are all presented in Table 7.2. The choice of $\tilde{\rho}$ would ultimately result in a detuning of 0.2Hz between the two frequencies. The bridge offset h_1 and h_2 are obtained by considering the string termination point and the bridge mass centre. One might notice that there is no Young's modulus, shear modulus and Timoshenko's parameter. This is because the string is deliberately simulated with the ideal linear wave equation to minimise actual simulation time. Furthermore, since only the lower string modes are in concern and the simulation only aims to obtain a qualitative comparison against experiment, it is not a necessity to include the stiffness, longitudinal displacement and nonlinear behaviour between the two transverse modes.

Table 7.2: Parameters for the simulation.

Parameter	Value
String length, L (m)	0.608
String diameter, d (m)	0.0013
String density, ρ (kg/m^3)	7850
String density, $\tilde{\rho}$ (kg/m^3)	7828.6
String tension, T_0 (N)	330.161
String damping	see Equation (7.1)
Initial condition, amplitude (m)	7.7 $\times 10^{-4}$
Initial condition, location (m)	0.168 from bridge end
Initial condition, excitation angle	-7 ° (vertical), +83° (horizontal)
Angular offset, γ	7 °
Time step, Δt (s)	2.5 $\times 10^{-6}$
Total time (s)	20
Number of elements (order 4)	50
Oscillator parameters	see Table 7.1
Bridge offset,h_1 (m)	0.01
Bridge offset, h_2 (m)	0.001

Figure 7.17 shows the simulated RMS displacement of the vertically and horizontally excited string coupled only to the vertical oscillator of 175.2Hz, constituting what could be known as a S200-B100 system. Straight line fits are obtained for the first 1.5s of the signal, and the rest of the 18.5s. Compared to Figure 7.14, the double decay is much more subtle (or perhaps non-existent in the horizontal case) and the interaction between the two displacements are comparatively weak as they are at least 10dB apart. Adding the horizontal and rotational oscillators (which makes it a S200-B201 system) do not introduce any tangible difference (and is thus not shown for brevity).

To simulate a stronger interaction between the two displacements, the angular offset is artificially increased from +7° to +22° and the results are as shown in Figure 7.18 where only the vertical oscillator is used. Compared to Figure 7.17, double decay is more obvious for both types of excitations. In Figure 7.18a, the horizontal and vertical displacements are of similar amplitude and in Figure 7.18b, the vertical displacement is at least 4dB below from the horizontal displacement. Although the decay rate is not the same and the observed beating is faster, these results are qualitatively consistent with the experimental results in Figure 7.14. Adding the horizontal and rotational oscillators do not give any tangible differences other than increasing the decay very slightly for both the initial and second decays. Again, the plots for these results are not shown for brevity as they are virtually identical to Figure 7.18.

Revisiting Observation I, while the observation remains true, it is important to add on that having an angular offset γ does not necessarily induce an *observable* double

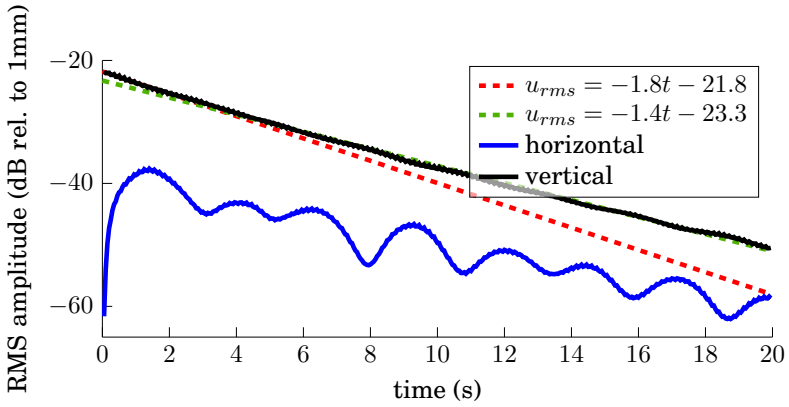

(a) Vertical.

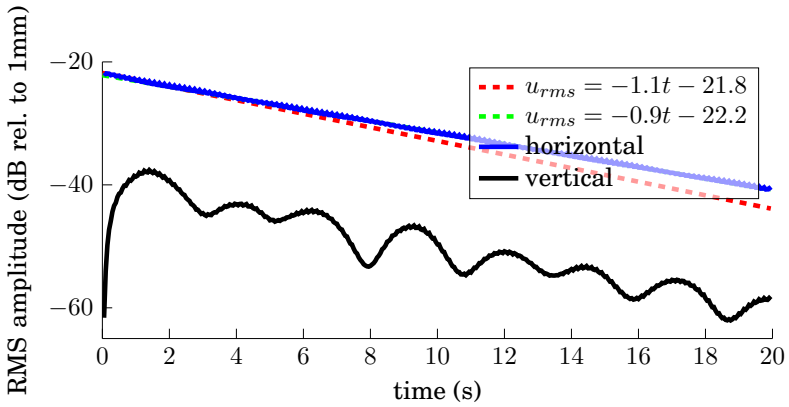

(b) Horizontal.

Figure 7.17: RMS displacements of (a) vertical and (b) horizontal excitation in simulation with parameters from Table 7.2 and using only vertical oscillator. The RMS displacement is sampled over a window of 50ms.

decay for a string with two slightly detuned fundamental frequencies. The double decay is only obvious when the out-of-plane displacement would gain comparable energy compared to the in-plane displacement. This happens naturally in the experiment with an angular offset of $\gamma = +7°$ but in simulation, an additional +15° correction needs to be applied to γ for a qualitative reproduction of the experiment. This discrepancy might be accounted by the seemingly complex zig-zag boundary condition. As the string is not entirely secured on the bridge at the contact point, it is possible that micro-slipping occurs between the string, the top surface of the bridge and the bridge pin [92]. This micro-slipping could affect the transfer of energy between the vertical and horizontal displacements in which the out-of-plane displacement would gain more energy from the zig-zag boundary condition than it would otherwise had.

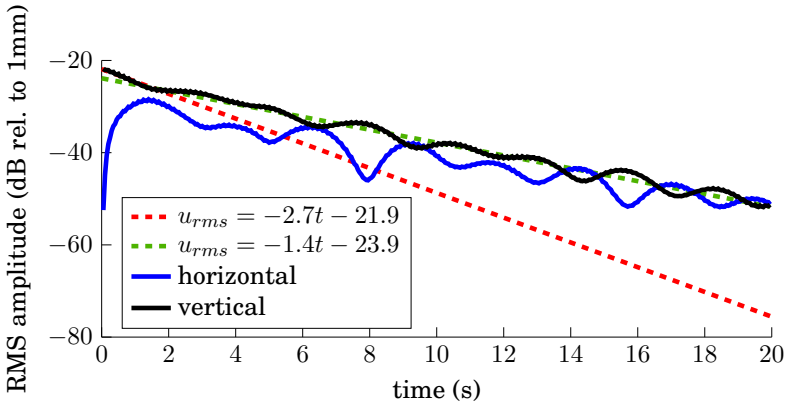

(a) Vertical.

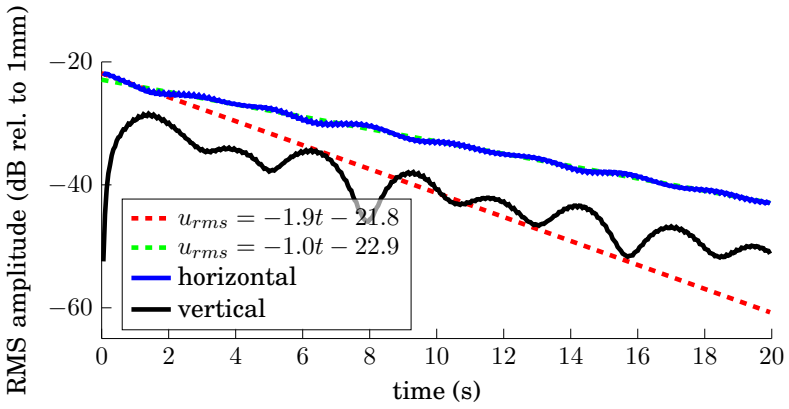

(b) Horizontal.

Figure 7.18: RMS displacements of (a) vertical and (b) horizontal excitation in simulation with parameters from Table 7.2 (except that $\gamma = +22°$) and using only vertical oscillator. To compensate for the change in angular offset, the initial condition angle is also changed to -22° and +68° for vertical and horizontal excitation respectively. The RMS displacement is sampled over a window of 50ms.

Another plausible discrepancy is that the oscillator's parameters are incorrect. Indeed, current work resorts to several simplifications to obtain the simulation parameters. For instance, the modal mass of the horizontal λ_2 oscillator is assumed to be 3kg, which might not be exactly correct. A proper characterisation of all the oscillators would be beyond the scope of the thesis but an idealised test case can be performed. Reusing $\gamma = +7°$, a vertically excited string is coupled to the same vertical oscillator and a less massive and stiff horizontal oscillator. The idea is to allow more movement horizontally to observe if that would allow more energy gained in the horizontal direction. This less rigid oscillator has the same frequency of 551.2Hz as the previous horizontal oscillator, but its mass and stiffness are both lowered by

a factor of 10, with a correspondingly adjusted damping coefficient. The oscillator parameters are now:

$$M_2 = 0.3\text{kg}, \quad S_2 = 197.51\text{/s}, \quad K_2 = 3.7 \times 10^7\text{N/m}, \tag{7.15a}$$

and the simulation results are as presented in Figure 7.19. Compared to Figure 7.17a, one could see that there is virtually no difference in the vertical displacement but horizontally, the string vibrates in a different pattern (horizontal displacement Figure 7.17a is plotted together for easy comparison). It is nonetheless still about 10dB less than the vertical displacement and as such double decay is not very obvious. In other word, it appears that artificially modifying the angular offset would still be a better choice in term of promoting energy exchange between the vertical and horizontal displacements of the string. To further investigate the horizontally ex-

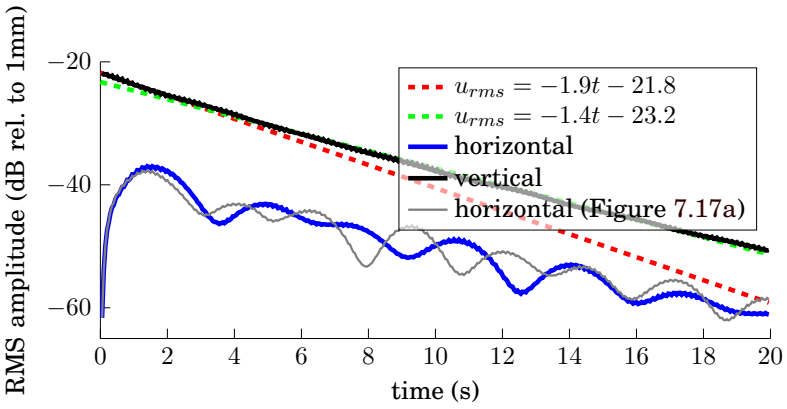

Figure 7.19: RMS displacements of vertically excited string in simulation with parameters from Table 7.2 but with a less rigid horizontal oscillator (see Equation (7.15) for parameter).

cited string, a simulation is made where only the horizontal oscillator is considered and the RMS displacements are as shown in Figure 7.20. An extremely massive and stiff undamped vertical oscillator is included where $M_1 = 10^7$kg, $S_1 = 0$ and $K_1 = 10^{18}$N/m with its natural frequency at about 50,300Hz. This is in effect a fixed boundary condition on the vertical displacement at the bridge and string contact point. A rotational oscillator remains not included in this analysis.
From Figure 7.20, single decay with beats is observed. There is an initial sharp drop before the decay slows down. This is because the string loses its energy to the horizontal oscillator before the energy is passed to the vertical displacement. As the horizontal displacement decreases due to the increase of vertical displacement, the energy transmitted to the horizontal oscillator slows down until the horizontal displacement increases again in which more energy is being transmitted through the oscillator. The pattern repeats without a global double decay.
The difference between the vertically excited string with only one vertical oscillator(see Figure 7.18a) and its horizontal counterpart (Figure 7.20) is that the os-

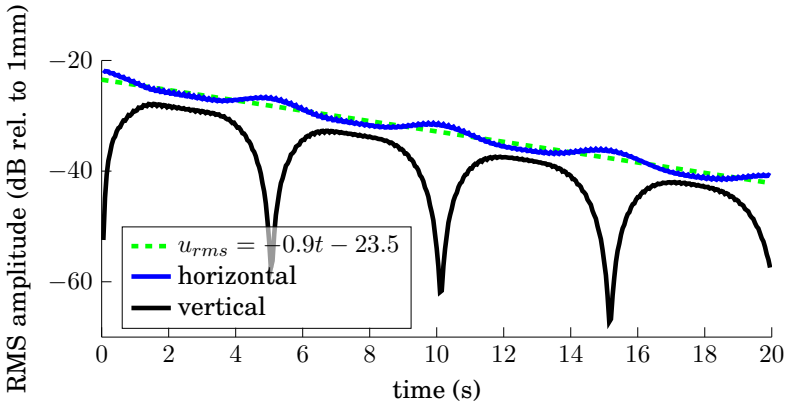

Figure 7.20: RMS displacements of horizontally excited string simulated with parameters from Table 7.2, except that $\gamma = +22°$ and with an extremely massive and stiff undamped vertical oscillator (i.e. $M_1 = 10^7$kg, $S_1 = 0$ and $K_1 = 10^{18}$N/m).

cillator the string is attached to have different frequencies (175.2Hz for vertical oscillator and 551.2Hz for horizontal oscillator). Since it has been shown in Figure 7.16 that energy is mostly concentrated at the lower modes of the string, having a similarly tuned vertical oscillator provides an outlet of the string's energy. This is because when the mobility is large, more energy would be lost to the oscillator [90]. The numerical results thus suggest that the manifestation of double decay is dependent on the closeness of the oscillator frequency to the fundamental frequency of the string. This in turn confirms that *even if the string is excited horizontally, the energy of the string principally leaks through the vertical oscillator* (Observation II) as is prefaced at the beginning of this section.

Lastly, the detuning between the two string's modes is manipulated to identify if it can be another source to promote double polarisation, and thus displaying more prominent double decay. Figure 7.21 shows the RMS displacements when the string is vertically excited and is coupled to a single vertical oscillator. The angular offset γ is kept at the experimentally determined 7° and the difference between the two string's frequencies have doubled from 0.2Hz to 0.4Hz. The horizontal displacement in Figure 7.17a is also replotted for easy comparison. Comparing Figure 7.21 to 7.17a where the only difference between them is the detuning, double decay remains difficult to spot. This is because the horizontal displacement is still 10dB lower than the vertical displacement. The only obvious change is the beatings of the horizontal vibrations, which has become more frequent. In other word, a larger detuning does not contribute to a noticeably prominent double polarisation and double decay. In an actual piano, there are a lot of modes in a piano soundboard that could correspond to a vertical oscillator. Considering only the bass unison strings, it is very likely they would have an angular offset with the bridge and are detuned within the two fundamental modes themselves. As they are struck by hammers,

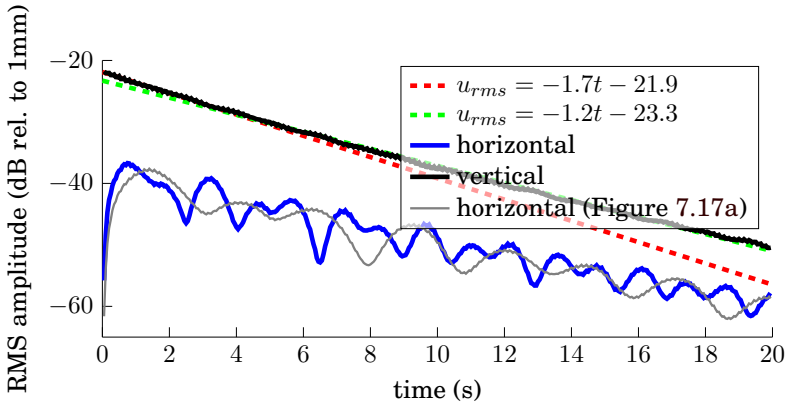

Figure 7.21: RMS displacements of vertically excited string in simulation with parameters from Table 7.2 (except that $\tilde{\rho} = 7807.3\text{km/m}^3$ forming a difference of 0.4Hz between the two frequencies). Only vertical oscillator is used.

they exhibit both double polarisations and double decays due to the detuning, angular offset and the presence of vertical oscillators of similar frequencies. The same effect is likely to occur for notes with duplets and triplets of strings as well. In addition to the above mechanism, they are also affected by closely detuned strings within their own groups of duplets or triplets. Without any further experiments or simulations, it is not clear which mechanism could be dominating the manifestation of the double decay effect.

7.4 Summary

In this chapter, an experiment is set up to investigate the vibration of the string coupled to a lumped bridge. The following outcomes are obtained:

- As the string is strung over the bridge, it exhibits a detuning of 0.2Hz and it has an angular offset, γ, of +7° between the string axes and the bridge axes (vertical and horizontal datums).
- By measuring the mobility and frequency responses of the lumped bridge, the parameters of 3 oscillators (vertical, horizontal and rotational) are identified.
- By initially pulling the string vertically and horizontally, double polarisation and double decay are both observed.
- From simulation results, double decay is obvious only if the out-of-plane displacement interacts strongly with the in-plane displacement. This can be artificially promoted by increasing the angular offset angle from +7° to +22°.

- Energy is principally transmitted through the vertical oscillator even if the string is initially excited horizontally. This is because the vertical oscillator's frequency is closer to the fundamental frequency of the string. This results in a higher mobility of the oscillator, and subsequently the string loses more energy through it.

Part III:

Source identification of piano

You've got your passion. You've got your pride,
But don't you know that only fools are satisfied?
Dream on, but don't imagine they'll all come true.
When will you realize Vienna waits for you?

Billy Joel, 1977

8

Source identification of piano

In this chapter, an exploratory study to inspect the third objective as outlined in Section 1.2 is made. To recap, the objective is:

> to determine the contribution of other constitutive components of the piano in the production of the sound.

This study was made at Wien, Austria during a 5-month scientific secondment in the BATWOMAN programme. As part of the BATWOMAN network which promotes inter-disciplinary research within the domain of acoustics, the study is conducted under the supervision of Antoine Chaigne of University of Music and Performing Arts Vienna (MDW) and in collaboration with Antonio Acri of Virtual Vehicle Graz and Politechnico Milano [1]. The culmination of the collaboration results in a conference presentation at the International Congress of Acoustic in Buenos Aires, Argentina in September 2016 [93]. In conjunction with the preparation of this thesis, the work was further extended submitted to *Applied Acoustics*. As such, this chapter is identical to the submitted manuscript, with its own abstract, introduction, contents, conclusion and acknowledgment.

8.1 Abstract

The piano sound is made audible by the vibration of its soundboard. A pianist pushes the key to release a hammer that strikes the strings, which transfer the energy to the soundboard, set it into vibration and the piano sound is heard due to the compression of air surrounding the soundboard. However, as piano is being played, other components such as the rims, cast-iron frame and the lid are also vibrating. This raises a question of how much their vibrations are contributing to the sound as compared to the soundboard. To answer this question, operational transfer path analysis, a noise source identification technique used widely in automotive acoustics, is carried out on a Bösendorfer 280VC-9 grand piano. The "noise" in a

[1] He is now affiliated with Brugola OEB Industriale Spa.

piano system would be the piano sound while the "sources" are soundboard and the aforementioned components. For this particular piano, it is found out that the soundboard is the dominant contributor, followed by the frame and the lid. Comparatively, the rims (inner and outer) are less significant.

8.2 Introduction

The study of piano acoustics has traditionally been focused on its piano action [16, 17], interaction between a piano hammer and string [25, 26], string vibration [32, 61, 94], soundboard vibration [42, 46, 95] and its radiation [8, 43]. As computational power becomes cheaper, it is possible to model the piano as a coupled system that involves the string, soundboard and surrounding air [62, 63]. However, this raises a question whether the considered system is complete enough to have a realistic reproduction of the piano sound. Is there any other components that are contributing to the piano sound production that has not been accounted for? Anecdotally, when a piano is played, vibration can be felt not only on the soundboard but also on the rim, the frame, the lid etc. In a Bösendorfer piano, spruce, a wood usually used for the soundboard by other manufacturers, is used extensively in building the case of the piano. Bösendorfer claims that the use of spruce, especially on the rim of the piano, allows the whole instrument to vibrate and is the reason that gives the unique Bösendorfer sound [72]. Based on the fact that vibration is felt on other parts of the piano and how Bösendorfer uses spruce extensively, it necessitates an investigation if the vibrations of these parts contribute to the production of the sound.
Current work takes inspiration from noise source identification techniques used commonly in automotive acoustics [96–98]. However, in the case of piano, the "noise" is the resulting piano sound and the "sources" to be identified are the piano components to be investigated. These "sources" may emit different "noise" contributions that characterise the resulting "noise", i.e. the piano sound. One technique that can be used to identify the contribution of the piano components to the final sound is the operational transfer path analysis (OTPA) [99]. OTPA computes a transfer function matrix to relate a set of input/source(s) measurements to output/response(s) measurements. In this case, the inputs are the vibration of the components of piano and the output is the resulting piano sound.
In Section 8.3, the theory of OTPA is presented. The experiment designed for OTPA is then detailed in Section 8.4 before the results are shown and discussed in Section 8.5.

8.3 The Operational Transfer Path Analysis (OTPA)

Operational transfer path analysis (OTPA) is a signal processing technique that studies the noise source propagation pathways of a system based on its operational data [100]. This is in contrast to classical transfer path analysis (TPA) where the

source propagation pathways are established by means of experimental investigations with specific inputs. Indeed, OTPA was developed in wake of the need of a fast and robust alternative to the classical TPA. In both methods, the source propagation pathways are determined by studying the transfer functions between the sources (inputs) and the responses (outputs). In TPA, the relationship between sources (excitation signals) and responses are estimated by frequency response functions and these are meticulously determined by series of experimental excitation of known forces (e.g. by shaker or impact hammer). Where necessary, part of the system is also removed or isolated. In this way, TPA is able to trace the flow of vibro-acoustic energy from a source through a set of known structure- and air-borne pathways, to a given receiver location by studying the frequency response functions. On the other hand, OTPA measures directly the source and response signals when the system is operated and establishes the source propagation pathways based on the experimentally determined transfer functions. OTPA is a response-response model where measurement data are collected and analysed while the system, when operated, provides the excitation. Detailed comparisons between the classical TPA and OTPA can be found in [101–103].
While OTPA may appear to be simpler to use, it is also prone to error if it is not designed and analysed properly. OTPA requires prior knowledge of the system as neglected pathways could not be easily detected. In a multi-component system, cross-coupling between the components could affect the accuracy of an OTPA model. Several techniques, which are detailed in the following Section 8.3.2, can be employed to mitigate the effects of cross-coupling [100].

8.3.1 Theory of OTPA

In a linear system, the input $\mathbf{X}$ and output $\mathbf{Y}$ can be related by:

$$\mathbf{Y}(j\omega) = \mathbf{X}(j\omega)\mathbf{H}(j\omega), \tag{8.1}$$

where:
$\mathbf{Y}(j\omega)$ is the output vector/matrix at the receivers;
$\mathbf{X}(j\omega)$ is the input vector/matrix at the sources;
$\mathbf{H}(j\omega)$ is the operational transfer function matrix, also known as the transmissibility matrix.
The inputs and outputs signals can be the forces, displacements, velocities or pressures of the components in the system. Given that there are m inputs and n outputs with p set of measurements, Equation (8.1) can be written in the expanded form:

$$\begin{bmatrix} y_{11} & \cdots & y_{1n} \\ \vdots & \ddots & \vdots \\ y_{p1} & \cdots & y_{pn} \end{bmatrix} = \begin{bmatrix} x_{11} & \cdots & x_{1m} \\ \vdots & \ddots & \vdots \\ x_{p1} & \cdots & x_{pm} \end{bmatrix} \begin{bmatrix} H_{11} & \cdots & H_{1n} \\ \vdots & \ddots & \vdots \\ H_{m1} & \cdots & H_{mn} \end{bmatrix}, \tag{8.2}$$

where for clarity purposes, the frequency dependency $j\omega$ is dropped. In order to quantify the contributions of the inputs to the outputs, the transfer function matrix

needs to be solved. If the input matrix $\mathbf{X}$ is square and invertible, this can be solved by simply multiplying the inverse of $\mathbf{X}$ on both sides:

$$\mathbf{H} = \mathbf{X^{-1}Y}. \tag{8.3}$$

However, in most cases, $p \neq m$. Thus, for the system to be solvable, it is required that the number of measurement sets is larger than or equal to the number of inputs, i.e.

$$p \geq m. \tag{8.4}$$

Then $\mathbf{H}$ can be solved by:

$$\mathbf{H} = (\mathbf{X}^T\mathbf{X})^{-1}\mathbf{X}^T\mathbf{Y} + \mu = \mathbf{X}^+\mathbf{Y} + \mu, \tag{8.5}$$

where the symbol $+$ denotes the Moore-Penrose pseudo-inverse [104] and the term μ is the residual vector from the overdetermined system.

8.3.2 Enhanced OTPA with singular value decomposition and principal component analysis

In essence, the basics of OTPA is analogous to the multiple-input multiple-output (MIMO) technique in experimental modal analysis [105]. However, solving the transfer function $\mathbf{H}$ directly is prone to error if the input signals are highly coherent between each other. High coherence is caused by unavoidable cross-talks between the measurement channels as they are sampled simultaneously. To mitigate this error, an enhanced version of OTPA can be employed. Singular value decomposition (SVD) and principal component analysis (PCA) can be carried out [99, 100]. There are two main reasons in using SVD. Firstly, it can be used to solve for $\mathbf{X}^+$, even though it is not the only way to solve for Moore-Penrose pseudo-inverse. Secondly, the singular value matrix can later be repurposed to carry out PCA to reduce the measurement noise.
The input matrix $\mathbf{X}$, as decomposed by SVD, can be written as

$$\mathbf{X} = \mathbf{U\Sigma V^T}, \tag{8.6}$$

where
$\mathbf{U}$ is a unitary column-orthogonal matrix;
$\mathbf{\Sigma}$ is a diagonal matrix with the singular values;
$\mathbf{V^T}$ is the transpose of a unitary column-orthogonal matrix, $\mathbf{V}$.

The singular values obtained along the diagonal of $\mathbf{\Sigma}$ are also the principal components (PC). The PC are defined such that the one with the largest variance within the data is the first PC (the first singular values), the next most varying is the second PC and so on. The smallest singular value thus corresponds to the weakest PC that has little to no variation. A matrix of PC scores can then be constructed as:

$$\mathbf{Z} = \mathbf{XV} = \mathbf{U\Sigma}. \tag{8.7}$$

The contribution of each PC can be evaluated by dividing $\mathbf{Z}$ with the sum of all the PC scores. For each PC, this yields a value between 0 to 1. The larger the number, the more significant the PC is. In other words, a weakly contributing PC can be identified and thus be removed by setting it to zero. Then, the inverse of the singular value matrix $\mathbf{\Sigma}^{-1}$ can be recalculated by:

$$\mathbf{\Sigma_e^{-1}} = \begin{cases} 1/\sigma_n & \text{if } \sigma_n \geq \text{threshold}, \\ 0 & \text{otherwise}, \end{cases} \tag{8.8}$$

where the subscript e indicates that the matrix has been enhanced by SVD and PCA. Subsequently, the modified pseudo-inverse of $\mathbf{X}$ can be written as:

$$\mathbf{X_e^+} = \mathbf{V\Sigma_e^{-1}U^T}. \tag{8.9}$$

Introducing Equation (8.9) into Equation (8.5), the treated transmissibility matrix $\mathbf{H_e}$ can then be written as:

$$\mathbf{H_e} = \mathbf{X_e^+ Y}. \tag{8.10}$$

Lastly, it is possible to synthesise the response contributions of the measurements $\mathbf{Y_s}$ by performing a pointwise multiplication between $\mathbf{X}^T$ and $\mathbf{H_e}$ [99]:

$$\mathbf{Y_s} = \mathbf{X}^T \,.\, \mathbf{H_e}. \tag{8.11}$$

It is then possible to quantify the individual contribution of each input has on the synthesised output $\mathbf{Y_s}$.

8.4 Experimental setup

The soundboard, inner rim, outer rim, the cast-iron frame and the lid are all considered to be potential transmission paths of the piano sound (see Figure 8.1). The vibrations of these components are sampled by sets of accelerometers and can be treated to be the inputs of OTPA, $\mathbf{X}$. To fully capture all the modes of interest, the accelerations are sampled extensively over the surfaces in grids of 20cm x 20cm. For the cast-iron frame, only the part highlighted in the green area in Figure 8.1 are sampled. The other part has a comparatively small surface area, and it is assumed that its contribution does not play a significant role in the final sound. In the same figure, the surface sampled for inner rim and outer rim are also highlighted (albeit partially) in blue and purple respectively. Of course, the outer rim measurement is also extended to the straight part of the rim which is not seen in the figure. The soundboard and lid measurement are sampled on the surface that is visible in Figure 8.1 (i.e. the soundboard surface that faces up and the lid surface that faces down) but are not highlighted so as to not obscure the presentation. The total number of measurements for each components is outlined in Table 8.1. Meanwhile, the output $\mathbf{Y}$ is the sound pressure at a point away from the piano, recorded by a microphone, marked M in Figure 8.2. The experiment is conducted

in the anechoic chamber of the University of Music and Performing Arts Vienna on a Bösendorfer 280VC-9 equipped with a CEUS Reproducing System. This allows minimal interference in the sound pressure data from the wall reflections.

Figure 8.1: A Bösendorfer VC280-9. Highlighted green, blue and purple areas are the surfaces considered in the OTPA for frame, inner rim and outer rim respectively. Note that there are four beams at the frame that terminates at the keyboard end which splits the key range into 5 parts.

One of the advantages of OTPA is its flexibility to use operational data rather than controlled excitation from a shaker or impact hammer. Thus, measurement data are collected as the piano is being played. As vibrational data need to be taken in batches due to limited number of accelerometers, the CEUS Reproducing System is used where the piano playing can be reproduced with the same force and timing. The CEUS system can be controlled via pre-produced .boe files, which contains information on the keys to play, their pushing profiles and the hammer velocities [106]. For this experiment, two .boe files are prepared via in-house MATLAB/GNU Octave script, each corresponding to different excitation patterns.
For an OTPA, it is desired that the inputs are as incoherent as possible to minimise cross-couplings between them. The two excitations are designed with that in mind. The first is simply playing each of the 88 notes sequentially, from the lowest A0 (27.5Hz) to the highest C8 (4186 Hz). Each note is played for 3 seconds with a rest

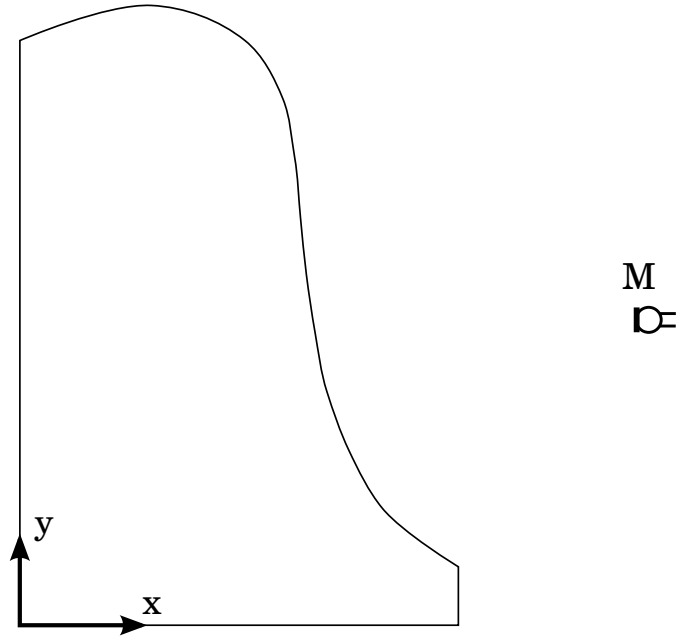

Figure 8.2: Location of the microphone with respect to the outline of the piano soundboard. Assuming that the origin of an (x,y) coordinate system as shown in the figure, the microphone is at x=2.2m, y=1.0m and is the same height with the soundboard. The image is to scale.

interval of 0.6 seconds in between. Each 3-second sequence is a unique measurement and thus $p = 88$ as is defined in Equation (8.2). The second sets of measurement contains 12 playing sequences with each of them playing all the same notes, starting with all A (i.e. A0, A1, A2 ... A7) and followed by all of the A#s, all of the Bs, all of the Cs until finally all of the G#s as is illustrated in Figure 8.3. Each sequence is played for 5 seconds with a 1 second interval in between and yields $p = 12$. Both sequences are played at a moderate dynamic level that gives a subjective loudness of *mezzoforte*.

As outlined in Table 8.1, there are a total of 154 vibration signals that can be treated as inputs. This would violate Equation (8.4) if $m = 154$. It is thus necessary to either increase the number of measurements or reduce the number of inputs. For this study, the latter is performed where the vibrational signals are summed via Rayleigh integral so as to obtain an input variable with the dimension of a sound pressure. The net pressure p at point $\mathbf{R}$ as summed by Rayleigh integral can be defined as:

$$p(\mathbf{R}, \omega) = \frac{\rho}{2\pi} \sum_i \frac{a_i(\omega) S_n}{r_i} e^{-jkr_i}, \tag{8.12}$$

where ρ, a_i, r_i, k and S_i represent density of the air, the acceleration, distance to the summed point, wavenumber and area covered by source point i respectively

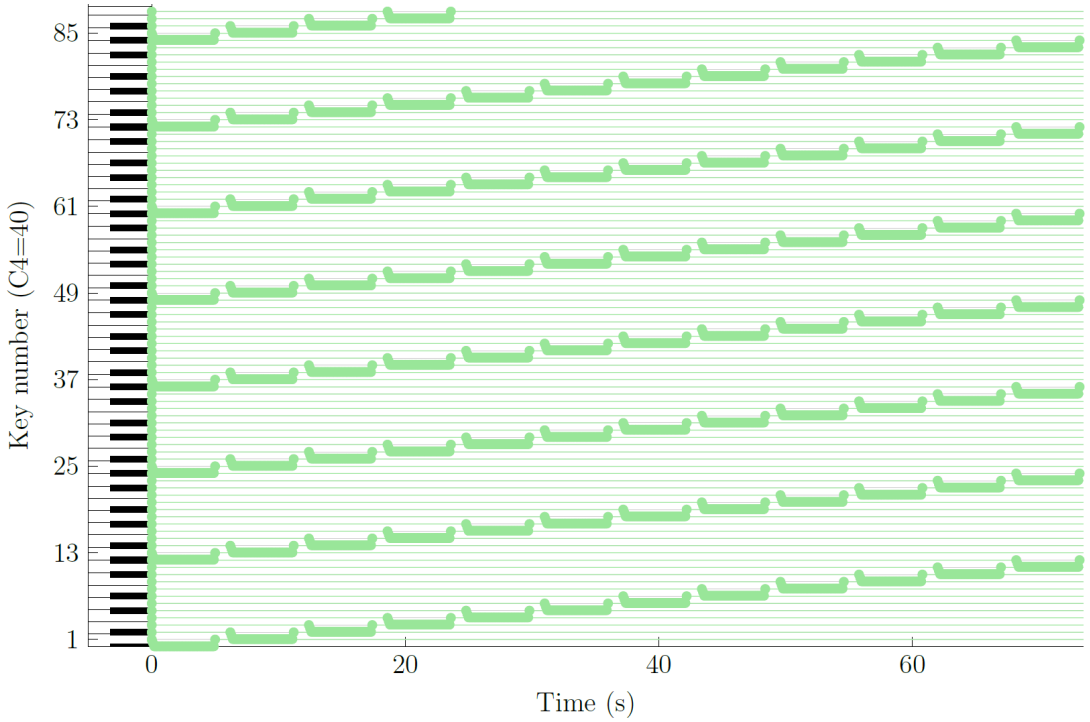

Figure 8.3: Illustration of the 12-sequence excitation. Vertical axis indicates the note number played. The dips indicate the keys being pressed.

and the term ω indicates dependence on frequency. The acceleration data of each component are summed to the midpoint of the accelerometer locations, with an averaged uniform area assumed (i.e. total calculated area divided by number of measurements on each component). As a result, this yields a total of only 5 sources, i.e. $m = 5$, making them suitable to be used for OTPA.

Table 8.1: Number of accelerometers for each components.

Components	Number of accelerometers
Soundboard	35
Inner rim	24
Outer rim	24
Frame	25
Lid	46

The use of Rayleigh integral is an approximation as it is defined for an infinitely large flat baffle [90]. A rapid calculation allows to estimate the frequency range for which the Rayleigh approximation may lead to an overestimation of the sound pressure. The soundboard and lid have a nominal length L_n of about 1.47m. With this order of magnitude for the acoustic wavelength, an acoustical short circuit might

appear for wave modes below 230Hz in the reality, thus leading to a sound pressure lower than the one predicted by the Rayleigh integral. However, the overestimation may not be so prominent due to the complex shape of the piano and the presence of the semi-opened cavity defined by the rim and the lid. In practice, this overestimation should not have appreciable consequences in the analysis, since the Rayleigh integral is used here for the purpose of reducing the number of inputs, only, and also it is a comparative study. The only consequence is that the contributions of the smaller components (such as the frame) might be slightly overestimated in the low-frequency range, compared to the large components (soundboard, lid) through the use of the Rayleigh integral.

8.5 Results and discussion

A quality check of OTPA can be performed by comparing the experimentally measured output against the synthesised output as obtained from Equation (8.11). In practice, both output should be similar to each other with the discrepancies due to noise, unidentified source or nonlinear behaviour [100]. The first 400Hz of the outputs of the first sequence of both 88-sequence and 12-sequence excitations are as shown in Figure 8.4. It can be seen there are very good agreements between the data except at the frequency range below 40Hz. At this range, the modes are correctly identified at their eigenfrequencies but at lower amplitude levels. A further check on the residual vector of Equation (8.5) reveals that the residues are large at the low frequencies but otherwise insignificant at higher frequencies. Given that the peaks of the eigenfrequencies are actually correctly identified, this rules out any unidentified sources. With overall small amplitude vibrations, it is also not expected that there is a nonlinear behaviour in the system. Thus, it could be an inherent limitation of the current set of data or the OTPA method as it affects both types of excitations. Regardless, the models are suitable for analysis above 40Hz.
The next part of the analysis is to study the contributions of each source in the output. The contribution level of each input can be obtained by the average of the synthesised output of all p measurements when multiplied with that input alone (see Equation (8.11)). In Figure 8.5, the contribution of each source up to 220Hz (key number 37) is shown for both sets of excitation, where each group of bars corresponds to an octave on a piano. For key number 14 to 37 (55 to 220Hz), both sets of excitation show good agreement between each other where the soundboard is the dominant contributor to the piano sound, with comparable secondary contributor for both the cast-iron frame and the lid at 10-15dB less than soundboard. However, at the lowest frequency group, i.e. key number 1-13 ($<$55Hz), the two excitations are noticeably different. In the 12-sequence excitation, the soundboard is only 5dB more dominant than frame and lid, with the inner and outer rim a further 5dB behind. For 88-sequence excitation, all of the sources are less than 5dB apart. The discrepancy is caused by the inaccuracy of the model as discussed earlier (where the synthesised outputs do not match the measured outputs below 40Hz). For this

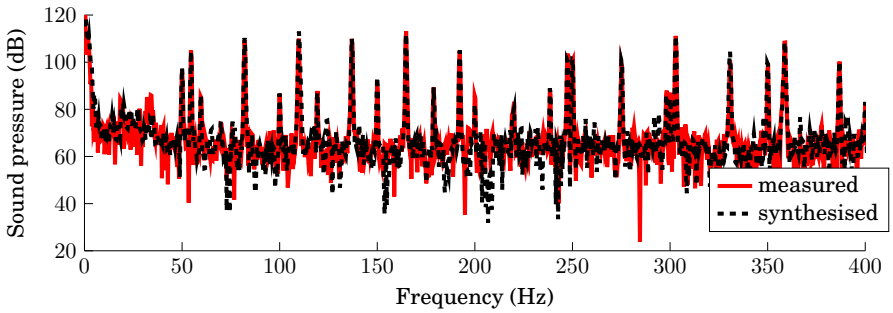

(a) 88-sequence excitation, playing only A0 note.

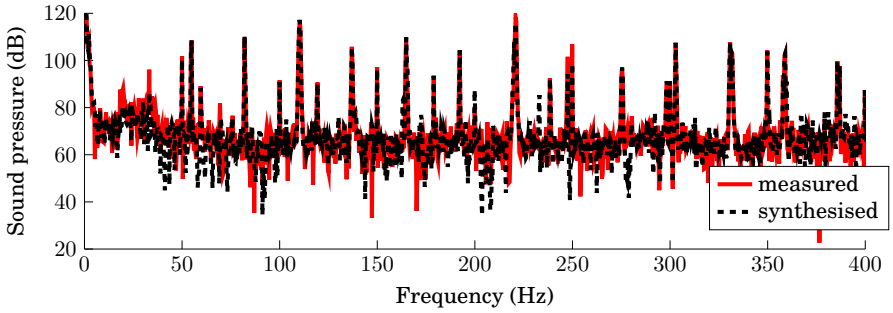

(b) 12-sequence excitation, playing all A note.

Figure 8.4: Comparison of the synthesised and measured output (sound pressure at M as shown in Figure 8.2). Good agreements between the data indicate that the models are representative of the measurements.

range, it is thus inconclusive to comment on the relative contribution of the soundboard, frame and lid on the final sound.

The same analysis is repeated but is extended to the full frequency range of the piano as is shown in Figure 8.6. The frequency is categorised into 5 groups which are based on the 5 sections partitioned by the cast-iron frame as can be seen in Figure 8.1. As a result, findings from Figure 8.5 have been replotted into the first two groups in Figure 8.6, which shows the soundboard being the dominant contributor, followed by the lid and frame. The dominance of soundboard is also observed up to key number 72 (1661.2Hz) and both sets of excitations also show good agreement between each other, with the exception at the highest frequency range (key number 73-88). While both excitations identify the lid as the main contributor, the 12-excitation analysis suggests that the soundboard and frame is about 2dB less than the lid but in the 88-excitation data, the difference between the lid and both the soundboard and frame is about 5dB. This is because in the 12-excitation measurement, each excitation sequence plays notes across the whole frequency range. As such, higher harmonics of lower modes are also excited which leads to an overall higher estimation of contribution.

The dominance of piano soundboard is expected as it is designed to be the primary

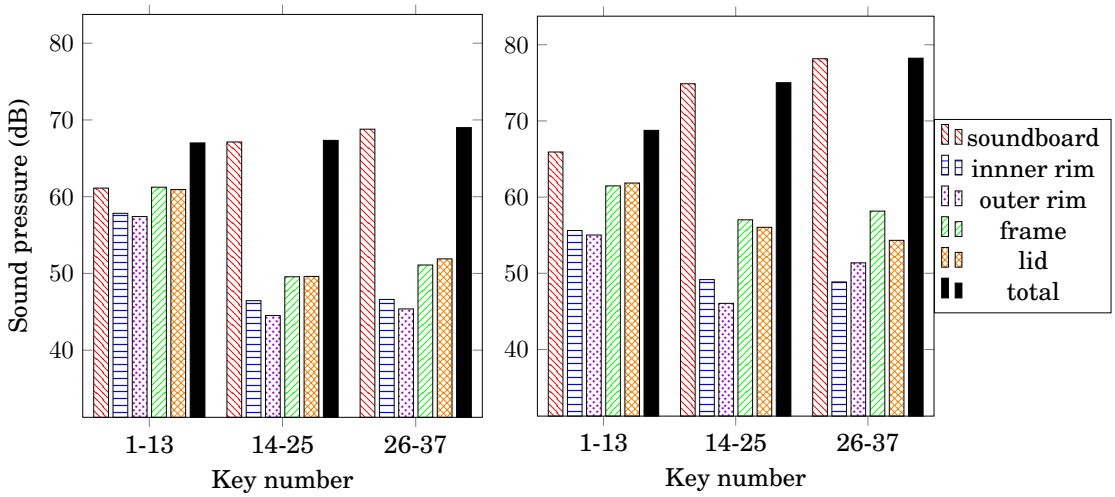

Figure 8.5: Average contribution level from the analysis for (on the left) 88-sequence excitation and (on the right) 12-sequence excitation. The frequency range is defined based on the piano key number. Key number 1, 13, 25 and 37 correspond to 27.5Hz, 55.0Hz, 110.0Hz and 220.0Hz respectively.

resonator, with appropriate characteristics in terms of thickness, density and rigidity. Nonetheless, as evident from the results, not all the acoustic components are radiated by the soundboard. Energy is leaked through the edge of the soundboard to the rims and, subsequently, to frame and lid. At higher frequency, as the strings are not damped past the bridge, it is possible that energy could be leaked directly from the string to the frame as well. It is also possible that the lid prop (the beam that supports the lid when it is being raised) could have transferred some energy to the lid which may explain the contribution of lid vibration at higher frequencies (see Figure 8.6 key number 73-88). As the soundboard is driven by the strings at the right end, the energy is transferred to the lid via the prop.

The difference of the soundboard dominance between key number 1 to 72 (27.5Hz to 1661.2Hz) and 73 to 88 (1760Hz to 4186Hz) can be further illustrated in Figure 8.7 and 8.8. Figure 8.7 shows the contributions of the five inputs for the synthesised output (labeled "Total") for the 28th sequence of the 88-sequence excitation, i.e. playing the C3 note (130.8 Hz). On the other hand, Figure 8.8 shows the contributions of the five inputs for the synthesised output when the 80th note (E7 at 2637Hz) is played. Both of the played notes' fundamental frequencies are indicated by a dashed line. It must be noted that both played notes' fundamental frequencies are not exactly on 130.8Hz and 2637Hz respectively but rather at 131.1Hz and 2672Hz. This could be the preference of the tuner of the piano or the piano has gone slightly out of tune since it was last serviced. More importantly, the plotted frequency of Figure 8.7 covers the 21st to 38th keys (the second group of bars in top figure of Figure 8.6) while Figure 8.8 covers 81th to 84th keys and represents a

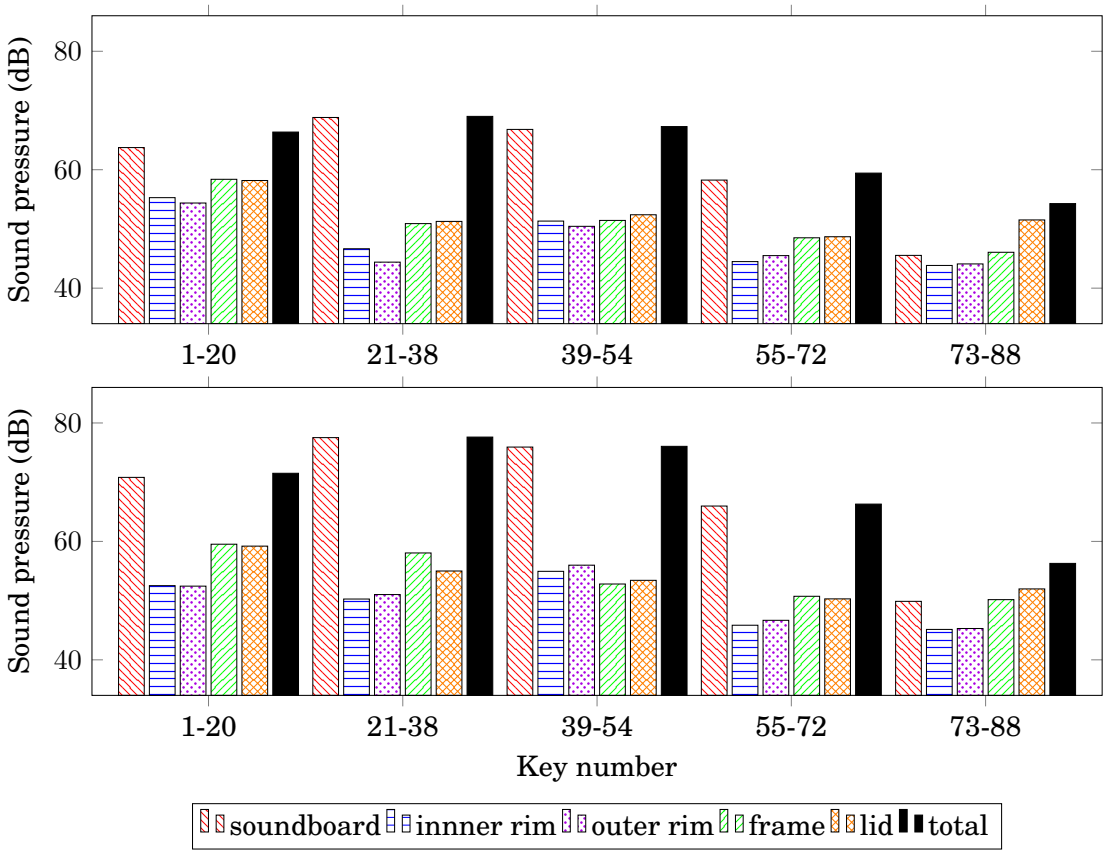

Figure 8.6: Average contribution level from the analysis for (on the top) 88-sequence excitation and (on the bottom) 12-sequence excitation. The frequency range is defined based on the piano key number. Key number 1, 20, 38, 54, 72 and 88 correspond to 27.5Hz, 82.4Hz, 233.1Hz, 587.3Hz, 1661.2Hz and 4186.0Hz respectively.

snippet of the fifth group (key number 73-88). Although each of these figures represents only one excitation, they provide insights on the contributions of each of the components. When the peaks of a particular component matches the amplitude of the peaks of output signal (labelled "Total"), it means that the matched frequencies of the output are contributed by the particular component. At lower frequency range (Figure 8.7), the frequencies of output are mostly contributed by soundboard. On the other hand, at higher frequency range as shown in Figure 8.8, the output contains largely modes from the lid, with the soundboard mostly contributing at the note played (2672Hz). The output signal also contains modes from the frame (e.g. at 3000Hz) which explains its contribution at the highest frequency range. For both cases, inner and outer rim do not contribute significantly to the piano sound. This suggests that some of the tonal properties of a piano sound could actually be originating from the vibration of the frame and lid while the rims play only a marginal role.

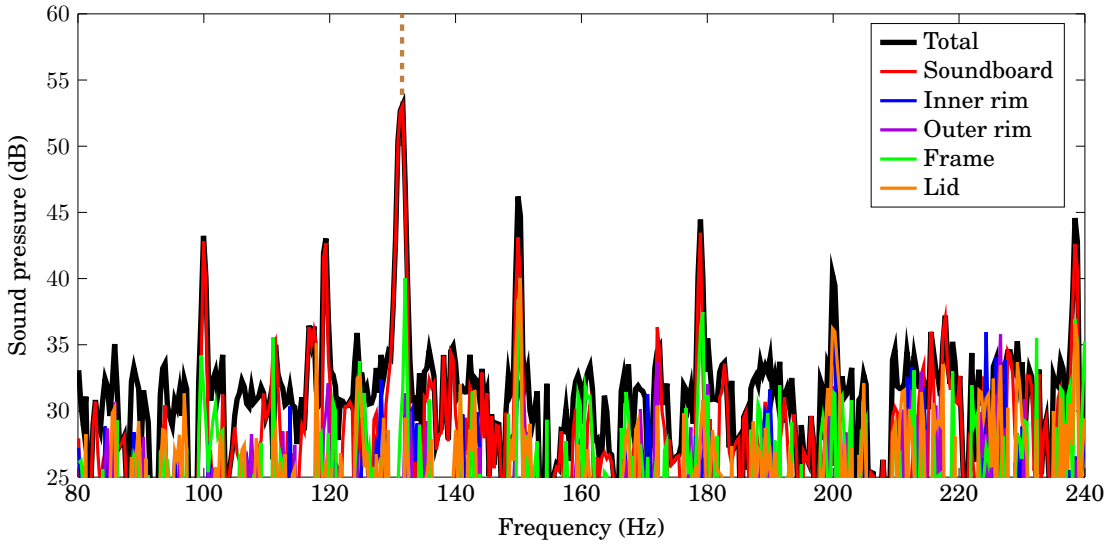

Figure 8.7: Contribution of the five inspected components for the synthesised output (labeled "Total") for the 28th sequence of the 88-sequence excitation. The dashed vertical line corresponds to the fundamental frequency of the played note (C3).

It is perhaps slightly surprising that the inner rim does not play a significant role in contributing to the piano sound. In Bösendorfer piano, the inner and outer rim are constructed separately. In their marketing material, the inner rim is specially constructed so as to complement the soundboard in the sound formation process. However, in the analysis conducted, both inner and outer rims are marginal in their contributions compared to the soundboard, frame and the lid. Regarless, the result does not necessarily invalidate Bösendorfer's claim as the role of the rims in sound formation might have been accounted for by another mechanism.

8.6 Conclusion

An operational transfer path analysis (OTPA) has been conducted for a Bösendorfer piano to identify any additional vibrating components (other than the soundboard) that could contribute to the sound production. Across the frequency range inspected, the soundboard has been the major contributor except for the highest frequency range ($\geq$ 1661.2Hz). The piano sound is also made up of vibration from the frame and lid. The latter is the most significant contributor at the highest frequency range as the frequency contents of the sound at that range are primarily satisfied by the lid. On the other hand, both inner and outer rims appear to be insignificant in the analysis.
Current study represents a rare interdisciplinary example of technique originally developed for automotive analysis being applied to musical instruments. However, it is indeed possible to apply other source identification techniques to investigate

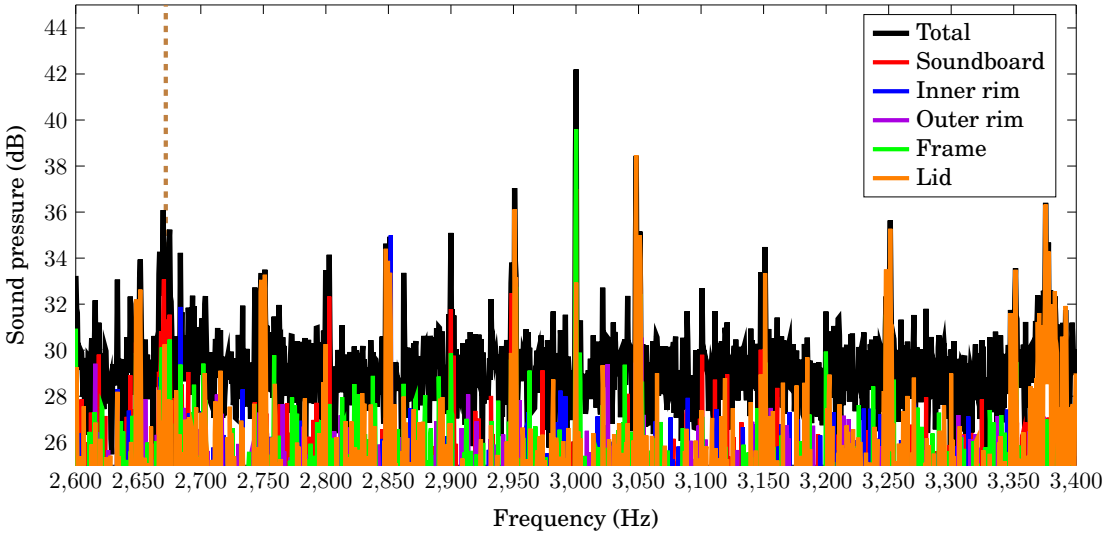

Figure 8.8: Contribution of the five inspected components for the synthesised output (labeled "Total") for the 80th sequence of the 88-sequence excitation. The dashed vertical line corresponds to the fundamental frequency of the played note (E7).

current problem and obtain a better understanding on the transfer pathways from the strings to the listener. For recommendation, one can conduct a full-fledged classical transfer path analysis. Components like lid can be removed and boundary conditions between the soundboard and the rims can be artificially modified to isolate the components.

8.7 Acknowledgement

The research work presented is funded by the European Commission (EC) within the BATWOMAN Initial Training Network (ITN) of Marie Skłodowska-Curie action, under the seventh framework program (EC grant agreement no. 605867). The authors thank the Network for the generous funding and support. The research has been further supported by the Lise-Meitner Fellowship M1653-N30 of the Austrian Science Fund (FWF) attributed to Antoine Chaigne.
The authors also thank Werner Goebl for his guidance on using the CEUS Reproducing System and Alexander Mayer for his contribution in setting up the experiment.

9

Conclusion

In the grand scheme of improving realism in piano sound synthesis, advances have been made in the understanding of double polarisation in piano strings. From the study of multiple-scale analysis, it is shown that energy exchange occurs nonlinearly between the two string's polarisations due to 1:1 internal resonance under fixed boundary conditions at both ends. Specifically, if the polarisations are slightly detuned from one another and the polarisation with lower fundamental frequency is excited by a sufficiently large amplitude, the other polarisation will gain energy and begins to vibrate. However, if the polarisation with higher fundamental frequency is excited, energy exchange does not occur. These findings have been numerically validated from solving the Kirchhoff-Carrier equations and the geometrically exact nonlinear equations.

Experimentally, from a monochord setup, it is found out that the two string's polarisations are indeed slightly detuned from one another. In addition to the string's detuning, it is also identified that the string's polarisations do not necessarily fall on the vertical and horizontal planes. Instead, they lie on planes as defined by their natural polarisation angles and an original method has been proposed to identify these angles. Exciting specifically on their natural polarisation angles with increasing amplitudes, the theoretical findings via multiple-scale analysis have been successfully validated experimentally.

To relate more closely to the case of a piano, the interaction between the string and the bridge is studied in the linear regime. This is modeled by considering a set of oscillators coupled to one end of the string. The eigenfrequencies of such systems are derived, analysed and they are subsequently used to validate the finite-element numerical implementation. One hallmark feature of the numerical model is its inclusion of the angular offset between the string's and bridge's axes.

To complement the string-bridge model, a bass bridge cutout is added to the monochord experimental setup in which the string is strung over in a zig-zag configuration. Experimentally, two phenomena are identified. First, it has been observed that the string's natural polarisation angles change after the bridge is mounted. Secondly, it has been experimentally identified that the angular offset is non-negligible

at 7°. However, numerically, the double polarisation effect is only prominent when the angular offset is artificially increased to 22°. In addition to double polarisation, double decay is also observed on the coupled string-bridge system both experimentally and numerically. Qualitatively, the double decay phenomenon is also more obvious if the angular offset is larger. From numerical ivnestigations, this double decay phenomenon is largely influenced by the vertical oscillations of the bridge, which has a resonant frequency in between the first two frequencies of the string. In contrast, the impact of the bridge's horizontal and rotational oscillations, both of which are experimentally identified at higher frequencies, is insignificant.
During a research stay at MDW in Vienna, the contributions of various components of a Bösendorfer piano to its sound have been investigated experimentally via operational transfer path analysis. At low and mid frequencies, the soundboard makes up most of the frequency contents in the piano sound. At higher frequencies, the vibrations of the frame and the lid are found to be significant. The study represents a rare and novel case of interdisciplinary application of a noise source identification technique developed originally for automotive acoustics that is applied to a research problem in musical acoustics.

Future work

On the subject of double polarisation, there are two research directions that can be pursued. First, the detuning and string's polarisation angles are very difficult to measure and further understanding on the subjects is necessary. While the origin of these characteristics can be attributed to the imperfection on a string, there are no predictable and reproducible methods to identify and manipulate these parameters. To this end, several studies can be made, such as:

1. Comparison of detuning and string's polarisation angles between tin-plated and nickel-plated strings. Piano strings are traditionally tin-plated but are suspectible to natural rusting. Nickel-plated strings are more resistant to rusting and theoretically the two string's modes will be much less detuned. If so, it can be established that rusting is indeed a source of detuning and strings can thus be artificially exposed to rust of different degrees or at different spots to investigate their influences on the detuning and polarisation angles.

2. As the string's polarisation angles change after it is mounted onto the bridge, a more detailed physical interpretation of the zig-zag boundary condition could shed light on how the polarisation angles change. The string meets the top surface of the bridge and the bridge pin at an angle. It is likely that the geometry of these physical contacts influence the polarisation angles. It is also not known if the bridge introduces a new sets of polarisation planes or it simply rotates the polarisation angles of the string.

The other research directions would be on a more detailed understanding of how detuning, nonlinear behaviour and string's polarisation angles could affect the double polarisation and double decay, and subsequently the piano sound. To this end, it would be natural to extend the current numerical investigation to a more comprehensive model, such as the S212-B213 string-bridge system proposed. A further extension would be to include the coupling with soundboard and air, thus constituting a complete piano model. It is also intriguing if the aforementioned string characteristics do really play a part in shaping the piano sound. In this regard, it would be insightful to conduct the experiments that were performed in this thesis on an actual piano.

As for the identification of vibroacosutic sources in a piano, further verification of the findings from the operational transfer path analysis is highly recommended. For example, a classical transfer path analysis can be conducted where components in the piano are isolated, individually excited and measured. The idea is to identify the physical transfer pathways from the strings to the frame and lid at higher frequencies. Subsequently, the physical observations can thus be modeled in a numerical framework for more accurate and realistic synthesis of piano sound.

Appendix A

Analytical solution of the lumped bridge

In Part II, the lumped bridge is modeled as a set of oscillators that can be represented in translational and rotational directions. The numerical schemes to solve the coupling between the string and the lumped bridge are presented in Chapter 6. The string is solved via a finite element method (see Section 2.4.3) and the lumped bridge is solved analytically with the coupling between them achieved by Lagrange multipliers. In this Appendix, the analytical solution the lumped bridge is presented.

Consider a problem:

$$\ddot{\Upsilon}(t) + \mathbb{A}\dot{\Upsilon}(t) + \mathbb{D}\Upsilon(t) = F, \tag{A.1a}$$
$$\Upsilon(t_0) = \Upsilon_0, \tag{A.1b}$$
$$\dot{\Upsilon}(t_o) = \Upsilon_1, \tag{A.1c}$$

where

$$\mathbb{A} = \mathrm{diag}(2a_i), \qquad \mathbb{D} = \mathrm{diag}({d_i}^2).$$

The solution to this problem is thus:

$$\Upsilon(t) = \mathcal{S}^0_{t-t_0}\Upsilon_0 + \mathcal{S}^1_{t-t_0}\Upsilon_1 + \mathcal{R}_{t-t_0}F, \tag{A.2a}$$
$$\dot{\Upsilon}(t) = \dot{\mathcal{S}}^0_{t-t_0}\Upsilon_0 + \dot{\mathcal{S}}^1_{t-t_0}\Upsilon_1 + \dot{\mathcal{R}}_{t-t_0}F. \tag{A.2b}$$

For brevity, it is convenient to define that $\tilde{d_i} = \sqrt{|{a_i}^2 - {d_i}^2|}$. The coefficients $\mathcal{S}^0_{\Delta t}$,

$\mathcal{S}^1_{\Delta t}$, $\mathcal{R}_{\Delta t}$, $\dot{\mathcal{S}}^0_{\Delta t}$, $\dot{\mathcal{S}}^1_{\Delta t}$ and $\dot{\mathcal{R}}_{\Delta t}$ can thus be defined as follows, for $|a_i| < d_i$:

$$
\begin{aligned}
(\mathcal{S}^0_t)_{i,i} &= e^{-a_i t}\left[\cos(\tilde{d}_i t) + \frac{a_i}{\tilde{d}_i}\sin(\tilde{d}_i t)\right],\\
(\mathcal{S}^1_t)_{i,i} &= \frac{1}{\tilde{d}_i} e^{-a_i t}\sin(\tilde{d}_i t),\\
(\mathcal{R}_t)_{i,i} &= \frac{1}{\tilde{d}_i {d_i}^2}\left[\tilde{d}_i(1 - e^{-a_i t}\cos(\tilde{d}_i t)) - a_i e^{-a_i t}\sin(\tilde{d}_i t)\right],\\
(\dot{\mathcal{S}}^0_t)_{i,i} &= -a_i(\mathcal{S}^0_t)_{i,i} + e^{-a_i t}\left[-\tilde{d}_i\sin(\tilde{d}_i t) + a_i\cos(\tilde{d}_i t)\right],\\
(\dot{\mathcal{S}}^1_t)_{i,i} &= -a_i(\mathcal{S}^1_t)_{i,i} + e^{-a_i t}\cos(\tilde{d}_i t),\\
(\dot{\mathcal{R}}_t)_{i,i} &= \frac{1}{\tilde{d}_i} e^{-a_i t}\sin(\tilde{d}_i t),
\end{aligned}
$$

and for $|a_i| \geq d_i$:

$$
\begin{aligned}
(\mathcal{S}^0_t)_{i,i} &= e^{-a_i t}\left[\cosh(\tilde{d}_i t) + \frac{a_i}{\tilde{d}_i}\sinh(\tilde{d}_i t)\right],\\
(\mathcal{S}^1_t)_{i,i} &= \frac{1}{\tilde{d}_i} e^{-a_i t}\sinh(\tilde{d}_i t),\\
(\mathcal{R}_t)_{i,i} &= \frac{1}{\tilde{d}_i {d_i}^2}\left[\tilde{d}_i(1 - e^{-a_i t}\cosh(\tilde{d}_i t)) - a_i e^{-a_i t}\sinh(\tilde{d}_i t)\right],\\
(\dot{\mathcal{S}}^0_t)_{i,i} &= -a_i(\mathcal{S}^0_t)_{i,i} + e^{-a_i t}\left[-\tilde{d}_i\sinh(\tilde{d}_i t) + a_i\cosh(\tilde{d}_i t)\right],\\
(\dot{\mathcal{S}}^1_t)_{i,i} &= -a_i(\mathcal{S}^1_t)_{i,i} + e^{-a_i t}\cosh(\tilde{d}_i t),\\
(\dot{\mathcal{R}}_t)_{i,i} &= \frac{1}{\tilde{d}_i} e^{-a_i t}\sinh(\tilde{d}_i t).
\end{aligned}
$$

Appendix B

Manual to use new rules related to "*StiffNL2T" and "StringBridge*"

The following manual is intended for users who have had experiences in using MONTJOIE, particularly on the rules pertaining to the simulation of the whole or part of a piano.
From the version <insert version number> onwards, MONTJOIE has a few new rules that could carry out simulations for non-planar string vibrations as well as its coupling to a lumped bridge model. These new rules are:

- multistringLINTL
- multistringNL2T
- multistringStiffNL2T
- StringBridgeLIN
- StringBridgeLIN2T
- StringBridgeNL
- StringBridgeStiffNL
- StringBridgeStiffLIN
- StringBridgeNL2T
- StringBridgeStiffNL2T

"**multistringLINTL**" would compile for the following equation:

$$\rho A\ddot{u} - T_0 u'' = 0, \tag{B.1a}$$

$$\rho A\ddot{w} - EAw'' = 0. \tag{B.1b}$$

"**multistringNL2T**" would compile for the following equation:

$$\rho A\ddot{u} - T_0 u'' - (EA - T_0)\frac{\partial}{\partial x}\left[u'\left(w' - w'^2 + \frac{u'^2 + v'^2}{2}\right)\right] = 0, \tag{B.2a}$$

$$\rho A\ddot{v} - T_0 v'' - (EA - T_0)\frac{\partial}{\partial x}\left[v'\left(w' - w'^2 + \frac{u'^2 + v'^2}{2}\right)\right] = 0, \tag{B.2b}$$

$$\rho A\ddot{w} - EAw'' - (EA - T_0)\frac{\partial}{\partial x}\left[\left(\frac{1}{2} - w'\right)\left(u'^2 + v'^2\right)\right] = 0, \tag{B.2c}$$

while "**multistringStiffNL2T**" would include the stiffness effect by solving for the string equation with Timoshenko stiff string modell as presented below:

$$\rho A\ddot{u} - T_0 u'' - (EA - T_0)\frac{\partial}{\partial x}\left[u'\left(w' - w'^2 + \frac{u'^2 + v'^2}{2}\right)\right] + AG\kappa\frac{\partial}{\partial x}(\phi - u') = 0, \tag{B.3a}$$

$$\rho A\ddot{v} - T_0 v'' - (EA - T_0)\frac{\partial}{\partial x}\left[v'\left(w' - w'^2 + \frac{u'^2 + v'^2}{2}\right)\right] + AG\kappa\frac{\partial}{\partial x}(\psi - v') = 0, \tag{B.3b}$$

$$\rho A\ddot{w} - EAw'' - (EA - T_0)\frac{\partial}{\partial x}\left[\left(\frac{1}{2} - w'\right)\left(u'^2 + v'^2\right)\right] = 0, \tag{B.3c}$$

$$\rho I\ddot{\phi} - EI\phi'' + AG\kappa(\phi - u') = 0, \tag{B.3d}$$

$$\rho I\ddot{\psi} - EI\psi'' + AG\kappa(\psi - v') = 0. \tag{B.3e}$$

For the other rules:

- **StringBridgeLIN** solves for a coupled case between the linear wave equation and a harmonic oscillator, i.e. S100-B100. It is possible to use "ExtraBridge = TRUE" to solve for S100-B101.
- **StringBridgeLIN2T** solves for a coupled case between the linear transverse and longitudinal string equation (see Equation (B.1)) and a harmonic oscillator, i.e. S200-B201. It is possible to use "ExtraBridge = TRUE" to solve for S200-B201.
- **StringBridgeNL** solves for a coupled case between the nonlinear string equation and a two translational harmonic oscillators, i.e. S20-B20.
- **StringBridgeStiffNL** solves for a coupled case between the nonlinear stiff string equation and two translational harmonic oscillators and one rotational harmonic oscillator, i.e. S201-B201.

- **StringBridgeStiffLIN** solves for a coupled case between the linear stiff string equation and two translational harmonic oscillators and one rotational harmonic oscillator, i.e. S201-B201.

- **StringBridgeNL2T** solves for a coupled case between nonlinear nonplanar string (Equation (B.2)) and three translational harmonic oscillators, i.e. S210-B210. It is *not possible* to solve for extra rotational oscillator via "ExtraBridge = TRUE".

- **StringBridgeStiffNL2T** solves for a coupled case between nonlinear nonplanar stiff string (Equation (B.3) and 3 translational, 2 rotational harmonic oscillators, each corresponding to the displacement of the string, i.e. S212-B212. It is possible to use "ExtraBridge = TRUE" to solve for S212-B213.

To fully utilise the family of StringBridge* and the *StiffNL2T modules, a few new keywords can be added to the configuration .ini file.

- "LumpedBridgeHeight = h0 h1 h2"
  Adding this new line will specify the height of the bridge, or otherwise understood as the offset between the attachment point of the string and the bridge mass centre. By default, MONTJOIE will assume a bridge height of zero for all three of them if this keyword is not specified.

- "ExtraBridge = TRUE"
  Adding this new line will use an extra rotational oscillator in the direction of θ_2 for StringBridgeLIN, StringBridgeNL, StringBridgeLINTL (all planar strings) or θ_3 for StringBridgeStiffNL2T (non-planar string model)

- "MatchNLaMuToStringDOF = TRUE"
  Adding this new line will allow the use of more than 2 (default) Lagrange multipliers. By default, MONTJOIE solves for up to two Lagrange multipliers, i.e. the vertical and horizontal forces. When "MatchNLaMuToStringDOF" is set to true, MONTJOIE will attempt to solve as many Lagrange multipliers as the dimension of the string, e.g. in StringBridgeStiffNL2T, 5 Lagrange multipliers will be solved instead.

- "BridgeStringPolarisationAngle = gamma"
  Using this keyword will set an angle for γ as defined in subsection 5.1.5. This angle defines an offset between the string polarisation (u and v) and the translational displacement of the bridge (λ_1 and λ_2), see Figure 5.6.

- StringInitialData = SINUSMULTI a0 n0 d0 a1 n1 d1
  To further leverage the higher dimensional string equations, it is possible to individually excite the string with a mode shape of self-defined mode number and amplitude. For instance, the syntax above will an initial displacement to the string of dimension "d0" with amplitude "a0" and the "n0"-th mode shape.

It will also apply an initial condition of amplitude "a1" of "n1"-th mode shape to string dimension "d1". It is not possible to input more data than the available dimension of the string.

- StringInitialData = NONZERO
  This is a simple initial condition where all the string is lightly excited with a half-sine mode shape at 1e-16m amplitude. This could be necessary to observe the nonlinear exchange of energy between the two transverse modes when hammer is used.

- StringInitialData = PLUCK x0 a0 d0
  This initial condition simulates a triangular initial condition. User is allowed to define the pluck position "x0", pluck height "a0" and in which dimension "d0" the initial condition is.

- StringInitialData = PLUCKANGLE x0 a0 d0 theta
  An extension of the PLUCK initial condition, PLUCKANGLE allows the plucking action to occur at an angle "theta" to the initial dimension defined.

- "String = L A rho T0 E I G k_prime amo(0) amo(1) detune Nx is_struck K_hammer R_hammer"
  It is possible to define a detuning between the two polarisation by defining a value "detune" for the string using the above syntax. The "detune" value defines a proportional difference between the density ρ of the two polarisation, such that:
  $$\text{detune} = \frac{\rho_1}{\rho_0} \tag{B.4}$$
  where ρ_0 and ρ_1 are the density for the string dimension 0 (u) and 1 (v) respectively. If "detune" < 1, v would have a slightly higher fundamental frequency than u.

Bibliography

[1] E. Blackham. The physics of the piano. *Scientific american*, 213(6):88–95, 1965.

[2] A. Dolge. *Pianos and Their Makers: A comprehensive history of the development of the piano from the monochord to the concert grand player piano*. Pianos and Their Makers. Covina Publishing Company, 1911.

[3] Kawai America Corporation - Kawai Canada Music. http://www.kawaius.com/technology/abs-c_action.html. Accessed: 2017-06-14.

[4] PHOENIX CARBIANO - Phoenix Piano Systems Ltd - Carbiano - The Carbon Fibre Piano. http://www.phoenixpianos.co.uk/phoenix-carbiano/. Accessed: 2017-06-14.

[5] Innovations - Stuart & Sons Handcrafted Grand Pianos Australia. http://www.stuartandsons.com/innovations.html. Accessed: 2017-08-14.

[6] Concept | Pianos Stephen Paulello. http://www.stephenpaulello.com/en/concept. Accessed: 2017-08-14.

[7] H. Helmholtz. On the sensations of tone (original work by 1877). *Translated. A. J. Ellis, Dover, New York*, pages 390–394, 1954.

[8] H. Suzuki and I. Nakamura. Acoustics of pianos. *Applied Acoustics*, 30:147, 1990.

[9] E. Lieber. On the possibilities of influencing piano touch. *Das Musikinstrument*, 34:58–63, 1985.

[10] A. Askenfelt and E. Jansson. From touch to string vibrations—the initial course of the piano tone. *The Journal of the Acoustical Society of America*, 81(S1):S61–S61, 1987.

[11] B. Gillespie. The virtual piano action: Design and implementation. In *Proceedings of the international Computer Music Conference*, pages 167–167. International Computer Music Association, 1994.

[12] B. Gillespie. *Haptic display of systems with changing kinematic constraints: The virtual piano action*. PhD thesis, Stanford University, 1996.

[13] M. Hirschkorn, J. McPhee, and S. Birkett. Dynamic modeling and experimental testing of a piano action mechanism. *Journal of Computational and Nonlinear Dynamics*, 1(1):47–55, 2006.

[14] A. Izadbakhsh, J. McPhee, and S. Birkett. Dynamic modeling and experimental testing of a piano action mechanism with a flexible hammer shank. *Journal of Computational and Nonlinear Dynamics*, 3(3):031004, 2008.

[15] R. Masoudi, S. Birkett, and J. McPhee. Dynamic model of a vertical piano action mechanism. In *ASME 2009 International Design Engineering Technical Conferences and Computers and Information in Engineering Conference*, pages 389–398. American Society of Mechanical Engineers, 2009.

[16] R. Masoudi and S. Birkett. Experimental validation of a mechanistic multibody model of a vertical piano action. *Journal of Computational and Nonlinear Dynamics*, 10(6):061004, 2015.

[17] A. Thorin, X. Boutillon, J. Lozada, and X. Merlhiot. Non-smooth dynamics for an efficient simulation of the grand piano action. *Meccanica*, pages 1 – 18, 2017.

[18] A. Thorin. *Non-smooth model of the grand piano action*. Thèses, École Polytechnique, 2013.

[19] J. Chabassier and M. Duruflé. Energy based simulation of a Timoshenko beam in non-forced rotation. Influence of the piano hammer shank flexibility on the sound. *Journal of Sound and Vibration*, 333(26):7198–7215, 2014.

[20] W. Kaufmann. Uber die bewegungen geschlagener klaviersaiten. *Ann. Phys*, 54:675–712, 1895.

[21] X. Boutillon. Model for piano hammers: Experimental determination and digital simulation. *The Journal of the Acoustical Society of America*, 83(2):746–754, 1988.

[22] A. Chaigne and A. Askenfelt. Numerical simulations of piano strings. ii. comparisons with measurements and systematic exploration of some hammer-string parameters. *The Journal of the Acoustical Society of America*, 95(3):1631–1640, 1994.

[23] A. Stulov. Experimental and computational studies of piano hammers. *Acta Acustica united with Acustica*, 91(6):1086–1097, 2005.

[24] C. Vyasarayani, S. Birkett, and J. McPhee. Modeling the dynamics of a compliant piano action mechanism impacting an elastic stiff string. *The Journal of the Acoustical Society of America*, 125(6):4034–4042, 2009.

[25] S. Birkett. Experimental investigation of the piano hammer-string interaction. *The Journal of the Acoustical Society of America*, 133(4):2467–2478, 2013.

[26] A. Chaigne. Reconstruction of piano hammer force from string velocity. *The Journal of the Acoustical Society of America*, 140(5):3504–3517, 2016.

[27] G. Weinreich. Coupled piano strings. *The Journal of Acoustical Society of America*, 7:926, 2004.

[28] N.J. Giordano. *Physics of the Piano*. Oxford University Press, 2016.

[29] I. Nakamura. Fundamental theory and computer simulation of the decay characteristics of piano sound. *Journal of the Acoustical Society of Japan (E)*, 10(5):289–297, 1989.

[30] O. Thomas, D. Rousseau, R. Caussé, and E. Marandas. Comparison of the effect of and mistuning on the double decay of piano tones. In *ISMA: International Symposium of Music Acoustics*, pages 253–258, 1998.

[31] M. Aramaki, J. Bensa, L. Daudet, P. Guillemain, and R. Kronland-Martinet. Resynthesis of coupled piano string vibrations based on physical modeling. *Journal of New Music Research*, 30(3):213–226, 2001.

[32] J. Chabassier and S. Imperiale. Stability and dispersion analysis of improved time discretization for simply supported prestressed Timoshenko systems. Application to the stiff piano string. *Wave Motion*, 50(3):456–480, 2013.

[33] M. Ducceschi and S. Bilbao. Linear stiff string vibrations in musical acoustics: Assessment and comparison of models. *The Journal of the Acoustical Society of America*, 140(4):2445–2454, 2016.

[34] H. Conklin Jr. Generation of partials due to nonlinear mixing in a stringed instrument. *The Journal of the Acoustical Society of America*, 105(1):536–545, 1999.

[35] N. Giordano and A. Korty. Motion of a piano string: Longitudinal vibrations and the role of the bridge. *The Journal of the Acoustical Society of America*, 100(6):3899–3908, 1996.

[36] B. Bank and L. Sujbert. Generation of longitudinal vibrations in piano strings: From physics to sound synthesis. *The Journal of the Acoustical Society of America*, 117(4):2268–2278, 2005.

[37] J. Chabassier and P. Joly. Energy preserving schemes for nonlinear hamiltonian systems of wave equations: Application to the vibrating piano string. *Computer Methods in Applied Mechanics and Engineering*, 199:2779–2795, 11 2010.

[38] E. Kurmyshev. Transverse and longitudinal mode coupling in a free vibrating soft string. *Physics Letters A*, 310(2):148–160, 2003.

[39] A. Mamou-Mani, J. Frelat, and C. Besnainou. Numerical simulation of a piano soundboard under downbearing. *The Journal of the Acoustical Society of America*, 123(4):2401–2406, 2008.

[40] K. Ege. *The piano soundboard - Modal studies in the low- and the mid-frequency range*. Phd thesis, École Polytechnique, 2009.

[41] A. Askenfelt. Sound radiation and timbre. *Mechanics of Playing and Making Musical Instruments*, 2006.

[42] J. Berthaut, M. Ichchou, and L. Jézéquel. Piano soundboard: structural behavior, numerical and experimental study in the modal range. *Applied Acoustics*, 64(11):1113–1136, 2003.

[43] H. Suzuki. Vibration and sound radiation of a piano soundboard. *The Journal of the Acoustical Society of America*, 80(6):1573–1582, 1986.

[44] K. Ege, X. Boutillon, and M. Rébillat. Vibroacoustics of the piano soundboard : (non) linearity and modal properties in the low-and mid-frequency ranges. *Journal of Sound and Vibration*, 332(5):1288–1305, 2013.

[45] T. Moore and S. Zietlow. Interferometric studies of a piano soundboard. *The Journal of the Acoustical Society of America*, 119(3):1783–1793, 2006.

[46] A. Chaigne, B. Cotté, and R. Viggiano. Dynamical properties of piano soundboards. *The Journal of the Acoustical Society of America*, 133(4):2456–2466, 2013.

[47] K. Wogram. Acoustical research on pianos: vibrational characteristics of the soundboard. *Das Musikinstrument*, 24:694–702, 1980.

[48] I. Nakamura. The vibrational character of the piano soundboard. In *Proceedings of the 11th ICA*, volume 4, pages 385–388, 1983.

[49] H. Conklin. Design and tone in the mechanoacoustic piano. part ii. piano structure. *The Journal of the Acoustical Society of America*, 100(2):695–708, 1996.

[50] N. Giordano. Mechanical impedance of a piano soundboard. *The Journal of the Acoustical Society of America*, 103(4):2128–2133, 1998.

[51] X. Boutillon and G. Weinreich. Three-dimensional mechanical admittance: Theory and new measurement method applied to the violin bridge. *The Journal of the Acoustical Society of America*, 105(6):3524–3533, 1999.

[52] X. Boutillon and K. Ege. Vibroacoustics of the piano soundboard: Reduced models, mobility synthesis, and acoustical radiation regime. *Journal of Sound and Vibration*, 332(18):4261–4279, 2013.

[53] B. Trévisan, K. Ege, and B. Laulagnet. A modal approach to piano soundboard vibroacoustic behavior. *The Journal of the Acoustical Society of America*, 141(2):690–709, 2017.

[54] V. Debut, J. Antunes, M. Marques, and M. Carvalho. Physics-based modeling techniques of a twelve-string portuguese guitar: A non-linear time-domain computational approach for the multiple-strings/bridge/soundboard coupled dynamics. *Applied Acoustics*, 108:3–18, 2016.

[55] J. Smith. Physical modeling using digital waveguides. *Computer Music Journal*, 16(4):74–91, 1992.

[56] B. Bank. *Physics-based sound synthesis of the piano*. PhD thesis, Helsinki University of Technology, 2000.

[57] J. Bensa, S. Bilbao, R. Kronland-Martinet, and J. Smith III. The simulation of piano string vibration: From physical models to finite difference schemes and digital waveguides. *The Journal of the Acoustical Society of America*, 114(2):1095–1107, 2003.

[58] J. Rauhala, V. Välimäki, and H.-M. Lehtonen. Multi-ripple loss filter for waveguide piano synthesis. In *Proceeding of International Computer Music Conference*, 2005.

[59] J. Bensa, S. Bilbao, R. Kronland-Martinet, J. Smith, and T. Voinier. Computational modeling of stiff piano strings using digital waveguides and finite differences. *Acta Acustica united with Acustica*, 91(2):289–298, 2005.

[60] S. Bilbao. *Numerical Sound Synthesis: Finite Difference Scheme and Simulation in Musical Acoustics*. Wiley Online Library, 2009.

[61] A. Chaigne and A. Askenfelt. Numerical simulations of piano strings. i. a physical model for a struck string using finite difference methods. *The Journal of the Acoustical Society of America*, 95(2):1112–1118, 1994.

[62] N. Giordano and M. Jiang. Physical modeling of the piano. *EURASIP J. Appl. Signal Process.*, 2004:926–933, January 2004.

[63] J. Chabassier, A. Chaigne, and P. Joly. Modeling and simulation of a grand piano. *The Journal of the Acoustical Society of America*, 134(1):648–665, 2013.

[64] A. Stulov. Hysteretic model of the grand piano hammer felt. *The Journal of the Acoustical Society of America*, 97(4):2577–2585, 1995.

[65] N. Giordano. Simple model of a piano soundboard. *The Journal of the Acoustical Society of America*, 102(2):1159–1168, 1997.

[66] A. Chaigne, M. Hennet, J. Chabassier, and M. Duruflé. Comparison between three different Viennese pianos of the nineteenth century. In *Proceedings of the 22nd International Congress on Acoustics*, pages ICA2016–025, 2016.

[67] J. Chabassier. Modeling the influence of the piano hammer shank flexibility on the sound. *The Journal of the Acoustical Society of America*, 136(4):2133–2133, 2014.

[68] J. Chabassier, A. Chaigne, and P. Joly. Time domain simulation of a piano. Part 1: model description. *ESAIM: Mathematical Modelling and Numerical Analysis*, 48(5):1241–1278, 2014.

[69] G. Weinreich. The coupled motions of piano strings. *Scientific American*, 240:118–127, 1979.

[70] R. Hanson, J. Anderson, and H. Macomber. Measurements of nonlinear effects in a driven vibrating wire. *The Journal of the Acoustical Society of America*, 96(3):1549–1556, 1994.

[71] R. Hanson, H. Macomber, A. Morrison, and M. Boucher. Primarily nonlinear effects observed in a driven asymmetrical vibrating wire. *The Journal of the Acoustical Society of America*, 117(1):400–412, 2005.

[72] Viennese Craftsmanship - About - Bösendorfer. https://www.boesendorfer.com/en/about/craftsmanship. Accessed: 2017-06-13.

[73] P. Morse and K. Ingard. *Theoretical Acoustics*. McGraw-Hill, 1968.

[74] A.H. Nayfeh and D.T. Mook. *Nonlinear Oscillations*. Wiley, 1979.

[75] J. Chabassier. *Modélisation et simulation numérique d'un piano par modèles physiques*. PhD thesis, École Polytechnique, 2012.

[76] S. Bilbao. Conservative numerical methods for nonlinear strings. *The Journal of the Acoustical Society of America*, 118(5):3316–3327, 2005.

[77] C. Touzé, O. Thomas, and A. Chaigne. Asymmetric non-linear forced vibrations of free-edge circular plates. part 1: Theory. *Journal of Sound and Vibration*, 258:649, 2002.

[78] O. Thomas, A. Lazarus, and C. Touzé. A harmonic-based method for computing the stability of periodic oscillations of non-linear structural systems. In *Proceedings of the ASME 2010 International Design Engineering Technical Conferences and Computers and Information in Engineering Conference*, 2010.

[79] A. Manevitch and L. Manevitch. Free oscillations in conservative and dissipative symmetric cubic two-degree-of-freedom systems with closed natural frequencies. *Meccanica*, 2003.

[80] C. Valette and C. Cuesta. Evolution temporelle de la vibration des cordes de clavecin. *Acta Acustica united with Acustica*, 66(1):37–45, 1988.

[81] Montjoie user's guide. http://montjoie.gforge.inria.fr/overview.php. Accessed: 2017-08-10.

[82] C. Desvages, S. Bilbao, and M. Ducceschi. Improved frequency-dependent damping for time domain modelling of linear string vibration. In *Proceedings of the 22nd International Congress on Acoustics*, pages ICA2016–821, 2016.

[83] C. Issanchou, S. Bilbao, J.-L. Le Carrou, C. Touzé, and O. Doaré. A modal-based approach to the nonlinear vibration of strings against a unilateral obstacle: Simulations and experiments in the pointwise case. *Journal of Sound and Vibration*, 393:229 – 251, 2017.

[84] B. Chabassier and M. Durufle. Physical parameters for piano modeling. Technical Report RT-0425, INRIA, April 2012.

[85] J.J. Thomsen. *Vibrations and Stability: Advanced Theory, Analysis, and Tools*. Springer complexity. Springer, 2003.

[86] J. J. Tan, C. Touzé, and B. Cotté. Double polarisation in nonlinear vibrating piano strings. In *Vienna talk 2015 on music Acoustics*, Vienna, Austria, September 2015.

[87] Corde | Pianos Stephen Paulello. http://www.stephenpaulello.com/cordes. Accessed: 2017-08-12.

[88] Jean-Loïc Le Carrou, François Gautier, and Roland Badeau. Sympathetic string modes in the concert harp. *Acta Acustica united with Acustica*, 95(4):744–752, 2009.

[89] K. Ege, X. Boutillon, and B. David. High-resolution modal analysis. *Journal of Sound and Vibration*, 325(4):852–869, 2009.

[90] A. Chaigne and J. Kergomard. *Acoustics of Musical Instruments*. Springer-Verlag, New York, 2016.

[91] Grégoire Derveaux. *Modélisation numérique de la guitare acoustique.* Thèses, École Polytechnique, 2002.

[92] A. Chaigne, J. Chabassier, and N. Burban. Acoustics of pianos: physical modeling, simulations and experiments. In *SMAC 2013-Stockholm Music Acoustics Conference 2013*, 2013.

[93] J.J. Tan, A. Chaigne, and A. Acri. Contribution of the vibration of various piano components in the resulting piano sound. In *Proceedings of the 22nd International Congress on Acoustics*, pages ICA2016–171, 2016.

[94] A. Stulov and D. Kartofelev. Vibration of strings with nonlinear supports. *Applied Acoustics*, 76:223–229, 2014.

[95] R. Corradi, S. Miccoli, G. Squicciarini, and P. Fazioli. Modal analysis of a grand piano soundboard at successive manufacturing stages. *Applied Acoustics*, 125:113–127, 2017.

[96] N. B. Roozen, Q. Leclere, and C. Sandier. Operational transfer path analysis applied to a small gearbox test set-up. In *Proceedings of the Acoustics 2012 Nantes Conference*, pages 3467–3473, 2012.

[97] D. De Klerk, M. Lohrmann, M. Quickert, and W. Foken. Application of operational transfer path analysis on a classic car. In *Proceedings of the International Conference on Acoustics NAG/DAGA 2009*, pages 776–779, 2009.

[98] J. Putner, H. Fastl, M. Lohrmann, A. Kaltenhauser, and F. Ullrich. Operational transfer path analysis predicting contributions to the vehicle interior noise for different excitations from the same sound source. In *Proc. Internoise*, pages 2336–2347, 2012.

[99] M. Toome. Operational transfer path analysis: A study of source contribution predictions at low frequency. Master's thesis, Chalmers University of Technology, Sweden, 2012.

[100] D. de Klerk and A. Ossipov. Operational transfer path analysis: Theory, guidelines and tire noise application. *Mechanical Systems and Signal Processing*, 24(7):1950–1962, 2010.

[101] A. Diez-Ibarbia, M. Battarra, J. Palenzuela, G. Cervantes, S. Walsh, M. Dela Cruz, S. Theodossiades, and .L Gagliardini. Comparison between transfer path analysis methods on an electric vehicle. *Applied Acoustics*, 118:83–101, 2017.

[102] P. Gajdatsy, K. Janssens, W. Desmet, and H. Van Der Auweraer. Application of the transmissibility concept in transfer path analysis. *Mechanical Systems and Signal Processing*, 24(7):1963–1976, 2010.

[103] C. Sandier, Q. Leclere, and N. B. Roozen. Operational transfer path analysis: theoretical aspects and experimental validation. In *Proceedings of the Acoustics 2012 Nantes Conference*, pages 3461–3466, 2012.

[104] R. Penrose. A generalized inverse for matrices. *Mathematical Proceedings of the Cambridge Philosophical Society*, 51(3):406–413, 1955.

[105] N. Maia, J. Silva, and A. Ribeiro. The transmissibility concept in multi-degree-of-freedom systems. *Mechanical Systems and Signal Processing*, 15(1):129–137, 2001.

[106] W. Goebl, R. Bresin, and I. Fujinaga. Perception of touch quality in piano tones. *The Journal of the Acoustical Society of America*, 136(5):2839–2850, 2014.

université PARIS-SACLAY
ÉCOLE DOCTORALE
Sciences mécaniques et énergétiques, matériaux et géosciences (SMEMAG)

Titre : Acoustique du piano : double polarisation de la corde et identification de sources

Mots clefs : modele physique de piano, simulation numerique, corde, chevalet, identification de sources

Résumé : L'objectif de cette thèse est d'améliorer la compréhension de l'acoustique du piano dans le contexte de la synthèse sonore par modèles physiques. Le manuscrit est décomposé en trois parties principales, dont les deux premières ont pour but la compréhension de l'origine de la double polarisation de la corde de piano, tandis que la dernière se focalise sur l'identification de sources d'un piano complet.
Dans la première partie, la non linéarité géométrique, intervenant lorsque les amplitudes de vibration sont grandes, est étudiée afin de comprendre si le couplage non linéaire peut transmettre de l'énergie à une polarisation non initialement excitée et mener ainsi au phénomène de double polarisation. Un développement en échelles multiples est mené sur un modèle de corde de Kirchhoff-Carrier avec les deux extrémités fixes, restreint au mode fondamental de chacune des polarisations. Les deux oscillateurs ont alors des fréquences très proches, on parle de résonance 1:1. La condition d'existence et le critère de stabilité pour l'apparition de double polarisation sont obtenus et validés numériquement sur la base des équations de Kirchhoff-Carrier, ainsi qu'avec un modèle de corde enrichi. Des expériences sont menées sur un dispositif monocorde où les angles de polarisation naturelle de la corde, le désaccord entre les deux polarisations et le comportement non linéaire son observés et identifiés.
La seconde partie se concentre sur le couplage entre la corde et le chevalet. Les degrés de liberté de la corde sont couplés au chevalet dont les mouvements (translation/rotation) sont représentés par un ensemble d'oscillateurs. Les fréquences propres des différents systèmes couplés sont analysés. Des schémas numériques sont proposés et mis en œuvre pour une résolution directe. Ces schémas résolvent les équations de corde par une méthode d'éléments finis d'ordre élevé et les équations du chevalet analytiquement. Les conditions de couplage entre corde et chevalet sont assurées par des multiplicateurs de Lagrange. Expérimentalement, la corde est tendue sur le chevalet dans une configuration de type zig-zag et excitée verticalement ou horizontalement. Dans les deux cas, les phénomènes de double polarisation et de double décroissance sont observés et des résultats qualitativement similaires sont obtenus avec les modèles numériques.
La dernière partie s'attache à décrire quantitativement les différentes sources vibro-acoustiques d'un piano complet. Une étude est menée en utilisant une analyse des chemins de transfert (transfer path analysis en anglais) sur un piano Bösendorfer 280VC-9. Les contributions de la table d'harmonie, des parties interne et externe de la ceinture, du cadre en fonte et du couvercle sont étudiées dans le domaine fréquentiel. L'analyse montre que la table d'harmonie est le principal contributeur mais que le cadre en fonte et le couvercle jouent également un rôle significatif, en particulier à hautes fréquences.

Title : Piano acoustics: string's double polarisation and piano source identification

Keywords : physical modelling of piano, numerical simulation, string, bridge, source identification

Abstract : The objective of this thesis is to improve the understanding of the acoustics of the piano in the context of physically-based sound synthesis. The manuscript is decomposed in three parts, the first two being devoted to the understanding of the origin of the double polarisation in piano string, while the third one is dedicated to the identification of sound sources of a complete piano.
In the first part, the geometric (large-amplitude) nonlinearity is studied in order to understand if the nonlinear coupling can transfer energy to an initially non excited polarisation, thus leading to the double polarisation phenomenon. A multiple-scale analysis is conducted on a Kirchhoff-Carrier string model with fixed boundary conditions at both ends. Each polarisation is restrained to its fundamental mode and thus presenting a 1:1 internal resonance. The existence condition and stability criteria for double polarisation to occur are obtained and validated numerically based on the Kirchhoff-Carrier equations, as well as a more enriched geometrically exact string model. Experiments are carried out on a monochord setup where the natural polarisation angles of the string, detuning between the two polarisations and its nonlinear behaviour are observed and identified.
The second part is devoted to the string/bridge coupling. The degrees of freedom of the string are coupled to the bridge whose translational and rotational motions are represented by a set of oscillators. The eigenfrequencies of various coupled systems are analysed. Numerical schemes are proposed and implemented where the string is solved via high-order finite-element method while the lumped bridge is solved analytically and coupled to the string by Lagrange multipliers. Experimentally, the string is strung over a bridge in a zig-zag configuration and excited vertically and horizontally. In both cases, double polarisation and double decay are observed and similar results are also obtained qualitatively in numerical models.
The last part is devoted to a quantitative description of the vibroacoustic sources of a Bösendorfer 280VC-9 piano via operational transfer path analysis. The contribution of the soundboard, inner and outer rim, iron frame and lid are investigated in the frequency domain. It is found out that the soundboard is the primary contributor but the iron frame and the lid also play a significant role, especially at high frequencies.

Université Paris-Saclay
Espace Technologique / Immeuble Discovery
Route de l'Orme aux Merisiers RD 128 / 91190 Saint-Aubin, France